A Study of the LHCb Experiment's Sensitivity to CP Violation in Mixing and to Production Asymmetry in B_s Mesons, Using Semi-Leptonic Decays

Kenneth Lessnoff

A dissertation submitted to the University of Bristol in accordance with the requirements of the degree of PhD in the Faculty of Science, Department of Physics

$\approx$ 32,000 words

Abstract

LHCb is a detector that will operate at the LHC at CERN. It is designed to make specialised studies of B physics, in particular studies of CP violation and rare decays. In this thesis, three studies pertaining to LHCb are presented.

The optical properties of the mirrors used in the RICH 1 subdetector were measured, and the aging effects of the LHCb environment investigated. All mirrors were within design specifications. No degradation of mirrors has been observed after 11 months exposure to C_4F_{10} gas, nor after a 10 kGy radiation dose.

The Monte Carlo generator Pythia is used by LHCb for event simulation. A re-tuning of Pythia was undertaken to improve the modeling of LEP data. A substantial improvement was achieved. A retuning of the $p_{\perp min}$ parameter, which controls Pythia's multiple-interaction model, was also required. The retuned value is $p_{\perp min} = 3.45\,\mathrm{GeV}$.

A study was made of LHCb experiment's ability to measure CP violation in mixing and production asymmetry using semi-leptonic B_s decays. The method uses kinematic constraints to calculate the momentum of the neutrino. CP violation is characterised by the parameter a_{fs}. The resolution for a_{fs} was found to be $\sigma_{a_{fs}} = 1.34 \times 10^{-3}$, and for the production asymmetry, $\sigma_{A_p} = 16.5 \times 10^{-3}$ for 2.2×10^6 events, one year's data.

Acknowledgements

Many people have helped me with the work presented in this thesis, and deserve great thanks for doing so.

First and foremost, I wish to thank my supervisor Prof. Nick Brook. He has provided help and support throughout my studies and with all aspects of this thesis; this has proved invaluable. While I regret descending into cliché, it is true to say that, without him none of this would have been possible. Thank you, Nick.

I would also like to thank Dr Paul Szczypka. He has provided help with and advice on all areas of study presented in this thesis. Further to this, he was kindly supportive during my move to Geneva, and altruistically provided proof-reading. Additionally, his constant badgering of me to finish my thesis has meant that I have finished in something vaguely approximating a respectable timescale.

I thank Dr Jonas Rademacker, Dr Marco Adinolfi and Dr Rob Lambert for their assistance and support with my study of CP violation in mixing and production asymmetry. Their help and insight with this section of my thesis has been enormously useful.

I thank the Dr Fabio Metlica, Dr Carmelo D'Ambrosio and Andre Bream and the LHCb RICH group for their help with my work characterising the RICH 1 mirrors.

Dr Gloria Corti and Dr Patrick Robbe deserve many thanks for their assistance in my work retuning Pythia, and their helping me understand the relevant software.

I would like to thank the various people I have shared an office with, for providing a pleasant and stimulating working environment. In no particular order: Dr Dave Evans, Dr Mark Grimes, Fern Watson, Dr Fabio Metlica, Dr Sajan Easo, Dr Paul Szczypka, Dr Jeremy Dickens and Jon Imong.

Lastly, I would like to thank my parents for their kind support, encouragement, proof-reading and whatnot.

Of course, the remaining mistakes in this thesis are my responsibility and not that of those who have assisted me.

AUTHOR'S DECLARATION

I declare that the work in this dissertation was carried out in accordance with the Regulations of the University of Bristol. The work is original except where indicated by special reference in the text and no part of the dissertation has been submitted for any other degree. Any views expressed in the dissertation are those of the author and in no way represent those of the University of Bristol. The dissertation has not been presented to any other University for examination either in the United Kingdom or overseas.

SIGNED: .... DATE: ....

Contents

List of Figures

List of Tables

Chapter 1

Introduction

The LHCb detector is designed to study CP violation and rare decays in B hadrons, at the LHC. Three studies relating to LHCb are presented in this thesis:

- A characterisation of the RICH 1 mirrors.
- A retuning of the Pythia parameters used for event generation.
- A study of the sensitivity to CP violation and production asymmetry in semi-leptonic B_s decays.

The structure of the thesis is as follows.

In chapter 2 brief overviews of the standard model of particle physics, and of CP violation are given. The formalism to describe neutral B mixing is developed.

In chapter 3 a discussion of the various LHC experiments is given. Particular focus is given to LHCb, with details given on its various subdetectors and software.

In chapter 4 the RICH 1 mirror studies are presented. Various studies were made of the RICH 1 spherical mirrors. The radius of curvature and D_0 were measured to ensure they met design specifications. The reflectivities of sample mirrors were measured, to ensure that an adequate reflective coating could be produced. The stability of the optical properties over time was examined. The physical dimensions and optical properties of the RICH 1 flat mirrors were also measured. The measurements of radius of curvature,

D_0 and the mirrors' physical dimensions were taken jointly by the author and Dr Fabio Matlica. The measurements of the mirrors' reflectivity were done by the author.

Pythia tuning studies are presented in chapter 5. A retuning was undertaken to give a better description of LEP data; the previous LHCb tune over-produced various types of meson and gave too high a charged multiplicity in e^+e^- collisions. An improved reproduction of LEP data was achieved by tuning the Pythia parameters PARJ(11),...,PARJ(17), which control the probabilities of mesons being produced in different spin states. Retuning these parameters lowered the modeled charged multiplicity in hadronic collisions, which had previously been correctly described. A further retuning, of Pythia's multiple interaction model, was therefore also required. The author was responsible for generating Monte Carlo data and for writing the code which compaired them with experimental data.

In chapter 6 a study of the sensitivity to CP violation and production asymmetry in semi-leptonic B_s decays is presented. The neutrino in the final state cannot be detected, however its momentum can be calculated if the direction of the B_s is known, and the momenta of the other daughters are known. The neutrino momentum is given by a quadratic equation, so there is ambiguity in the momentum solution. Different ways for dealing with this ambiguity are examined. The results are compared with alternative methods for measured CP violation in mixing and production asymmetry. The author is responsible for developing and testing the analysis strategies used for analising the the B_s data. The analysis required the use of various toy Monte Carlo simulations. These were written by the author, but based upon code originally written by Dr Paul Szczypka. Fully reconstructed data are used to inform the toy Monte Carlo, these were generated by Dr Rob Lambert using the LHCb analysis software.

Chapter 2

Theory

In this chapter a brief introduction to the Standard Model is given. The operators C, P and T are introduced, and the CKM mixing matrix is discussed. The formalism for discussing neutral B mixing is developed, and the three different types of CP violation are introduced.

2.1 The Standard Model

The interactions of fundamental particles are currently best described by the Standard Model of particle physics [1, 2]. Within the Standard Model, SM, there are two types of fundamental matter particle: quarks and leptons. They interact via three forces: the strong force, the weak force and the electromagnetic force; gravity is omitted. The leptons are distinguished from the quarks in that they do not interact via the strong force. Both quarks and leptons are spin 1/2 fermions. There are six leptons and six quarks, together with their anti-particles. These are listed below

$$\text{Leptons}: \quad \begin{pmatrix} e^- \\ \nu_e \end{pmatrix} \quad \begin{pmatrix} \mu^- \\ \nu_\mu \end{pmatrix} \quad \begin{pmatrix} \tau^- \\ \nu_\mu \end{pmatrix}$$

$$\text{Quarks}: \begin{pmatrix} u \\ d \end{pmatrix} \begin{pmatrix} c \\ s \end{pmatrix} \begin{pmatrix} t \\ b \end{pmatrix}$$

Interactions are introduced by requiring that the SM Lagrangian exhibits local gauge invariance. This requires the inclusion of fields which describe the spin 1 bosons that mediate the forces. Specifically, the theory is invariant under local gauge transforms of the group

$$SU(3) \times SU(2) \times U(1) \tag{2.1}$$

The $SU(3)$ symmetry results in interactions via the strong force, the $SU(2) \times U(1)$ symmetry gives rise to the electroweak interaction. The bosons which mediate the electroweak force are the photon, the $W^{\pm}$ and the Z, the strong force is mediated by gluons. Masses are given to these particles via their interaction with the Higgs field.

2.2 CP Violation

It was once believed that physics was invariant under the discreet symmetries of charge conjugation, which replaces particles with their anti-particles, and parity, which inverts the space coordinate axes. However, physics is not invariant under either of these operations. Neutrinos provide an example of non-invariance under these operations. Neutrinos only exist in a left-handed state, and anti-neutrinos exist only in a right-handed state. The act of charge conjugation, C, replaces a left-handed neutrino with a left-handed anti-neutrino. It can be seen, therefore, that C is not conserved. The parity operation, P, replaces a left-handed neutrino with a right-handed neutrino, and so it can be seen that P is not conserved.

The combined operation of CP was once thought to be a conserved quantity, however this is not the case. CP violation was first observed in the kaon system [3]. CP violation is an important phenomenon; it is a necessary condition for there to be a matter anti-matter asymmetry in the universe [4]. The degree of CP violation found in the standard model is not sufficient to explain the extent of the observed asymmetry however, and so the study of CP violation is ongoing.

2.2.1 The Operators C, P and T

The charge conjugation operator, C, replaces particles with their anti-particles. The parity operator, P, effects an inversion of the space coordinate axes. An inversion of the time coordinate is given by the time reversal operator, T. All of these operators are self-inverse and have eigenvalues of ± 1. The operators have the following effect on the fermion fields [5, 6]

$$\Psi(t, \boldsymbol{x}) \rightarrow \Psi^C(t, \boldsymbol{x}) = i\gamma^2 \Psi^*(t, \boldsymbol{x}) \tag{2.2}$$

$$\Psi(t, \boldsymbol{x}) \rightarrow \Psi^P(t, \boldsymbol{x}) = \gamma^0 \Psi(t, -\boldsymbol{x}) \tag{2.3}$$

$$\Psi(t, \boldsymbol{x}) \rightarrow \Psi^T(t, \boldsymbol{x}) = -\gamma^1 \gamma^3 \Psi(-t, \boldsymbol{x}) \tag{2.4}$$

where the Ψ is a 4 component spinor. The γ matrices and 4×4 matrices, defined by

$$\gamma^0 = \beta; \quad \gamma^i = \beta \alpha^i, \quad i = 1, 2, 3 \tag{2.5}$$

with the matrices α and β defined by their commutation relations

$$\begin{aligned} \beta^2 = I; \quad \alpha_1^2 = \alpha_2^2 &= \alpha_3^2 = I \\ \alpha_i \alpha_j + \alpha_j \alpha_i = 0, &\qquad i \neq j \\ \alpha_i \beta + \beta \alpha_i, &\qquad i = 1, 2, 3 \end{aligned} \tag{2.6}$$

The α and β matrices appear in the Dirac equation, which describes spin 1/2 particles. The conditions 2.6 ensure that particles have the correct energy-momentum relationship, $E^2 = p^2 + m^2$. The simplest objects satisfying equation 2.6 are 4×4 matrices. It is for this reason that fermions are described by four-component spinors.

Under C, P and T, spin 1 fields transform as [6]

$$A_\mu(t,\boldsymbol{x}) \to A_\mu^C(t,\boldsymbol{x}) = -A_\mu(t,\boldsymbol{x}) \tag{2.7}$$

$$A_\mu(t,\boldsymbol{x}) \to A_\mu^P(t,\boldsymbol{x}) = A^\mu(t,-\boldsymbol{x}) \tag{2.8}$$

$$A_\mu(t,\boldsymbol{x}) \to A_\mu^T(t,\boldsymbol{x}) = A^\mu(-t,\boldsymbol{x}) \tag{2.9}$$

2.2.2 The CPT Theorem

The CPT Theorem states that any local field theory is invariant under the combined operation of CPT. A consequence of this theorem is that the masses and widths of particles are equal to the masses and widths of their anti-particles

$$M(P) = M(\bar{P}), \quad \Gamma(P) = \Gamma(\bar{P}) \tag{2.10}$$

Another consequence is that any violation of CP symmetry must also correspond to a violation of T symmetry.

2.3 CP Violation and the CKM Matrix

The quarks that interact via the weak interaction are superpositions of mass eigenstates. The CKM matrix, V, links the mass eigenstates for the down-type quarks, (d, s, b), with the weak eigenstates, $(\tilde{d}, \tilde{s}, \tilde{b})$

$$\begin{pmatrix} \tilde{d} \\ \tilde{s} \\ \tilde{b} \end{pmatrix} = \begin{pmatrix} V_{ud} & V_{us} & V_{ub} \\ V_{cd} & V_{cs} & V_{cb} \\ V_{td} & V_{ts} & V_{tb} \end{pmatrix} \begin{pmatrix} d \\ s \\ b \end{pmatrix} \tag{2.11}$$

The CKM matrix enters the SM Lagrangian density in the terms describing the interaction of quarks with $W^\pm$ bosons

$$\mathcal{L}_{qW} = -\frac{e}{\sqrt{2}\sin\theta_w} \sum_{i,j} \left(\bar{u}_{Li}\gamma^\mu V_{ij} d_{Lj} W_\mu^+ + \bar{d}_{Li}\gamma^\mu V_{ij}^* u_{Lj} W_\mu^- \right) \tag{2.12}$$

where θ_w is the weak mixing angle, e is the electron charge. The factor premultiplying the summation defines the strength of the interaction. $u_{L,i}$ and $d_{L,i}$ are the spinors describing the three up-type and the three down-type quarks, $W_\mu^\pm$ are the fields which describe the charged weak bosons. The summation is over the three generations of quarks.

Under the operation of CP equation 2.12 becomes

$$\mathcal{L}_{qW}^{CP} = -\frac{e}{\sqrt{2}\sin\theta_w}\sum_{i,j}\left(\bar{d}_{Li}\gamma^\mu V_{ij} u_{Lj} W_\mu^- + \bar{u}_{Li}\gamma^\mu V_{ij}^* d_{Lj} W_\mu^+\right) \tag{2.13}$$

It can be seen from a comparison of equations 2.12 and 2.13 that CP is only conserved if the elements of the CKM matrix are real.

The CKM matrix is 3×3 unitary matrix. Such matrices have nine free parameters. In the case of the generalised CKM matrix, five of these may be absorbed into the quark phases, leaving four parameters. These correspond to three rotation angles and a complex phase, which is the source of CP violation in the SM. The three angles describe quark mixing, and allow for transitions between the different generations.

In the quark system, the mass eigenstates are not the same as the states which interact via the weak force. Similarly, the neutrino states e, μ, τ are not mass eigenstates, but rather superpositions of them. They are linked to mass eigenstates by a 3×3 unitary mixing matrix. As with the CKM matrix, there are four free parameters to be determined by experiment. As with the quark system, there are three mixing angles and a phase. This allows for CP violation, but at the time of writing, no CP violation has been observed in neutrinos.

2.3.1 The Wolfenstein Parameterisation

A common parameterisation for the CKM matrix is the Wolfenstein Parameterisation [7, 5], given in equation 2.14. The CKM elements are expanded in powers of $\lambda = |V_{us}| \approx 0.22$. There are four Wolfenstein parameters, λ, A, ρ and η. The parameterisation is chosen such that they are all of order unity. The CP violating phase is η.

$$\begin{pmatrix} V_{ud} & V_{us} & V_{ub} \\ V_{cd} & V_{cs} & V_{cb} \\ V_{td} & V_{ts} & V_{tb} \end{pmatrix} = \begin{pmatrix} 1-\frac{\lambda^2}{2} & \lambda & A\lambda^3(\rho - i\eta) \\ -\lambda & 1-\frac{\lambda^2}{2} & A\lambda^2 \\ A\lambda^3(1-\rho-i\eta) & -A\lambda^2 & 1 \end{pmatrix} + \mathcal{O}(\lambda^4) \tag{2.14}$$

2.3.2 Unitarity Triangles

The CKM matrix is a unitary matrix, that is

$$V^\dagger V = VV^\dagger = I \tag{2.15}$$

Six of the unitarity conditions that arise from equation 2.15 can be expressed as triangles, known as unitarity triangles, in the complex plane. These conditions are

$$V_{us}V_{ub}^* + V_{cs}V_{cb}^* + V_{ts}V_{tb}^* = 0 \tag{2.16}$$

$$V_{ud}V_{ub}^* + V_{cd}V_{cb}^* + V_{td}V_{tb}^* = 0 \tag{2.17}$$

$$V_{ud}V_{us}^* + V_{cd}V_{cs}^* + V_{td}V_{ts}^* = 0 \tag{2.18}$$

$$V_{ud}V_{td}^* + V_{us}V_{ts}^* + V_{ub}V_{tb}^* = 0 \tag{2.19}$$

$$V_{cd}V_{tb}^* + V_{cs}V_{ts}^* + V_{cb}V_{tb}^* = 0 \tag{2.20}$$

$$V_{ud}V_{cd}^* + V_{us}V_{cs}^* + V_{ub}V_{cb}^* = 0 \tag{2.21}$$

All of the triangles have the same area [6], $|J|/2$ where J is given by

$$J = \mathrm{Im}\left(\sum_{m,n=1}^{3} V_{ij}V_{kl}V_{il}^*V_{kj}^*\epsilon_{ikm}\epsilon_{jln} \right) \tag{2.22}$$

where ϵ_{abc} is the Levi-Civita symbol.

Of the six triangles, two have sides of roughly equal length. These are the triangles given by equations 2.17 and 2.19, and they are shown in figure 2.1. These two triangles are especially important in the study of CP; the relative length of their sides means that

Element	Value	Measurement Channel
$\lvert V_{ud}\rvert$	0.97418 ± 0.00027	Nuclear beta decays.
$\lvert V_{us}\rvert$	0.2255 ± 0.0019	Semi-leptonic kaon decays.
$\lvert V_{cd}\rvert$	0.230 ± 0.011	Neutrino scattering from valence d quarks.
$\lvert V_{cs}\rvert$	1.04 ± 0.06	Semi-leptonic D meson decays.
$\lvert V_{cb}\rvert$	$(41.2 \pm 1.1) \times 10^{-3}$	Semi-leptonic B meson decays.
$\lvert V_{ub}\rvert$	$(3.93 \pm 0.36) \times 10^{-3}$	Semi-leptonic B meson decays.
$\lvert V_{td}\rvert$	$(8.1 \pm 0.6) \times 10^{-3}$	B^0 mixing assuming $\lvert V_{tb}\rvert = 1$.
$\lvert V_{ts}\rvert$	$(38.7 \pm 2.3) \times 10^{-3}$	B^0_s mixing assuming $\lvert V_{tb}\rvert = 1$.
$\lvert V_{tb}\rvert$	> 0.74 (95% confidence limit)	Lower limit from semi-leptonic top decays.

Table 2.1: The current experimental status of the CKM elements.

measurements of the internal angles are feasible, which provides a test of CKM physics. The triangle given by equation 2.17 is given the name the "Unitarity Triangle." The angles of the Unitarity Triangle are given by

$$\alpha \equiv \arg\left[-\frac{V_{td}V^*_{tb}}{V_{ub}V^*_{ub}}\right], \quad \beta \equiv \arg\left[-\frac{V_{cd}V^*_{cb}}{V_{td}V^*_{tb}}\right], \quad \gamma \equiv \arg\left[-\frac{V_{ud}V^*_{ub}}{V_{cd}V^*_{cb}}\right] \tag{2.23}$$

An alternative naming scheme for the angles is sometimes used where α, β and γ are replaced with ϕ_2, ϕ_1 and ϕ_3 respectively.

Expanding up to $\mathcal{O}(\lambda^3)$, the only complex elements are V_{ub} and V_{td}. The angles β and γ therefore become

$$\beta = \arg V_{td} \tag{2.24}$$

$$\gamma = \arg V_{ub} \tag{2.25}$$

Physical processes suitable for measuring β and γ are therefore easily identifiable. They can be measured in processes involving $t \to d$ transitions and $b \to u$ transitions respectively. The current experimental status of the CKM elements is given in table 2.1. All data are taken from the Particle Data Group [8]

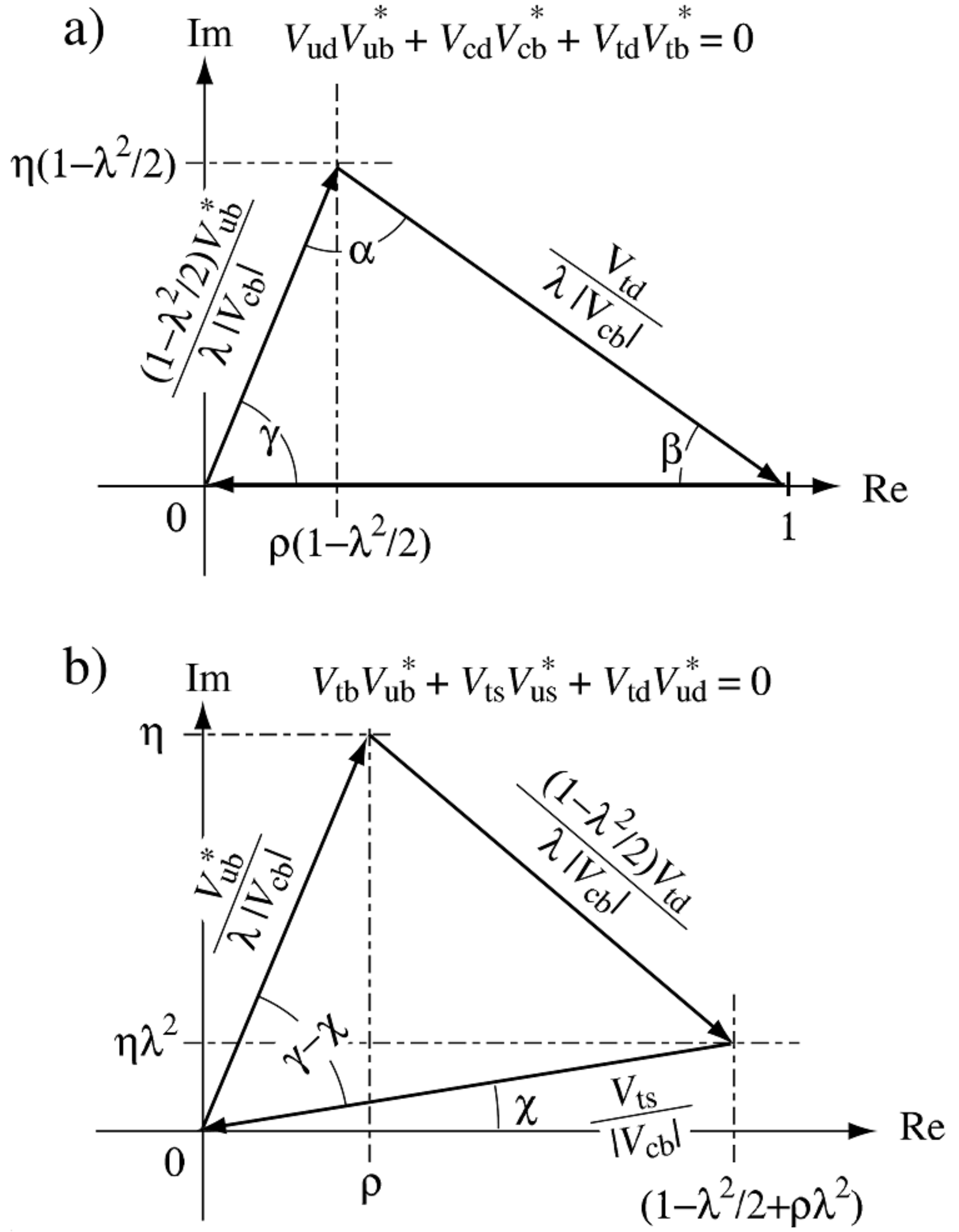

Figure 2.1: The unitarity triangles coming from equations 2.17 and 2.19. Both triangles have been scaled by a factor $V_{cd}V_{cb}^*$, meaning one side of the Unitarity Triangle lies along the real axis.

2.4 The Three Types of CP Violation

There are three distinct ways in which CP may be violated, which are discussed below. The three types of CP violation are

- Direct CP violation, which is also known as CP violation in decay.
- CP violation in mixing.
- CP violation in the interference between decays with and without mixing.

2.4.1 Direct CP Violation

It is useful to consider decays from an initial state B^0 or $\bar{B}^0$ to a final state f or $\bar{f}$, and to define the following amplitudes

$$A_f = \langle f|B^0\rangle \tag{2.26}$$
$$\bar{A}_f = \langle f|\bar{B}^0\rangle \tag{2.27}$$
$$A_{\bar{f}} = \langle \bar{f}|B^0\rangle \tag{2.28}$$
$$\bar{A}_{\bar{f}} = \langle \bar{f}|\bar{B}^0\rangle \tag{2.29}$$

CP is violated if

$$\left|\frac{A_f}{\bar{A}_{\bar{f}}}\right| \neq 1 \tag{2.30}$$

CP violation characterised by equation 2.30 is called Direct CP violation, or CP violation in decay.

Any complex term in the Lagrangian terms contributing to the amplitude A_f will appear in conjugate form in the CP conjugate amplitude. In the SM such terms only come from the CKM matrix, so the phases are called weak phases. Other phases may appear in A_f which do not change under CP. These come from contributions from intermediate on-shell states, and are dominated by the strong interaction and are hence called strong phases [5]. It is useful to write each contribution to A_f in three parts: its magnitude, A_i; its weak phase, $e^{i\phi_i}$; and its strong phase $e^{i\delta_i}$. The amplitudes are then given by

$$A_f = \sum_i A_i e^{i(\delta_i + \phi_i)}, \quad \bar{A}_{\bar{f}} = \sum_i A_i e^{i(\delta_i - \phi_i)} \tag{2.31}$$

where the sum is over all contributions to the decay amplitude. In a simple case, with just two contributions to the amplitudes

$$A_f = A_1 e^{i(\delta_1 + \phi_1)} + A_2 e^{i(\delta_2 + \phi_2)}, \quad \bar{A}_{\bar{f}} = A_1 e^{i(\delta_1 - \phi_1)} + A_2 e^{i(\delta_2 - \phi_2)} \tag{2.32}$$

the difference between the square of the amplitudes is

$$|A_f|^2 - |\bar{A}_{\bar{f}}|^2 = -4A_1 A_2 \sin(\phi_1 - \phi_2)\sin(\delta_1 - \delta_2) \tag{2.33}$$

Both the strong and the weak phases must differ for there to be direct CP violation. Any CP violation in charged B decays is direct CP violation; the other forms of CP violation require neutral meson mixing.

2.4.2 CP Violation in Mixing

CP violation can occur in neutral meson mixing. The formalism to describe $B_s^0 - \bar{B}_s^0$ mixing is developed below. The same formalism, with an appropriate change of notation, describes the mixing of other mesons.

The Schrödinger equation describing a superposition of flavour eigenstates, $a\,|B_s^0\rangle + b\,|\bar{B}_s^0\rangle$, is

$$i\frac{\mathrm{d}}{\mathrm{dt}}\begin{pmatrix} a \\ b \end{pmatrix} = \mathrm{H}\begin{pmatrix} a \\ b \end{pmatrix} \tag{2.34}$$

To describe the decay of the $a\,|B_s^0\rangle + b\,|\bar{B}_s^0\rangle$ state, H must be non-Hermitian. A general form for H can be constructed from two Hermitian matrices, M and Γ,

$$\mathrm{H} = \mathrm{M} - i\frac{1}{2}\Gamma \tag{2.35}$$

M represents the energy of the system, $i\frac{1}{2}\Gamma$ represents decay to other systems [9].

A consequence of CPT invariance is

$$\langle B_s^0 | \, \mathrm{H} \, | B_s^0 \rangle = \langle \bar{B}_s^0 | \, \mathrm{H} \, | \bar{B}_s^0 \rangle \tag{2.36}$$

which means that the diagonal elements of H are identical. H may therefore written as

$$\mathrm{H} = \begin{pmatrix} m - \frac{i}{2}\gamma & \mathrm{M}_{12} - \frac{i}{2}\Gamma_{12} \\ \mathrm{M}_{12}^* - \frac{i}{2}\Gamma_{12}^* & m - \frac{i}{2}\gamma \end{pmatrix} \tag{2.37}$$

where $m = \mathrm{M}_{11} = \mathrm{M}_{22}$ and $\gamma = \Gamma_{11} = \Gamma_{22}$ The eigenstates of H have well defined masses and decay widths. The eigenvalues, λ, are

$$\lambda_{H,L} = m - \frac{i}{2}\gamma \pm pq \tag{2.38}$$

where

$$p = \sqrt{\mathrm{M}_{12} - \frac{i}{2}\Gamma_{12}} \tag{2.39}$$

$$q = \sqrt{\mathrm{M}_{12}^* - \frac{i}{2}\Gamma_{12}^*} \tag{2.40}$$

p and q are the amplitudes which describe how the flavour eigenstates contribute to the mass eigenstates, given in equation 2.41.

$$|B_H\rangle = p\,|B^0\rangle - q\,|\bar{B}^0\rangle \,, \quad |B_L\rangle = p\,|B^0\rangle + q\,|\bar{B}^0\rangle \tag{2.41}$$

where the subscripts stand for heavy and light. Under CP the flavour eigenstates transform as

$$CP\,|B^0\rangle = -\,|\bar{B}^0\rangle \,, \quad CP\,|\bar{B}^0\rangle = -\,|B^0\rangle \tag{2.42}$$

For CP to be conserved the Hamiltonian operator must commute with the CP operator. For CP to be conserved, therefore, the mass eigenstates must also be CP eigenstates.

CP is therefore violated if

$$\left|\frac{q}{p}\right| \neq 1 \tag{2.43}$$

CP violation arising from 2.43 is referred to as CP violation in mixing.

2.4.2.1 Contributions to M_{12} and Γ_{12}

The off-diagonal elements of the matrices M and Γ are associated with flavour changing transitions. Γ_{12} is associated with transition via on-shell intermediate states, M_{12} with off-shell intermediate states [9, 8]. The main contributions to M_{12} and Γ_{12} come from the box diagrams shown in figure 2.2.

Γ_{12} receives contributions from diagrams containing u or c quarks. It is dominated by CKM-favoured tree-level decays and is therefore largely insensitive to new physics. M_{12} is, on the other hand, dominated by short range physics, and is much more susceptible to new physics contributions.

Measuring CP violation in mixing can constrain new physics. New physics can potentially lead to greater CP violation in mixing than the standard model, with some models leading to predictions of up to two orders of magnitude [10]. Measurement of CP violation is further discussed in section 2.5 and chapter 6.

2.4.3 CP Violation in the Interference Between Decays With and Without Mixing

CP violation can arise when a final state f is accessible via more than one decay path. Interference between the different paths can lead to CP violation, even if there is no direct CP violation or CP violation in mixing. To describe this, it is useful to define

$$\lambda_f = \frac{q}{p}\frac{\bar{A}_f}{A_f}, \quad \lambda_{\bar{f}} = \frac{q}{p}\frac{\bar{A}_{\bar{f}}}{A_{\bar{f}}} \tag{2.44}$$

CP is violated if

$$\lambda_{f,\bar{f}} \neq \pm 1 \tag{2.45}$$

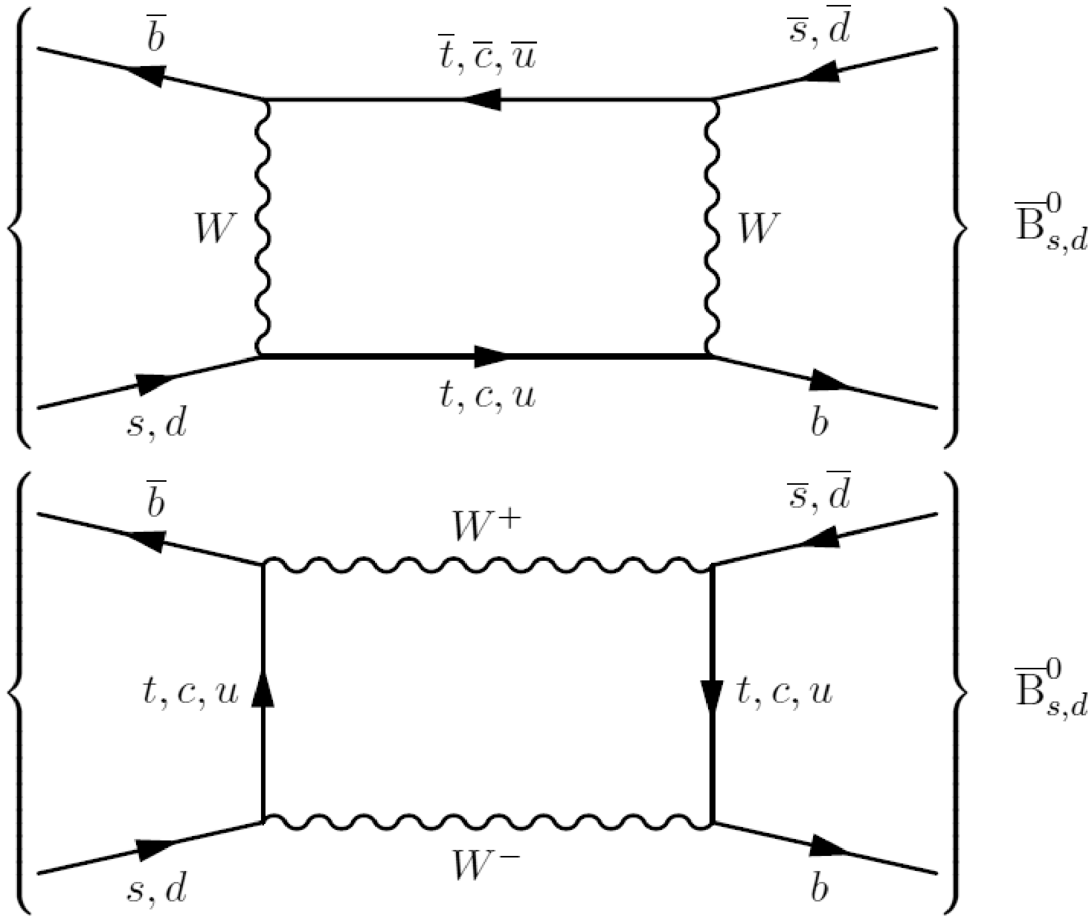

Figure 2.2: Leading order diagrams contributing to Γ_{12} and M_{12}.

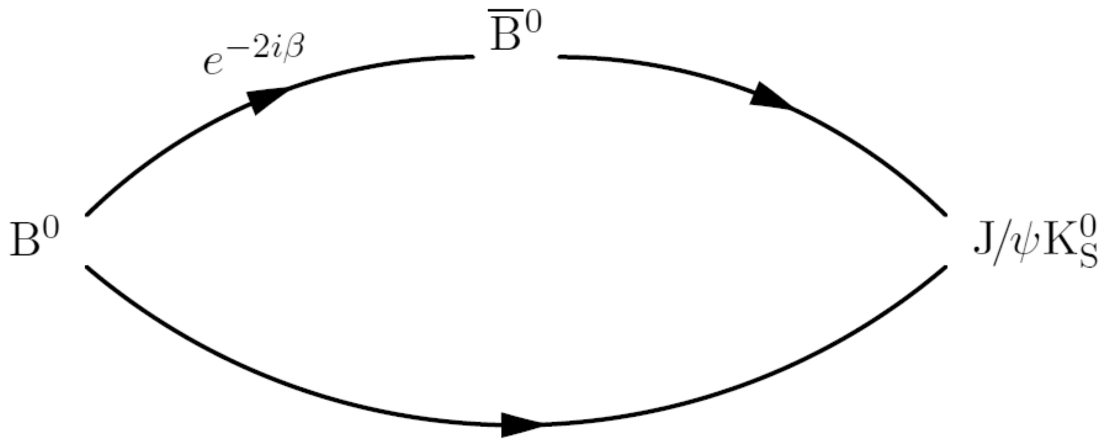

Figure 2.3: A schematic of the decay $B_d^0 \rightarrow J/\psi K_s^0$. The mixing introduces a phase difference between the two paths, which leads to CP violation.

Both direct CP violation and CP violation in mixing lead to condition 2.45. However, it is possible for 2.45 to be satisfied even if $|q/p| = 1$ and $|A_f/\bar{A}_{\bar{f}}| = 1$. The required condition is

$$\mathrm{Im}(\lambda_f) \neq 0 \tag{2.46}$$

Consider decays to CP eigenstates $|f\rangle$. Such states are available in both B_s^0 and $\bar{B}_s^0$ decays. An example is the decay $B_d^0 \rightarrow J/\psi K_s^0$, which is depicted in figure 2.3. The two paths interfere and produce a time dependent asymmetry in the decay rates $\Gamma_{B\rightarrow f}(t)$ and $\Gamma_{\bar{B}\rightarrow f}(t)$. The asymmetry is

$$a_f(t) = \frac{\Gamma_{B\rightarrow f}(t) - \Gamma_{\bar{B}\rightarrow f}(t)}{\Gamma_{B\rightarrow f}(t) + \Gamma_{\bar{B}\rightarrow f}(t)} \tag{2.47}$$

These time-dependent decay rates are derived in section 2.6. They contain terms in $\mathrm{Im}(\lambda_f)$, which mean $a_f(t)$ can be non-zero even if $|\lambda_f| = 1$.

2.5 Physical Observables Relating to Mixing

In section 2.4.2 CP violation in mixing was discussed. Mixing was described in terms of equation 2.34 and elements of the Hamiltonian 2.35. To measure CP violation in mixing one must relate these elements to physical observables. To do this, one must consider the time evolution of the states. This is governed by the Hamiltonian

$$|B_{L,H}, t\rangle = e^{-i\mathrm{H}t}\,|B_{L,H}, t = 0\rangle \tag{2.48}$$

For the mass eigenvectors, the Hamiltonian operator in equation 2.48 may be replaced with the eigenvalues. Doing so allows one to identify the masses and widths of the two eigenstates

$$m_{H,L} = m \pm \mathrm{Re}\left(\sqrt{\left(M_{12} - \frac{i}{2}\Gamma_{12}\right)\left(M_{12}^{*} - \frac{i}{2}\Gamma_{12}^{*}\right)}\right) \tag{2.49}$$

$$\Gamma_{H,L} = \gamma \mp 2\mathrm{Im}\left(\sqrt{\left(M_{12} - \frac{i}{2}\Gamma_{12}\right)\left(M_{12}^{*} - \frac{i}{2}\Gamma_{12}^{*}\right)}\right) \tag{2.50}$$

from which it follows that the mass and width differences are

$$\Delta m = 2\mathrm{Re}\left(\sqrt{\left(M_{12} - \frac{i}{2}\Gamma_{12}\right)\left(M_{12}^{*} - \frac{i}{2}\Gamma_{12}^{*}\right)}\right) \tag{2.51}$$

$$\Delta\Gamma = -4\mathrm{Im}\left(\sqrt{\left(M_{12} - \frac{i}{2}\Gamma_{12}\right)\left(M_{12}^{*} - \frac{i}{2}\Gamma_{12}^{*}\right)}\right) \tag{2.52}$$

It follows from equations 2.51 and 2.52 that

$$(\Delta m)^2 - \frac{1}{4}(\Delta\Gamma)^2 = |M_{12}|^2 - |\Gamma_{12}|^2 \tag{2.53}$$

It is true experimentally that $\Delta m \gg \Delta\Gamma$ [11], it therefore follows from equation 2.53 that $|M_{12}| \gg |\Gamma_{12}|$.

It is useful to define the phase

$$\phi = \arg(-M_{12}/\Gamma_{12}) \tag{2.54}$$

It is useful to relate the three parameters, $|M_{12}|$, $|\Gamma_{12}|$ and ϕ to three observables: the mass difference, Δm; the width difference, $\Delta\Gamma$; and a_{fs}, defined by equation 2.57. It is shown in chapter 6 that a_{fs} is proportional to the charge difference in final states of un-tagged[1] flavour specific decays of neutral B mesons.

$$\Delta m = 2|M_{12}| \tag{2.55}$$

$$\Delta\Gamma = 2|\Gamma_{12}|\cos\phi \tag{2.56}$$

$$a_{fs} \equiv \left|\frac{\Gamma_{12}}{M_{12}}\right| \sin\phi \tag{2.57}$$

The parameter a_{fs} is related to p and q by

$$\left|\frac{q}{p}\right| = 1 - \frac{a_{fs}}{2} \tag{2.58}$$

a_{fs} is therefore a measure of CP violation in mixing. Equations 2.55, 2.56 and 2.58 are approximations in which terms of order $\left|\frac{\Gamma_{12}}{M_{12}}\right|^2$ and higher have been dropped.

The subscript on a_{fs} stands for flavour specific, because it is measured in flavour specific decays. a_{fs} is sometimes given a superscript, $a_{fs}^{s,d}$ to distinguish between the CP asymmetry in the B_s^0 system and the B^0 system. Superscripts are occasionally used in this thesis, where the distinction needs to be made clear, however, if no superscript is used than a_{fs} should be taken to mean a_{fs}^s. A technique for measuring a_{fs}^s is described in chapter 6.

[1]Un-tagged decays are ones where it is unknown if the initial state is B_s^0 or $\bar{B}_s^0$

2.6 Time-Dependent Decay Rates

In chapter 6 a technique for measuring a_{fs} from semi-leptonic B_s^0 decays is discussed. This method relies upon knowing the time-dependent decay rates for these decays. To determine these it is necessary to consider how a state beginning in a flavour eigenstate at time $t = 0$ evolves over time. Equations 2.41 shows the mass eigenstates in terms of the flavour eigenstates. These may be inverted to give

$$\begin{aligned} |B^0(t)\rangle &= \frac{1}{2p}\left(|B_L(t)\rangle + |B_H(t)\rangle\right) \\ |\bar{B}^0(t)\rangle &= \frac{1}{2q}\left(|B_L(t)\rangle - |B_H(t)\rangle\right) \end{aligned} \tag{2.59}$$

The time-dependence may be written more explicitly as

$$\begin{aligned} |B^0(t)\rangle &= \frac{1}{2p}\left(e^{-\left(im_L+\frac{1}{2}\Gamma_L\right)t}|B_L\rangle + e^{-\left(im_H+\frac{1}{2}\Gamma_H\right)t}|B_H\rangle\right) \\ |\bar{B}^0(t)\rangle &= \frac{1}{2q}\left(e^{-\left(im_L+\frac{1}{2}\Gamma_L\right)t}|B_L\rangle - e^{-\left(im_H+\frac{1}{2}\Gamma_H\right)t}|B_H\rangle\right) \end{aligned} \tag{2.60}$$

rewriting the mass eigenstates on the right hand side of equations 2.60, in terms of the flavour eigenstates gives

$$\begin{aligned} |B^0(t)\rangle &= g_+(t)\,|B^0\rangle + \frac{q}{p}g_-(t)\,|\bar{B}^0\rangle \\ |\bar{B}^0(t)\rangle &= \frac{p}{q}g_-(t)\,|B^0\rangle + g_+(t)\,|\bar{B}^0\rangle \end{aligned} \tag{2.61}$$

where $g_\pm(t)$ are defined by

$$g_\pm = \frac{1}{2}\left[e^{\left(-im_L+\frac{1}{2}\Gamma_L\right)t} \pm e^{\left(-im_H+\frac{1}{2}\Gamma_H\right)t}\right] \tag{2.62}$$

these can be rewritten as

$$g_+ = e^{-imt}e^{-\frac{1}{2}\Gamma t}\left[\cos\left(\frac{\Delta mt}{2}\right)\cosh\left(\frac{\Delta\Gamma t}{4}\right) - i\sin\left(\frac{\Delta mt}{2}\right)\sinh\left(\frac{\Delta\Gamma t}{4}\right)\right] \tag{2.63}$$

$$g_- = e^{-imt}e^{-\frac{1}{2}\Gamma t}\left[-\cos\left(\frac{\Delta mt}{2}\right)\sinh\left(\frac{\Delta\Gamma t}{4}\right) + i\sin\left(\frac{\Delta mt}{2}\right)\cosh\left(\frac{\Delta\Gamma t}{4}\right)\right] \tag{2.64}$$

where

$$\begin{aligned} m &= \frac{m_L + m_H}{2} \\ \Gamma &= \frac{\Gamma_L + \Gamma_H}{2} \end{aligned} \tag{2.65}$$

For mesons beginning in a state $|B\rangle$, the time-dependent decay rate for decays to a final state $|f\rangle$ is defined as

$$\Gamma_{B\to f}(t) = \frac{1}{\mathrm{N}}\frac{\mathrm{dN}(B\to f)}{\mathrm{d}t} \tag{2.66}$$

where $\mathrm{dN(B \to f)}$ is the number of mesons, initially in a state $|B\rangle$, that decay to a final state $|f\rangle$ in the time interval t to $t + \mathrm{d}t$, and N is the total number of mesons produced in a $|B\rangle$ state at $t = 0$. There are similar expressions for states $\Gamma_{B\to\bar{f}}(t)$, $\Gamma_{\bar{B}\to f}(t)$ and $\Gamma_{\bar{B}\to\bar{f}}(t)$. In terms of the probability amplitudes the decay rates are

$$\Gamma_{B\to f}(t) = \mathcal{N}_f \left|\langle f|B(t)\rangle\right|^2 \tag{2.67}$$

$$\Gamma_{\bar{B}\to f}(t) = \mathcal{N}_f \left|\langle f|\bar{B}(t)\rangle\right|^2 \tag{2.68}$$

$$\Gamma_{B\to\bar{f}}(t) = \mathcal{N}_f \left|\langle \bar{f}|B(t)\rangle\right|^2 \tag{2.69}$$

$$\Gamma_{\bar{B}\to\bar{f}}(t) = \mathcal{N}_f \left|\langle \bar{f}|\bar{B}(t)\rangle\right|^2 \tag{2.70}$$

where $\mathcal{N}_f$ is a time-independent normalisation factor that depends on the decay kinematics.

Substituting equations 2.58, 2.61, 2.63, 2.64, 2.44 and 2.26 to 2.29 into equations 2.67 to 2.70 gives the following

$$\begin{aligned}\Gamma_{B\to f}(t) &= \frac{1}{2}\mathcal{N}_f|A_f|^2e^{-\Gamma t}\left[\frac{1+|\lambda_f|^2}{2}\cosh\left(\frac{\Delta\Gamma t}{2}\right)\right.\\ &\left.+\frac{1-|\lambda_f|^2}{2}\cos(\Delta mt)-\mathrm{Re}(\lambda_f)\sinh\left(\frac{\Delta\Gamma t}{2}\right)-\mathrm{Im}(\lambda_f)\sin(\Delta mt)\right]\end{aligned} \tag{2.71}$$

$$\begin{aligned}\Gamma_{\bar{B}\to f}(t) &= \frac{1}{2}\mathcal{N}_f|A_f|^2(1+a_{fs})e^{-\Gamma t}\left[\frac{1+|\lambda_f|^2}{2}\cosh\left(\frac{\Delta\Gamma t}{2}\right)\right.\\ &\left.-\frac{1-|\lambda_f|^2}{2}\cos(\Delta mt)-\mathrm{Re}(\lambda_f)\sinh\left(\frac{\Delta\Gamma t}{2}\right)+\mathrm{Im}(\lambda_f)\sin(\Delta mt)\right]\end{aligned} \tag{2.72}$$

$$\begin{aligned}\Gamma_{B\to \bar{f}}(t) &= \frac{1}{2}\mathcal{N}_f|\bar{A}_{\bar{f}}|^2(1-a_{fs})e^{-\Gamma t}\left[\frac{1+|\lambda_{\bar{f}}|^{-2}}{2}\cosh\left(\frac{\Delta\Gamma t}{2}\right)\right.\\ &\left.-\frac{1-|\lambda_{\bar{f}}|^{-2}}{2}\cos(\Delta mt)-\mathrm{Re}(\frac{1}{\lambda_f})\sinh\left(\frac{\Delta\Gamma t}{2}\right)+\mathrm{Im}(\frac{1}{\lambda_f})\sin(\Delta mt)\right]\end{aligned} \tag{2.73}$$

$$\begin{aligned}\Gamma_{\bar{B}\to \bar{f}}(t) &= \frac{1}{2}\mathcal{N}_f|A_f|^2e^{-\Gamma t}\left[\frac{1+|\lambda_{\bar{f}}|^{-2}}{2}\cosh\left(\frac{\Delta\Gamma t}{2}\right)\right.\\ &\left.+\frac{1-|\lambda_{\bar{f}}|^{-2}}{2}\cos(\Delta mt)-\mathrm{Re}(\frac{1}{\lambda_f})\sinh\left(\frac{\Delta\Gamma t}{2}\right)-\mathrm{Im}(\frac{1}{\lambda_f})\sin(\Delta mt)\right]\end{aligned} \tag{2.74}$$

The sine and cosine terms reflect the oscillation of the $|B(t)\rangle$ and $|\bar{B}(t)\rangle$ states.

2.6.1 Flavour Specific Decays with no CP Violation in Decay

For flavour specific decays with no direct CP violation the expressions 2.71 to 2.74 simplify considerably. For flavour specific decays, $B\to f$ and $\bar{B}\to\bar{f}$ decays are allowed, and $B\to\bar{f}$ and $\bar{B}\to f$ decays are forbidden. Therefore

$$\bar{A}_f = A_{\bar{f}} = 0 \tag{2.75}$$

which leads to

$$\lambda_f = \frac{1}{\lambda_{\bar{f}}} = 0 \tag{2.76}$$

If there is no direct CP violation in the decay then

$$|A_f| = \left|\bar{A}_{\bar{f}}\right| \tag{2.77}$$

Substituting equations 2.76 and 2.77 into equations 2.71 to 2.74 gives

$$\Gamma_{B\to f}(t) = \mathcal{N}_f \left|A_f\right|^2 e^{-\Gamma t}\left[\cosh\left(\frac{1}{2}\Delta\Gamma t\right) + \cos\left(\Delta m t\right)\right] \tag{2.78}$$

$$\Gamma_{B\to \bar{f}}(t) = \mathcal{N}_f (1-a_{fs}) \left|A_f\right|^2 e^{-\Gamma t}\left[\cosh\left(\frac{1}{2}\Delta\Gamma t\right) - \cos\left(\Delta m t\right)\right] \tag{2.79}$$

$$\Gamma_{\bar{B}\to f}(t) = \mathcal{N}_f (1+a_{fs}) \left|A_f\right|^2 e^{-\Gamma t}\left[\cosh\left(\frac{1}{2}\Delta\Gamma t\right) - \cos\left(\Delta m t\right)\right] \tag{2.80}$$

$$\Gamma_{\bar{B}\to \bar{f}}(t) = \mathcal{N}_f \left|A_f\right|^2 e^{-\Gamma t}\left[\cosh\left(\frac{1}{2}\Delta\Gamma t\right) + \cos\left(\Delta m t\right)\right] \tag{2.81}$$

2.7 Current Experimental Status of a_{fs}

Indirect measurements of a^s_{fs} have been made at both CDF and D0. At the Tevatron experiments, the terms A^s_{SL} and A^d_{SL} are used instead of $a^{s,d}_{fs}$. The subscript refers to the fact that the parameters are measured in semi-leptonic decays. A_{SL}, a linear combination of A^s_{SL} and A^d_{SL}, is measured and A^s_{SL} extracted using knowledge of A^d_{SL} from elsewhere. The measurement is made from a di-muon sample containing both B^0_s and B^0 decays. A_{SL} is extracted from measuring the time integrated asymmetry in the rate of same charge muon pairs. The measurements are [12, 13]

$$\mathrm{D0-indirect}: A^s_{SL} = -(6.4 \pm 10.1) \times 10^{-3} \tag{2.82}$$

$$\text{CDF} - \text{indirect}: A_{SL}^s = -(20 \pm 21(stat) \pm 16(syst) \pm 9(inputs)) \times 10^{-3} \tag{2.83}$$

D0 has also made a direct measurement of A_{SL}^s using the $B_s^0 \to D_s^{\pm}\mu^{\mp}\nu_\mu$ channel [13]. After correcting for detector asymmetries, they measure

$$A_{SL}^s = a_{fs}^s = \frac{N(\mu^+ D_s^-) - N(\mu^- D_s^+)}{N(\mu^+ D_s^-) - N(\mu^- D_s^+)} \tag{2.84}$$

where $N(\mu^{\pm} D_s^{\mp})$ is the time integrated number of $B_s^0 \to D_s^{\mp}\mu^{\pm}\nu_\mu$ decays. The measured value of A_{SL}^s was

$$\text{D0} - \text{direct}: A_{SL}^s = (2.45 \pm 1.92(stat) \pm 0.35(syst)) \times 10^{-2} \tag{2.85}$$

The direct measurement has a much smaller systematic error than indirect ones, but is severely limited by statistics.

2.8 Production Asymmetry

The LHC is a proton-proton collider. The collisions, therefore, are neither charge nor CP symmetric. This leads to an asymmetry in the production rates of particles and their anti-particles. Production asymmetry is important because it can mimic the effects of CP asymmetry.

Asymmetries arise in processes where valence quarks are scattered to high $p_\perp$ [15]. In such processes parton showering will be profuse. If a gluon that is close to the scattered valence quark splits into a quark pair, the anti-quark may be in a colour singlet with the scattered valence quark. An asymmetry in the production arises because valence quarks in the initial state are all u or d quarks, and not $\bar{u}$ or $\bar{d}$, see figure 2.4.

The beam remnant is the collection of quarks and gluons remaining from the proton-proton interaction. The beam remnant may interact with scattered quarks via a coloured field. This has the effect of dragging the scattered quarks in the direction of the beam remnant, that is, to high rapidities. This process is known as beam drag. As the initial state is not CP symmetric, beam drag leads to asymmetries at high rapidity [15]. For example, an excess of $\bar{B}_d^0$ mesons compared to B_d^0 is expected.

Scattered quarks can hadronize directly with the beam remnant, if there is insufficient energy to produce multiple hadrons. This process is called cluster collapse, and is asymmetric in proton-proton collisions [15, 16]. For example, it enhances B_d^0 production, see figure 2.5.

There are also asymmetries in the production of B_s mesons, even though these do not contain any of the initial valence quarks of the protons. A process which favours the hadronization of $\bar{b}$ quarks into B_d^0 mesons, will leave an excess of b quarks. This leads to asymmetries in other B hadrons [14].

Monte Carlo studies of production asymmetry have been made [14]. In [14] production asymmetry is defined as

$$\delta_p = \frac{\bar{I}}{I} - 1 \tag{2.86}$$

where are I and $\bar{I}$ are the production rates for particles and anti-particles. The value of δ_p various depending on the particular Monte Carlo used, but is of order 10^{-3} with

$$|\delta_p^{B^\pm}| > |\delta_p^{B_d^0}| < |\delta_p^{B_s^0}| \tag{2.87}$$

In chapter 6 it is convenient to use a slightly different definition of production asymmetry, given by

$$A_p = \frac{I - \bar{I}}{I + \bar{I}} \tag{2.88}$$

The two definitions of production asymmetry are related by

$$A_p = \frac{-\delta_p}{2 + \delta_p} \tag{2.89}$$

that is, to first order the two definitions are proportional.

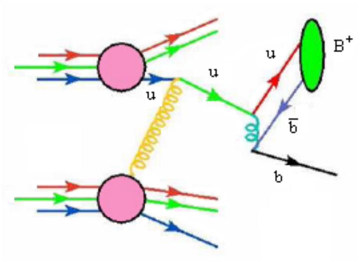

Figure 2.4: An illustration of the high $p_\perp$ asymmetry. The figure is taken from reference [14]

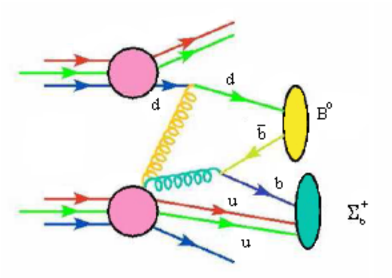

Figure 2.5: A cartoon of cluster collapse, showing enhancement of B_d^0 and Σ_b^+. The figure is taken from reference [14]

Chapter 3

The LHC and the LHCb Detector

3.1 Introduction

This chapter is intended to give a brief description of the Large Hadron Collider, LHC, and the experiments that will be operating during its running. Particular focus is given to the LHCb detector.

3.2 The Large Hadron Collider

The LHC is a proton-proton collider designed to operate at a centre of mass energy of 14 TeV and a luminosity of $10^{34}\,\mathrm{cm}^{-2}\mathrm{s}^{-1}$. The accelerator is located at CERN, in the 27 km long tunnel which was first used to house the Large Electron Positron, LEP, accelerator. Figure 3.1 shows the LHC marked on the French and Swiss countryside, and marks the positions of the experiments.

Six experiments will operate at the LHC: ALICE, ATLAS, CMS, LHCb, LHCf and TOTEM.

ALICE (A Large Ion Collider Experiment), is a dedicated heavy ion experiment. Its primary aim is to study nuclear collisions at the LHC. ALICE will look for evidence of QCD bulk matter and quark-gluon plasma. It will take data resulting from a number of nucleus-nucleus collisions, including Pb-Pb and Pb-p.

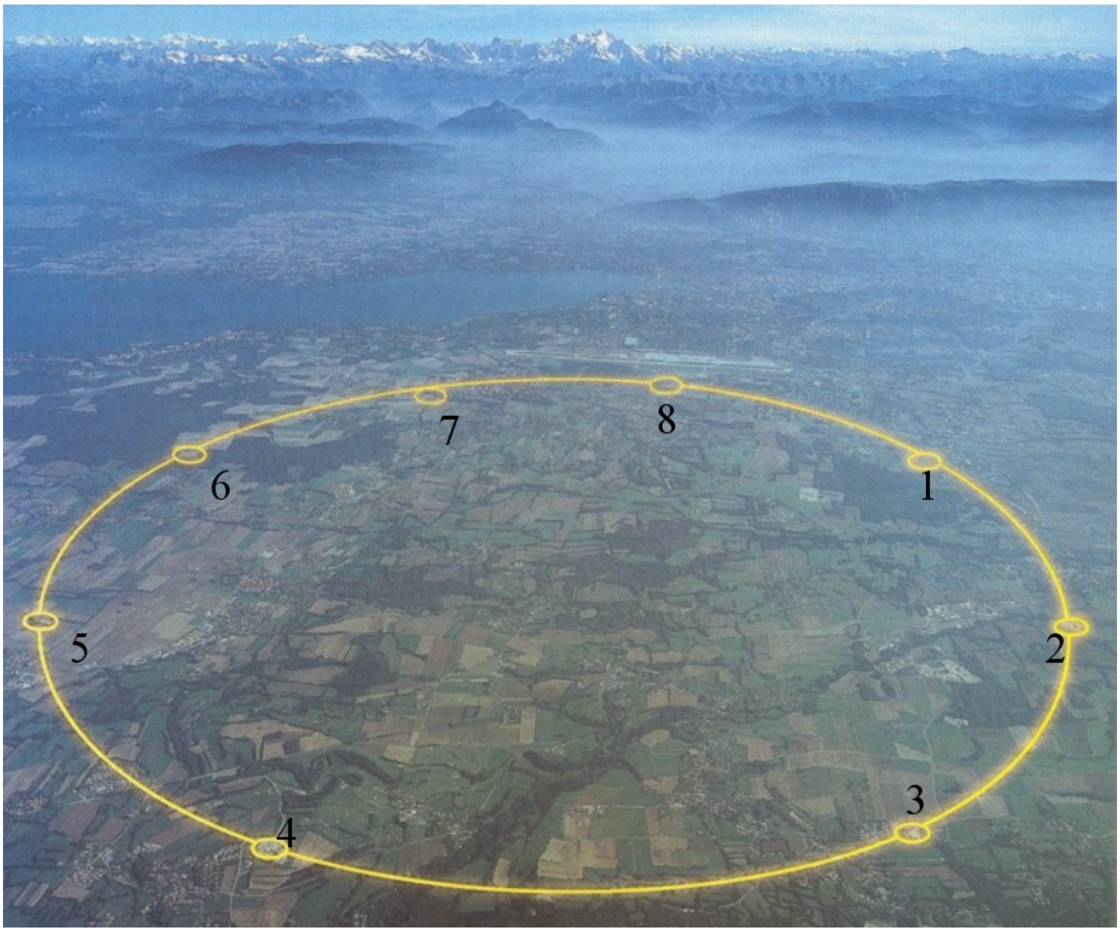

Figure 3.1: The position of the LHC in France and Switzerland. ATLAS is at point 1, ALICE point 2, CMS point 5 and LHCb point 8.

ATLAS (A Toroidal LHC ApparatuS) and CMS (Compact Muon Solenoid) are general purpose detectors, for the study of p-p collisions. They are designed for the direct detection of new physics particles and processes.

LHCf (LHC forward) aims to study the energy distribution of particles in the very forward region, with view to gaining a better understanding of cosmic rays. The LHCf detectors are placed at roughly $\pm 140\,\mathrm{m}$ from the ATLAS interaction point.

TOTEM (TOTal Elastic and diffractive cross section Measurement) is an experiment designed to measure the total elastic and diffractive cross sections. It shares point 5 with CMS.

3.3 The LHCb Detector

The Large Hadron Collider Beauty, LHCb, detector [17] [18] is a single-arm spectrometer dedicated to the study of CP violation and rare decays in hadrons containing b-quarks. It is intended to provide an understanding of quark flavour physics with the hope of revealing physics beyond the Standard Model.

The LHCb does not cover 4π sr but instead focuses on the high rapidity region on one side of the interaction point, see figure 3.2. This is because the majority of $b\bar{b}$ pairs produced are expected to be in a shallow cone about the beam pipe. The expected distribution of b and $\bar{b}$ hadron polar angles is shown in figure 3.3.

The LHCb will operate at a lower luminosity than the LHC design luminosity. This reduces the number of multiple p-p interactions and so simplifies lifetime measurements. Running at a lower luminosity also reduces radiation damage to the detector. The lower luminosity, $2 \times 10^{32}\,\mathrm{cm^{-2}s^{-1}}$, is achieved by having different beam focusing at the LHCb interaction point than the other interaction points.

The LHCb uses a right handed coordinate system in which the z-axis points along the beam-line from the nominal interaction point and the y-axis points upwards.

The detector is composed of numerous subdetectors. These are described below, together with the trigger and software.

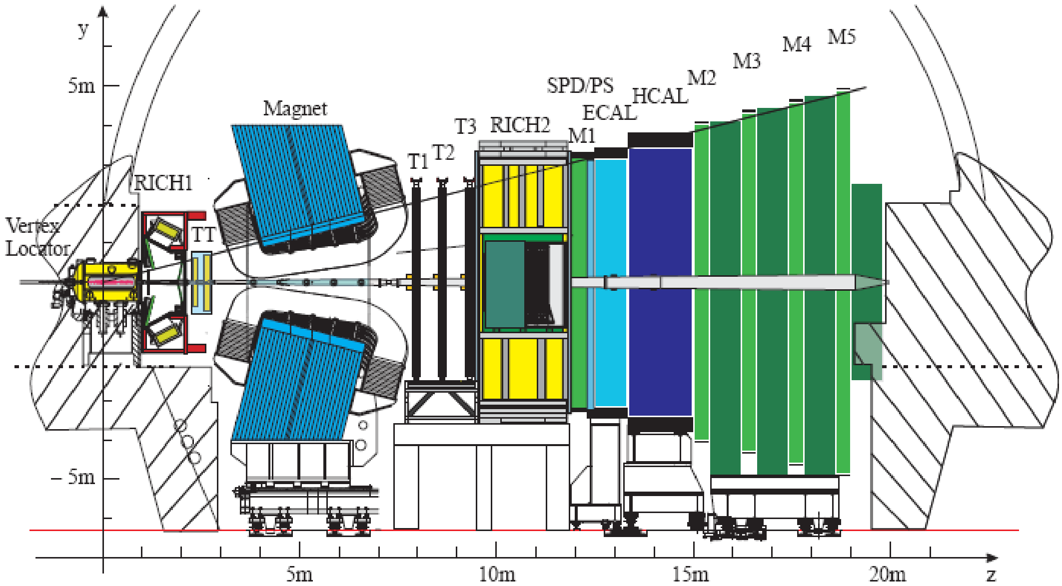

Figure 3.2: A schematic of the LHCb detector in the non-bending plane. The various subdetectors are: The Vertex Locator; the two Ring Imaging Čerenkov Detectors, RICH 1 and RICH 2; the magnet; the tracking stations; the calorimetry and the muon chambers. The tracking stations are labeled TT, T1, T2 and T3. The calorimetry comprises a scintillator pad detector, SPD; a pre-shower detector, PS; an electromagnetic calorimeter, ECAL; and a hadronic calorimeter, HCAL. The muon stations are labeled M1 to M5.

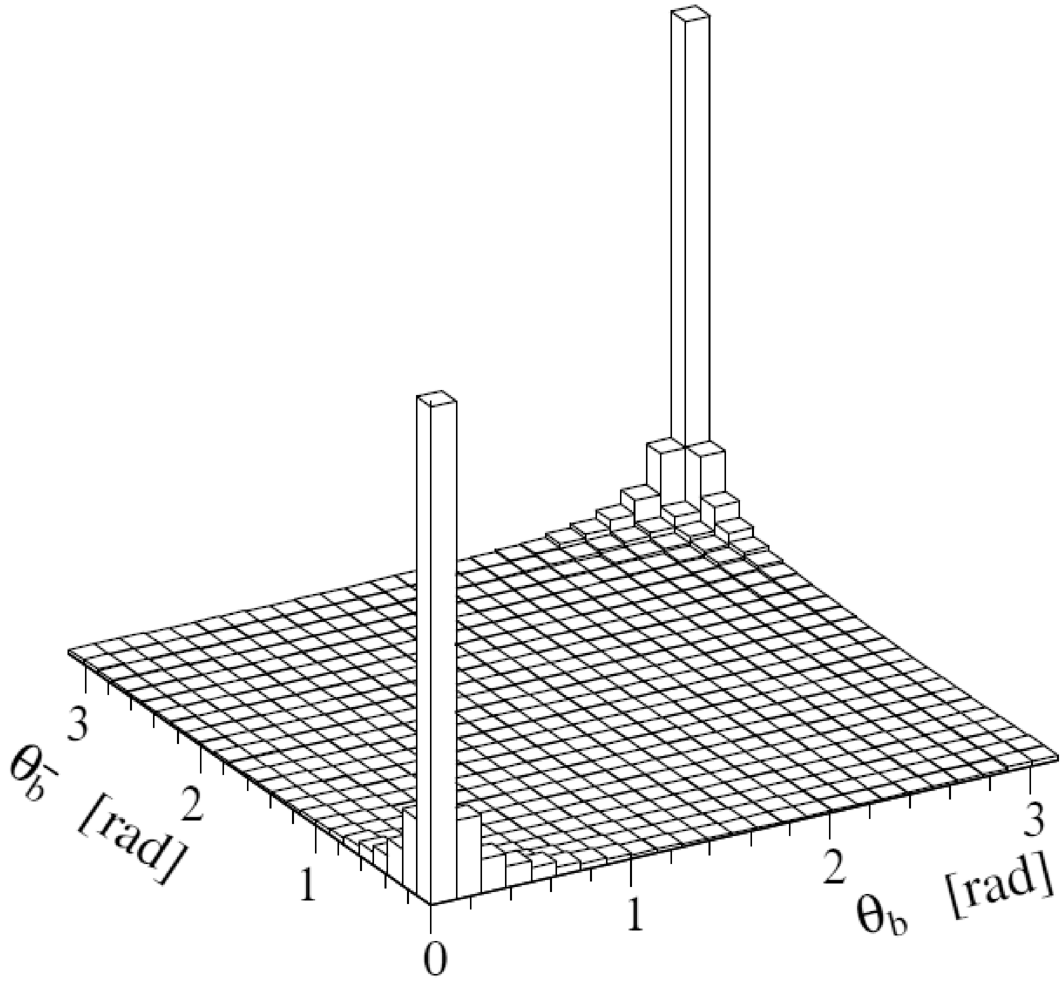

Figure 3.3: The polar angles of b and $\bar{b}$ hadrons, as calculated by the Pythia event generator.

3.4 The Beam Pipe

The beam pipe is needed to maintain the LHC vacuum. It is important that particles created in the proton-proton interaction interact with the beam pipe as little as possible. The beam pipe has four main sections [17]. The first three, accounting for 12 m of the beam pipe's 19 m length, are made from beryllium. Beryllium is suitable because of its high radiation length, however it is a toxic, fragile and expensive material. The fourth section of beam pipe occupies a region where transparency is less critical, and is made from steel. The beam pipe joins to the VELO, see section 3.5, via the VELO exit window, a spherical metal shell. The exit window is made from an aluminium alloy, as are the joins between the four sections of beam pipe. Figure 3.4 is a diagram of the beam pipe.

3.5 The VELO

The VErtex LOcator, VELO [20], is of fundamental importance to the LHCb. Displaced secondary vertices are a distinctive feature of b-hadron decays because of their relatively long lifetimes. It is the job of the VELO to provide the precise measurements of tracks near the interaction point which allow these vertices to be reconstructed. A precise measurement of the position of the primary and secondary vertices is essential. It allows a precise lifetime measurement to be made which is needed for many physics analyses. Data from the VELO is also used in the second level trigger.

For $b\bar{b}$ events in which a b-hadron was produced within 400 mrad of the beam axis, the resolution on the primary vertex position is $44\,\mu$m in the z-direction and $7.8\,\mu$m perpendicular to the beam [18].

The VELO is made up of a series of silicon strip sensors that are placed along the beam direction. The sensors are grouped together in VELO modules. The modules combine the silicon sensors, the readout electronics, cooling and provide mechanical support. The VELO operates in a vacuum separate to the LHC vacuum, within a detector vacuum box.

Charged tracks are identified with silicon strip sensors. Each is $300\,\mu$m thick and

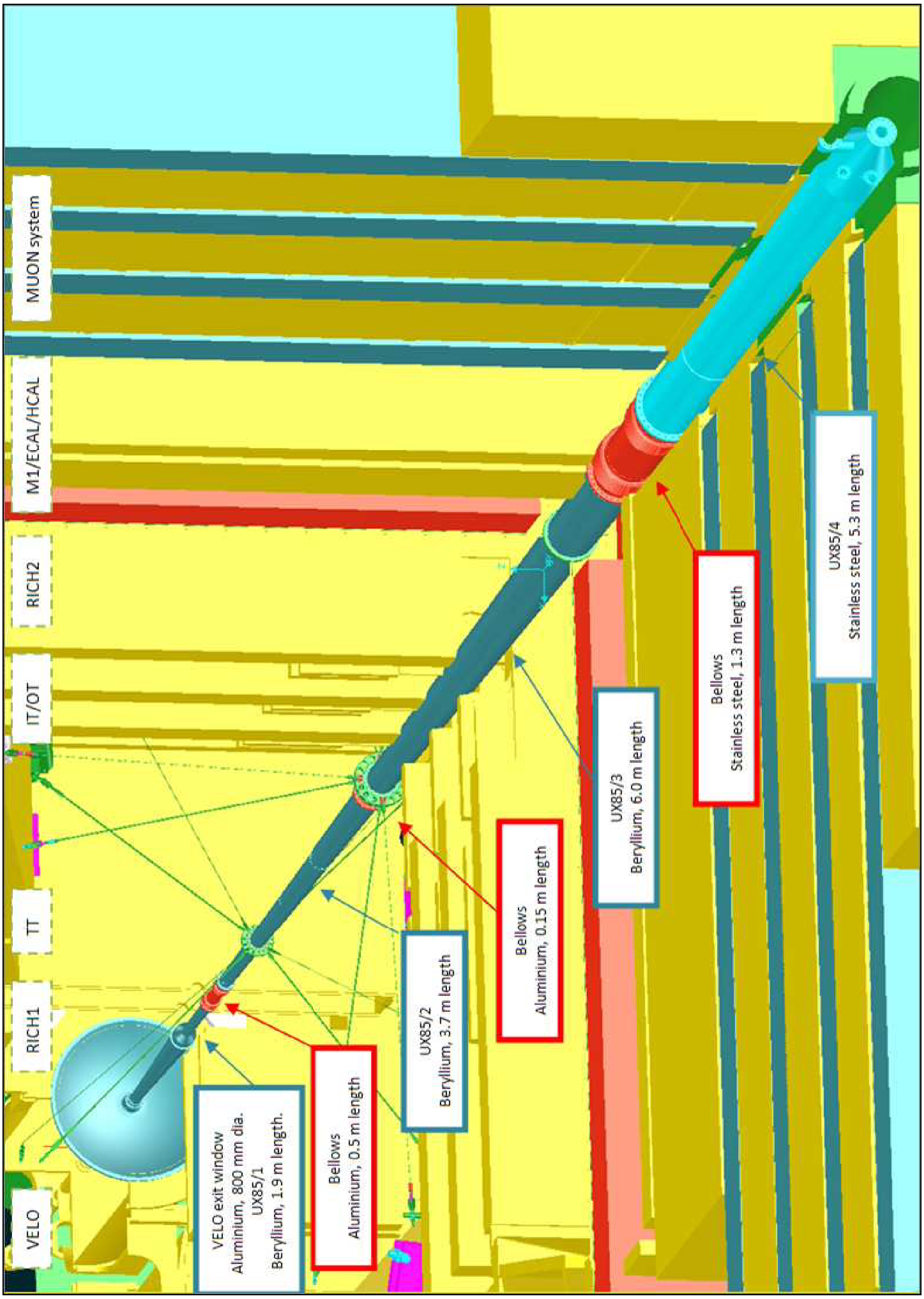

Figure 3.4: The beam pipe. It is divided into four sections, UX85/1 to UX85/4, the first three of which are beryllium the fourth stainless steel.

contains 2048 silicon strips. The sensors are roughly semi-circular[1] with a radius of 42 mm. The sensors come in two varieties. R-sensors measure the radial distance of the track from the beam, and are arrayed with azimuthal strips. The ϕ-coordinate of the track is measured by the ϕ-sensors, which have the silicon strips positioned in a quasi-radial fashion. Figure 3.5 depicts the two types of sensor.

The R-sensors have their silicon strips arranged in concentric semi-circles centered on the nominal beam position. The pitch of the strips increases linearly with increasing radius. The minimum pitch is $38\,\mu$m and the maximum $101.6\,\mu$m [17]. The strips are subdivided into 4 sectors, to reduce occupancy.

The ϕ-sensors are divided into inner and outer sections, with the border at a radius of 17.25 mm. The pitch in the inner section increases with increasing radius, from $37.7\,\mu$m to $79.5\,\mu$m. In the outer section, the pitch increases, with increasing radius, from $39.8\,\mu$m and $96.9\,\mu$m in the outer [17]. The strips are at an angle of 20° to the radial in the inner section and -10° in the outer. Sensors in adjacent modules are arranged such that adjacent ϕ-sensors have the opposite orientation to each other.

The sensors are mounted on VELO modules. Each module has one R-sensor and one ϕ-sensor. The module also contains the readout electronics for the sensors, the cooling system and the support structure. The modules are designed so that sensors are held in place to within less than $50\,\mu$m in the plane perpendicular to the beam axis, $800\,\mu$m along the beam direction and so that sensor to sensor alignment within individual modules is better than $20\,\mu$m. There are a total of 42 modules. Figure 3.6 is a diagram of a module.

The detectors operate within a vacuum, to reduce the material in the detector acceptance. This vacuum is separate to the LHC vacuum, and for it to be maintained the VELO sensors are housed in a box. The box has a second rôle of reducing the effect of wake-fields produced by the beam bunches passing through the detector. Part of the box lies within the detector acceptance. This is a thin corrugated aluminium foil, called the RF-foil, 0.3 mm thick. Figure 3.7 shows the arrangement of modules and the RF-foil.

[1]The sensors are sectors of circles covering 182°

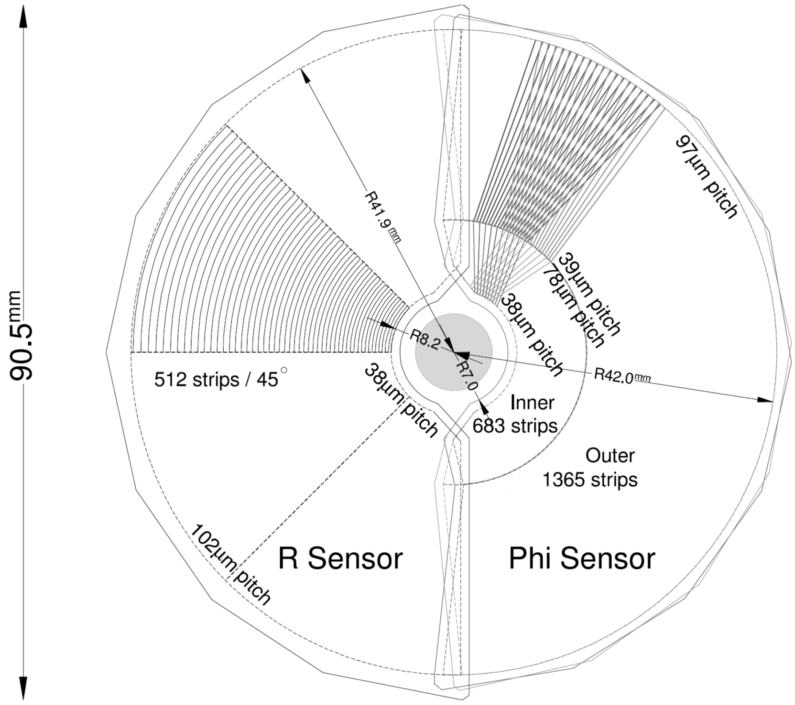

Figure 3.5: The two types of silicon detector in the VELO. For clarity only some of the silicon strips are highlighted. In the case of the ϕ-sensors, strips from two adjacent modules are shown, to indicate the angle between them.

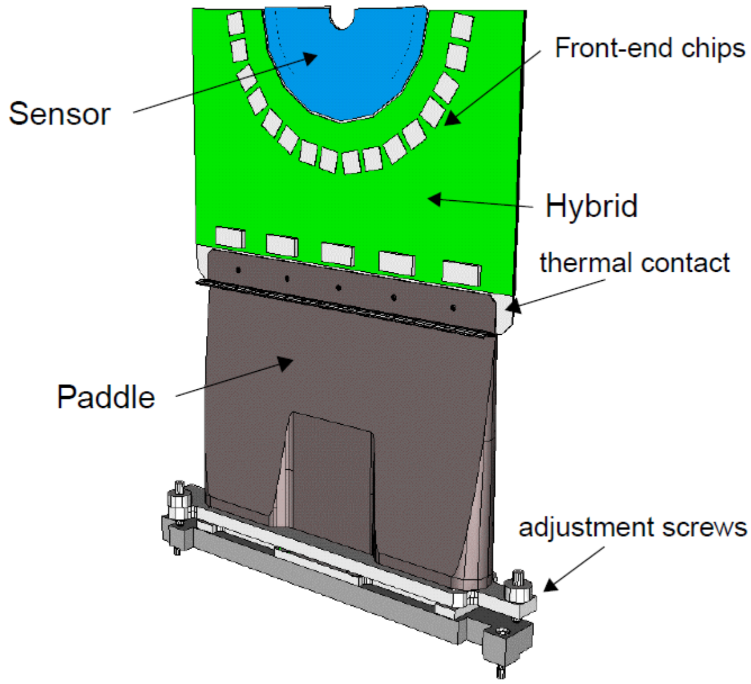

Figure 3.6: A VELO module. The hybrid is a substrate for thermal management and stability, onto which two circuits are laminated.

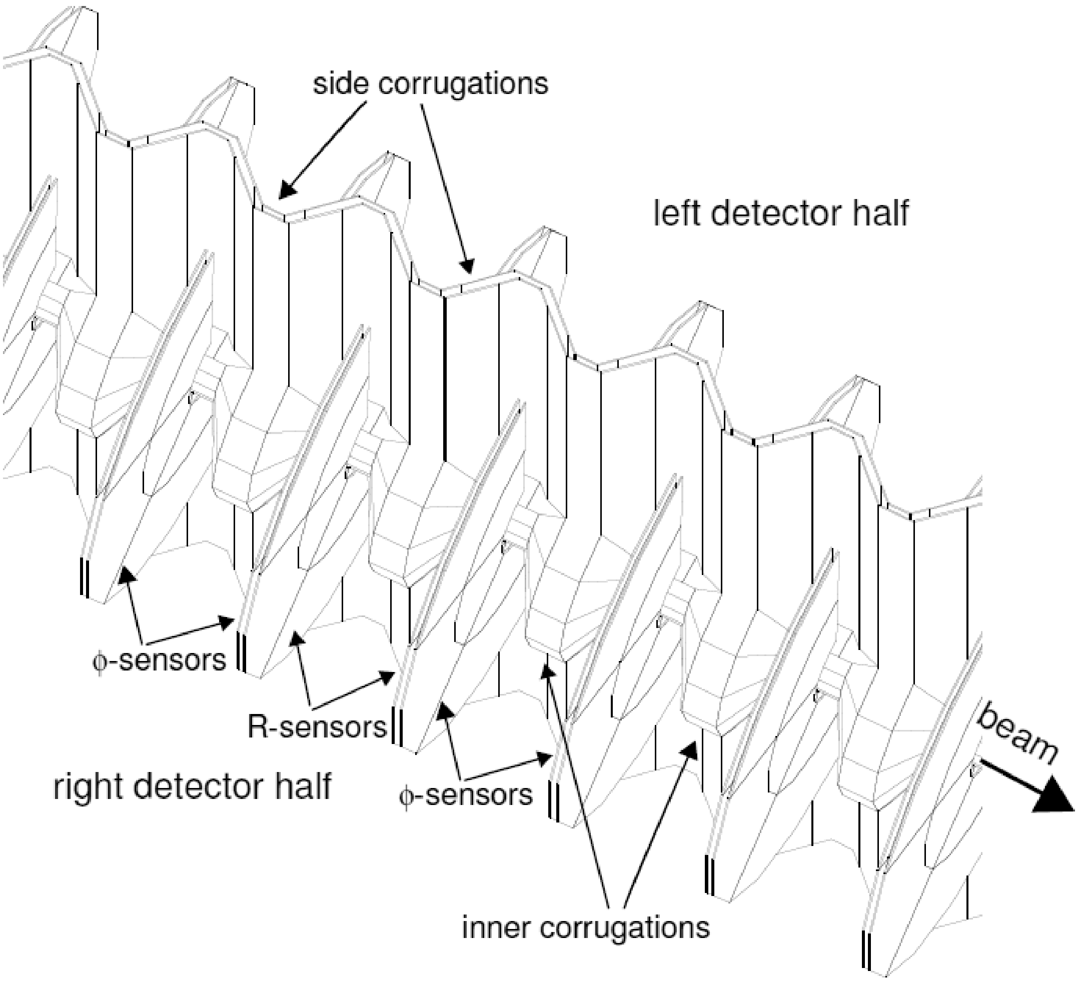

Figure 3.7: The VELO modules and the RF-foil.

3.6 The Magnet

Charged particles passing through a magnetic field have their paths bent. The curvature of their trajectory allows a particle's momentum and charge to be determined. The LHCb uses a warm dipole magnet [21]. A warm magnet was found to have numerous advantages over superconducting technology, notably: price, faster construction, faster ramping up of fields and potential for field inversions.

A diagram of the magnet is shown in figure 3.8. The magnet comprises two trapezoidal coils. These are bent at each end, at $45°$ in the x-y plane. The two coils are housed in an iron yoke. The magnet is wedge shaped in both the horizontal and the vertical planes, so that it matches the detector acceptance. The conductor in the coils is aluminium. The coils are made up of 15 mono-layer pancakes, each of which contains 15 turns of the conductor. The magnet provides an integrated field of 4 Tm for tracks that originate close to the interaction point.

The iron yoke guides the magnetic field produced by the magnet, producing a vertical field between the poles. The yoke comprises two identical vertical pieces and two identical horizontal pieces. The horizontal pieces are orthogonal to the plane of the coils.

3.7 The Tracking System

The LHCb tracking system consists of the VELO and four planar tracking stations: the Tracker Turicensis and three tracking stations T1-T3. The Tracker Turicensis, TT, is located upstream of the magnet. The tracking stations are located downstream of the magnet. The TT uses silicon microstrip detectors. T1-T3 are each divided into two regions, the Inner Tracker, IT [22], and the Outer Tracker, OT [23]. The IT use silicon microstrip detectors, while the OT uses straw-tubes. Figure 3.9 depicts the tracking stations.

The reconstruction efficiency for tracks traversing all of the tracking stations is 94% [17]. The momentum resolution for such tracks varies from $\delta p/p = 0.35\%$ to $\delta p/p = 0.55\%$, with worse resolution for higher momentum tracks [17].

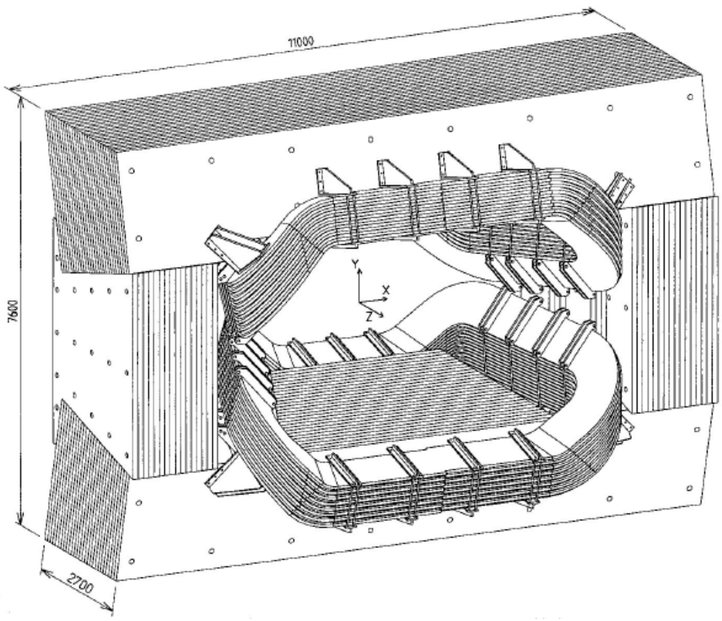

Figure 3.8: A schematic of the LHCb magnet and yolk.

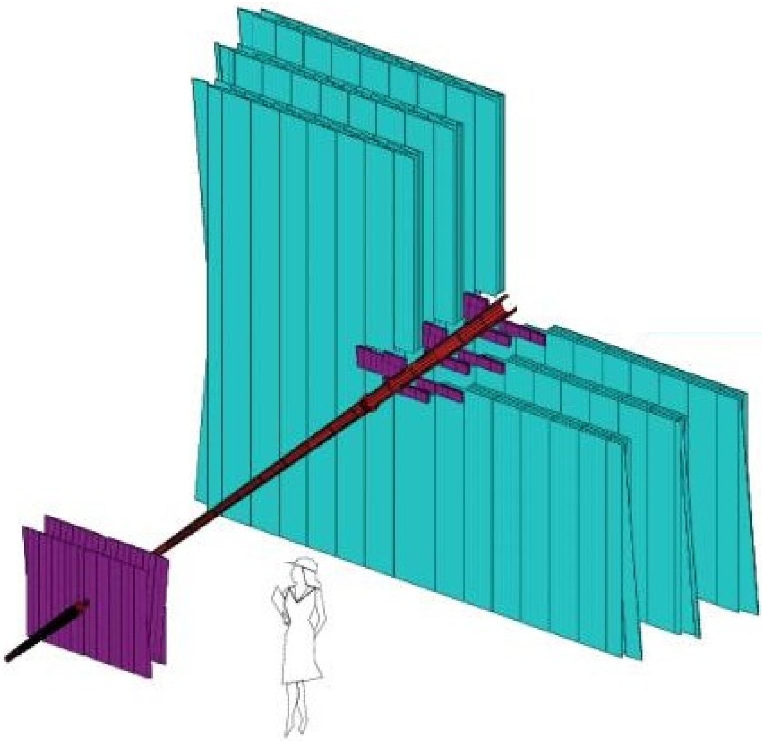

Figure 3.9: The LHCb tracking stations and beam pipe. The Purple detectors are those constructed with silicon microstrip detectors, with the TT shown on the bottom left and the inner trackers on the right. The outer trackers are in blue.

3.7.1 The Tracker Turicensis

The TT is located upstream of the LHCb magnet and is 150 cm wide by 130 cm high. It has an active area of 8.4 m^2 and four detection layers. These are housed in a single light-tight, thermally and electrically insulated detector volume. Its temperature is maintained below 5°C.

Figure 3.10 shows the layout of one of the TT layers. The detection layers are made up from elements called half modules. A half module covers half the height of the LHCb acceptance and comprises seven silicon sensors. The readout hybrids for all of the sectors are mounted at one end of the module. The seven silicon sensors are grouped into either two or three readout sectors, with three sectors in the half modules closest to the beam pipe and two in those further away. The silicon sensors are 500 μm thick, 9.64 cm wide and 9.44 cm long. They carry 512 readout strips with a strip pitch of 183 μm.

The regions above and below the beam pipe are covered by a half module. The regions to the sides of the beam pipe are covered by 14 half modules in the first two layers, and 16 in the second two, see figure 3.10.

The four layers are arranged in what is called an (x-u-v-x) arrangement. The two x layers have vertical modules, the u and v layers have the modules rotated at an angle of $-5°$ and $+5°$ to the vertical respectively. The layers are separated into two pairs, grouped as (x-u) and (v-x), which are roughly 26 cm apart along the beam axis.

3.7.2 The Tracking Stations

3.7.2.1 The Inner Trackers

The three IT stations are each made up of four detector boxes, which are grouped around the beam pipe, see figure 3.11. The boxes are all light-tight, electrically and thermally insulated and maintained at a temperature below 5°C. Each box contains four detection layers, comprising seven detector modules. The detector layers are arranged with the same (x-u-v-x) orientation as those in the TT. The modules are staggered by 4 mm in z, and have an overlap of 3 mm in x that allows for relative alignment of the modules

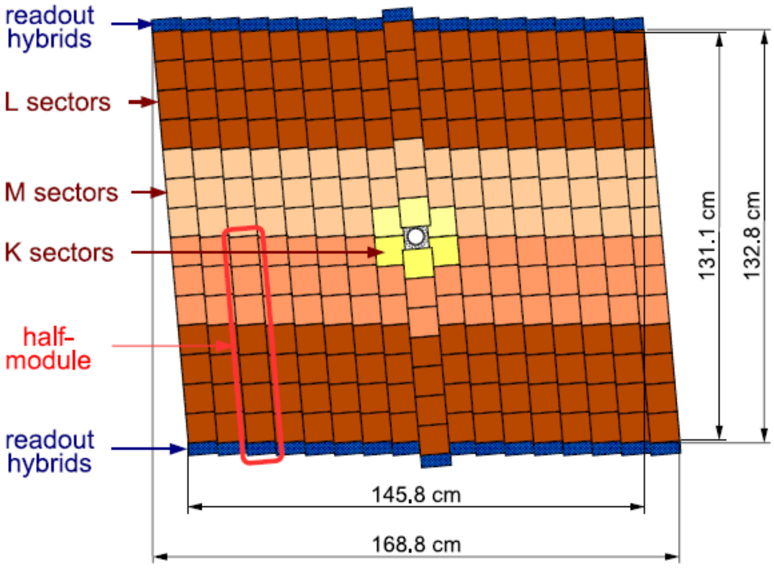

Figure 3.10: The third TT detection layer. The different sectors, L, M and K are connected to individual readout circuits.

and eliminates the possibility of acceptance gaps. Above and below the beam pipe the detector modules comprise a single silicon sensor and a readout hybrid. The modules to the sides of the beam pipe have two silicon sensors, see figure 3.12. The silicon sensors are 7.6 cm wide and 11 cm long and have 384 readout strips with a pitch of 198 μm. The sensors on the one-sensor modules are 320 μm thick, those on the two-sensor modules are 410 μm thick.

3.7.2.2 The Outer Trackers

The outer tracker is designed to track charged particles over a large acceptance range. It comprises an array of gas-tight straw tubes modules. Each of the modules contains two staggered layers of drift-tubes. In each of the tracking stations, the OT comprises four layers arranged in (x-u-v-x) geometry like that of the TT and IT stations. The total area of an OT station is 5971 $\times$4850 mm^2. The OT extends to 300 mrad in the magnet bending plane and 250 mrad in the non-bending plane. The position of the boundary with the IT was determined by the requirement that the occupancies should not exceed

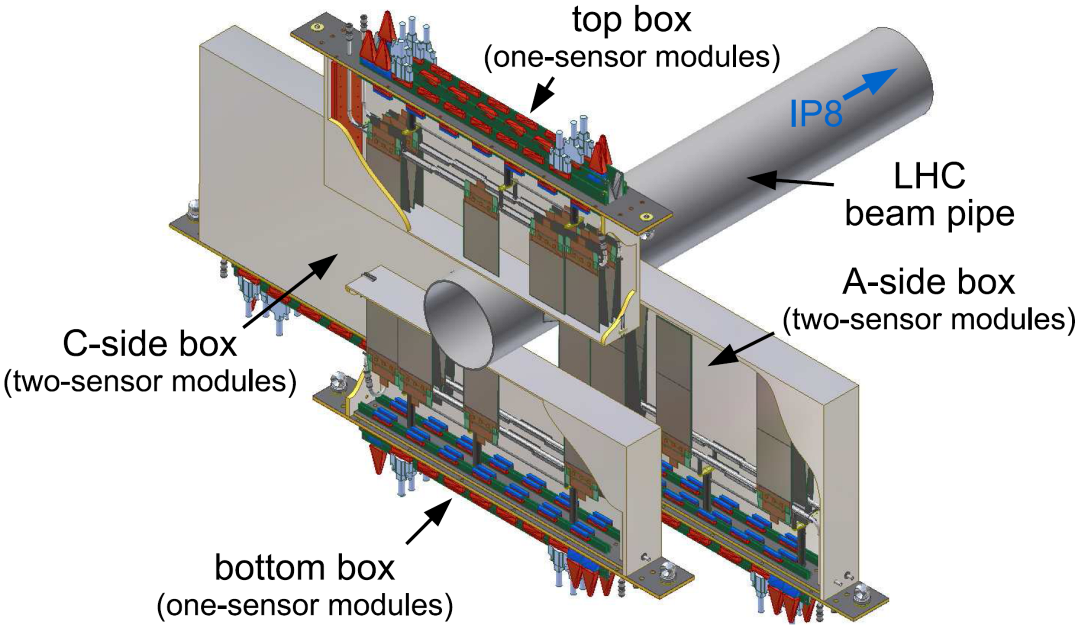

Figure 3.11: The layout of boxes in the IT.

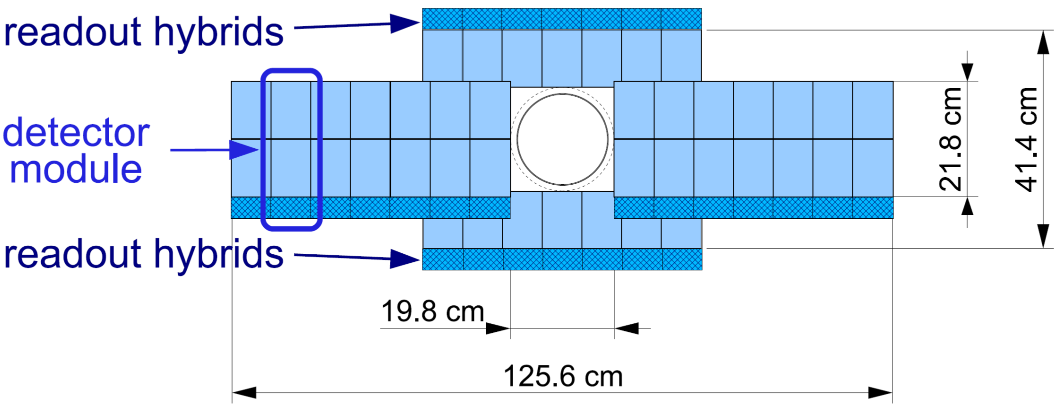

Figure 3.12: The layout of an x detector layer in the IT.

10% at a luminosity of $2 \times 10^{32}\,\mathrm{cm}^{-2}\mathrm{s}^{-1}$.

The detector modules are held in place on aluminium support structures. The tracking stations are made of two independent halves, one each side of the beam pipe. These may be retracted. The halves each consist of two C-frames. These also provide routing for all the detector services, such as gas, low and high voltage and data fibres.

The tubes are made by winding two foil strips together. The inner foil, the cathode, is $40\,\mu$m thick and made from carbon doped polyimide. The outer foil is made from $25\,\mu$m polyimide and $12.5\,\mu$m aluminium. The tubes have an inner diameter of 4.9 mm. The gas used is a mixture of Argon and CO_2 in the ratio 7:3.

3.8 The RICH Detectors

The LHCb contains two Ring Imaging Čerenkov, or RICH, detectors [17] [18]. These two detectors, RICH 1 and RICH 2, use Čerenkov radiation to gain information on a particle's velocity. This, combined with momentum measurements, allows for particle identification, which is crucial for many of LHCb's physics programmes. The RICH detectors are especially useful for distinguishing pions from kaons. The average efficiency for kaon identification over the momentum range of 2 to 100 GeV/c is $\epsilon(\mathrm{K} \to \mathrm{K}) \sim 95\%$, with the average pion misidentification rate at $\epsilon(\pi \to \mathrm{K}) \sim 5\%$ [17].

Čerenkov light is emitted by charged particles traveling though a medium faster than light does. The medium is called the radiator. The light is emitted in a cone about the particle's trajectory, with the angle at which the light is emitted given by $\theta_c = 1/n\beta$, where n is the refractive index of the radiator, and the particle's velocity, v, is related to β via $\beta = v/c$. Figure 3.13 shows the Čerenkov angle for different types of particles, in different radiators, as a function of momentum. The Čerenkov light is reflected from two sets of mirrors onto photo detectors. The reflected light forms a pattern of rings. Overlapping rings are formed in high multiplicity events. The Čerenkov angle, θ_c, can be determined from the diameter of the rings. RICH 1 covers a momentum range of 1 to 60 GeV/c, while RICH 2 covers higher momentum particles, up to ~ 100 GeV/c. Figure 3.14 shows the coverage of the two RICH detectors in terms track momentum and angle.

Both the RICH detectors use spherical mirrors to focus the Čerenkov light onto photon detectors. The spherical mirrors are angled so that the photon detectors can be positioned outside the LHCb acceptance. Plain mirrors are used to reduce the length of both RICH 1 and RICH 2. Hybrid Photon Detectors, HPDs, are used in both RICHes. They are sensitive to photons in the wavelength range 200 to 600 nm. The HPDs are cylindrical and, after close packing, the active area makes up 64 % of the total area of the photodetector plane. They have a pixel size of 2.5×2.5 mm.

RICH 1 is situated between the VELO and the TT. Its spatial dimensions are roughly $2\,\mathrm{m} \times 3\,\mathrm{m} \times 1\,\mathrm{m}$. It covers the full angular acceptance of the LHCb: 300 mrad horizontally by 250 mrad vertically. RICH 1 uses two radiators: silica aerogel, which has a refractive index of $n = 1.03$, and C_4F_{10}, which has a refractive index of $n = 1.015$ at STP.

The spherical mirrors in RICH 1 are made from carbon fibre, which results in a low material budget within the detector acceptance, and are coated with aluminium and MgF_2. There are four spherical mirrors, two above and two below the beam pipe. The radius of curvature is approximately 2.7 m. RICH 1 contains two sets of flat mirrors, each consisting of 8 mirrors arranged in a 4×2 array. A schematic of RICH 1 is shown in figure 3.15.

RICH 2 is located immediately downstream of the tracking stations and immediately upstream of the first muon station. RICH 2 uses CF_4 as its radiator, which has a refractive index of $n = 1.0005$.

The optical system of the RICH 2 is similar to that of RICH 1. It has two sets of spherical mirrors and two corresponding sets of flat mirrors which reflect the Čerenkov light onto one of two banks of HPDs. The mirrors are made from 6 mm thick Simax glass. The spherical mirrors are made from hexagonal mirrors with a diameter of 510 mm. There are 26 mirrors in each plane. Each of the flat mirror planes contains 20 rectangular mirrors of $410\,\mathrm{mm} \times 380\,\mathrm{mm}$.

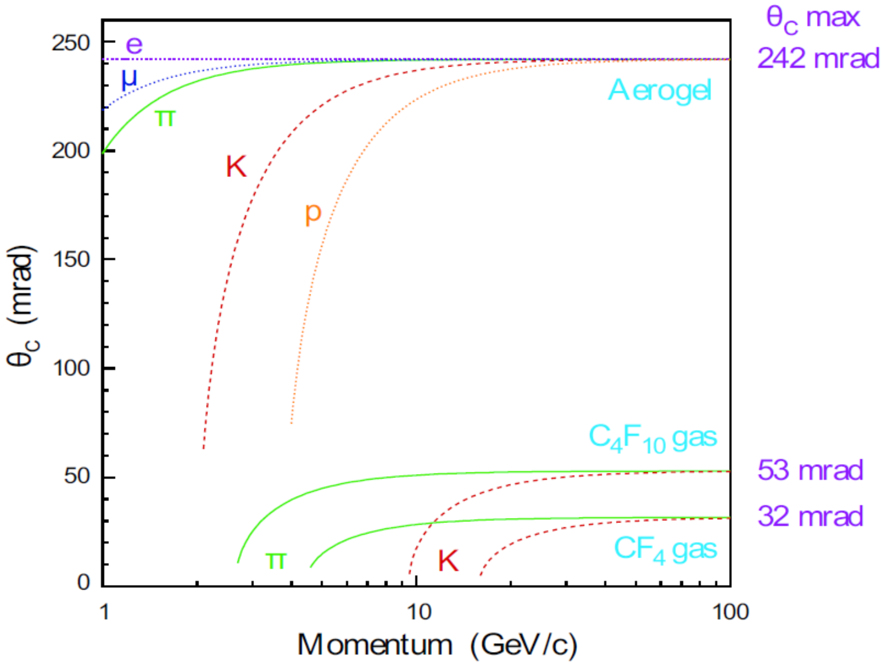

Figure 3.13: Čerenkov angle as a function of momentum for the different radiators used in LHCb and the different particles of interest. Aerogel and C_4F_{10} are used in RICH 1, CF_4 in RICH 2. The figure is taken from reference [17]

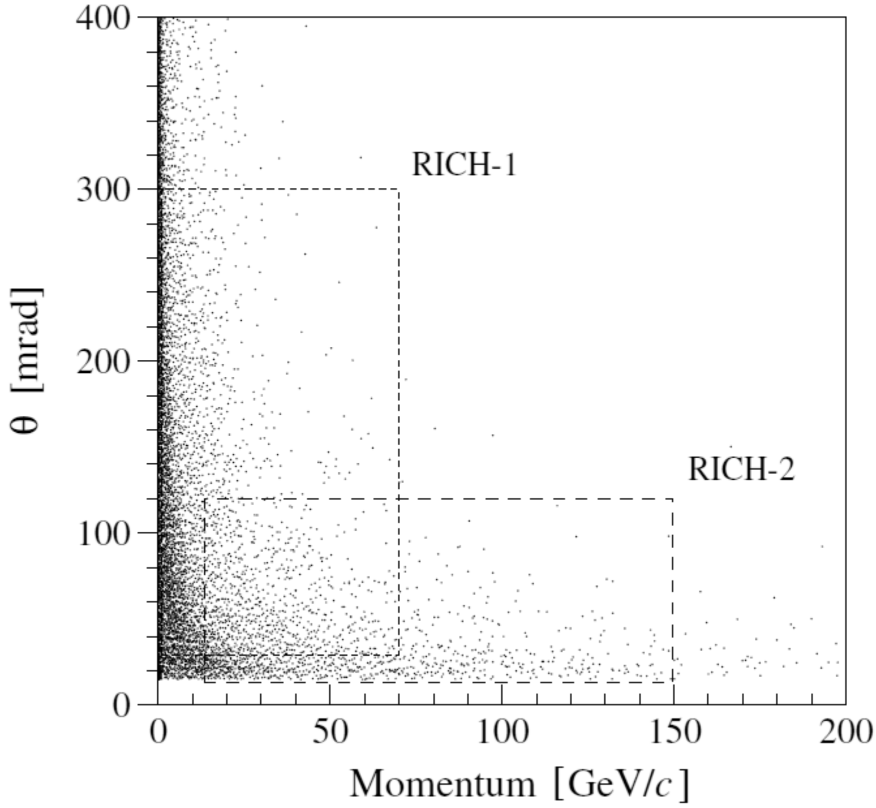

Figure 3.14: The coverage of the two RICH detectors. The figure is taken from reference [19]

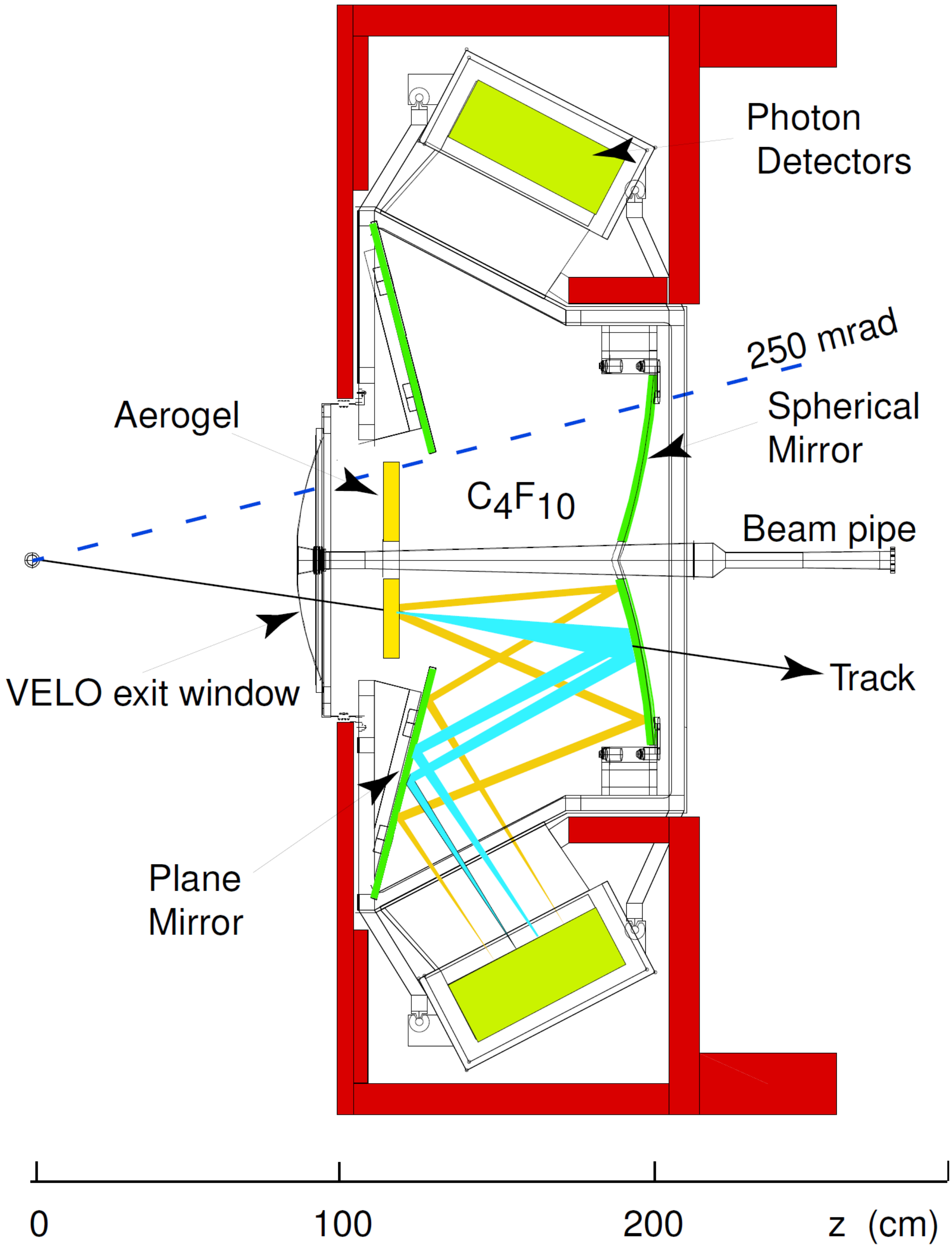

Figure 3.15: A schematic of RICH 1.

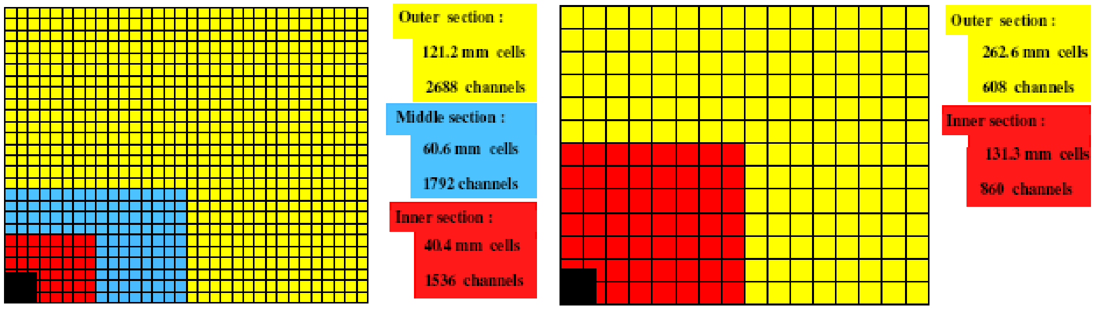

Figure 3.16: The segmentation of the calorimeters. The left figure depicts the segmentation of the PS, SPD and ECAL. The cell sizes listed refer to the ECAL. The right figure depicts the segmentation of the HCAL. In both cases one quarter of the detector face is shown.

3.9 The Calorimeters

The calorimetry [24] is used to select high transverse energy electron, photon and hadron candidates for the trigger. It is also used for identification of photons, electrons and hadrons, as well as measuring their energies.

LHCb has an electromagnetic calorimeter, ECAL, immediately upstream of a hadronic calorimeter, HCAL. Upstream of the ECAL is the preshower detector, PS. The PS provides additional information on the shower shape, which is used for distinguishing charged pions from electrons. Upstream of the PS is a scintillator pad detector, SPD, which allows the electron trigger to reject neutral pions with high E_T. The electron Level 0 trigger is required to reject 99% of inelastic pp collisions while enriching b events by at least a factor of 15 [17].

The hit density varies by two orders of magnitude over the calorimeter surface. Due to this the PS, SPD, ECAL and HCAL have a variable lateral segmentation. The ECAL, PS and SPD are segmented into three different sections. The HCAL has two sections, see figure 3.16.

Each of the calorimeters operate on the same principle: scintillation light transmitted to a Photo-Multiplier Tube, PMT, by wavelength-shifting, WLS, fibres.

3.9.1 The Scintillator Pad and Preshower Detector

The scintillator pad/preshower, SPD/PS, detector is composed of 15 mm of lead, $2.5\,X_0$ thick, sandwiched between two planes of rectangular scintillator pads. The sensitive area is 7.6 m wide and 6.2 m high. The scintillator pads are of a high granularity, with a total of 12032 detection channels. The centers of the PS and SPD are 56 mm apart in the z-direction. To achieve a one-to-one correspondence with the segmentation of the ECAL, the PS and SPD planes are divided into inner, middle and outer-sections. These contain 3072, 3584 and 5376 cells respectively and approximate cell sizes of $4 \times 4, 6 \times 6$ and $12 \times 12\,\text{cm}^2$. Achieving a one-to-one correspondence between the sections of the SD and the PS, the dimensions of the SPD are roughly 0.45% smaller than those of the PS.

The cells are packed in boxes of dimension approximately $48 \times 48\,\text{cm}^2$, which are called detector units. The detector units are grouped into supermodules, 2 detector units wide and 13 high. The PMTs are located on the top and bottom of the supermodule supports.

The electron pion separation performance of the PS prototype was measured in the test beam at the CERN SPS with electrons and pions between 10 and 50 GeV/c. For a threshold of four Minimum Ionizing Particles, MIPs, pion rejection factors of 99.6%, 99.6% and 99.7% with electron retentions of 91%, 92% and 97% are achieved for 10, 20 and 50 GeV/c particle momentum.

3.9.2 The Electromagnetic Calorimeter

The Electromagnetic calorimeter uses shashlik technology, that is a sampling scintillator/lead structure with plastic WLS readout fibres. The outer dimensions of the ECAL match projectively those of the tracking system. The acceptance of the ECAL is from 25 to 250 mrad in the y direction and 25 to 300 mrad in the x-direction.

The ECAL is made up of a number of modules. The ECAL is segmented into a three sections. Modules in the different sections contain a different number of readout cells. In the inner most section the modules contain 9 cells, in the middle section they contain 4 and in the outer section one. The lead absorber plates used in all the modules are the same, but the modules differ in the number of cells are thus the number of scintillating tiles per module. The detector is built as two separate halves from modules that are fixed to a surrounding frame. The ECAL begins 12.49 m downstream of the interaction point, and extends for 835 mm.

The ECAL is designed to have an energy resolution of $\sigma_E/E = 10\%/\sqrt{E} \oplus 1\%$ with E in GeV. This gives a mass resolution of 65 MeV/c^2 for the $B \to K^*\gamma$ decay and 75 MeV/c^2 for $B \to \rho\pi$.

3.9.3 The Hadronic Calorimeter

The HCAL is made from iron and scintillator tiles. The tiles are orientated so that they are parallel to the beam axis. In the lateral direction the tiles are interspersed with 1 cm of iron. In the longitudinal direction the length of the tile and iron spacer is equal to the hadron interaction length of steel.

The HCAL is segmented transversely into square cells. In the inner section these have a width of 131.3 mm, and in the outer section a width of 262.6 mm. The dimensions of inner and outer sections are ±2101 mm and ±4202 mm in the x-direction and ±1838 mm and ±3414 mm in the y-direction. The HCAL begins at a distance of 13.33 m from the interaction point, and is 1.65 m deep. It is 8.4 m high and 6.8 m wide.

The energy resolution of the HCAL is $\sigma_E/E = (69 \pm 5)\%/\sqrt{E} \oplus (9 \pm 2)\%$ with E in GeV.

3.10 The Muon System

Muon identification is of fundamental importance to the LHCb experiment for a number of reasons.

- Muons are final state particles in many B decays of interest, including $B^0_d \to J/\Psi(\mu^+\mu^-)K^0_S$ and $B^0_s \to J/\Psi(\mu^+\mu^-)\phi$.

- Muons from semi-leptonic B decays provide a flavour tag for the accompanying neutral B meson.

- Information from the muon system is used in the trigger.

The main requirement of the muon system is to provide high p_T muon candidates for the L0 trigger [17]. The muon trigger is based on standalone muon track reconstruction and p_T measurement with a resolution of 20%. A combination of Multi Wire Proportional Chambers, MWPC, and Gas Electron Multiplier, GEM, detectors are used [17] [25].

The muon system comprises five stations, M1 to M5, placed along the beam axis. To aid muon selection, 80 cm of iron is placed between stations M2 to M5. This shielding, combined with the calorimeter system, corresponds to roughly 20 nuclear interaction lengths. M1 is stationed downstream of the calorimeters, M2 to M5 upstream. To trigger, a muon must pass through all five stations.

The transverse dimensions of the stations scale with distance from the interaction point, see figure 3.18. The muon stations are divided into four regions, R1 to R4, with R1 closest to the beam pipe and R4 furthest. The linear dimensions and segmentation of the regions R1 to R4 have the ratio 1:2:4:8. Such a ratio gives the regions approximately equal particle flux and occupancy. Each of the stations contains 276 chambers which are divided into logical pads, which return a binary output. The size of the logical pads defines the x and y resolution. Figure 3.17 shows the segmentation of a station into the four regions, the chambers and logical pads.

Multi Wire Proportional chambers, MWPC, are used in all regions except the R1 region of M1. In this region an MWPC would age too quickly, because of the high particle flux; Gas Electron Multiplier, GEM, detectors are used.

There are total of 1368 MWPCs in the muon system. The gas used is a combination of Ar, CO_2 and CF_4 in the ratio 40:55:5. It was found that a time resolution of 5 ns could be achieved in a gas gap of 5 mm, using a wire plane of 2 mm spacing [17]. In station M2 to M5 chambers are composed of four equal gas gaps rigidly stacked together. Two adjacent gas gaps have their read out electronics wired together in a logical OR to form a double gap layer. The M1 chambers contain only two gas gaps. This is to minimise the material in front of the electromagnetic calorimeter.

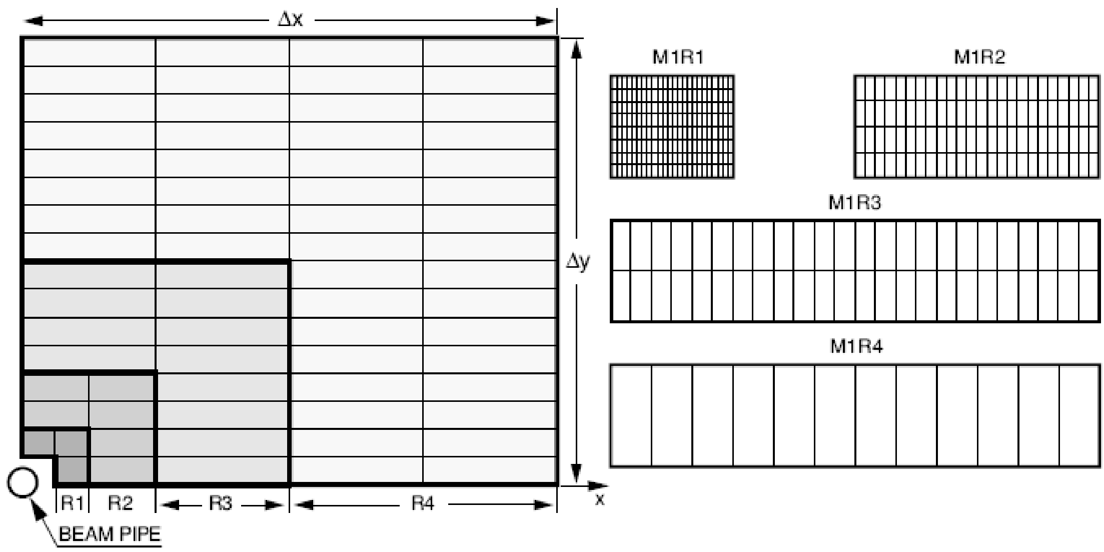

Figure 3.17: The segmentation of the muon chambers: the diagram on the left represents one quadrant of the muon station. Each rectangle represents one chamber. The diagram on the right shows the division of chambers into logical pads in station M1. In stations M2 and M3 the number of pad columns in each chamber is twice that of M1. In stations M4 and M5 the number of pad columns is half that of M1.

In the region R1 of M1 the most stringent requirement of the detector is a rate capability of 500 kHz/cm^2. This is not easy to achieve with MWPCs, so triple GEM detectors are used instead. The detectors comprise three gas electron multiplier foils sandwiched between anode and cathode planes. 12 chambers are used, each formed from two triple GEM detectors forming two sensitive layers. The two layers are connected as a logical OR.

Stations M1 to M3 have higher spatial resolution than M4 and M5 in the x-coordinate. M1 to M3 are used to measure the track direction and p_T, M4 and M5 are mainly used to select muons based on their penetrating power. Using a sample of $B_d^0 \to J/\Psi K_S^0$ the muon identification efficiency, $\epsilon(\mu \to \mu) \sim 94\%$ [17]. The pion misidentification fraction is $\epsilon(\mu \to \pi) \sim 3\%$ [17]. The identification efficiency is a flat function of momentum above 10 GeV/c.

3.11 The Trigger System

The LHCb plans to run at a luminosity of $2 \times 10^{32}\,\mathrm{cm}^{-2}s^{-1}$. The bunch crossing frequency is 40 MHz, while the frequency of visible interactions is 10 Mhz. A visible interaction is defined as one which produces at least two tracks that leave sufficient hits in the VELO and tracking stations to be reconstructible [17]. This is to be reduced to 2 kHz by the trigger, a rate at which events may be written to storage for offline analysis. The trigger is designed to reject as many uninteresting background events as possible.

There are two levels of trigger: the Level-0, L0, and the High Level trigger, HLT. L0 comprises custom made electronics and operates synchronously with the 40MHz bunch crossing. The HLT is run on a processing farm and runs asynchronously.

3.11.1 The Level-0 Trigger

The L0 trigger must reduce the data rate from the 40 MHz of the LHC bunch crossings to 1 MHz, at which the entire detector output may be readout [17]. The L0 trigger comprises three components: the pile-up system, the L0 calorimeter trigger and the L0

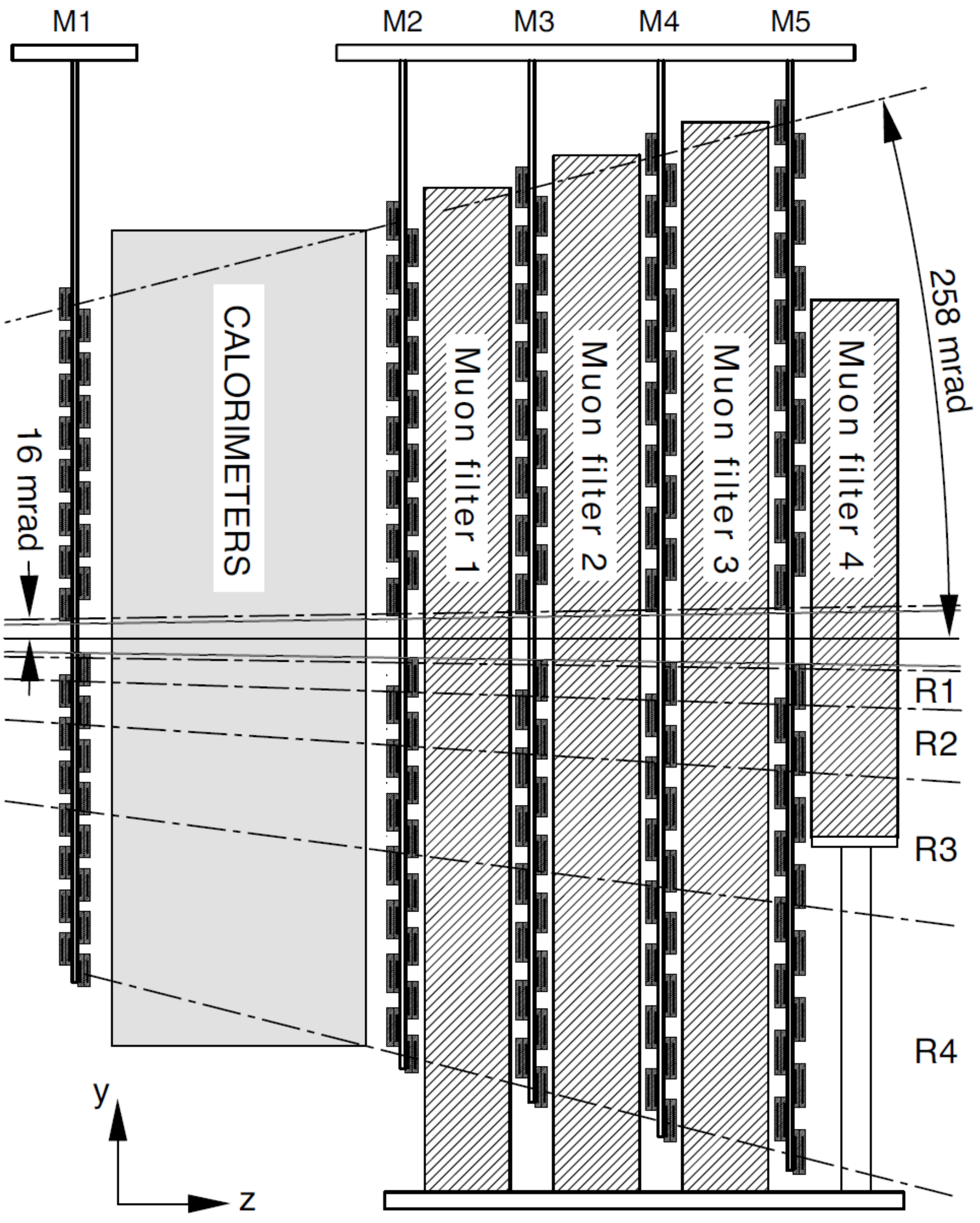

Figure 3.18: The Muon stations.

muon trigger. These are each connected to the Level 0 Decision Unit, L0DU, which collects all information from the trigger systems for the final decision.

The pile-up system attempts to find the number of primary p-p interactions in each bunch crossing. Bunch crossings with more than one p-p interaction have a tendency to trigger on combinatorics rather than genuine B decays. In addition they occupy a large proportion of the available processing power. The pile-up system is used to veto such events. The pile-up system uses four silicon sensors of the same type as those in the VELO, section 3.5, to measure the position of primary vertex candidates and measure of total backward charged track multiplicity, that is tracks with negative pseudorapidity [26].

The calorimeter and muon triggers look for particles with high E_T and high P_T. These are characteristic of B decays. The calorimeter trigger forms clusters by adding E_T of 2×2 cells and selecting the clusters with the largest E_T. Clusters are identified as electron, γ or hadron based on the information from the SPD, PS, ECAL and HCAL. The E_T of all HCAL cells is summed to reject crossings without visible interactions and to reject triggers on muon from the halo. The total number of SPD cells with a hit are counted to provide a measure of the charged track multiplicity in the crossing. The muon chambers allow for standalone muon reconstruction with a P_T resolution of roughly 20%. The muon trigger looks for the two highest transverse momentum muons.

3.11.2 The High Level Trigger

The High Level Trigger is a C++ application run on about 2000 nodes in the Event Filter Farm, EFF. The HLT has access to all the data from each event, but given the 1 MHz data rate and limited computing power it aims to use only part of the information available to make a decision. The HLT is implemented in two stages, HLT1 and HLT2.

HLT1 is designed to refine the L0 decision, outputting at a frequency of 30 kHz. The HLT starts with what are called alleys. Each of the alleys addresses one of the triggers from the L0 trigger. They enrich B-content by refining the L0 objects and adding impact parameter information. Most events which pass L0 are triggered on only one of the L0

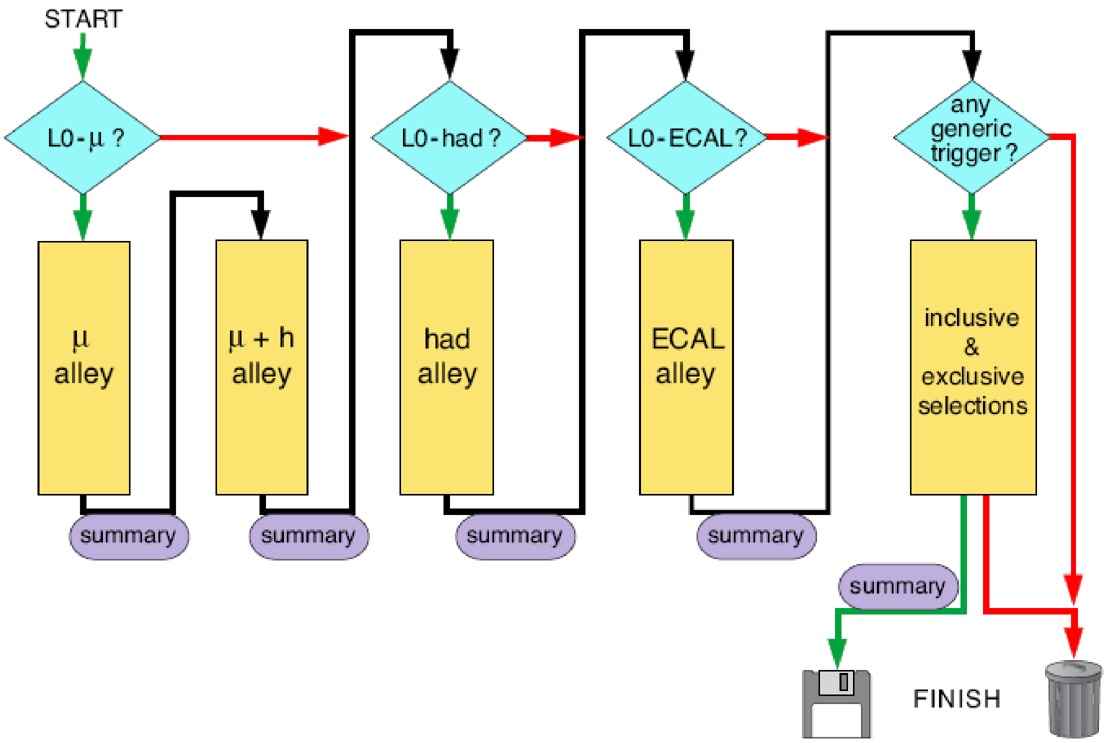

Figure 3.19: The HLT alleys. Rectangles represent reconstruction algorithms. Diamonds indicate where the trigger decisions are made.

triggers, and are analysed in only one HLT alley. Around 15% of events are selected by multiple triggers and are thus dealt with by multiple alleys.

If an event is selected by at least one alley then it is processed by two types of trigger algorithms in HLT2. The HLT2 trigger runs a full reconstruction, similar to that performed in an offline analysis. The HLT2 consists of inclusive and exclusive selections that cover the various decay channels required by the LHCb physics goals. The inclusive selections pass triggered events based upon a partial reconstruction of a given decay. The exclusive selections require the full decay and all final state particles to be reconstructed. The events passed by the HLT2 are then written to disk for further offine analysis. Figure 3.19 is schematic of the different alleys in the HLT decision process [17].

3.11.3 Triggering for $B_s \to D_s\mu\nu$ Events

In chapter 6 an analysis concerning the measurement of CP violation in mixing and production asymmetry using $B_s \to D_s\mu\nu$ events is presented. Selection criteria for these events have been developed in a separate study [69]. In a typical $B_s \to D_s\mu\nu$ event, the high-momentum muon might trigger the L0 Muon trigger and muon alley of the HLT. Equally, the hadronic part of the decay might trigger the calorimeter trigger and hadronic alley of the HLT. Additionally, the remainder of the event, be it the opposite side B-decay, prompt J/Psi production or just a high-momentum Kaon, could ensure the event triggers. For the analysis presented in 6 it does not matter what triggered the event, as long as it was triggered by something. The minimisation of background will be done primarily in the offline selection [69].

3.12 The LHCb Software

All of the LHCb software packages are based upon a software architecture known as Gaudi [27]. This supports both online and offline software. The framework is designed to be able to accommodate changes in requirements and detector technology. The LHCb software was developed in C++.

Event simulation is carried out by the Gauss application. This operates in two stages. Firstly, a generation stage, which simulates proton proton collisions and models the decays of the resulting secondary particles. The second phase simulates the particles interaction with the LHCb experiment. In the generation phase Gauss maybe interfaced with a number of specialist software packages, such as Pythia [28], Herwig [29] and EvtGen [30]. In its second phase, Gauss makes use Geant4 [31].

The Boole application digitises the data from Gauss, to model the detector response. The digitisation process includes simulation of the detector response, the readout electronics and the L0 trigger hardware.

Reconstruction is carried out by the Brunel application. It can process both experimental data from the LHCb DAQ system, or the output from Boole, which simulates this.

Physics analysis is carried out using the DaVinci application. Event and detector visualisation is performed with Panoramix.

A distributed computing system called the grid has been developed for analysis of LHC data. It allows users to run analysis jobs on remotely, wherever processing power is available, without having to know precisely where the jobs are running. Job submission is managed by Ganga [32], a software package developed jointly by LHCb and ATLAS.

3.13 Data Model and Computing Model

3.13.1 Data Model

The processing of data is done in several stages. Figure 3.13.2 is a schematic of the various stages. The process begins with RAW data, either experimental data or Monte Carlo simulation. The experimental data comes from via the EFF, where the HLT is run.

The simulated RAWmc data sets contain simulated hit information, but also truth information. The truth information is used to record the physics history of the event and the relationships of hits to incident particles. RAWmc data sets are therefore larger than the experimental data sets, but otherwise identical.

The RAW data must be reconstructed in order to provide physical quantities. The pattern reconstruction algorithms in the reconstruction program require calibration and alignment data, and information on the detector. The calibrated and alignment data will be produced from online monitoring and/or offline from a pre-processing of the data associated with each of the sub-detectors. The reconstruction process will be repeated to accommodate improvements in the algorithms and improved determination of the calibration.

The event reconstruction results in new data. These data are stored in Data Summary Tapes, DSTs, and reduced Data Summary Tapes, rDSTs. The rDSTs are analysed to determine the momentum four-vectors corresponding to the measured particle tracks, to locate primary and secondary vertices and algorithms applied to identify candidates for composite particles whose four-momenta are reconstructed. Each particular channel of interest will provide such a pre-selection algorithm. The rDSTs will contain only sufficient data to allow the pre-selection algorithms to be run. Events passing the selection will be fully re-reconstructed, recreating the full information associated with the event. The DSTs are the outputs of the stripping and will contain more information than the rDSTs.

An event tag collection will also be created to aid reference to selected events. It contains a summary of each event's characteristic and a reference to the DST record. The event tags are stored separate files to the DSTs. Individual physics analyses are carried out by processing data in the DSTs.

3.13.2 Computing Model

A schematic of the LHCb computing model is shown in figure 3.21. The model comprises CERN, the Tier-1 sites and the Tier-2 sites. CERN is the central production centre and is responsible for distributing RAW data to the Tier-1 sites. CERN also acts as one of the Tier-1 centres. The Tier-1 centres will be responsible for all the production-processing phases associated with the experimental data. The other Tier-1 centres are CNAF (Italy), FZK (Germany), IN2P3 (France), NIKHEF (The Netherlands), PIC (Spain) and RAL (UK). RAW data will be stored in its entirety at CERN, with another copy distributed across the six Tier-1 centres. The production of the stripped DSTs will be at these sites, and it is envisaged that the majority of the user analyses will be at CERN and the Tier-1 sites. The Tier-2 sites are primarily Monte Carlo production sites. CERN and the Tier-1 sites will act as repositories for the Monte Carlo data.

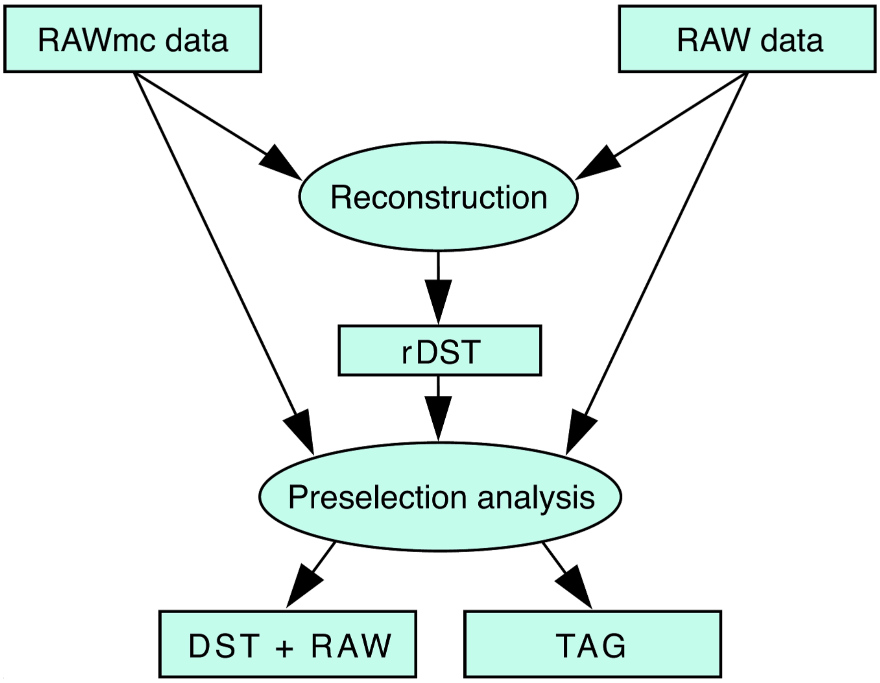

Figure 3.20: The LHCb computing dataflow model.

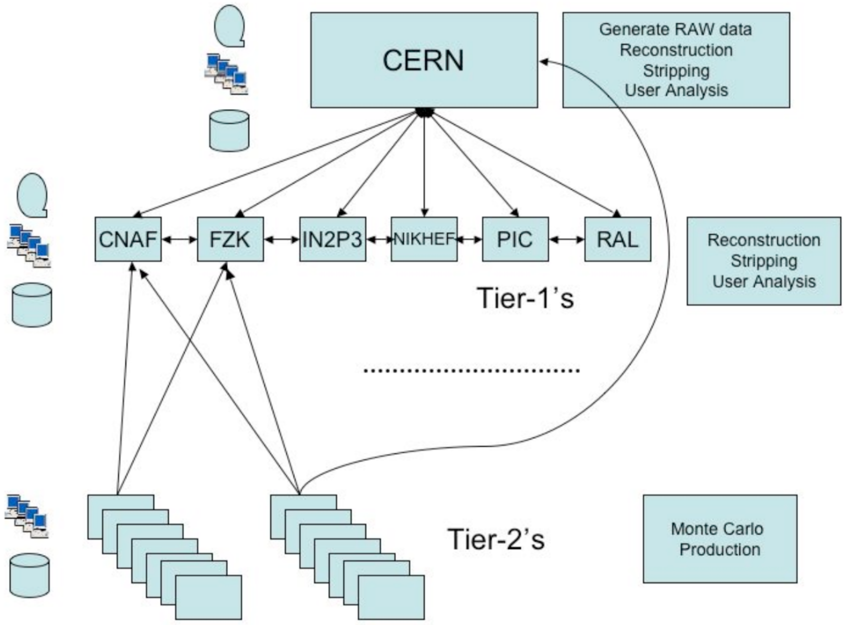

Figure 3.21: Schematic of the LHCb Computing Model

Chapter 4

The RICH 1 Mirrors

4.1 Introduction

The RICH 1 subdetector was introduced in chapter 3. This chapter details a number of tests made of the RICH 1 mirrors, necessary to ensure their adequate production and to determine their likely performance within the running LHCb experiment.

4.2 The RICH 1 Mirrors

The RICH 1 subdetector contains two sets of mirrors: a set of plane glass mirrors, and a set of spherical carbon fibre mirrors. The plane mirrors were manufactured by COMPAS [33]. The spherical mirrors were manufactured by Composite Mirror Applications Inc., CMA [34]. The following sections detail a number of tests that were performed on the mirrors.

The tests focused mainly on three properties of the mirrors: the reflectivity, the radius of curvature and the D_0. The D_0 is defined as the diameter of the smallest circle at the centre of curvature of the mirror, through which 95% of light from a point source at the centre of curvature is reflected, see figure 4.1. In the case of the spherical mirrors, the measurements performed fulfilled three purposes:

- Firstly, measurements were made to determine how quickly the mirrors can be expected to degrade in the running LHCb experiment. These tests were performed on three mirrors, one of which was tested for the effects of radiation exposure, the other two being tested for the effects of exposure to C_4F_{10} gas. The results are described in section 4.4.

- Secondly, a series of tests were made to assess the quality of the reflective coating. Tests were made on a number of glass and carbon fibre samples coated by two companies, CMA and SESO [35]. These determined if the coatings were of a sufficiently high standard and, where necessary, the results were used to inform improvements in the coating procedure. These measurements are described in section 4.5.

- Thirdly, the final mirrors were tested to determine if the radius of curvature, D_0 and reflectivity met the design specifications. The results of these measurements are given in section 4.6

RICH 1 uses sixteen plane mirrors. Twenty four were received, and each had its D_0, radius of curvature[1] and physical dimensions measured, to determine if it met the design specifications. The results are discussed in 4.7. The coating of the plane mirrors was carried out at CERN and is not discussed here.

4.3 Measurement Apparatus

Two pieces of equipment were used to measure the reflectivity of the various mirrors tested: a reflectometer that was built at CERN, by a team lead by Andre Braem, and a Lambda 15 spectrophotometer manufactured by Perkin Elmer[36]. The reflectometer is discussed in section 4.3.1. Section 4.3.2 gives a comparison of the reflectometer and the spectrophotometer. A description of the equipment used for measurements of radius of curvature and D_0 given in section 4.3.3.

[1] Although the term plane mirrors is used to describe one set of the RICH 1 mirrors, the mirrors are in fact spherical with a very large radius of curvature ($> 90m$), and therefore it is possible to define a radius of curvature and D_0 for them.

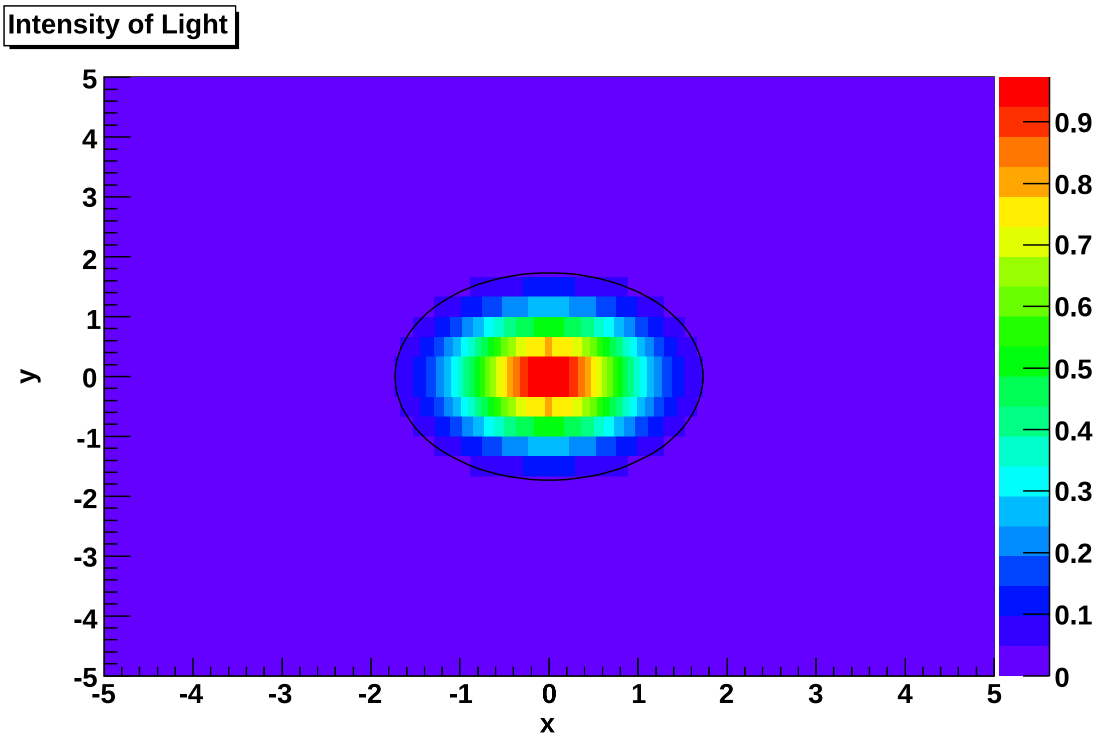

11

Figure 4.1: A schematic representation of the D0. The intensity of the light is described by a two-dimensional gaussian function. The black circle marks the D0, the smallest circle containing 95% of the light. The intensity and length scales are arbitrary. The distribution of the light is not intended to be realistic, and is used simply to illustrate the concept of the D0. The figure was generated using ROOT.

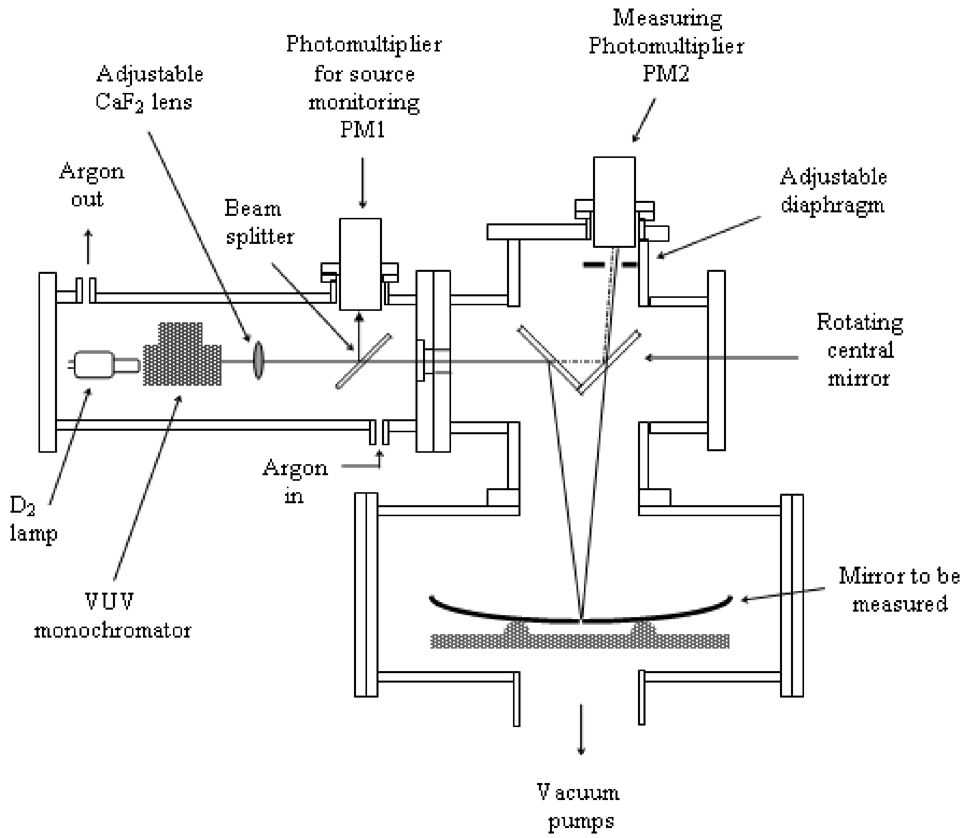

Figure 4.2: A schematic of the reflectometer

4.3.1 The Reflectometer

4.3.1.1 Basics of the Reflectometer Design

The reflectometer discussed in this section was used in the aging tests of the CMA sample mirrors and also to test the reflectivity of various mirror coatings. A schematic of this reflectometer is shown in figure 4.2.

The reflectometer has a Deuterium, D_2, light source; the light from which passes through a monochrometer, allowing measurements to be made at a particular wavelength. The beam is then split by a beam splitter, with the two subsequent beams each falling on one of two photomultiplier tubes, PM 1 and PM 2. PM 1 monitors the intensity of the light from the D2 lamp. The light falling on PM 2 reaches it by one of two paths, depending on the position of the central rotating mirror. With the rotating mirror in one position, the measurement position, the light is reflected onto the mirror that is to have its reflectivity measured and then onto PM2. With the rotating mirror in the normalisation position, the light is reflected directly onto PM 2. The reflectivity, R, is then given by the following ratio of the currents through the photomultiplier tubes

$$R = \frac{I_2^{meas}/I_1^{meas}}{I_2^{norm}/I_1^{norm}}$$

where I_1^{meas} is the current through PM 1 when the rotating mirror is in the measurement position, with I_2^{meas}, I_1^{norm} and I_2^{norm} defined similarly.

The position of the rotating mirror, lens and monochrometer were controlled automatically by computer software based on LabVIEW[2].

4.3.1.2 Calibration and Stability of the Reflectometer

To determine if the measurements made with the reflectometer were reliable, two issues were examined: the extent to which the performance of PM2 affected the reflectivity measurements and the extent to which the measurements were repeatable.

The light that reaches PM 2 follows one of two paths, and the beam does not illuminate precisely the same area on the surface of PM 2 in the two cases. Thus there was a need to determine whether non-uniformities in response across the surface of the photomultiplier tube affected the measured reflectivity. Such non-uniformities were seen by measuring the current through PM 2 with the central rotating mirror in a number of different positions and therefore illuminating different regions of PM 2's surface.

Three different photomultiplier tubes were tested in the rôle of PM 2. For each, the response across the surface was examined and the reflectivity of a single sample, designated mirror 142, was measured. The change in response across the surface of the PMT was examined by measuring the current through the PMT with the central

[2]LabVIEW is a visual programming language and development environment produced by National Instruments [37].

rotating mirror in different positions, and thus illuminating different parts of the surface. Mirror 142 was a small glass mirror with an aluminium and hafnium oxide coating, that had originally been used in reflectivity tests for previous work on RICH 2. The photomultiplier responses, at a wavelength of 350 nm, are shown in figure 4.3.

Figure 4.4 shows the reflectivity of mirror 142 measured using the different photomultiplier tubes. The difference is small, despite the obvious inhomogeneity of the photomultiplier tubes. This is, in part at least, due to correct positioning of mirror 142. The position of this mirror, or any that is to be measured, can, and must, be adjusted so that the area of PM 2 illuminated is as similar as possible when the central rotating mirror is in the measurement position and when it is in the normalisation position. The choice of photomultiplier tube was thus found not to be of critical importance. The third photomultiplier tube tested was used in the rôle of PM 2. Further evidence that results gained with this photomultiplier tube are reliable came from comparison with the spectrophotometer, see section 4.3.2

It is important to establish the reproducibility of measurements made with the reflectometer. This was done by making several measurements of mirror 142. Between each measurement the mirror was removed and then replaced in the reflectometer. Figure 4.5 shows the results. The variation of the measured reflectivity is small. Figure 4.6 shows the standard deviation of the reflectivity measurements as a function of wavelength. No dependance on wavelength is seen. These results were used to estimate an error on the reflectivity measurements. The error is 0.7 %, it is not shown on the reflectivity plots for reasons of clarity.

4.3.2 The Spectrophotometer

The Perkin Elmer Lambda 15 spectophotometer was used in addition to the CERN reflectometer to test the quality of the mirror coating. It was not used in the aging tests since the sample mirrors in question were too large to be placed inside it.

To assess the reproducibility of measurements made with the spectrophotometer, a small glass mirror designated mirror 148, had its reflectivity measured repeatedly in

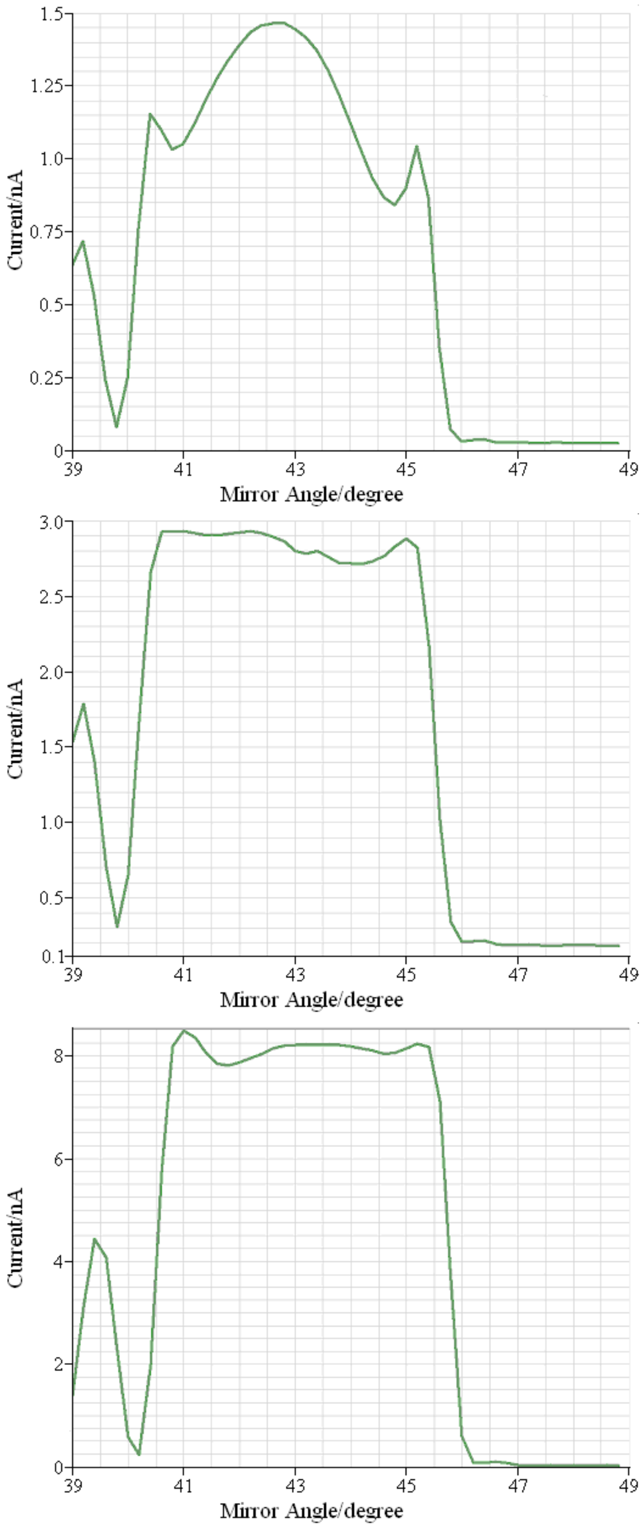

Figure 4.3: Photomultiplier tube responses. From top to bottom, the first, second and third photomultiplier tubes tested in the rôle of PM2.

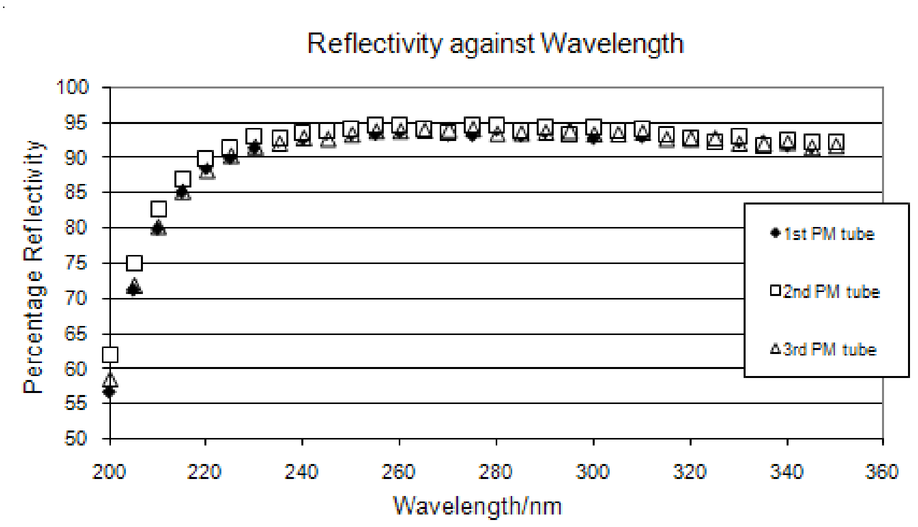

Figure 4.4: The reflectivity of mirror 142 as measured using three different photomultiplier tubes. For clarity errors are not shown, but are estimated to be around 0.7%, see figures

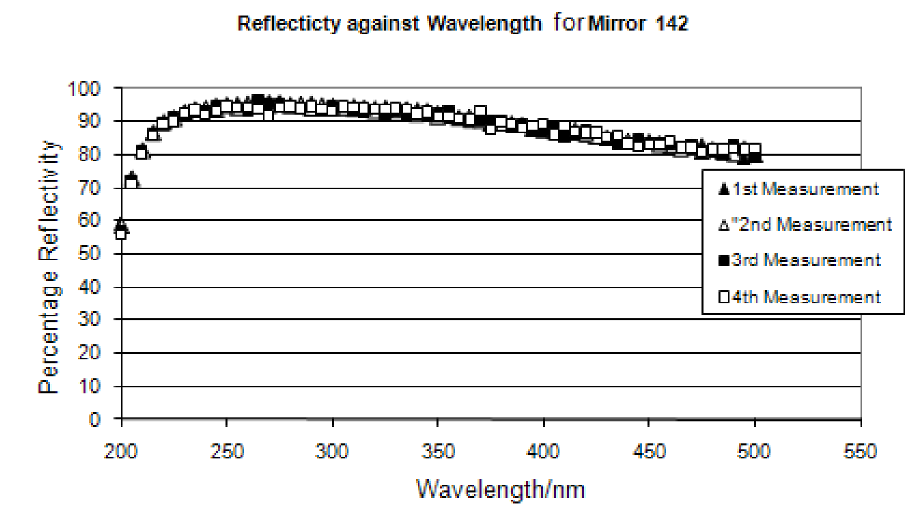

Figure 4.5: Repeated reflectivity measurements of mirror 142.

the spectrophotometer. Mirror 148, like mirror 142, was a mirror first used for previous coating tests and had an aluminium coating. The variation in the results was slightly less than in the case of the reflectometer, see figure 4.7.

Figure 4.8 shows a comparison of the reflectivity of mirror 142 as measured by the spectrophotometer with that obtained with the reflectometer. There is a small, but noticeable, difference in the results, with the reflectivity measured by the spectrophotometer being slightly higher. The exact nature of this difference has never been fully investigated. Reflectivity is a function of polarization, and this is likely to be a contributing factor to the difference in the measurements. Measurements are made with light of different polarization in the two machines. The light is polarized through reflection, and it is reflected a different number of times, and at different angles in the two machines.

4.3.3 The Optical Equipment for the D_0 and Radius of Curvature Measurements

The measurements of D_0 and radius of curvature were made in a dark room at CERN. The mirrors were mounted on a three point support stand, which stood on a bench. They were illuminated by a diode laser, and the light was reflected onto a CCD camera. Both the camera and the light source were mounted on a sliding table. The mirror stand and the sliding table were positioned so that the distance between the mirror and the CCD was roughly equal to the expected radius of curvature of the mirror. The camera was then moved, under the control of a LabVIEW programme, through a series of 1 mm steps over a distance of 40 mm, centred on its original position. In each position a photograph was taken. The LabVIEW programme then analysed the photographs, and for each calculated the diameter of the circle containing 95% of the light, the smallest such diameter being the D_0 and the distance of the camera from the mirror at this point being taken as the radius of curvature. Figure 4.9 depicts this setup.

Studies have been made of the reproducibility of measurements made by this optical equipment[38]. These found the expected error on the D_0 measurements to be 0.06 mm, and the error on radius of curvature measurement to be 0.7 mm. The circumstances

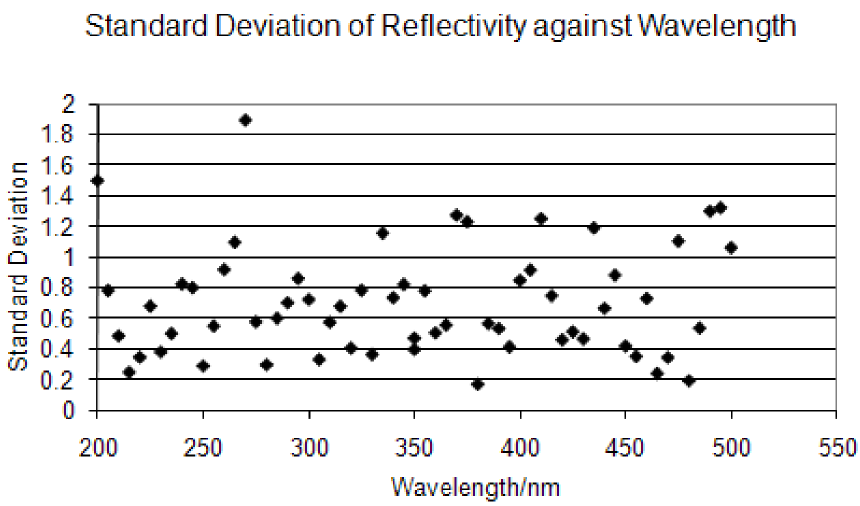

Figure 4.6: Standard deviations of the measurements of mirror 142's reflectivity. The mean standard deviation is about 0.7%.

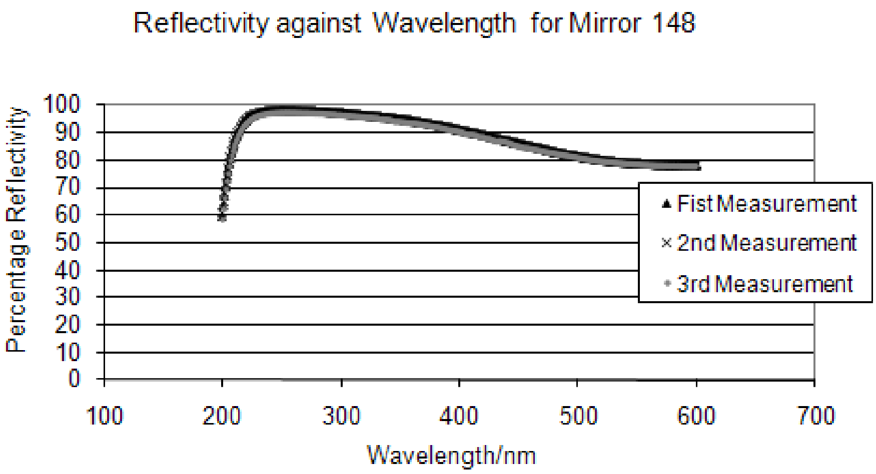

Figure 4.7: Repeated measurements of a single mirror in the spectrophotometer.

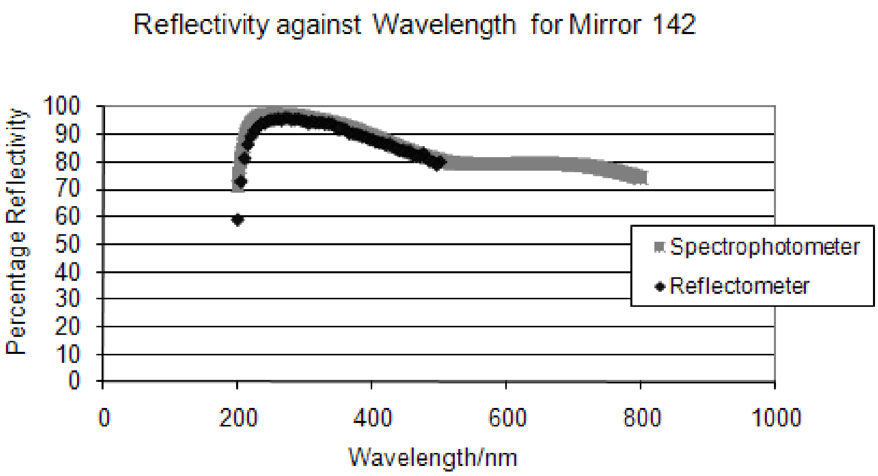

Figure 4.8: A comparison of mirror 142's reflectivity as measured by the reflectometer and the spectophotometer.

under which the aging tests described in sections 4.4.1 and 4.4.2 were not identical to those under which these studies were made, however, and there are reasons to believe the uncertainty on the radius of curvature measurements is larger for the aging tests. There were long periods of time between the different measurements during which the equipment was used for other purposes, meaning that the mirror support would have to be repositioned, a source of error in the radius of curvature measurements not considered in [38]. An initial input separation of camera and mirror is required by the LabVIEW programme. This required knowledge of the position of the stand relative to the bench, the position of the sliding table relative to the origin of a tape measure, knowledge of the origin of the tape measure relative to the bench and knowledge of the thickness of the mirror. The first three of these had to be measured each time a radius of curvature measurement was made. These error on these measurements is estimated as $\sim 1\,\mathrm{mm}$, the precision offered by the tape measure. There are, therefore, four independent sources of error, each with an error of $\sim 1\,\mathrm{mm}$; a total error of $\sim 2\,\mathrm{mm}$ is expected.

4.4 Spherical Mirror Aging Tests

The spherical mirrors will be mounted within the C_4F_{10} radiator and exposed to high levels of radiation. It is important that the performance of the mirrors does not degrade significantly due to this environment.

The effects of subsistence in such an environment have been examined using two sample mirrors supplied by CMA, designated CMA 1 and CMA 2. Tests were designed to measure changes in the radius of curvature, D_0 and reflectivity of the samples as a result of exposure to C_4F_{10} or as result of radiation damage. CMA 1 was used to test the effects of C_4F_{10} exposure, CMA 2 was used to test the effects of irradiation. Figure 4.10 shows the two mirrors. A third mirror, named the demonstrator mirror, was also tested for the effects of C_4F_{10} exposure. The demonstrator mirror is a carbon fibre mirror of similar size and optical properties to the mirrors used in RICH 1, it was manufactured by CMA primarily to demonstrate their ability to produce large mirrors with the desired radius of curvature and D_0. Due to its size it could not be placed in the reflectometer

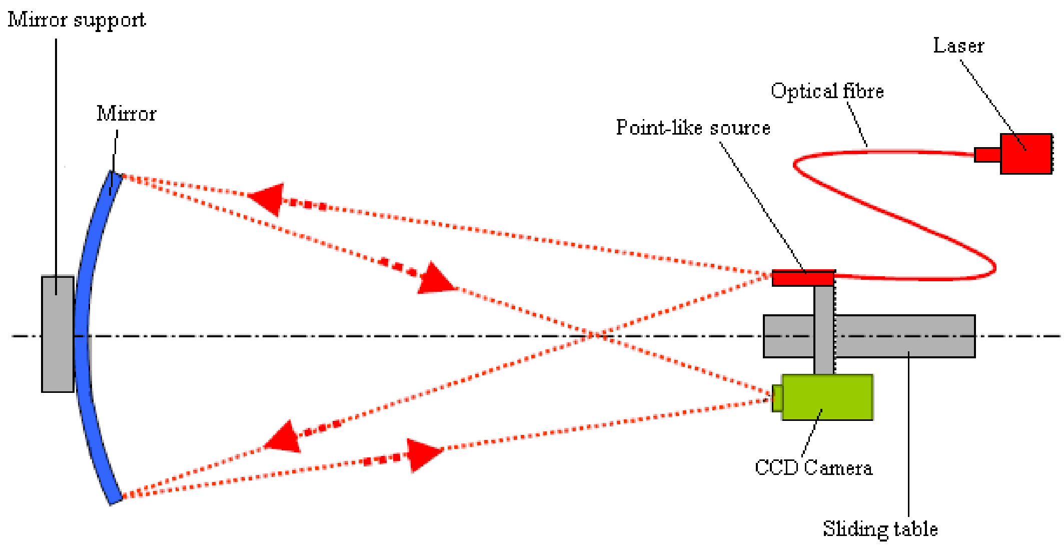

Figure 4.9: A diagram of the equipment used in D_0 and radius of curvature measurements of the spherical mirrors.

Time in C_4F_{10}	Radius of curvature/mm	D_0/mm
None	1876 ± 2	0.97 ± 0.06
1 month	1887 ± 2	0.77 ± 0.06
2 months	1891 ± 2	0.78 ± 0.06
4 months	1889 ± 2	0.75 ± 0.06
7 months	1890 ± 2	0.71 ± 0.06
11 months	1889 ± 2	0.80 ± 0.06

Table 4.1: Radius of curvature and D_0 of CMA1 after various exposures to C_4F_{10}.

so only its D_0 and radius of curvature were measured. It is shown in figure 4.10.

4.4.1 C_4F_{10} Exposure

The reflectivity of CMA 1 was measured using the reflectometer described in section 4.3.1. At the time of writing, the mirror has been given a total of 11 months exposure to C_4F_{10}. No degradation in radius of curvature, D_0 or reflectivity was observed. This can be contrasted with previous attempts to manufacture carbon fibre mirrors for RICH 1 which did degrade due to fluorocarbon exposure [39]. The previous mirrors were also manufactured by CMA, but no explanation of their different behaviour in C_4F_{10} has been offered by them.

Reflectivities measured after the various exposures are graphed in figure 4.11. The radius of curvature and D_0 measurements for CMA 1 are listed in table 4.1 and for the demonstrator mirror in table 4.2. The variation in the radius of curvature measurements is slightly greater than the error obtained in [38], a result of slightly different circumstances. The initial D_0 and R measurements for CMA 1 are outside the errors of the other measurements, however, this is most likely due to improper mounting of the mirror putting undue stress on the mirror in the first measurement, indeed the subsequent results show an improved D_0 so the change is unlikely to have come from C_4F_{10} exposure.

After the measurements were made at 11 months exposure the mirrors were replaced in the C_4F_{10}, and the tests are to be continued.

Figure 4.10: The mirrors used for the aging tests. Above are mirrors CMA1 and CMA2, below is the demonstrator mirror.

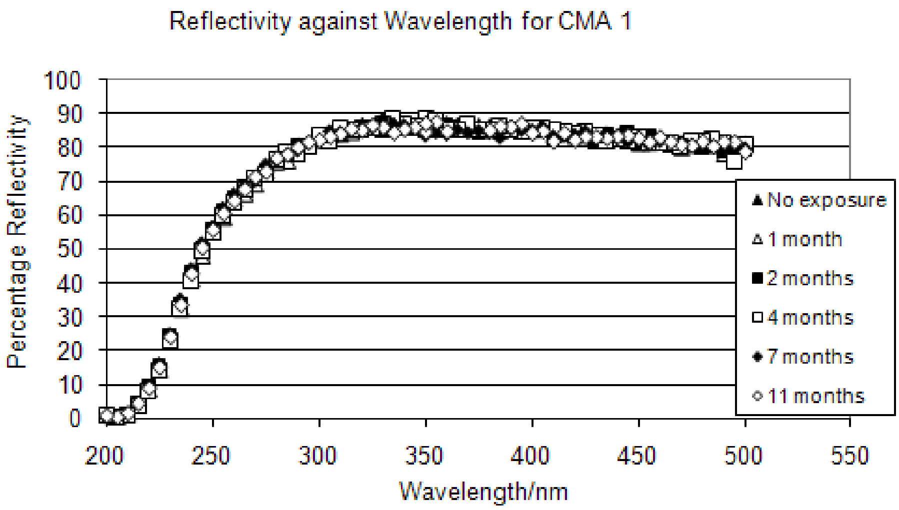

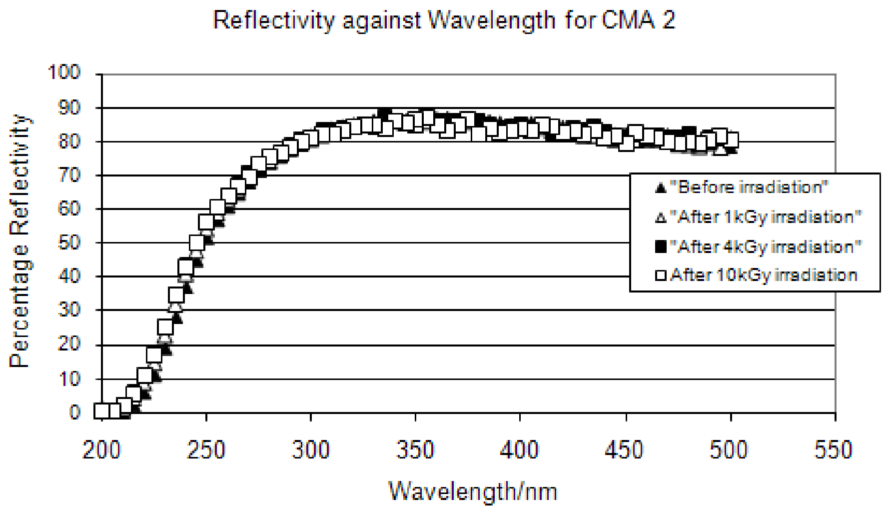

Figure 4.11: The reflectivity curves for CMA 1 and CMA 2 after their exposures to C_4F_{10} and radiation respectively. No decrease in reflectivity is seen in either case.

Time in C_4F_{10}	Radius of curvature/mm	D_0/mm
None	2201 ± 2	0.90 ± 0.06
1 month	2204 ± 2	1.11 ± 0.06
3 months	2205 ± 2	1.04 ± 0.06
6 months	2209 ± 2	1.15 ± 0.06
10 months	2205 ± 2	0.95 ± 0.06

Table 4.2: Radius of curvature and D_0 of the demonstrator mirror after various exposures to C_4F_{10}.

Radiation Dose	Radius of curvature/mm	D_0/mm
None	1890 ± 2	0.72 ± 0.06
1 kGy	1889 ± 2	0.85 ± 0.06
4 kGy	1896 ± 2	0.76 ± 0.06
10 kGy	1897 ± 2	0.59 ± 0.06

Table 4.3: Radius of curvature and D_0 of CMA 2 after various exposures to gamma ray radiation.

4.4.2 Radiation Exposure

The mirror CMA 2 was irradiated with a ^{60}Co gamma ray source on three occasions. The irradiation took place at the IONISOS cobalt-60 gamma facility[3]. The doses which CMA 2 received were 1 kGy, 3 kGy and 6 kGy, giving total exposures of 1 kGy, 4 kGy and 10 kGy. This corresponds roughly to the dose that the section of the mirror closest to the beam pipe will receive after 1, 4 and 10 years of LHC running [40]. No sign of degradation in radius of curvature, D_0 or reflectivity has been observed. Reflectivity curves measured after the various exposures are shown in figure 4.11, and the radius of curvature and D_0 measurements are listed in table 4.3. No further tests for the effect of radiation exposure are planned.

4.5 Spherical Mirror Coating

A high reflectivity is required of the RICH 1 spherical mirrors. The exact reflectivity specifications [44] are given in table 4.4. The mirrors were too large to be coated in any of the available facilities at CERN, therefore the prospects of CMA coating the mirrors were investigated. To this end CMA coated a number of carbon fibre and glass samples so that their ability to coat the mirror could be assessed. The reflectivity of these samples was measured to test the quality of the coating. In some cases an Auger Electron spectroscopy analysis was performed by M. Taborelli of the TS/MME group at CERN, to provide further information about the make up of the coating. The quality of the CMA coatings was initially below the required standard, but was seen to improve

[3]IONISOS, Dagneux, France; www.ionisos.fr.

Wavelength region	Required reflectivity
$250\,\text{nm} < \lambda < 600\,\text{nm}$	85 %
$200\,\text{nm} < \lambda < 250\,\text{nm}$	70 %

Table 4.4: The reflectivity requirements for the spherical mirrors.

over time. In total three sets were received from CMA.

Coating samples from a second company, SESO, were also examined and the measurements are presented here.

4.5.1 The First CMA Sample Set

The first set of samples comprised two glass and two carbon fibre mirrors. One carbon fibre and one glass mirror were coated with a nominal 80 nm aluminium and 80 nm MgF_2 The other two mirrors had a nominal coating of 80 nm aluminium and 20 nm MgF_2. The reflectivity curves for these samples are shown in figure 4.12. There are a number of features worth noting. The measured reflectivity is much lower than both the desired reflectivity, see table 4.4, and the simulated[4] reflectivity, with the discrepancy between simulation and measurement suggesting a major failing in the coating process. Indeed, the large drop in reflectivity at low wavelength is consistent with absorption by an impurity. There is little difference between the reflectivity of the glass sample and the carbon fibre sample, indicating that the problem lay with the coating process not the substance coated. Subsequently only glass samples were used.

The Auger electron analysis confirmed the presence of substantial impurities in the coating [42]. Specifically there was evidence of oxidisation of the aluminium layer. It was also found that in the sample with the nominal 80 nm aluminium and 80 nm MgF_2 coating, both layers were substantially thinner than desired. The MgF_2 layer was under 40 nm thick, and the aluminium layer was $\sim$ 60 nm thick. On the sample with the nominal 20 nm thick MgF_2 layer, there was no clear boundary between the MgF_2 and the aluminium.

The initial coating samples supplied by CMA did not provide the required reflectivity.

[4]The simulation of reflectivity of the coatings was done using FTG FilmStar software [41]

Consequently CMA undertook to improve their coating technique in consultation with Andre Braem of CERN. Improvements in the reflectivity were sought by achieving a greater control of the depth of the aluminium and MgF_2 and by reducing the time between the deposition of the two layers.

4.5.2 The Second CMA Sample Set

Figure 4.14 shows reflectivity curves for the nine samples that CMA coated for their second set of test coatings. The different samples were designated LHCb4, LHCb5, ..., LHCb12. The samples were coated in batches of three, in three runs, in an evaporation chamber. They were fixed on a rotating mount 762 mm above the aluminium and MgF_2 sources, which were evaporated to coat the mirrors. The different positions of the samples within the chamber are detailed in figure 4.13.

A significant improvement in the reflectivity was seen compared to the first set of coatings, although none of the samples had the desired reflectivity, see table 4.4. An Auger electron spectroscopy analysis revealed a number of interesting features [43]. Firstly, that the thickness of the coatings varied substantially between the samples, with many being substantially thinner than the nominal values of 80 nm aluminium and 80 nm. Secondly, there was a variable amount of oxygen and carbon contamination amongst the samples.

The samples with the highest reflectivity were those with the thickest coatings. The samples with the thickest coatings, LHCb4, LHCb7 and LHCb10, were placed a part of the evaporation chamber that did not correspond to part of the full scale mirror. The reflectivity of the other samples suffered because the reduction in thickness of the coating with distance from the sources was not taken into account. In addition to this, the thickness of coating even of samples LHCb4, LHCb7 and LHCb10 was below the desired level. Therefore an improved control of the thickness of coating was sought for the next set of samples, in addition improving the purity of the applied coatings

Because of the problems with the CMA coating that had been seen, a second company, SESO, were considered for the procedure.

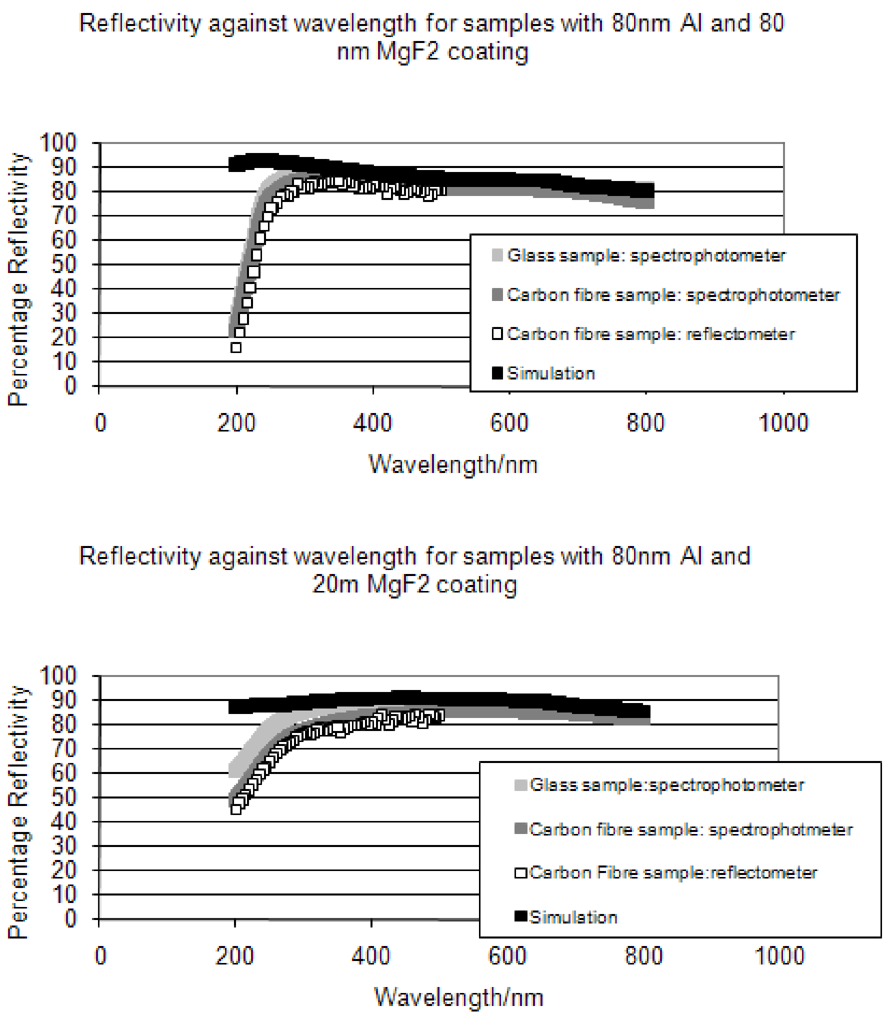

Figure 4.12: Reflectivity curves for the first CMA test coatings.

4.5.3 The First SESO Sample Set

SESO produced four samples on glass. The reflectivity curves for these samples are shown in figure 4.15. All of the samples have a reflectivity which satisfies the requirements, see table 4.4. Given the success of the SESO coating, it was decided that they would be used to coat the full scale mirrors.

4.5.4 The Third CMA Sample Set

The third set of samples coated by CMA comprised 20 mirrors. These were coated in four separate sessions, with five mirrors coated in each session. The details of the mirror positions within the evaporation chamber are given in figure 4.16. The samples mirrors in the fourth set were given the names LHCb13, LHCb14,...,LHCb17 and LHCb23, LHCb24,..., LHCb37.

Figures 4.17 show the reflectivity curves for these mirrors. Unlike any of the previous CMA samples, the majority of the forth set satisfied the requirements. However, by the point that the final CMA sample set had been tested, SESO had become the company of choice for the coating. The reason for this was that SESO appeared to have greater understanding of the coating procedure, as evidenced by the greater ease with which they produced a satisfactory coating. This gave a greater confidence that they could reliably produce adequate coatings.

4.6 The Final Spherical Mirrors

Before the installation of the four final mirrors, it was necessary to confirm they had the required optical properties. The requirements are $D_0 < 2.5\,\mathrm{mm}$ and radius of curvature $= 2700 \pm 27\,\mathrm{mm}$ [44]. Their D_0 and radius of curvature were measured both before and after their coating at SESO. Table 4.5 lists the measured values. In each case they meet the design specifications. The reflectivity was tested using small samples coated at the same time as the full scale mirrors. All were found to have the required reflectivity. Figure 4.18 shows the reflectivity curve measured for one of these samples. They are

Mirror	Radius of curvature/mm		D_0/mm	
	Before Coating	After Coating	Before Coating	After Coating
1	2708 ± 4	2706 ± 2	0.66 ± 4	1.06 ± 2
2	2709 ± 4	2707 ± 2	0.48 ± 4	0.91 ± 2
3	2707 ± 4	2707 ± 2	0.68 ± 4	0.96 ± 2
4	2708 ± 4	2707 ± 2	0.53 ± 4	0.50 ± 2

Table 4.5: Radius of curvature and D_0 of the final mirrors.

Quantity	Specification
Radius of Curvature	$> 90\,\mathrm{m}$
D_0	$< 2.5\,\mathrm{mm}$
Length	$380.5 \pm 0.5\,\mathrm{mm}$
Width	$347.45 \pm 0.5\,\mathrm{mm}$
Depth	$7.0 \pm 0.1\,\mathrm{mm}$

Table 4.6: Specifications for the plane mirrors.

compared to measurements made by SESO The results were consistent with each other and meet the required values. Figure 4.19 shows the four mirrors before coating.

4.7 RICH 1 Plane Mirrors

RICH 1 contains sixteen plane mirrors made from glass, arranged in two 4×2 arrays, one above and one below the beam pipe. Twenty four mirrors were received from COMPAS. Measurements were made of the radius of curvature, D_0 and physical dimension to determine if the mirrors were of the required quality. Although the mirrors are called plane, they are in fact spherical mirrors with a very large radius of curvature; D_0 and radius of curvature can be defined for them. The specifications for the different quantities are given in table 4.6.

Table 4.7 gives the measured values for D_0 and the radius of curvature for the plane mirrors. Figure 4.20 shows the dimensions of the flat mirrors and compare them to the desired value. The mirrors are consistently thinner than the specification, this however does not degrade their performance. The majority of the mirrors are slightly shorter than the specified length. This results in a slight loss of coverage compared to the specifications but was not considered a sufficient problem to reject the mirrors. Only 16

Mirror	Radius of Curvature/m	D_0/mm
1	1722 ± 356	1.14 ± 0.06
2	953 ± 107	0.59 ± 0.06
3	797 ± 75	0.78 ± 0.06
4	981 ± 113	1.18 ± 0.06
5	857 ± 86	0.66 ± 0.06
6	1185 ± 164	1.52 ± 0.06
7	633 ± 47	0.85 ± 0.06
8	610 ± 44	0.74 ± 0.06
9	1041 ± 127	0.79 ± 0.06
10	4936 ± 2825	1.11 ± 0.06
11	879 ± 91	0.71 ± 0.06
12	2654 ± 819	0.84 ± 0.06
13	1434 ± 240	0.96 ± 0.06
14	713 ± 60	0.68 ± 0.06
15	1640 ± 314	0.41 ± 0.06
16	5760 ± 3846	0.69 ± 0.06
17	1565 ± 286	0.66 ± 0.06
18	633 ± 47	1.05 ± 0.06
19	1813 ± 383	0.86 ± 0.06
20	-4335 ± 2163	0.61 ± 0.06
21	778 ± 72	0.90 ± 0.06
22	-1162 ± 153	0.89 ± 0.06
23	1565 ± 286	0.76 ± 0.06
24	1722 ± 346	0.86 ± 0.06

Table 4.7: The radius of curvature and D_0 measurements for the plane mirrors.

of the mirrors were needed. These were chosen on the basis of having the fewest defects on the surface.

4.8 Conclusions

The RICH 1 detector is one of the two RICH detectors within the LHCb. They are important for particle identification, particularly the separation of pions from kaons. The RICH 1 is useful for identifying lower momentum particles, RICH 2 higher momentum.

The Čerenkov light emitted by particles within RICH 1 is focused by spherical mirrors and reflected from an array of plane mirrors before it is detected. It is essential that these mirrors are of a high standard. The spherical and the plane mirrors were found to be manufactured to required standard. The spherical mirrors have been tested to see if they will degrade during the running of the experiment. Their performance is found to be unchanged by the equivalent of ten years' radiation exposure and 11 months exposure to C_4F_{10} gas.

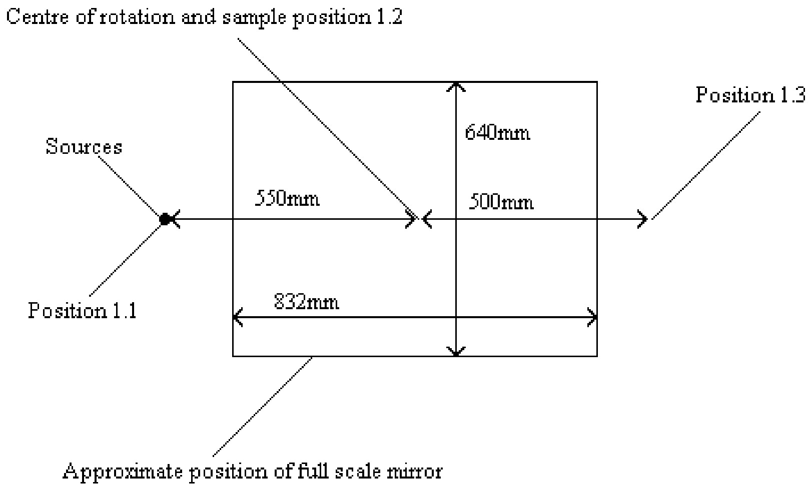

Position	Samples at this position
1.1	LHCb4, LHCb7 and LHCb10
1.2	LHCb5, LHCb8 and LHCb11
1.3	LHCb6, LHCb9 and LHCb12

Figure 4.13: The position of sample mirrors for the second CMA sample set.

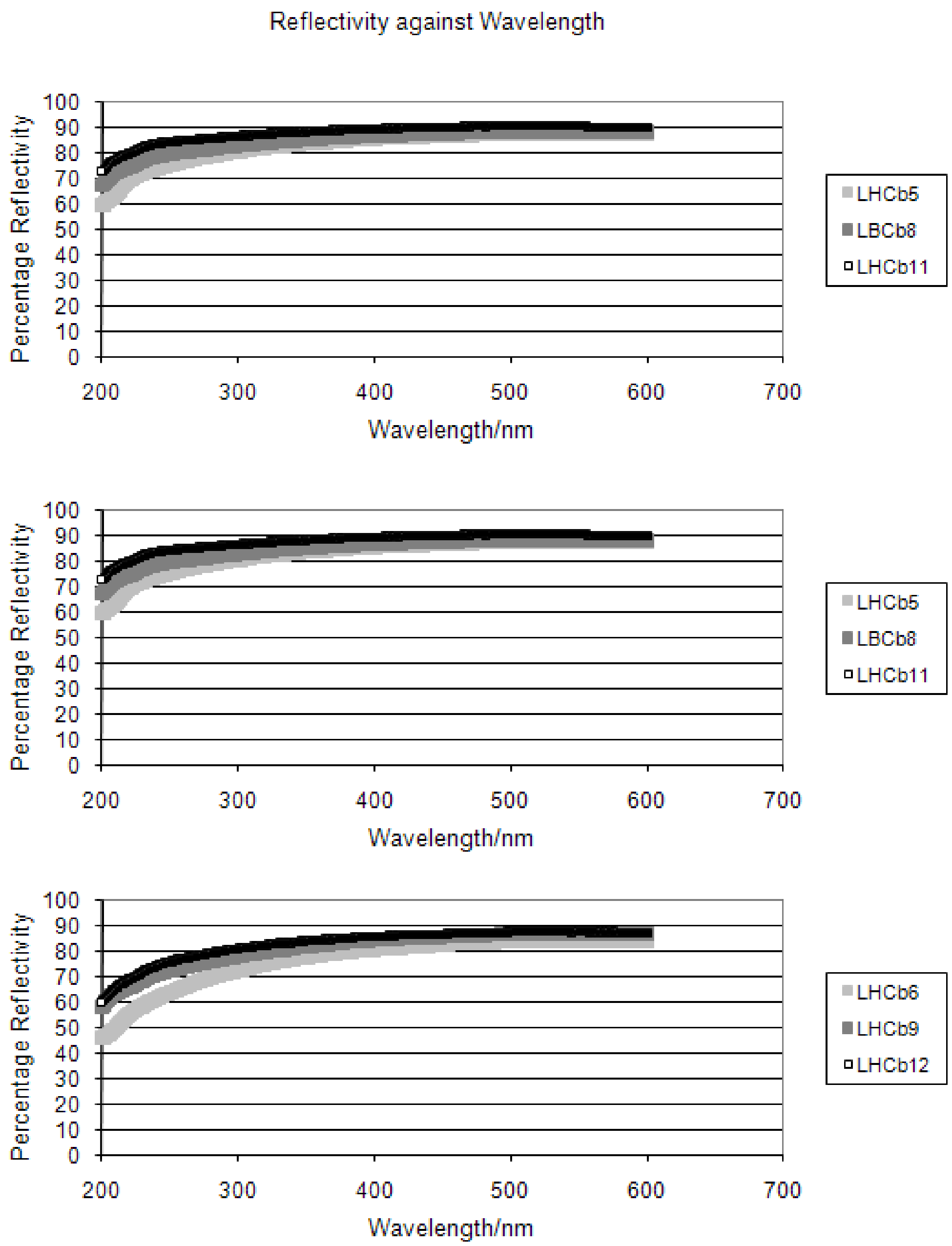

Figure 4.14: Reflectivity curves for mirrors from the second CMA sample set.

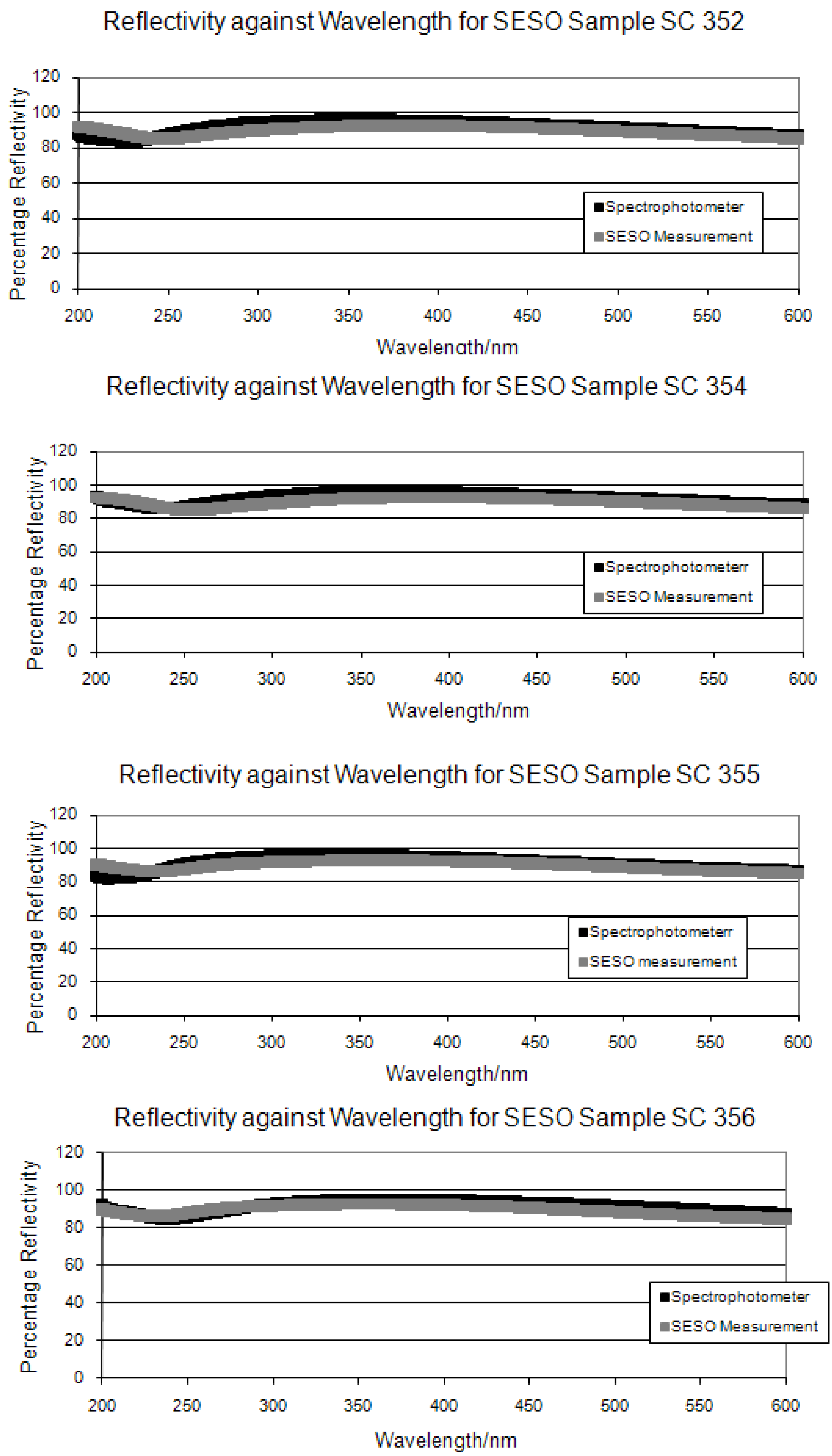

Figure 4.15: Reflectivity curves for the SESO samples, as measured by SESO and in the Lambda 15 spectrophotometer at CERN.

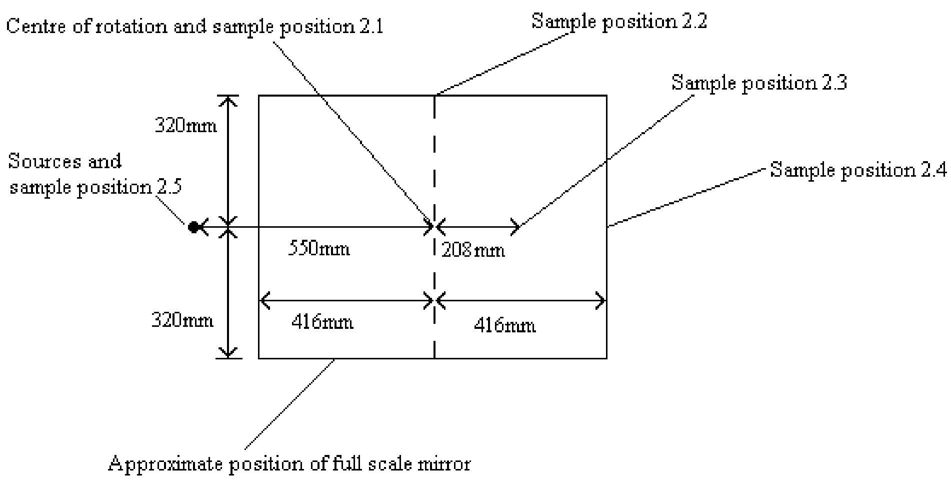

Position	Samples at this position
2.1	LHCb13, LHCb23, LHCb28, and LHCb33
2.2	LHCb14, LHCb24, LHCb29, and LHCb34
2.3	LHCb15, LHCb25, LHCb30, and LHCb35
2.4	LHCb16, LHCb26, LHCb31, and LHCb36
2.5	LHCb17, LHCb27, LHCb32, and LHCb37

Figure 4.16: The position of sample mirrors for the third CMA sample set

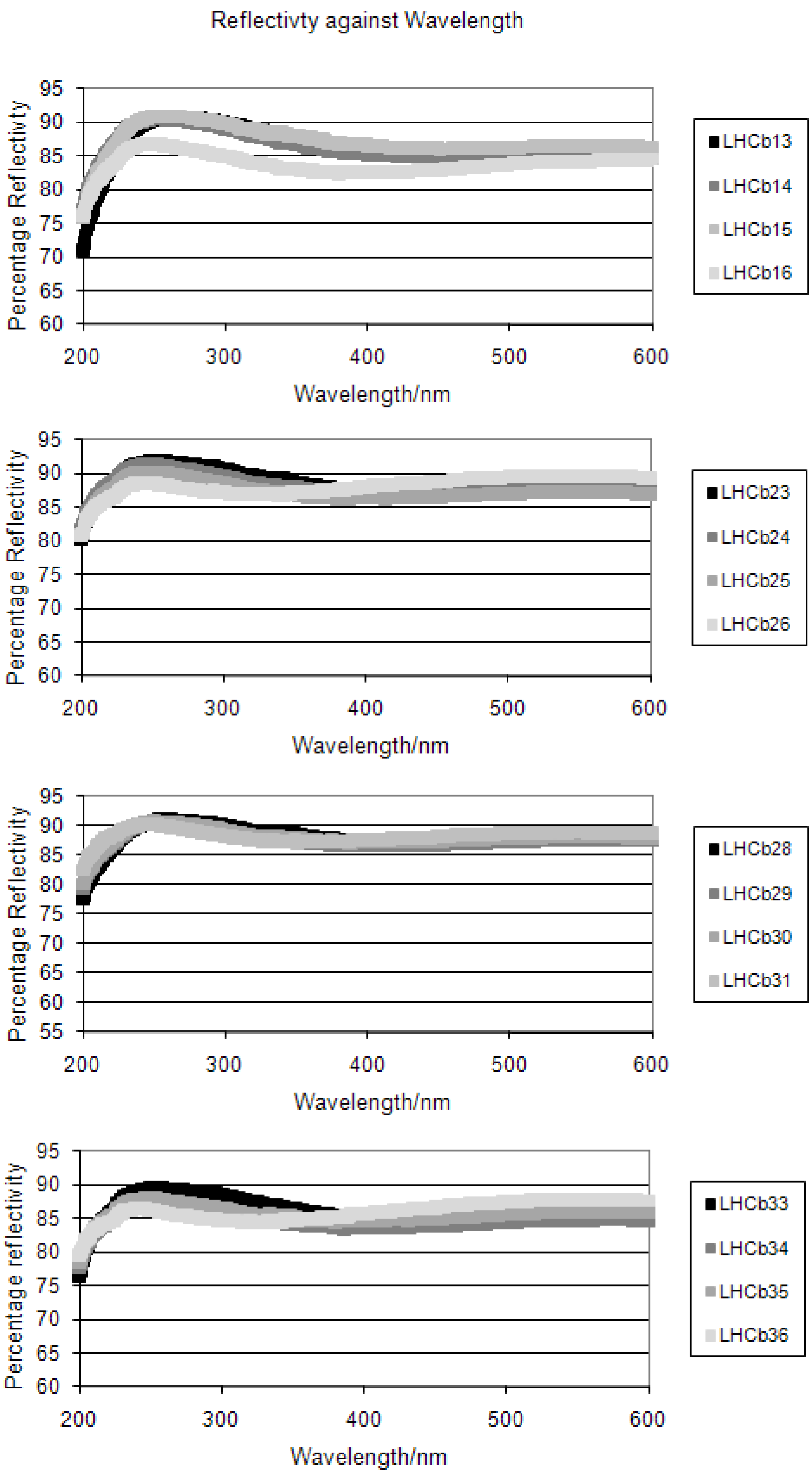

Figure 4.17: Reflectivity curves for the third CMA sample set.

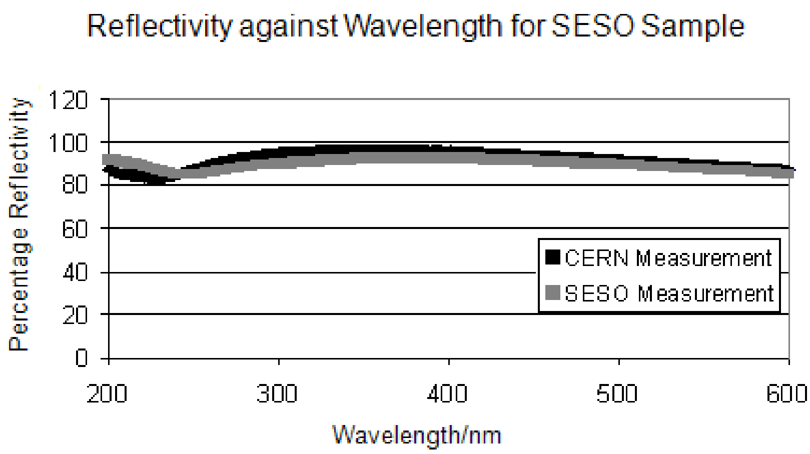

Figure 4.18: The reflectivity of one of the SESO sample mirrors that was used to test the reflectivity of the final mirrors.

Figure 4.19: The RICH 1 spherical mirrors prior to coating by SESO

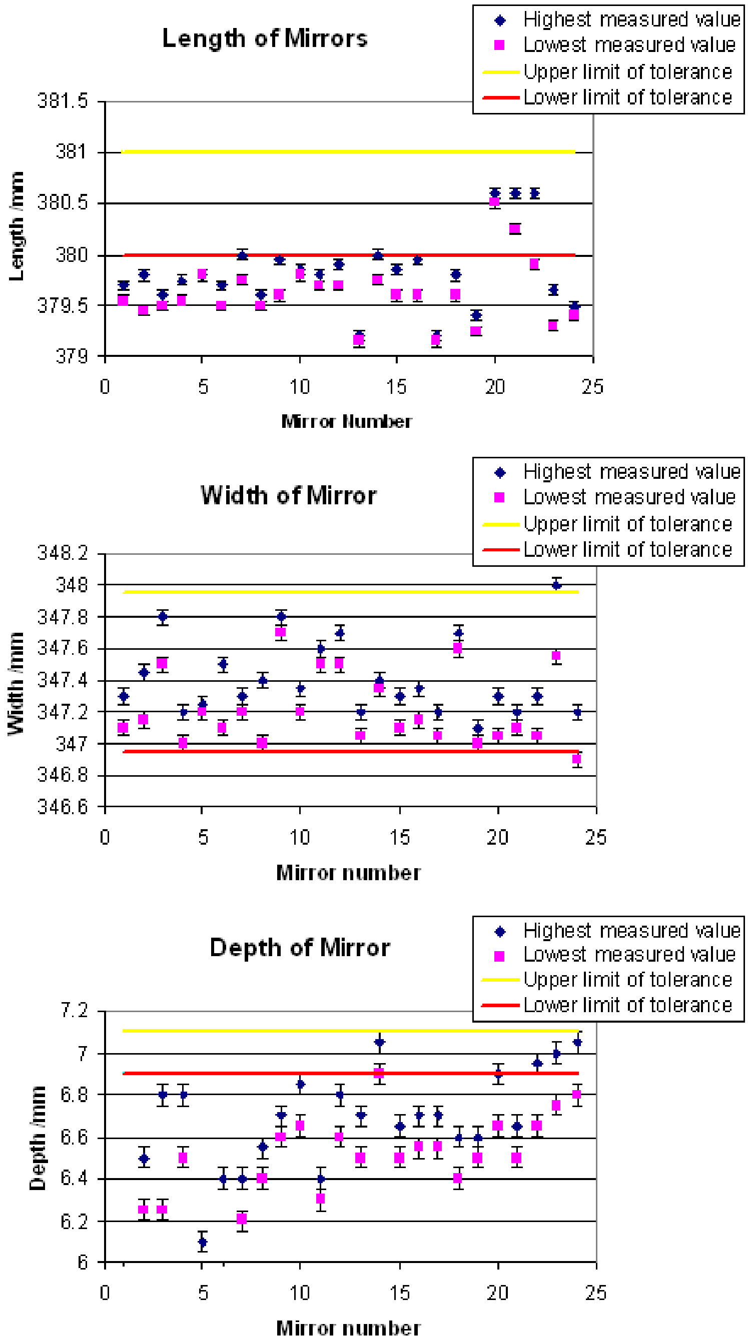

Figure 4.20: The dimensions of the flat mirrors. There are two measured values per mirror per dimension. This is because the measurement was made at different positions on the mirror to determine the regularity of the mirror. The error on each measurement represents the precision of the equipment used.

Chapter 5

The Tuning of Pythia for the LHCb, Using Gauss

5.1 Introduction

B-mesons will be abundantly produced at the LHC, and it is expected that a large fraction of these will be in excited states [45, 46, 47, 48]. It is important that any Monte Carlo simulation used for LHCb should accurately account for the production of excited B-mesons especially given their importance to same-side tagging. Same side tagging allows the initial flavour of b quark to be determined using correlations with particles produced, along side the B-meson, from the decay of the excited B-meson. These states were introduced into the LHCb Monte Carlo for the 2004 data production. The inclusion of these states increased the charged multiplicity of the simulated collisions. As a result, retuning was needed in order to reproduce the multiplicities measured at CDF and UA5. The details of this tuning process are presented in [49]. Specifically, this tuning focused on Pythia's simulation of parton-parton interactions. As a result, the multiplicity of hadron-hadron collisions was lowered to the observed level for collisions with a centre of mass energy in the range 53 GeV to 1800 GeV. However, the tuning process presented in [49] was only concerned with the overall charged multiplicity of events. No examination of the flavours of the particles was made. As a result, the simulated production rates of certain species of particles did not match the those measured at LEP.

The production of the following particles was studied in Gauss and compared to data from LEP, which is presented in reference [50]: $\rho(770)^0$, $\omega(782)$, $\phi(1020)$, $K^*(892)^\pm$ and $D^*(2010)^\pm$. Of these, only the production of the $\rho(770)^0$ was accurately reproduced by the LHCb tune, with the others all being produced in too great an abundance, see figures 5.3 to 5.5. The overall charged multiplicity was also studied. The multiplicity was within the errors of the LEP value, see figure 5.6.

Because of the failure to produce the $\omega(782)$, $\phi(1020)$, $K^*(892)^\pm$ and $D(2010)^\pm$ in the correct quantities, a new retuning process was undertaken in order to correctly model the charged multiplicity of both hadron-hadron and lepton-lepton events and correctly reproduce the production of the various mesons under study, whilst maintaining the desired production rates for excited B-mesons. This retuning was done in two stages: a tuning to fit data from the LEP experiments and then a further retuning to fit data from CDF and UA5. The first process was done by tuning various Pythia [28] parameters: PARJ(11), PARJ(12),..., PARJ(17) that control the probability of mesons being produced in various spin states. The second process was done by tuning the $p_{\perp min}$ parameter that controls the average multiplicity of parton-parton interactions in Pythia. The details of these processes are described below. In the case of the first stage of the tuning, that of fitting to the LEP data, two different tuning processes were undertaken.

Before the retuning processes are described, a brief description of the relevant Pythia functions is given.

5.2 Event Generation with Pythia

Pythia is a high energy physics Monte Carlo event generator. It forms the basis of most Monte Carlo data generated by LHCb. Pythia's event generation is governed by a number of parameters. Two sets of parameters are relevant to the work described in this chapter: those which determine the spin of mesons when formed in fragmentation or decays, and those which control the multiplicity of parton-parton interactions. Something is said of each, below.

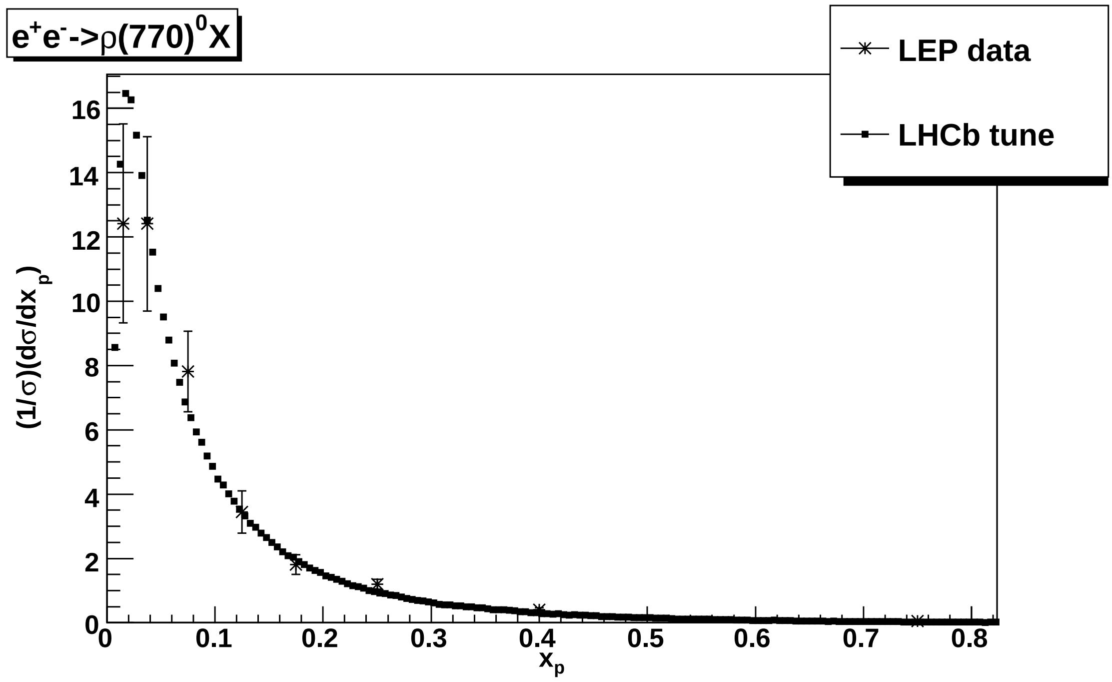

Figure 5.1: The production rate for $\rho(770)^0$in e^+e^- collisions at 91.2 GeV. The variables x_p is defined by x_P = particle's momentum/beam momentum.

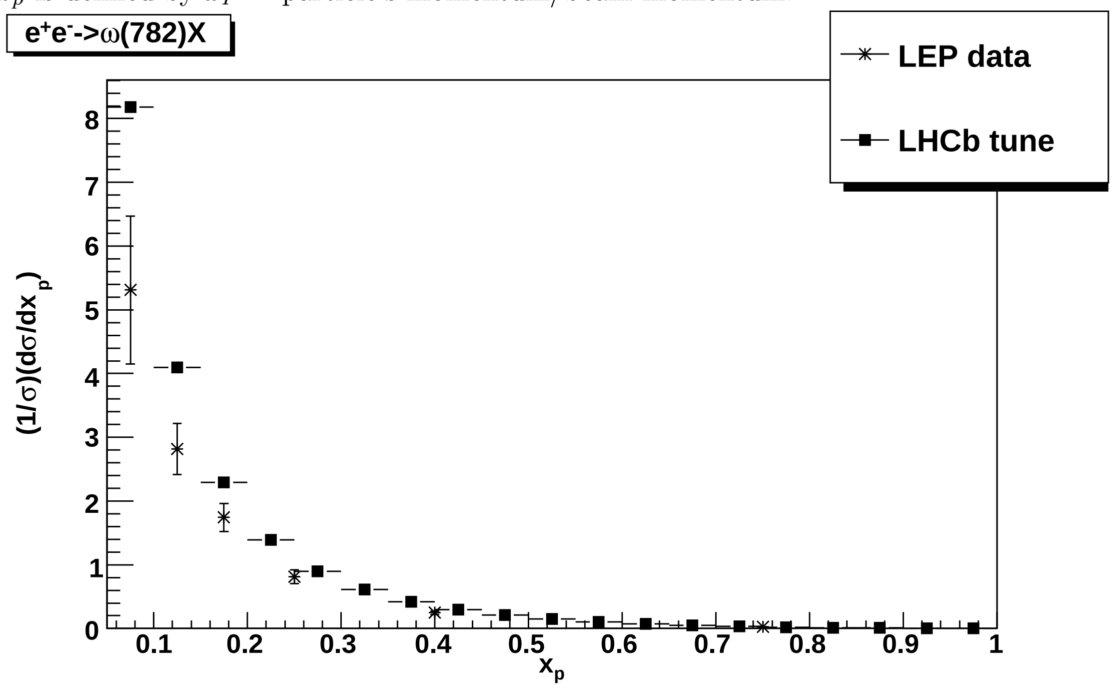

Figure 5.2: The production rate for $\omega(782)$ in e^+e^- collisions at 91.2 GeV. A discrepancy between experimental and Monte Carlo data can be seen. The variables x_p is defined by x_P = particle's momentum/beam momentum.

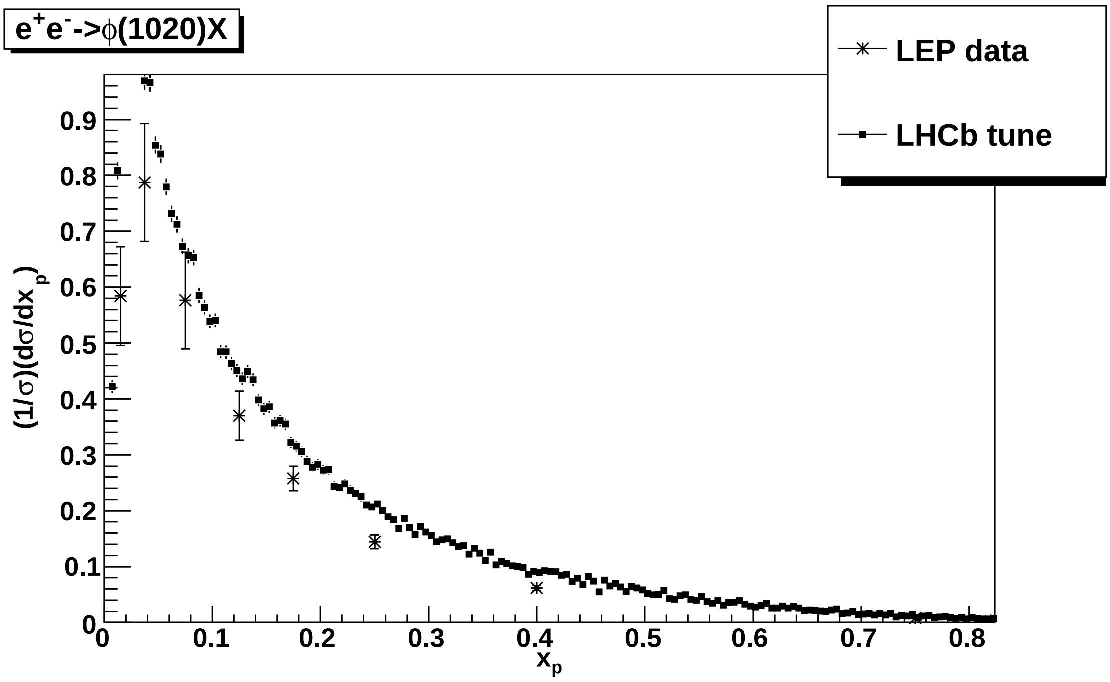

Figure 5.3: The production rate for $\phi(1020)$ in e^+e^- collisions at 91.2 GeV. A discrepancy between experimental and Monte Carlo data can be seen. The variables x_p is defined by x_P = particle's momentum/beam momentum.

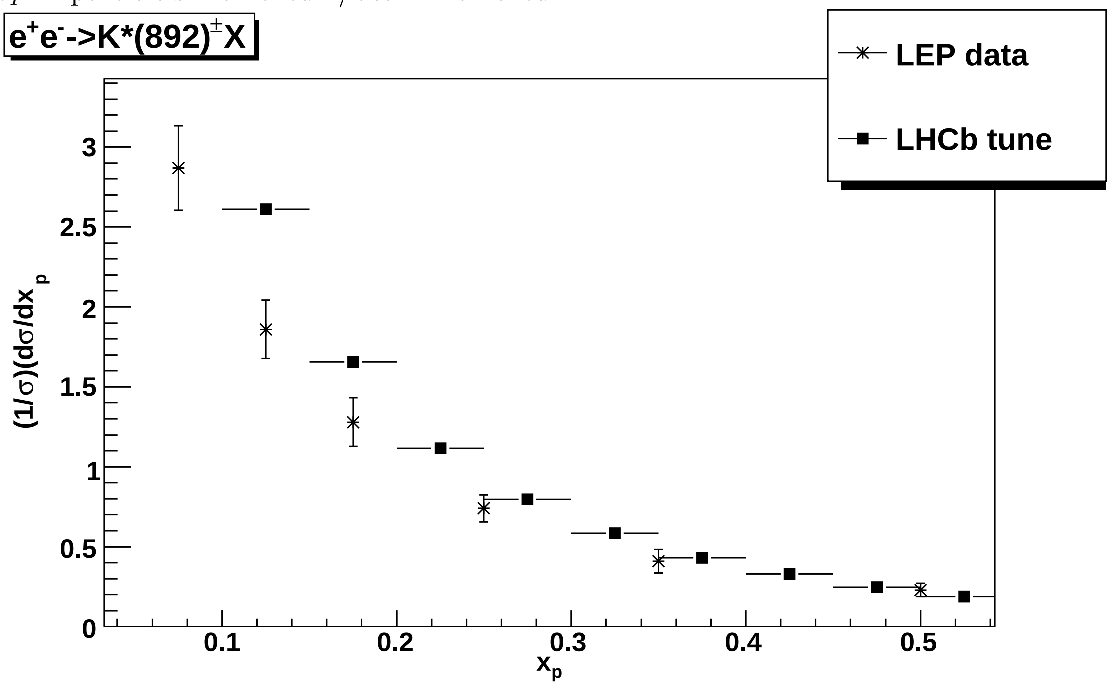

Figure 5.4: The production rate for $K^*(892)^\pm$ in e^+e^- collisions at 91.2 GeV. A discrepancy between experimental and Monte Carlo data can be seen. The variables x_p is defined by x_P = particle's momentum/beam momentum.

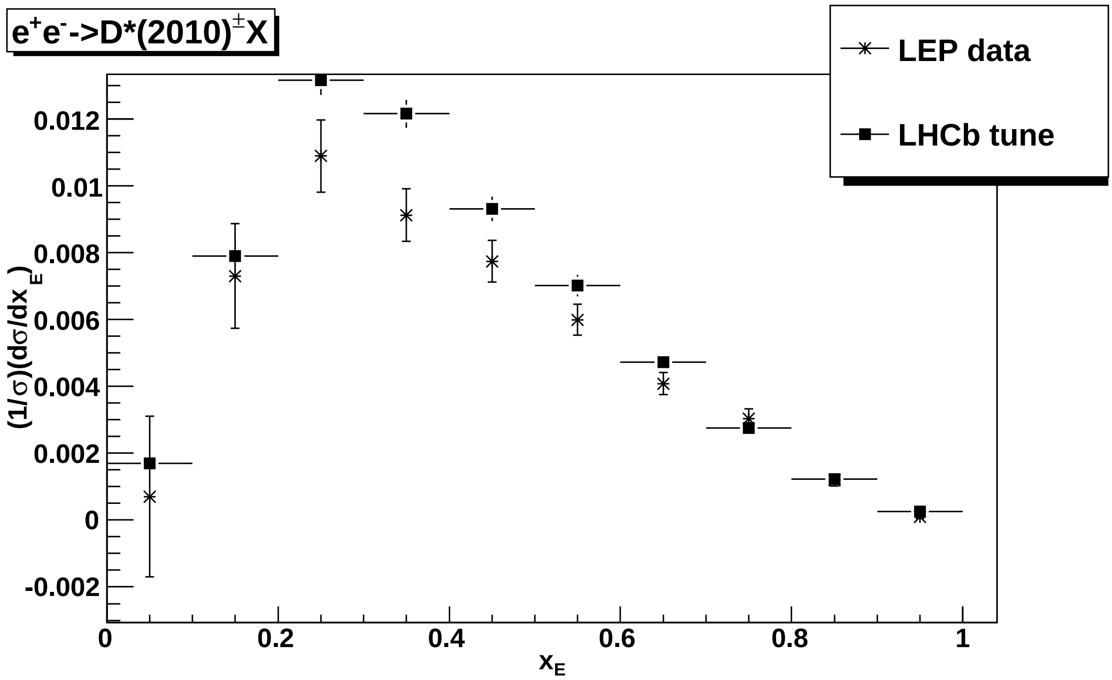

Figure 5.5: The production rate for $D^*(2010)^{\pm}$ in e^+e^- collisions at 91.2 GeV. A discrepancy between experimental and Monte Carlo data can be seen. The variables x_E is defined by x_E = particle's energy/beam energy.

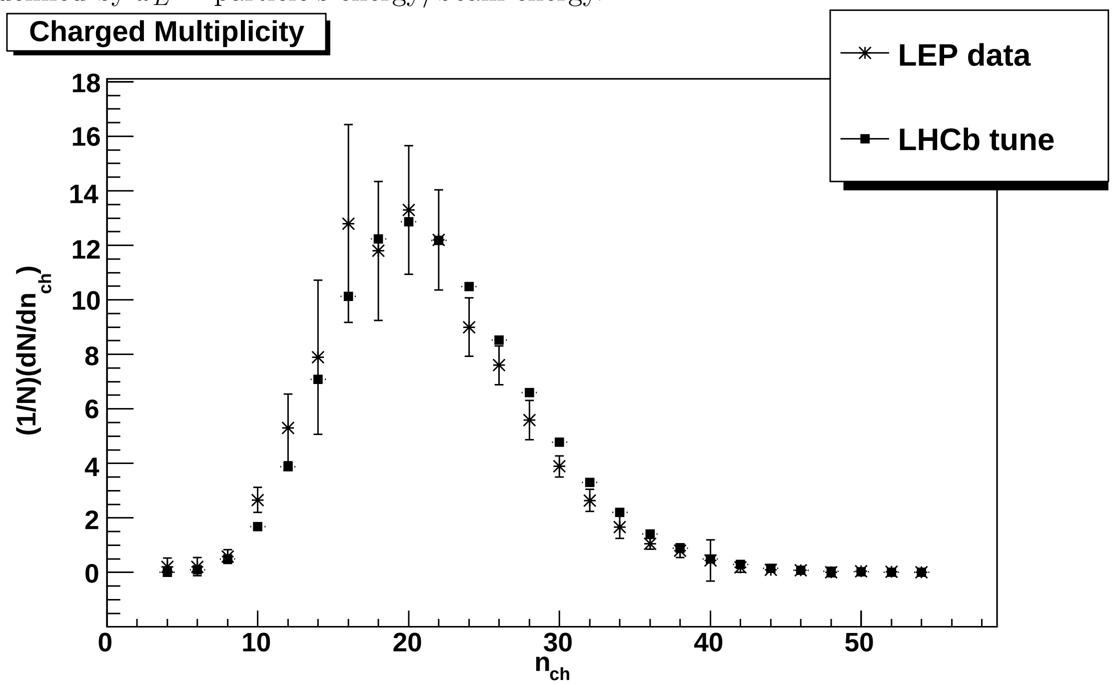

Figure 5.6: The charged multiplicity in e^+e^- collisions at 91.2 GeV. A discrepancy between experimental and Monte Carlo data can be seen.

5.2.1 Fragmentation and Decays

Perturbation theory for QCD is valid only at short distances. At long distances perturbation theory breaks down. In this regime, the coloured partons are transformed into colourless hadrons. This process is variously called hadronisation or fragmentation. Within Pythia it is called fragmentation, with hadronisation referring to a combination of fragmentation and the subsequent decay of the unstable hadrons resulting from fragmentation [51].

Fragmentation is a process not well understood [51]. The default model in Pythia is the Lund Model, which uses string fragmentation. In this model, the energy stored in the colour dipole field between charge and anti charge is modeled by a stretchable string, or colour flux tube. This string may snap, with the creation of a new quark anti-quark pair, leading to the quark anti-quark pairs connected by strings.. If the mass in either of these systems is large enough the process will continue [51]. It will continue until only on-mass-shell hadrons remain. As mentioned earlier, the parameters PARJ(11), PARJ(12),. . . , PARJ(17) control the probability of that the various different mesons are produced in various spin states, and these probabilistic rules are applied at each stage that a meson is produced. The precise meaning of each parameter is given in section 5.3. These same parameters also play a part in the production of mesons from the decay of other hadrons.

5.2.2 Multiple Interactions Model

From Pythia version 6.3 onwards there have been two multiple interaction models in Pythia. The tuning described in this chapter used the older model, and some detail of that model is given in this section. A fuller account can be found in the Pythia manual. A tuning of the newer multiple interactions model can be found in [39].

The multiple interactions model deals with scenarios in which more than one parton pair undergoes hard interactions in a hadron-hadron collision. The model assumes that the total rate of interactions, as a function of the transverse momentum scale, $p_\perp$, is given by perturbative QCD. This framework is then extended into the low $p_\perp$ region.

The cross section for hard scattering diverges as $p_\perp \to 0$. A cut-off is therefore imposed. The hard scattering cross section is given by

$$\sigma_{\text{hard}}(p_\perp) = \int_{p^2_{\perp min}}^{s/4} \frac{\mathrm{d}\sigma}{\mathrm{d}p^2_\perp} \mathrm{d}p^2_\perp \tag{5.1}$$

where $p_{\perp min}$ is the transverse momentum cut off. The cut-off may be motivated by noting that when the $p_\perp$ of an exchanged gluon is small, it has a large wavelength, and cannot resolve individual colour charges within the colourless hadron. For this reason, the effective coupling will decrease.

The value of $p_{\perp min}$ needed to describe experimental data changes with the energy of the collision. In Pythia, its energy dependance is assumed to be the same as that of the total cross section, namely increasing with some power $\epsilon \approx 0.08$:

$$p_{\perp min}(s) = X s^{\epsilon} \tag{5.2}$$

In terms of Pythia parameters, this relationship is

$$p_{\perp min}(s) = PARP(82) \left(\frac{\sqrt{s}}{PARP(89)} \right)^{PARP(90)} \tag{5.3}$$

The cut-off in the transverse momentum transferred controls the number of parton-parton interactions that can take place, and hence the multiplicity of the event. These parameters were tuned using pseudorapidity data, in a process described in section 5.4

5.3 Tuning of the PARJ Variables

5.3.1 First Tuning Method

The retuning was undertaken by adjusting the value of the variables that control the probability of a meson being produced with spin 1. These variables are:

- PARJ(11): The probability that a light meson is produced with spin 1.
- PARJ(12): The probability that a strange meson is produced with spin 1.

- PARJ(13): The probability that a charm or heavier meson is produced with spin 1.

PARJ(11) and PARJ(12) can be varied freely from 0 to 1, with the caveat that their chosen final values must allow the experimental data to be reproduced, but a more stringent condition must be placed on the varying of PARJ(13) as it affects the production fractions of the B, B^* and B^{**} mesons. Throughout the retuning process these fractions were fixed at the values used in the 2006 Monte Carlo production: 21%, 63% and 16% respectively. It is possible to maintain these ratios, and alter PARJ(13) if some of the following parameters are also retuned:

- PARJ(14): Probability that a spin = 0 meson is produced with orbital angular momentum 1,total spin = 1.

- PARJ(15) : Probability that a spin = 1 meson is produced with orbital angular momentum 1, total spin = 0.

- PARJ(16) : Probability that a spin = 1 meson is produced with orbital angular momentum 1, total spin = 1.

- PARJ(17) : Probability that a spin = 1 meson is produced with orbital angular momentum 1, total spin = 2.

Henceforth the variables PARJ(11), PARJ(12),. . . , PARJ(17) will be referred to, not by their names in Pythia, but by their physical meaning. PARJ(11), PARJ(12) and PARJ(13), the probabilities of producing various mesons in spin 1 states will be denoted in the following way:

- PARJ(11) as $P_{S=1}^{light}$

- PARJ(12) as $P_{S=1}^{strange}$

- PARJ(13) as $P_{S=1}^{heavy}$

Parameter	LHCb tune value	Value(s) in the retuning process
$P_{S=1}^{light}$	0.5	0 to 1
$P_{S=1}^{strange}$	0.6	0 to 1
$P_{S=1}^{heavy}$	0.75	0.68 to 0.79
$P_1^{0,1}$	0.162	$1-0.21/(1-P_{S=1}^{heavy})$
$P_0^{1,1}$	0.018	0.018
$P_1^{1,1}$	0.054	0.054
$P_2^{1,1}$	0.090	$0.928-0.63/(1-P_{S=1}^{heavy})$

Table 5.1: The values of the PARJ variables during the retuning. $P_1^{0,1}$ and $P_2^{1,1}$ take values dependent on $P_{S=1}^{heavy}$ to ensure the desired B fractions, see equations 5.4 to 5.6. The range over which $P_{S=1}^{heavy}$ may be varied is consequently reduced to ensure that $P_1^{0,1}$ and $P_2^{1,1}$ take values between 0 and 1.

The parameters PARJ(14),...,PARJ(17), which give the probabilities of different combinations of the spin quantum numbers S,L and J will be written in the form $P_J^{S,L}$, thus:

- PARJ(14) as $P_1^{0,1}$
- PARJ(15) as $P_0^{1,1}$
- PARJ(16) as $P_1^{1,1}$
- PARJ(17) as $P_2^{1,1}$

The required B meson fractions are produced if the following conditions are met:

$$P(B) = (1 - P_{S=1}^{heavy})(1 - P_1^{0,1}) = 0.21 \tag{5.4}$$

$$P(B^*) = P_{S=1}^{heavy}(1 - P_0^{1,1} - P_1^{1,1} - P_2^{1,1}) = 0.63 \tag{5.5}$$

$$P(B^{**}) = (1 - P_{S=1}^{heavy})P_1^{0,1} + P_{S=1}^{heavy}(P_0^{1,1} + P_1^{1,1} + P_2^{1,1}) = 0.16 \tag{5.6}$$

There are an infinite number of ways in which equalities 5.4 to 5.6 can be maintained whilst varying $P_{S=1}^{heavy}$. Initially $P_1^{0,1}$ and $P_2^{1,1}$ were chosen to be varied along with $P_{S=1}^{heavy}$, with $P_0^{1,1}$ and $P_1^{1,1}$ kept at their previous LHCb tune values. This places certain restrictions on how the different PARJ variables may be altered, see table 5.1. The

Data Set	χ^2 values for LHCb tune	χ^2 values for New tune
$K^*(892)^\pm$	67.95	4.233
$\omega(782)$	106.2	15.19
$\phi(1020)$	39.15	9.461
$\rho(770)^0$	15.12	16.96
$D(2010)^\pm$	30.21	23.65
$\langle n_{ch} \rangle$	27.92	3.809
All	286.6	73.31

Table 5.2: A comparison of the χ^2 between experiment and Monte Carlo for the different data sets, with data produced using the two different Monte Carlo tunings. In each case there is substantial improvement in the reproduction of the data, with the exception of the production of the ρ mesons. In this case there is very little change.

Parameter	Value in LHCb tune	Value after retune
$P_{S=1}^{light}$	0.5	0.5
$P_{S=1}^{strange}$	0.6	0.4
$P_{S=1}^{heavy}$	0.75	0.79
$P_1^{0,1}$	0.162	0.0
$P_2^{1,1}$	0.09	0.131

Table 5.3: The values of the PARJ parameters before and after retuning.

retuning was done in the following way: $P_{S=1}^{light}$ and $P_{S=1}^{strange}$ were varied from 0 to 1 in steps of 0.1, whilst $P_{S=1}^{heavy}$ was varied in steps of 0.01. For each of the different combinations of these values, Monte Carlo data was produced and the χ^2 statistic was calculated to measure the goodness of fit between experimental and Monte Carlo data, in the case of each of the five particle types being examined and the overall charged multiplicity. The set of PARJ values was chosen so as to minimise the sum of these χ^2. This set of PARJ variables gave a substantially improved reproduction of the e^+e^- data. This improvement can be seen in figures 5.7 to 5.12, which shows a comparison of LEP data with that simulated using the LHCb tune and with that using the modified tune. Table 5.2 lists the χ^2 values for the fit to the different data sets with the two different tunings. Table 5.3 gives the values of the PARJ settings after tuning.

The tuning results in $P_1^{0,1} = 0$ which is perhaps undesirable, as this means no spin 0 mesons are produced with orbital angular momentum 1 in the simulation. Such mesons are axial vector mesons, with $J^{PC} = 1^{++}$, where J is the total spin, and P and C are

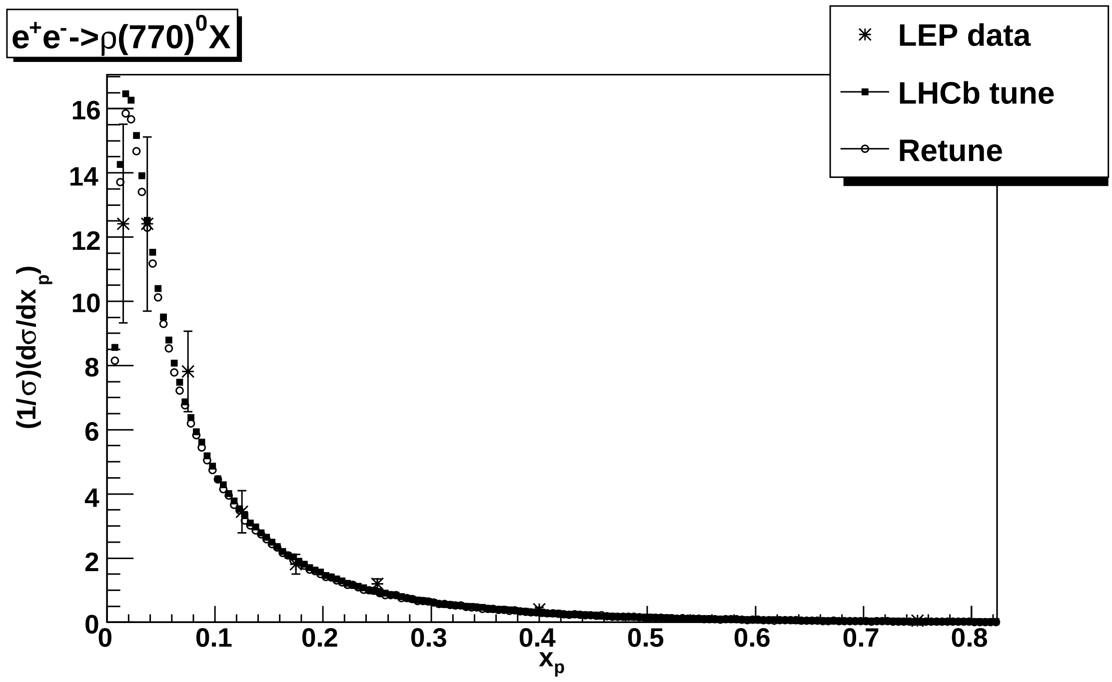

Figure 5.7: A comparison of LEP data and Monte Carlo data produced using the LHCb tune and the retune, for $\rho(770)^0$ production in e^+e^- collisions at 91.2 GeV.

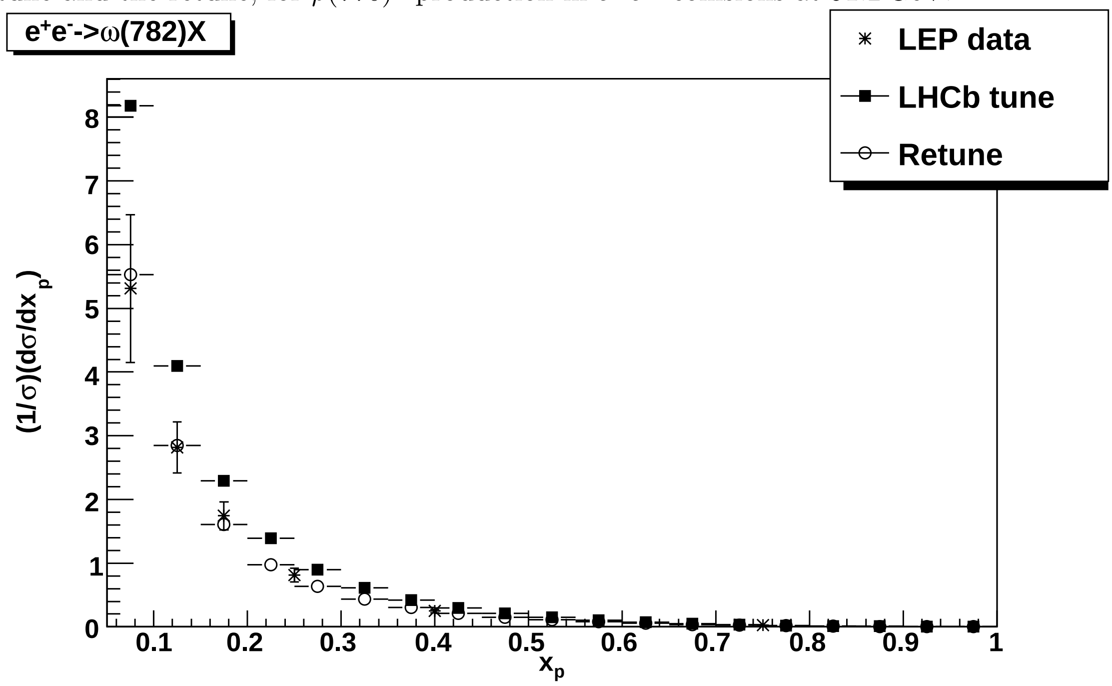

Figure 5.8: A comparison of LEP data and Monte Carlo data produced using the LHCb tune and the retune, for $\omega(782)$ production in e^+e^- collisions at 91.2 GeV.

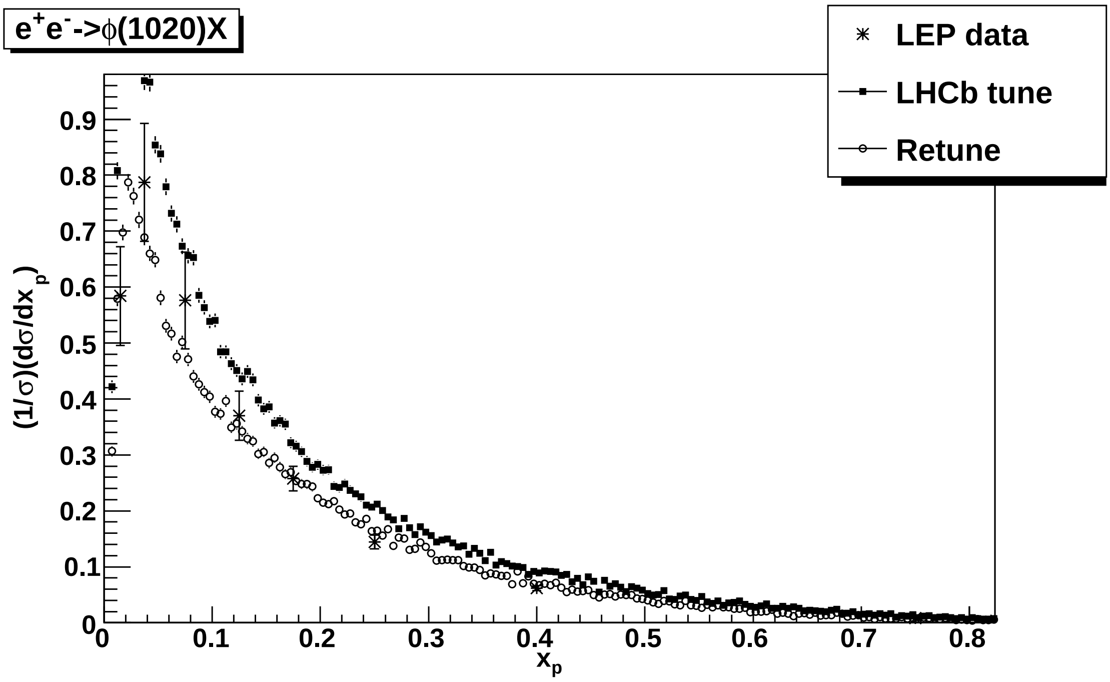

Figure 5.9: A comparison of LEP data and Monte Carlo data produced using the LHCb tune and the retune, for $\phi(1020)$ production in e^+e^- collisions at 91.2 GeV.

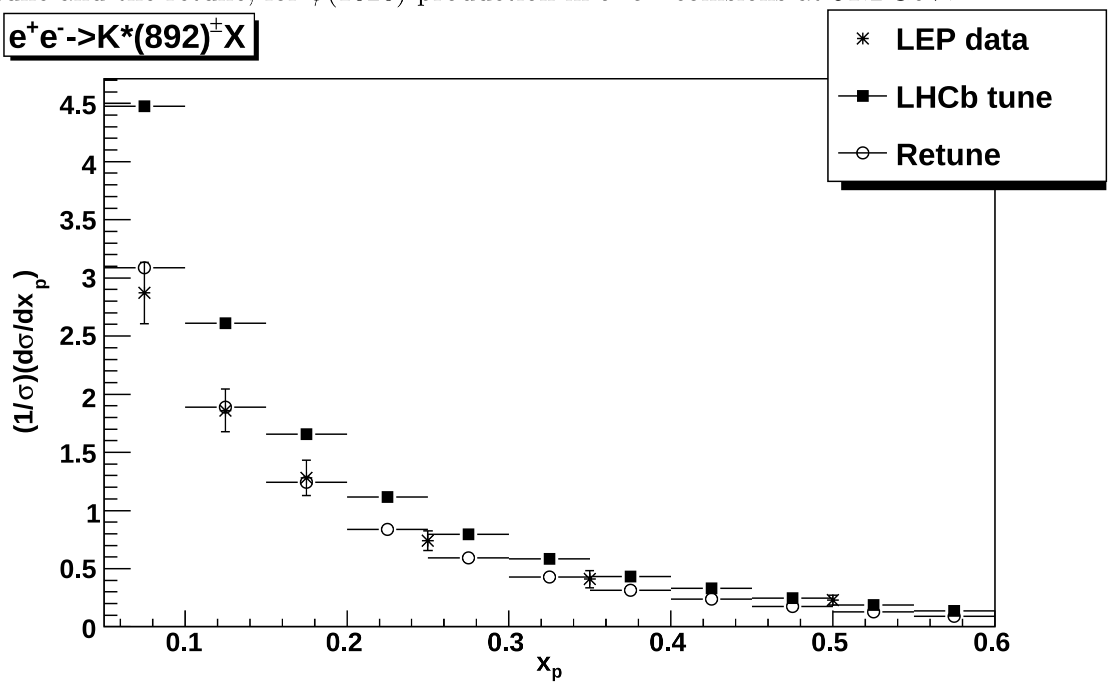

Figure 5.10: A comparison of LEP data and Monte Carlo data produced using the LHCb tune and the retune, for $K^*(892)^\pm$ production in e^+e^- collisions at 91.2 GeV.

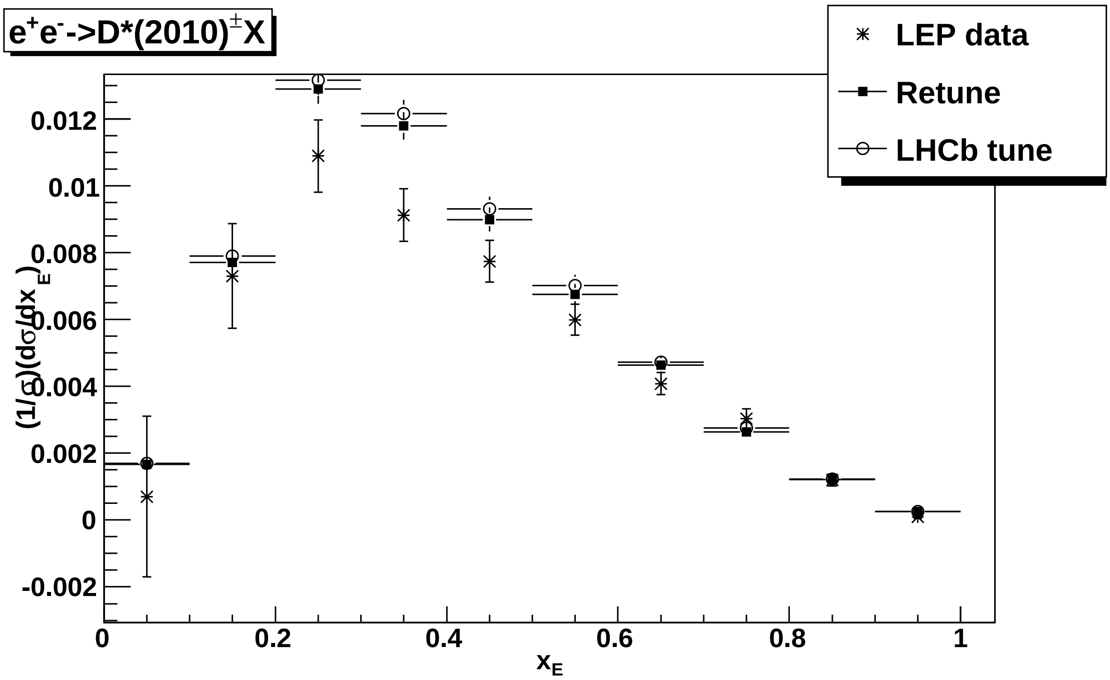

Figure 5.11: A comparison of LEP data and Monte Carlo data produced using the LHCb tune and the retune, for $D^*(2010)^{\pm}$ production in e^+e^- collisions at 91.2 GeV.

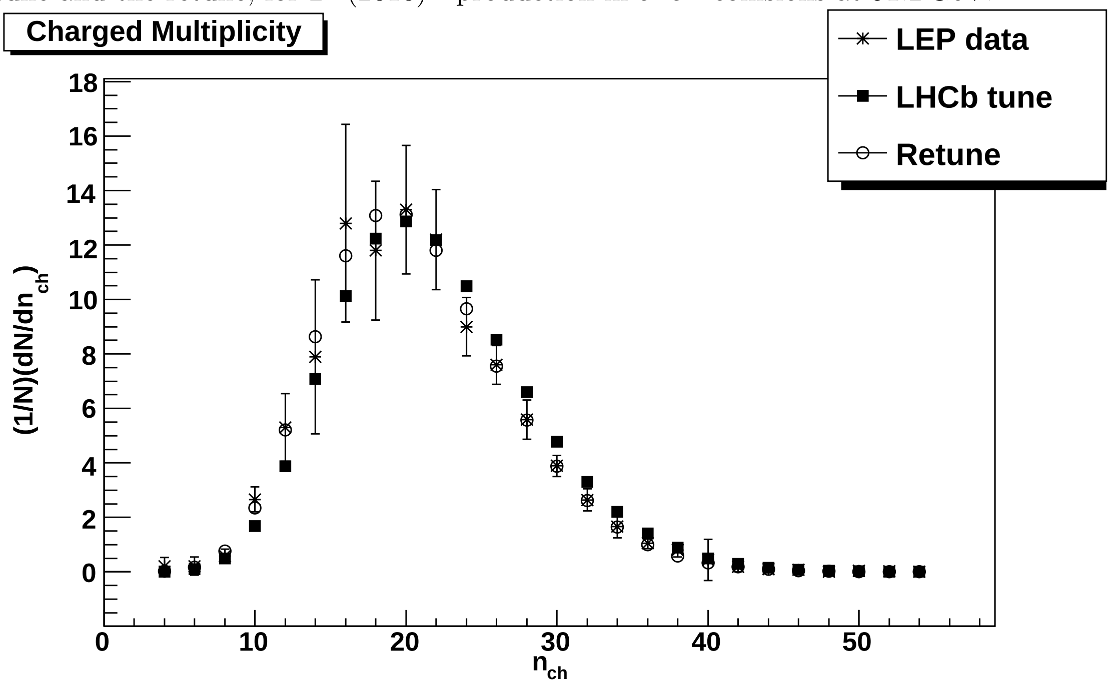

Figure 5.12: The charged multiplicity in e^+e^- collisions at 91.2 GeV. LEP data is compared with Monte Carlo data produced using the LHCb tune and the retune.

parity and C-parity respectively.

The problem arises because the χ^2 statistic that describes the goodness of fit between the experimental and Monte Carlo data, is minimised with $P_{S=1}^{heavy} = 0.79$. A solution to this problem was sought by modeling the χ^2 as a function of $P_{S=1}^{light}$, $P_{S=1}^{strange}$ and $P_{S=1}^{heavy}$, in the hope that this χ^2 function would have a minimum at $P_{S=1}^{heavy} \neq 0.79$. To fit a function to the χ^2 data points, errors on the χ^2 values were needed. These were estimated by generating five sets of Monte Carlo data with each of the PARJ setting combinations, and then taking the average χ^2 and its standard deviation. A fourth order polynomial equation was needed in order to give a good fit to the χ^2 data. However, this method also found the best value of $P_{S=1}^{heavy}$ to be 0.79 and so the problem of $P_1^{0,1}$=0 was not resolved. For this reason a second retuning was undertaken.

5.3.2 Second Tuning Method

For the second retuning process, $P_{S=1}^{light}$ and $P_{S=1}^{strange}$ were varied as before but $P_1^{0,1}$ was fixed to its DELPHI [54] tuning value of 0.09. To ensure the correct ratio of B, B^* and B^{**} states, this necessitated fixing $P_{S=1}^{heavy}$=0.769. The sum of $P_0^{1,1}$, $P_1^{1,1}$ and $P_2^{1,1}$ was then constrained. $P_0^{1,1}$ was kept at its LHCb tuning value of 0.018 which required $P_1^{1,1}$ + $P_2^{1,1}$ = 0.163. $P_1^{1,1}$ was varied from 0 to 0.163 in steps of 0.0163. As with the first retuning process an improvement is seen with respect to the LHCb tune, however it is not as pronounced in second retuning. Figures 5.13 to 5.18 show plots of the experimental and Monte Carlo data and table 5.4 lists the χ^2 values. This retuning method does not avoid the problems of the first method as the best fit to experimental data is produced with $P_1^{1,1} = 0$, see table 5.5. Such mesons are axial vector mesons, with $J^{PC} = 1^{+-}$.

The dependence of the overall χ^2 on $P_1^{1,1}$ is not strong in the region of the minimum. This can be seen in figure 5.19 and table 5.6. This weak dependence offers a solution, albeit of a somewhat arbitrary nature, to the problem of $P_1^{1,1} = 0$, as its value can be changed significantly without any substantial increase in the χ^2.

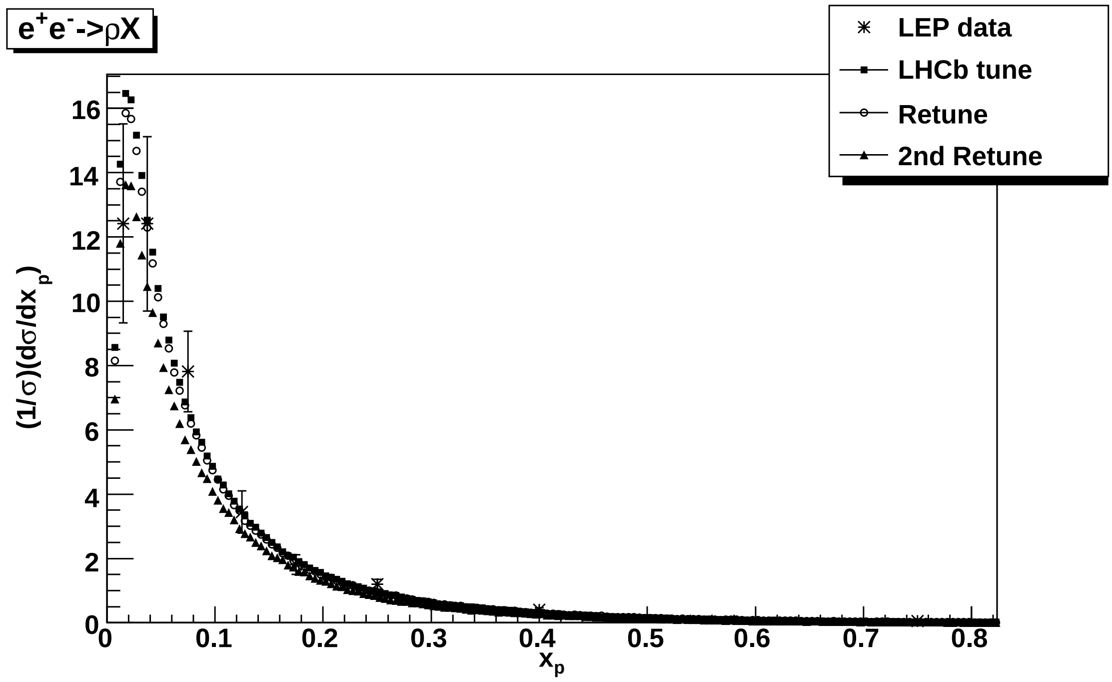

Figure 5.13: A comparison of LEP data and Monte Carlo data produced using the LHCb tune and the two retunings, for $\rho(770)^0$ production in e^+e^- collisions at 91.2 GeV.

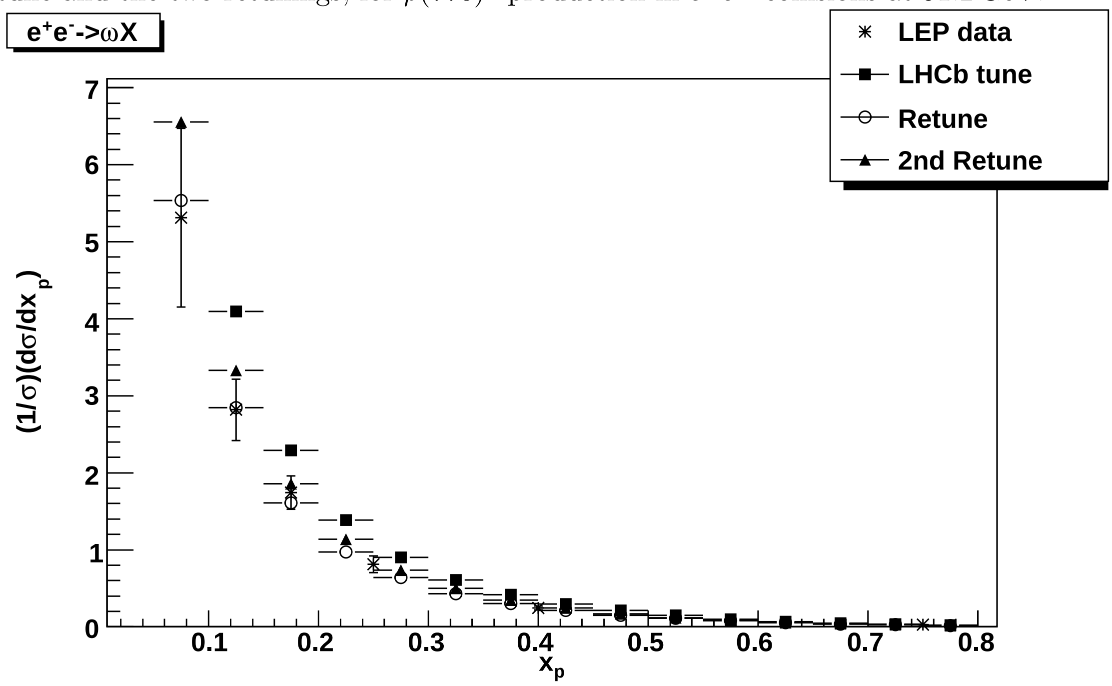

Figure 5.14: A comparison of LEP data and Monte Carlo data produced using the LHCb tune and the two retunings, for $\omega(782)$ production in e^+e^- collisions at 91.2 GeV.

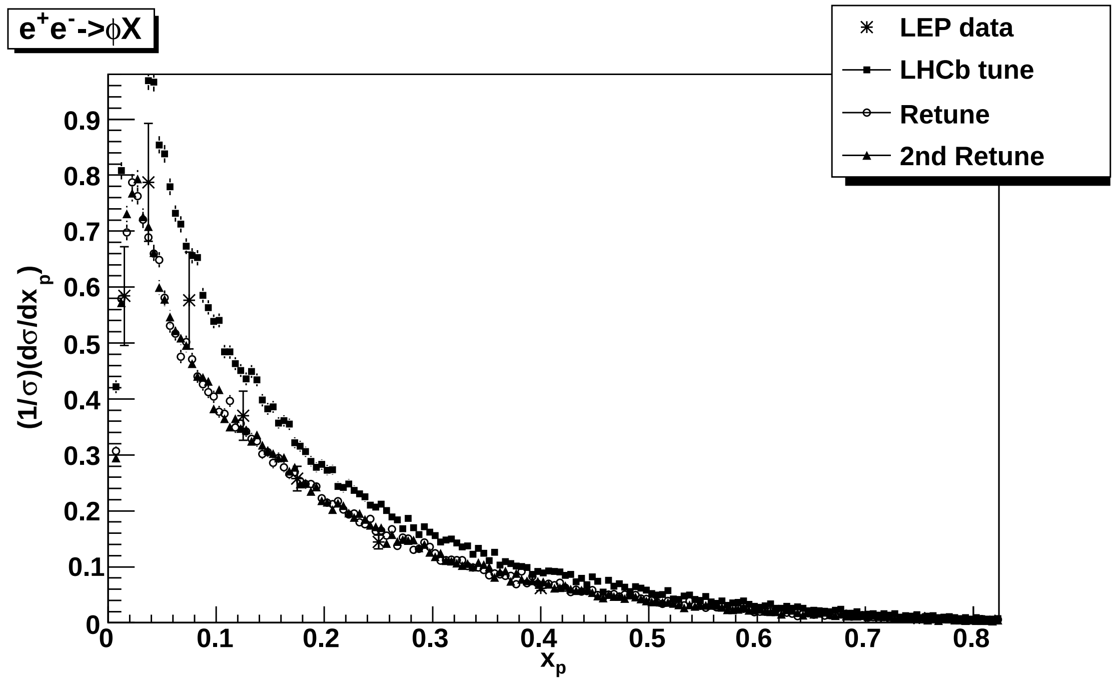

Figure 5.15: A comparison of LEP data and Monte Carlo data produced using the LHCb tune and the two retunings, for $\phi(1020)$ production in e^+e^- collisions at 91.2 GeV.

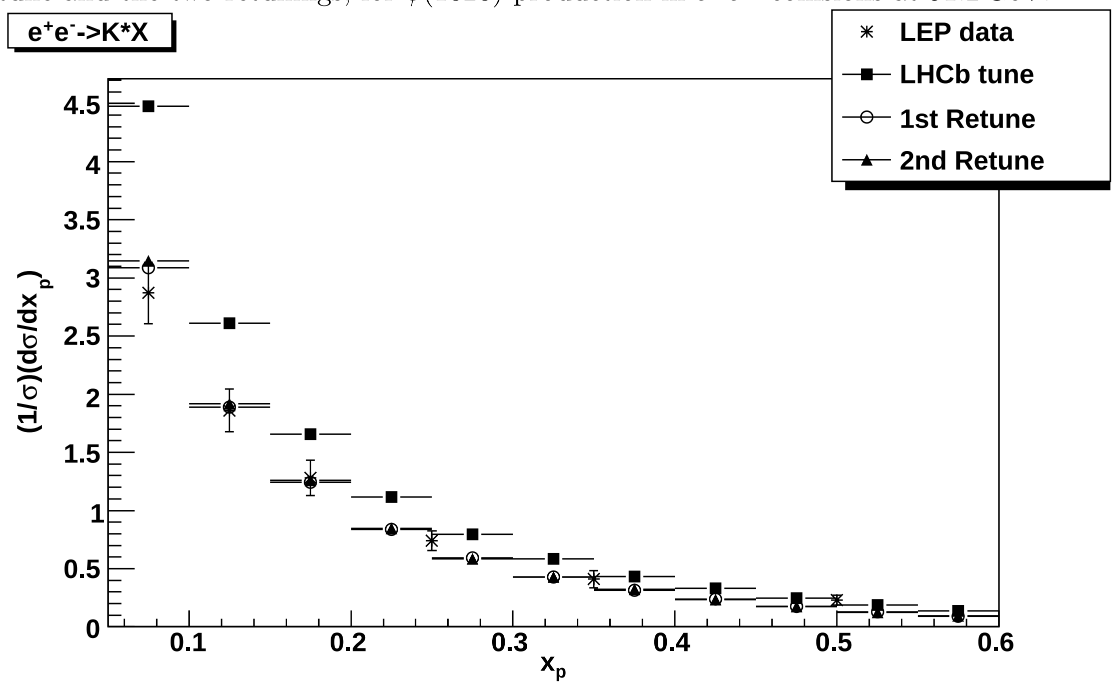

Figure 5.16: A comparison of LEP data and Monte Carlo data produced using the LHCb tune and the two retunings, for $K^*(892)^{\pm}$ production in e^+e^- collisions at 91.2 GeV.

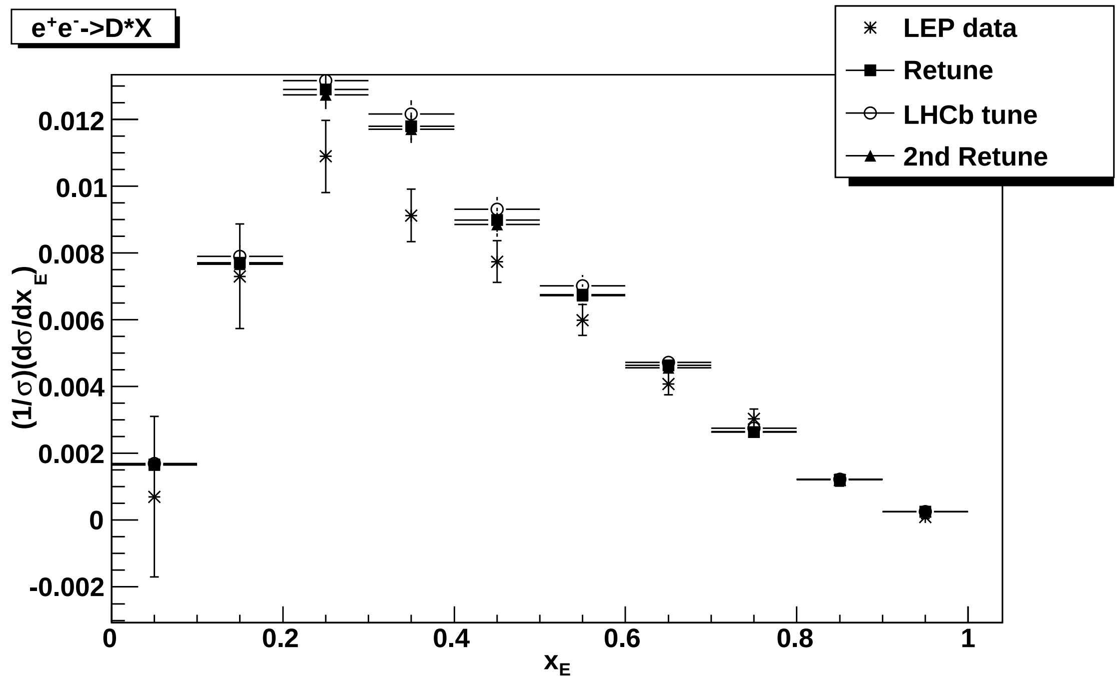

Figure 5.17: A comparison of LEP data and Monte Carlo data produced using the LHCb tune and the two retunings, for $D^*(2010)^{\pm}$ production in e^+e^- collisions at 91.2 GeV.

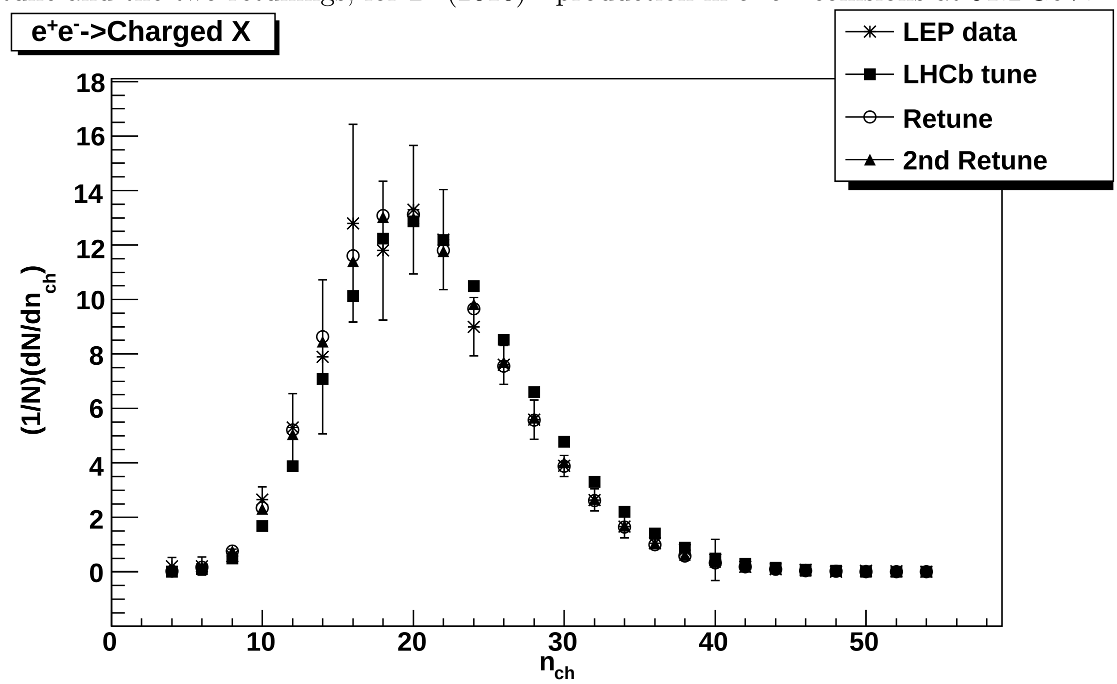

Figure 5.18: The charged multiplicity in e^+e^- collisions at 91.2 GeV. LEP data is compared with Monte Carlo data produced using the LHCb tune and the two retunings.

Data Set	χ^2 values for LHCb tune	χ^2 values for 2^{nd} retune
$K^*(892)^{\pm}$	67.95	4.72
$\omega(782)$	106.2	26.93
$\phi(1020)$	39.15	9.26
$\rho(770)^0$	15.12	33.69
$D(2010)^{\pm}$	30.21	21.89
$\langle n_{ch} \rangle$	27.92	3.86
All	286.6	100.35

Table 5.4: A comparison of the χ^2 between experiment and Monte Carlo for the different data sets. With the exception of the ρ meson data, the 2nd retune provides a closer fit to experiment than the LHCb tune. In the case of the ρ and ω mesons the 1st retune is significantly better.

Parameter	Value in LHCb tune	Value after 2^{nd} retune
$P_{S=1}^{light}$	0.5	0.4
$P_{S=1}^{strange}$	0.6	0.4
$P_{S=1}^{heavy}$	0.75	0.769
$P_1^{0,1}$	0.162	0.09
$P_0^{1,1}$	0.018	0.018
$P_1^{1,1}$	0.054	0.0
$P_2^{1,1}$	0.09	0.163

Table 5.5: Values of the PARJ variables after the second retuning, in comparison with their LHCb values.

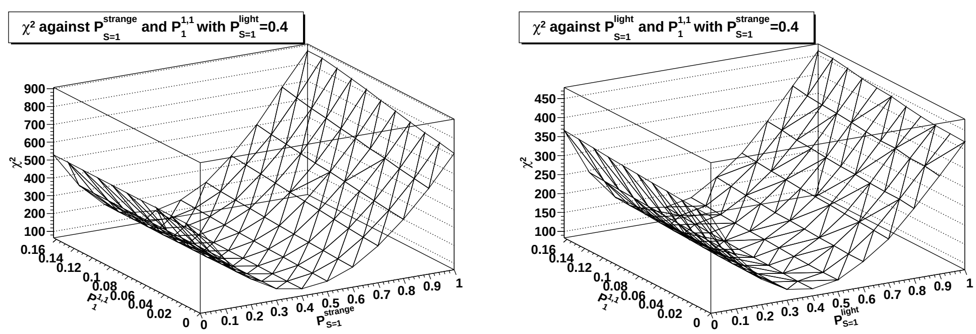

Figure 5.19: The dependence of χ^2 on $P_1^{1,1}$ in the second retuning.

$P_1^{1,1}$	χ^2	$P_{S=1}^{heavy}$	χ^2
0.0	100.35	0.68	550.09
0.0163	101.942	0.69	496.685
0.0326	102.9	0.70	442.549
0.0489	103.878	0.71	390.925
0.0652	105.075	0.72	338.716
0.0815	106.229	0.73	286.178
0.0978	108.791	0.74	236.889
0.1141	110.425	0.75	192.523
0.1304	112.987	0.76	152.861
0.1467	116.216	0.77	115.889
0.163	118.496	0.78	90.1016
		0.79	73.3051

Table 5.6: The dependence of χ_2 on $P_1^{1,1}$ in the 2nd retuning with $P_{S=1}^{light}$ and $P_{S=1}^{strange}$ fixed at their optimal values is compared to the dependence on $P_{S=1}^{heavy}$ in the 1st retuning. The dependence on $P_1^{1,1}$ is much weaker, allowing for an arbitrary change of $P_1^{1,1}$ away from zero without significant degradation of the data produced. Such a technique is not so applicable with the first tune.

5.3.3 Further Comparison of the Two Tuning Methods

Both of the tuning methods outlined above are beneficial in the sense that they both result in a more accurate reproduction of LEP data than the existing LHCb tune, the first method more so, especially in the case of the $\phi(770)^0$ and $\omega(782)$ mesons. Both methods result in one of the PARJ variables having a value of zero, which means mesons with certain combinations of the spin quantum numbers would not be produced. In the case of the second retuning this may be remedied without much affecting the overall quality of the data, but only in a somewhat arbitrary fashion. As a further comparison of these tunings, their reproduction of some other data was studied [59, 60]. These data were the mean production rates for various different particles at LEP, see tables 5.7 and 5.8. Data were also produced with a modified version of the 2nd set of retuned parameters in which $P_1^{1,1}$ was chosen to be 0.0815 rather than zero, and accordingly $P_2^{1,1}$ = 0.0815. This set of parameters is referred to as the 3rd retune.

The $f_0(980)$ is under-produced with all four tunings, but the other particles are produced in roughly the correct proportion. The three retunings each reproduce the

	LEP data	LHCb tune		^{1st} retune	
	$\langle N \rangle$	$\langle N \rangle$	χ^2	$\langle N \rangle$	χ^2
π^0	9.43 ± 0.37	10.165 ± 0.008	3.94	9.721 ± 0.08	0.619
$\pi^\pm$	17.06 ± 0.24	17.854 ± 0.014	10.9	16.75 ± 0.01	1.63
$K^\pm$	2.2 ± 0.056	2.248 ± 0.002	0.729	2.339 ± 0.002	6.19
K^0	2.067 ± 0.025	2.008 ± 0.002	5.55	2.142 ± 0.002	8.88
η	0.94 ± 0.08	0.985 ± 0.001	0.317	1.218 ± 0.001	12.0
η'	0.17 ± 0.05	0.2515 ± 0.0004	2.66	0.3142 ± 0.0004	8.32
$D^\pm$	0.2 ± 0.03	0.1791 ± 0.0003	0.485	0.1850 ± 0.0003	0.249
D^0	0.4 ± 0.06	0.4932 ± 0.0006	2.41	0.4923 ± 0.0006	2.37
$B^\pm$,B^0	0.34 ± 0.06	0.3893 ± 0.0006	0.677	0.3882 ± 0.0006	0.645
$f_0(980)$	0.147 ± 0.011	0.0206 ± 0.0001	132	0.0230 ± 0.0002	127
ρ^0	1.23 ± 0.1	1.405 ± 0.001	3.07	1.365 ± 0.001	1.81
$K^{*\pm}$	0.714 ± 0.043	0.974 ± 0.001	36.4	0.6857 ± 0.0007	0.432
K^{*0}	0.754 ± 0.034	0.988 ± 0.001	47.3	0.6924 ± 0.0007	3.28
ϕ	0.086 ± 0.018	0.1640 ± 0.003	18.8	0.1205 ±0.0003	3.67
$f_2(1270)$	0.169 ± 0.025	0.0961 ± 0.002	8.51	0.1472 ± 0.0003	0.762
$K^*(1430)$	0.084 ± 0.04	0.0173 ± 0.0001	2.78	0.0119 ± 0.0001	3.25
$D{*}^{*\pm}$	0.17 ± 0.02	0.2307 ± 0.0004	9.20	0.2288 ± 0.0004	8.64
			286		190

Table 5.7: A comparison of the LEP data with Monte Carlo data produced with the LHCb tune and the first set of retuned parameters. In most cases the retuned parameters give a better reproduction of the experimental data. The sum of the χ^2 statistics is also lower with the retuned parameters.

	LEP data	2^{nd} retune		3^{rd} retune	
	$\langle N\rangle$	$\langle N\rangle$	χ^2	$\langle N\rangle$	χ^2
π^0	9.43 ± 0.37	9.846 ± 0.008	1.26	9.912 ± 0.08	1.69
$\pi^\pm$	17.06 ± 0.24	16.89 ± 0.013	0.472	17.01 ± 0.031	0.0454
$K^\pm$	2.2 ± 0.056	2.314 ± 0.002	4.21	2.319 ± 0.002	4.53
K^0	2.067 ± 0.025	2.114 ± 0.002	3.52	2.114 ± 0.002	3.32
η	0.94 ± 0.08	1.257 ± 0.001	15.7	1.259 ± 0.001	15.9
η'	0.17 ± 0.05	0.3363 ± 0.0004	11.1	0.3387 ± 0.0005	11.4
$D^\pm$	0.2 ± 0.03	0.1882 ± 0.0003	0.155	0.1781 ± 0.0003	0.532
D^0	0.4 ± 0.06	0.4880 ± 0.0006	2.15	0.4968 ± 0.0006	2.60
$B^\pm$,B^0	0.34 ± 0.06	0.3882 ± 0.0006	0.646	0.3881 ± 0.0006	0.642
$f_0(980)$	0.147 ± 0.011	0.0187 ± 0.0001	136	0.0182 ± 0.0001	137
ρ^0	1.23 ± 0.1	1.184 ± 0.001	0.211	1.225 ± 0.001	0.00273
$K^{*\pm}$	0.714 ± 0.043	0.6910 ± 0.0008	0.286	0.7169 ± 0.0008	0.477
K^{*0}	0.754 ± 0.034	0.7041 ± 0.0008	2.16	0.7169 ± 0.0008	4.49
ϕ	0.086 ± 0.018	0.1239 ± 0.0003	4.43	0.1241 ±0.0003	4.49
$f_2(1270)$	0.169 ± 0.025	0.1470 ± 0.0003	0.775	0.2338 ± 0.0004	10.2
$K^*(1430)$	0.084 ± 0.04	0.0123 ± 0.0001	3.21	0.0717 ± 0.002	15.2
$D{*}^{*\pm}$	0.17 ± 0.02	0.2249 ± 0.0004	7.53	0.0127 ± 0.001	3.18
			194		211

Table 5.8: A comparison of the LEP data with Monte Carlo data produced with the second and third sets of retuned parameters. Both retunes show an improvement compared to the LHCb tune, although neither to the extent of the first set of retuned parameter values.

multiplicity of the majority of the particles more accurately than the LHCb tune.

It is possible that for a substantially better set of values for the PARJ variables to be found, a major change in the tuning process would be required: either using a greater number of data sets data when finding the optimal values of the PARJ variables and/or fixing fewer of the PARJ variables and so requiring substantially more Monte Carlo data to be produced. However, in spite of certain failings, many improvements with respect to the LHCb tune are achieved by the retuning processes outlined above. The first retuned set of parameters produces the lowest summed χ^2 value for the data shown in tables 5.7 and 5.8, as was the case with the distributions in x_P and x_E. On this basis it is preferred to the other retuned parameter sets and the LHCb tune and used in the following work on tuning the $p_{\perp min}$ parameter.

5.4 Tuning of $p_{\perp min}$

Retuning Pythia to improve the fit to the LEP data affected the simulation of hadron-hadron collisions, and so further retuning, which would not affect the lepton-lepton collisions, was needed.

In a hadronic collision it is possible for there to be several interactions in one event. Pythia's model of multiple interactions describes the situation where several partons from each beam take place in several $2 \rightarrow 2$ scatterings. Within Pythia 6.3's multiple interaction model there is a cut-off in the minimum transverse momentum which may be exchanged in a parton-parton interaction. It is this $p_{\perp min}$ parameter that was tuned, since varying this controls the number of parton-parton interactions which can take place, and so also the overall multiplicity. Pythia contains a number of models for the distribution of matter within the initial state hadrons. The distribution of matter affects the impact parameter in the collision, which affects the probability of multiple interactions taking place. In the tuning process described below, a single Gaussian distribution was used. This is the same as the existing LHCb tune [49]. The experimental data that was used for the tuning comprised stable charged particle pseudorapidity distributions from CDF and UA5 [55, 56, 57, 58] at a range of centre of mass energies from 200 GeV to 1800 GeV and $\langle dN_{ch}/d\eta\rangle_{|\eta|<0.25}$ at 53 GeV. In each case the data refer to non-single diffractive events.

The value of $p_{\perp min}$ which best describes the experimental data varies with the centre of mass energy of the collision. In Pythia it has a dependence of the form 5.3, and depends upon three parameters: PARP(82), PARP(89) and PARP(90). Determining the values of PARP(82), PARP(89) and PARP(90) that best describe the energy dependance of $p_{\perp min}$, is a two-part process. Firstly, the optimal value of $p_{\perp min}$ at a range of energies must be determined. This gives yields data points describing the energy dependence of $p_{\perp min}$. Secondly, a function of the form 5.3 is fitted to these data, and the optimal values of PARP(82), PARP(89) and PARP(90) found.

For convenience, during the first step PARP(90) was set to zero, meaning that $p_{\perp min}$ = PARP(82). At each energy between 53 GeV and1800 GeV, $p_{\perp min}$ was then varied incrementally, and a set of Monte Carlo data was produced for each value of $p_{\perp min}$. The goodness of fit between the Monte Carlo and experimental data was found by calculating the χ^2 statistic. A set of data points describing χ^2 as a function of $p_{\perp min}$ was thus produced for each energy. The χ^2 was minimised by fitting a quadratic function through the data points, and minimising this. To fit a function through the χ^2 data points it was necessary to estimate their errors. The errors were found by producing five different sets of Monte Carlo data for each of the values of $p_{\perp min}$, at each energy, and then taking the average χ^2 and its standard deviation. The errors on the value of $p_{\perp min}$ were taken to be the change from its optimum value required to produce an increase in the χ^2, as estimated by the quadratic function, of 1. The fitting of functions through data points was performed in ROOT [53], using its Minuit package. Plots of the variation of the χ^2 statistic with $p_{\perp min}$ are shown below in figure 5.20. Table 5.9 lists the optimum values of the $p_{\perp min}$ parameter.

To find the values of PARP(82) and PARP(90) that are appropriate for LHC collisions, PARP(89) was fixed at 14 TeV and the values of PARP(82) and PARP(90) were determined by fitting a function of the form of 5.3 through the values of $p_{\perp min}$ that were found at various the different energies from 53 GeV to 1800 GeV. ROOT was used to fit

Collision Energy/GeV	$p_{\perp min}$/GeV in LHCb tune	$p_{\perp min}$/GeV after retune
53	1.40±0.06	1.31±0.05
200	1.72±0.04	1.58±0.01
546	2.02±0.02	1.907±0.004
630	2.05±0.07	2.00±0.04
900	2.16±0.03	2.085±0.009
1800	2.49±0.08	2.39±0.04

Table 5.9: The values of the $p_{\perp min}$ parameter at different energies. As expected they are lower after the retuning, raising the multiplicity after its reduction due to the changes in the PARJ variables.

Parameter	Value in LHCb tune	Value after retuning
PARP(82)	3.41 GeV	3.45 GeV
PARP(89)	14 TeV	14 TeV
PARP(90)	0.162	0.183

Table 5.10: The differences in the multiple interaction model parameters after retuning.

a function of the form 5.3 through the data points listed in table 5.9. A plot is shown in figure 5.21 and the values obtained for the parameters PARP(82) and PARP(90) are listed in table 5.10.

The quality of fit to the CDF and UA5l data after the retuning is comparable to that of the previous LHCb tune. The tuning was done using the parton distribution function, pdf, CTEQ6ll, the same as is used by the LHCb tune. This is not, however, the pdf used when the original tuning process was done, namely CTEQ4l [49]. A comparison of pseudorapidity data produced using the LHCb tune with both of these pdfs and with the new tune is found in figures 5.22 to 5.26. Charged multiplicity distributions at 3 centre of mass energies are also compared with the new tune and the LHCb tune in figures 5.27 to 5.29. The χ^2 values describing the goodness of fit are shown in table 5.11. The new tune was not tuned using this data, but there is a small improvement in its reproduction. There is, however, still a noticeable discrepancy between experimental and Monte Carlo data.

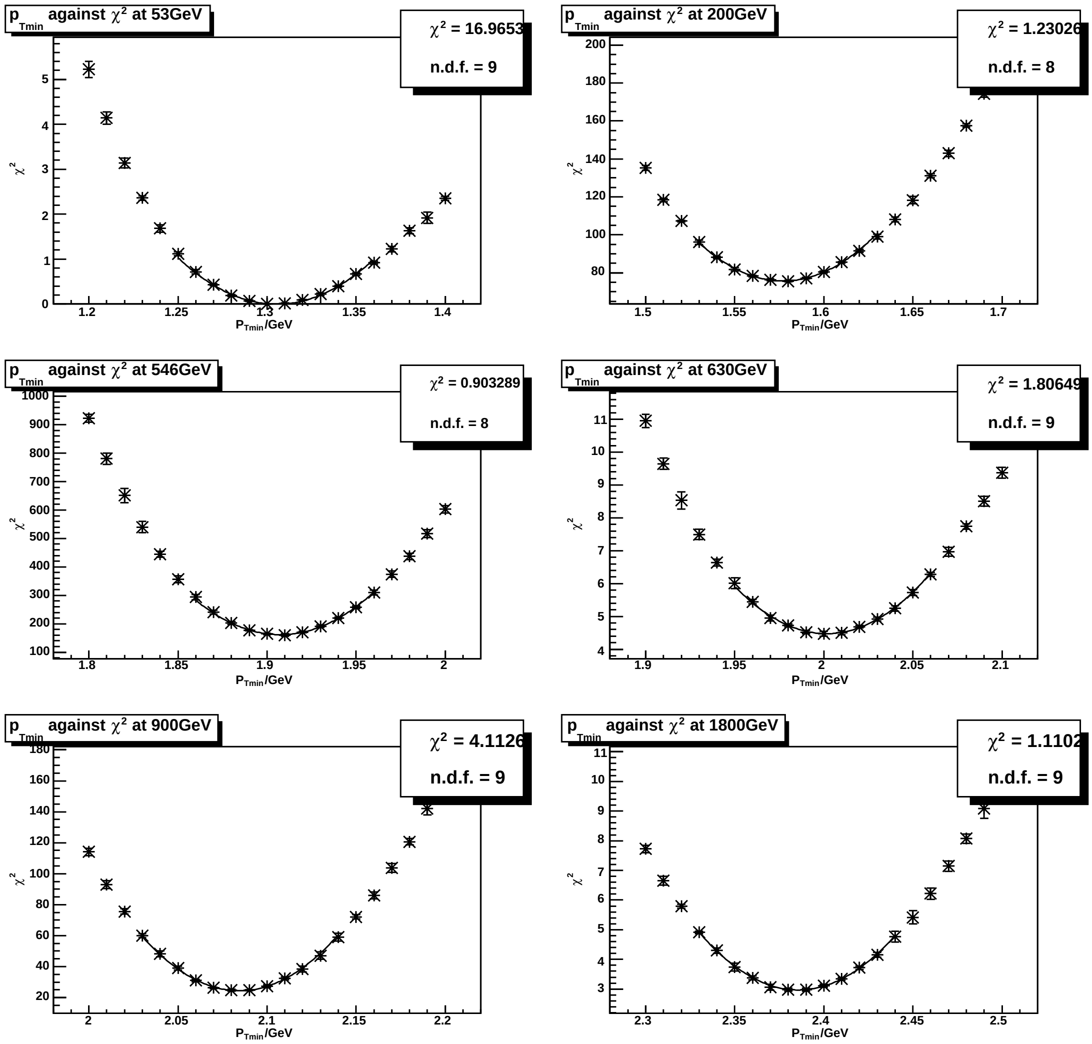

Figure 5.20: Plots of χ^2 against $p_{\perp min}$ obtained from a comparison of experimental and Monte Carlo data. A quadratic function is fitted through the data points in the region of the minimum. Its goodness of fit to the data points is indicated by the χ^2 and number of degrees of freedom listed in the legend.

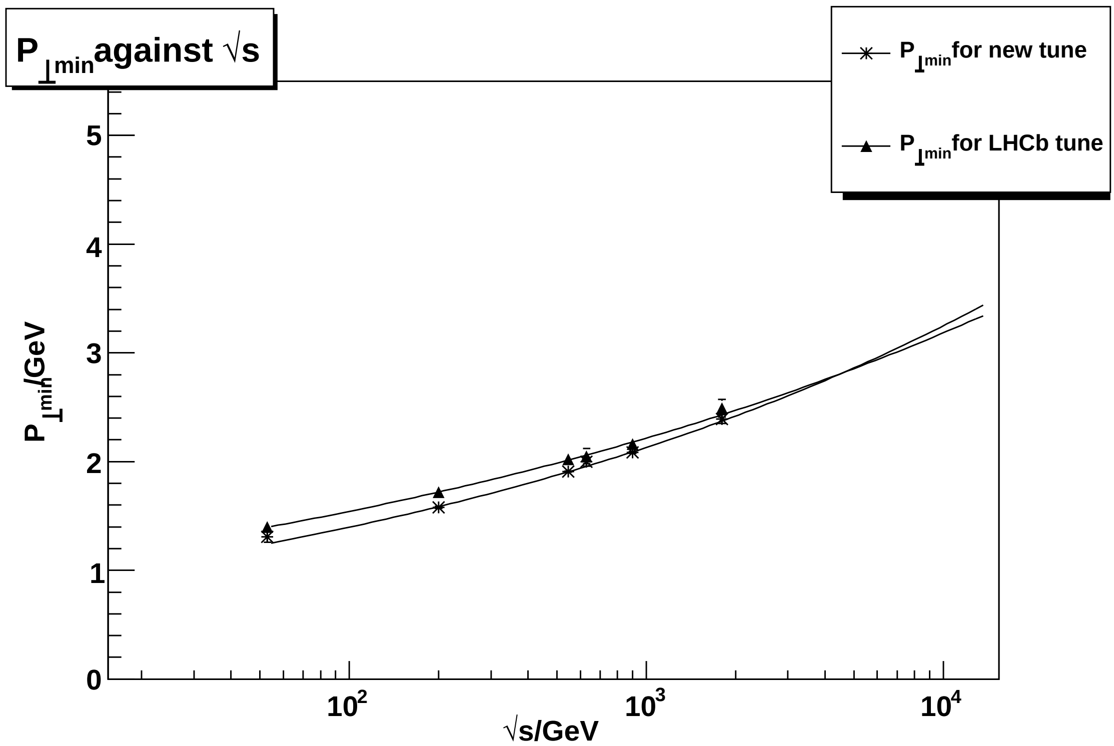

Figure 5.21: The variation of $p_{\perp min}$ with centre of mass energy for both the LHCb tune and the retune.

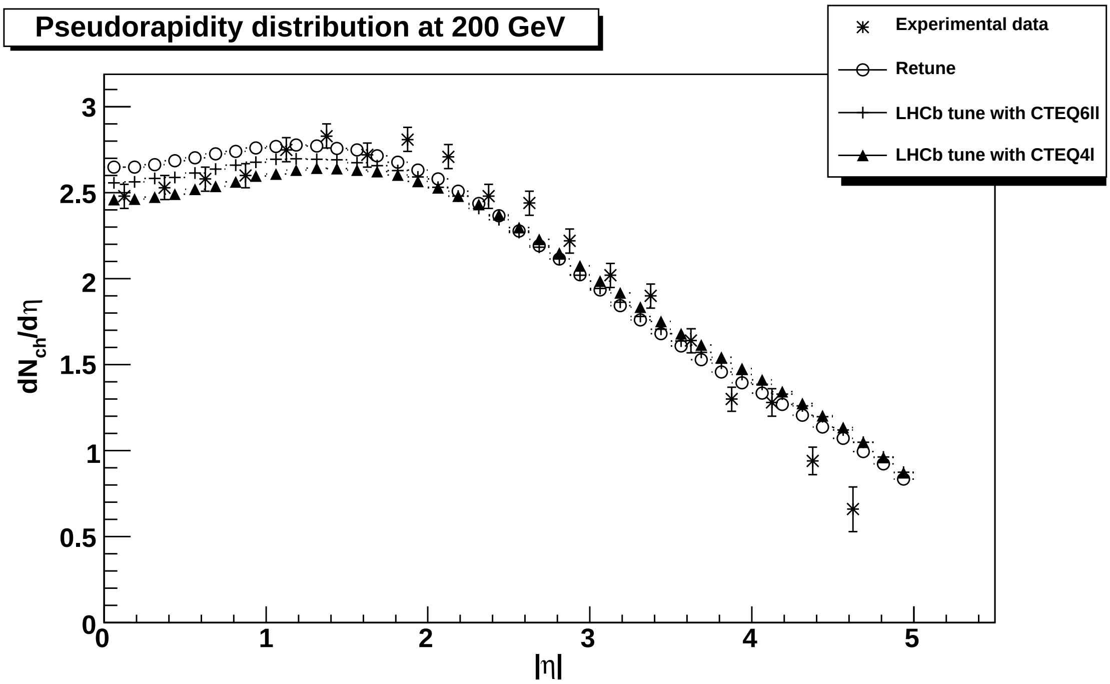

Figure 5.22: A comparison of pseudorapidity distribution produced with three different Monte Carlo settings, at 200 GeV.

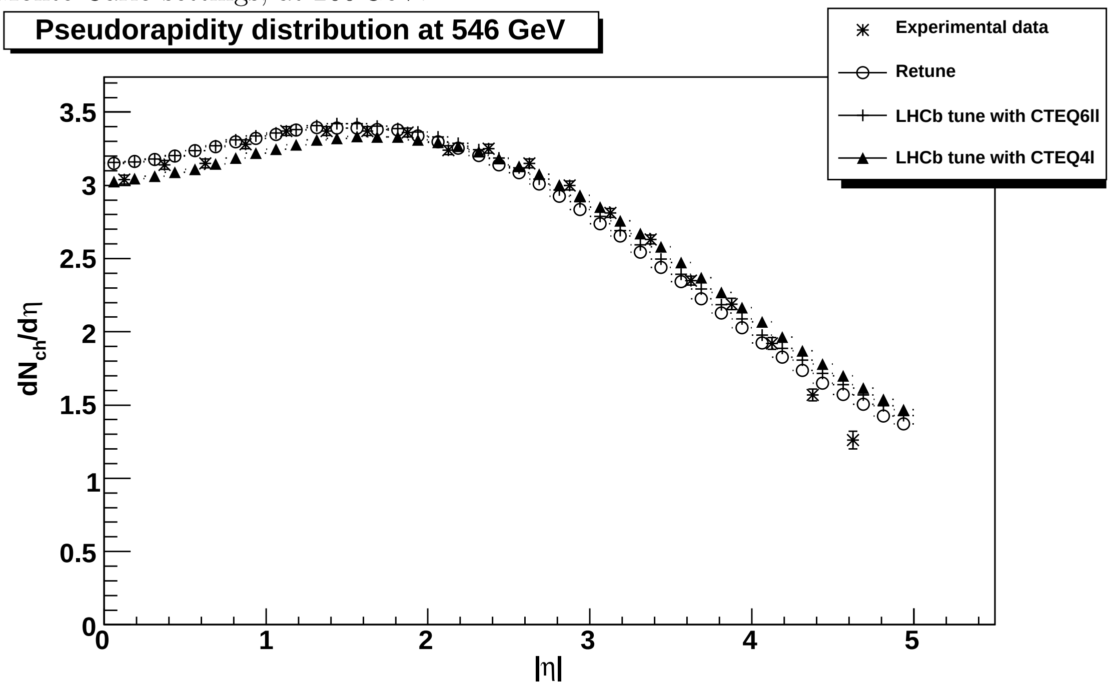

Figure 5.23: A comparison of pseudorapidity distribution produced with three different Monte Carlo settings, at 546 GeV.

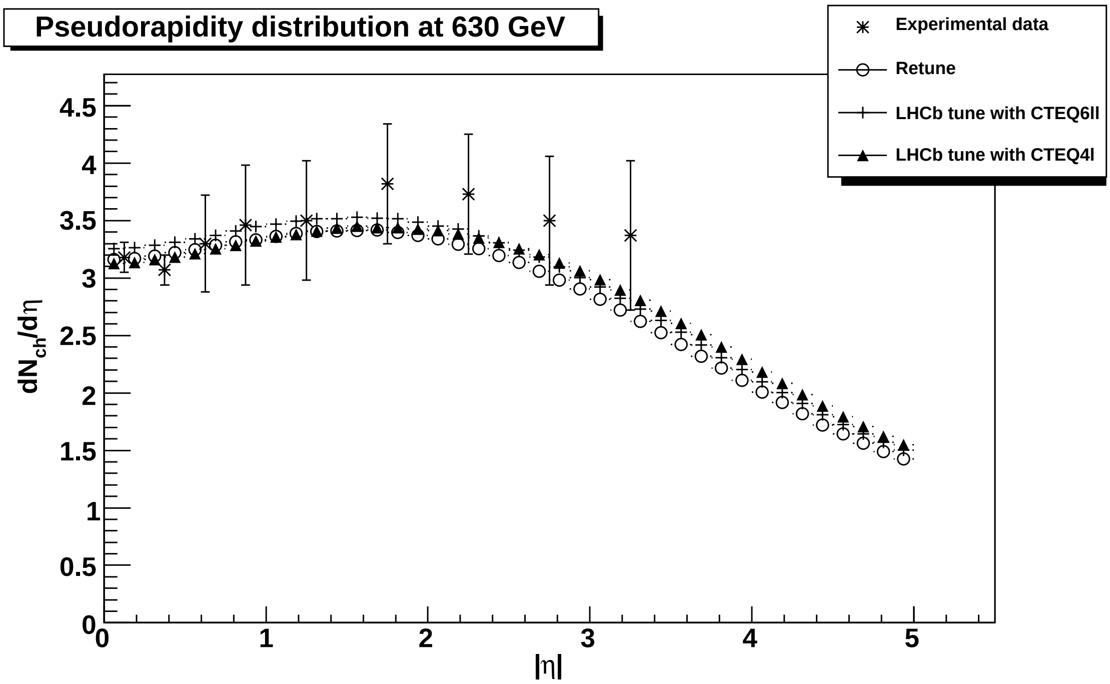

Figure 5.24: A comparison of pseudorapidity distribution produced with three different Monte Carlo settings, at 630 GeV.

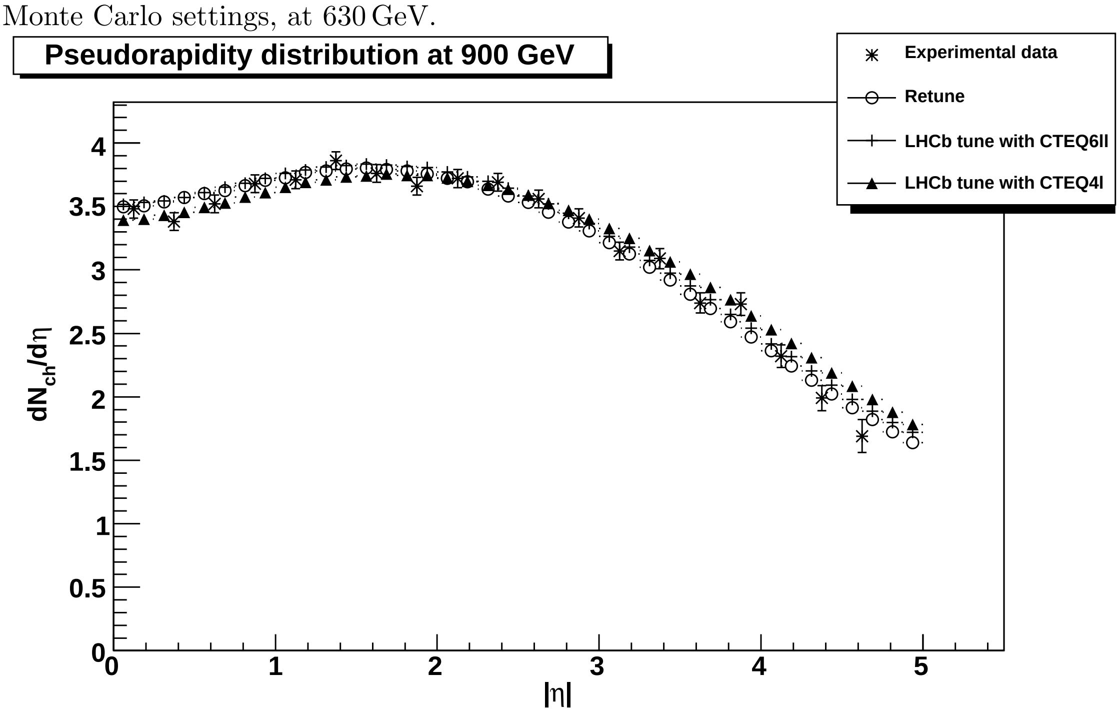

Figure 5.25: A comparison of pseudorapidity distribution produced with three different Monte Carlo settings, at 900 GeV.

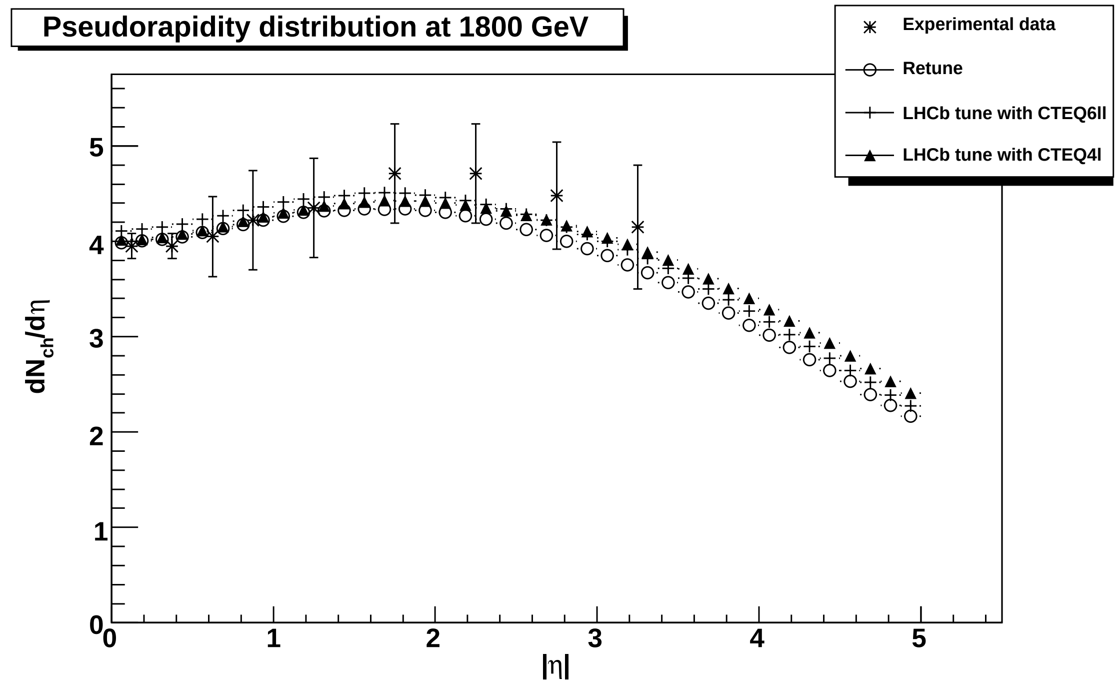

Figure 5.26: A comparison of pseudorapidity distribution produced with three different Monte Carlo settings, at 1800 GeV.

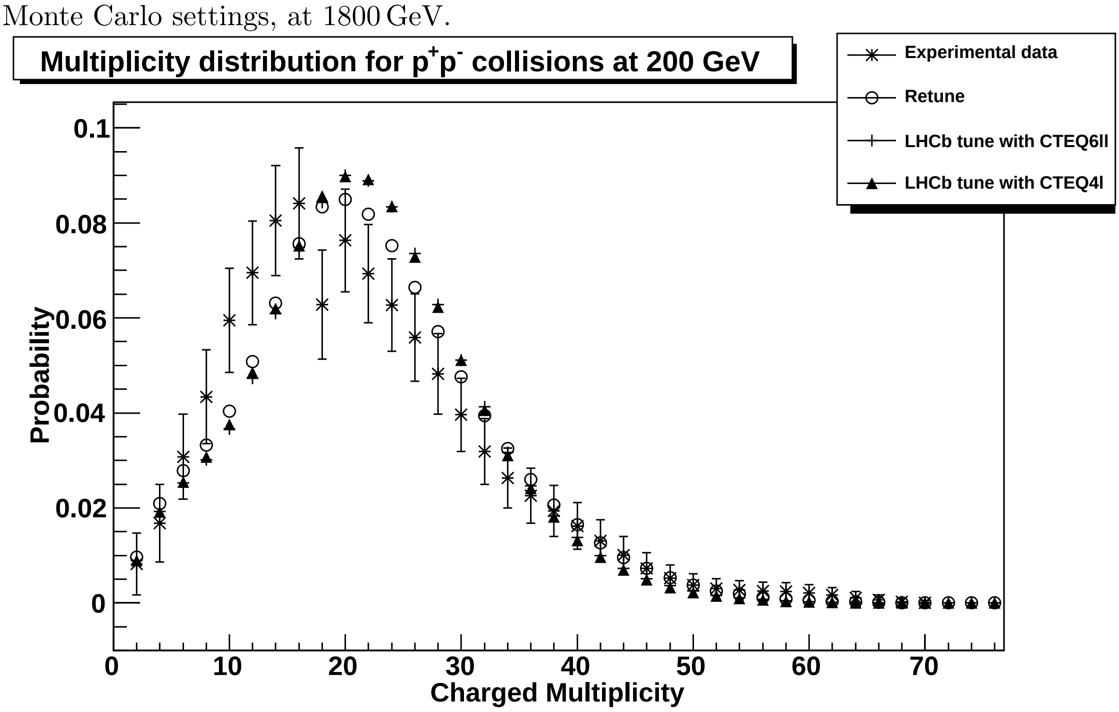

Figure 5.27: A comparison of the multiplicity distributions at 200 GeV with Monte Carlo data produced with three different sets of settings. A slight improvement is seen in the new tune compared to the LHCb one.

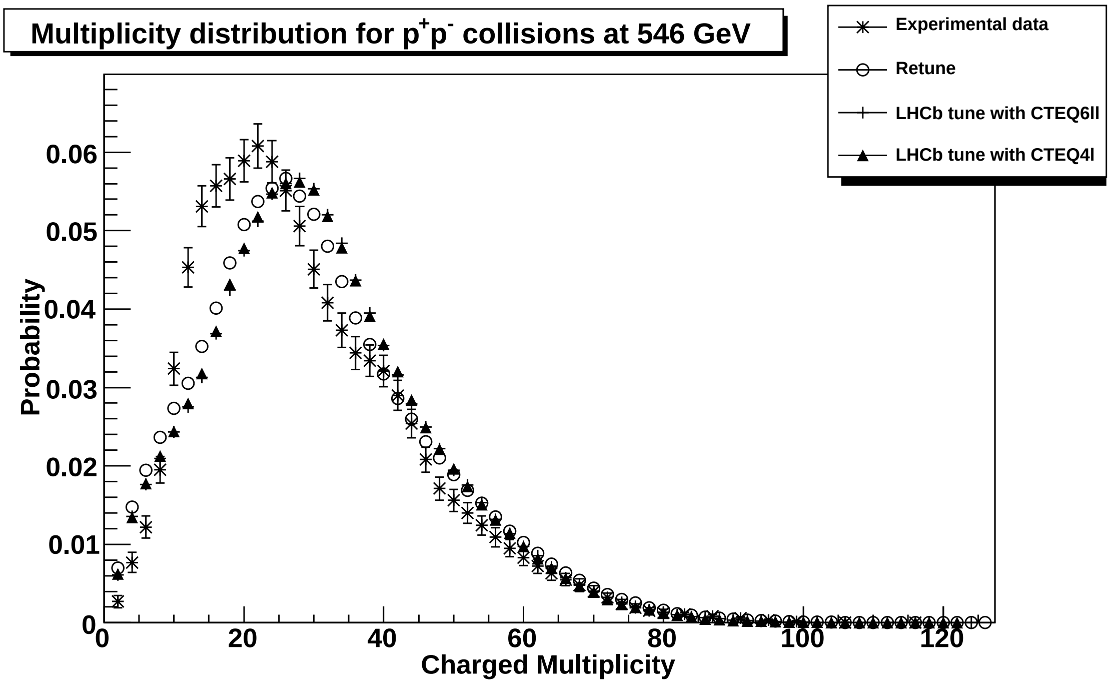

Figure 5.28: A comparison of the multiplicity distributions at 546 GeV with Monte Carlo data produced with three different sets of settings. A slight improvement is seen in the new tune compared to the LHCb one.

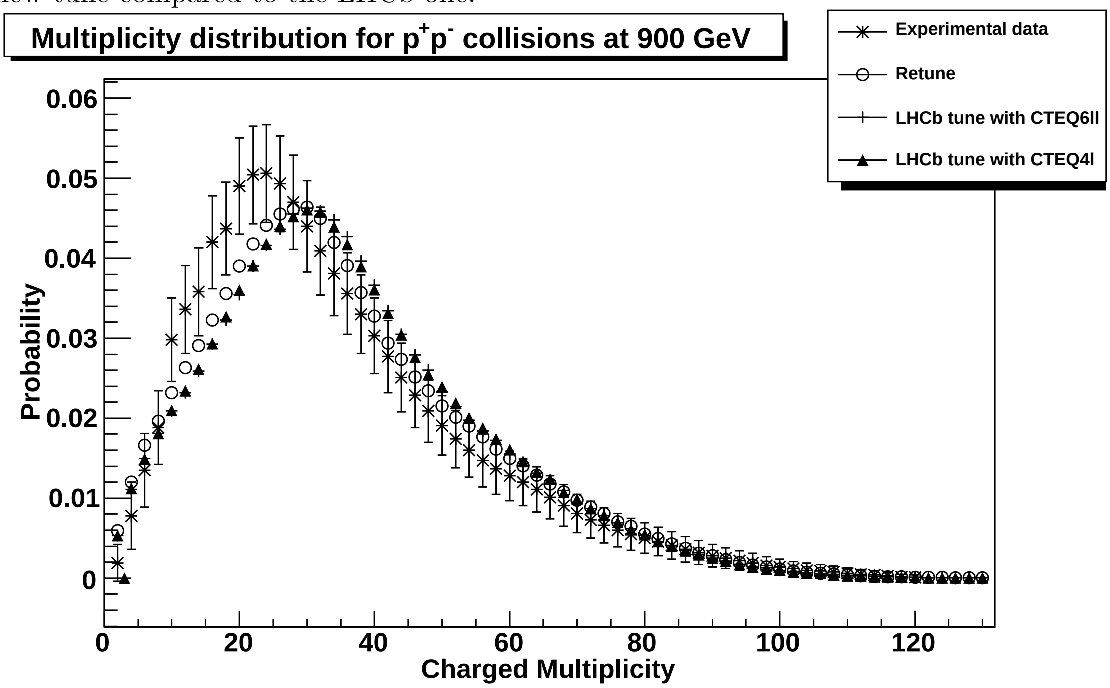

Figure 5.29: A comparison of the multiplicity distributions at 900 GeV with Monte Carlo data produced with three different sets of settings. A slight improvement is seen in the new tune compared to the LHCb one.

Energy/GeV	Distribution	Monte Carlo	χ^2
53	Pseudorapidity	LHCb tune with CTEQ6ll	2.6×10^{-4}
53	Pseudorapidity	LHCb tune with CTEQ4l	6.7×10^{-2}
53	Pseudorapidity	Retune	1.5×10^{-2}
200	Pseudorapidity	LHCb tune with CTEQ6ll	80.2
200	Pseudorapidity	LHCb tune with CTEQ4l	80.9
200	Pseudorapidity	Retune	75.7
546	Pseudorapidity	LHCb tune with CTEQ6ll	140.2
546	Pseudorapidity	LHCb tune with CTEQ4l	152.4
546	Pseudorapidity	Retune	167.4
630	Pseudorapidity	LHCb tune with CTEQ6ll	5.5
630	Pseudorapidity	LHCb tune with CTEQ4l	2.9
630	Pseudorapidity	Retune	4.5
900	Pseudorapidity	LHCb tune with CTEQ6ll	27.7
900	Pseudorapidity	LHCb tune with CTEQ4l	35.4
900	Pseudorapidity	Retune	24.9
1800	Pseudorapidity	LHCb tune with CTEQ6ll	5.8
1800	Pseudorapidity	LHCb tune with CTEQ4l	2.1
1800	Pseudorapidity	Retune	3.0
200	Multiplicity	LHCb tune with CTEQ6ll	47.5
200	Multiplicity	LHCb tune with CTEQ4l	46.9
200	Multiplicity	Retune	26.9
546	Multiplicity	LHCb tune with CTEQ6ll	495.2
546	Multiplicity	LHCb tune with CTEQ4l	465.0
546	Multiplicity	Retune	416.1
900	Multiplicity	LHCb tune with CTEQ6ll	60.3
900	Multiplicity	LHCb tune with CTEQ4l	58.9
900	Multiplicity	Retune	32.4

Table 5.11: The χ^2 values describing the goodness of fit to CDF and UA5 data.

5.5 Proton-Proton Collisions at 14 TeV

It is worth comparing the predictions of the LHCb tune with the new tune for proton-proton collisions at the LHC energy. A comparison of the predicted pseudorapidity distributions shows that new tune predicts a somewhat lower multiplicity than the LHCb tune does. This decrease is due almost entirely to the retuning of the PARJ variables, which reduced the number of excited mesons being produced; $p_{\perp min}$ is left almost unchanged for 14 TeV collisions. Until data is taken from the LHC one cannot say which of these predictions is more accurate, however, one may extrapolate data from lower energy experiments to the LHC energy to see whether the predictions of the new tune are at least reasonable. It has been found that the variation of $\langle dN_{ch}/d\eta\rangle_{|\eta|<0.25}$ with energy is phenomenologically well described by the following form [49]

$$\langle dN_{ch}/d\eta\rangle_{|\eta|<0.25} = A\ln^2(s) + B\ln(s) + C \tag{5.7}$$

Fitting a function of this form to the data from CDF and UA5 yields a value

$$\langle dN_{ch}/d\eta\rangle^{LHC}_{|\eta|<0.25} = 6.27 \pm 0.50 \tag{5.8}$$

The predictions of both the new tune and LHCb tune are in agreement with this, see figure 5.30.

An additional comparison is shown below, where the value of $p_{\perp min}$ used in the retune has been adjusted by 3 sigma to increase the multiplicity towards that seen in the LHCb tune, see figure 5.31.

Further comparisons between the two tunings were made by looking at generic B events, specifically stable charged particle pseudorapidity, inclusive charged particle P_T and stable charged particle multiplicity distributions. There is little difference between the two tunings, although the new tune predicts a lower multiplicity, see figures 5.32 to 5.35. This is consistent with the changes made in the retuning: the retuned $p_{\perp min}$ value is slightly higher than the old value resulting in slightly fewer multiple parton-parton

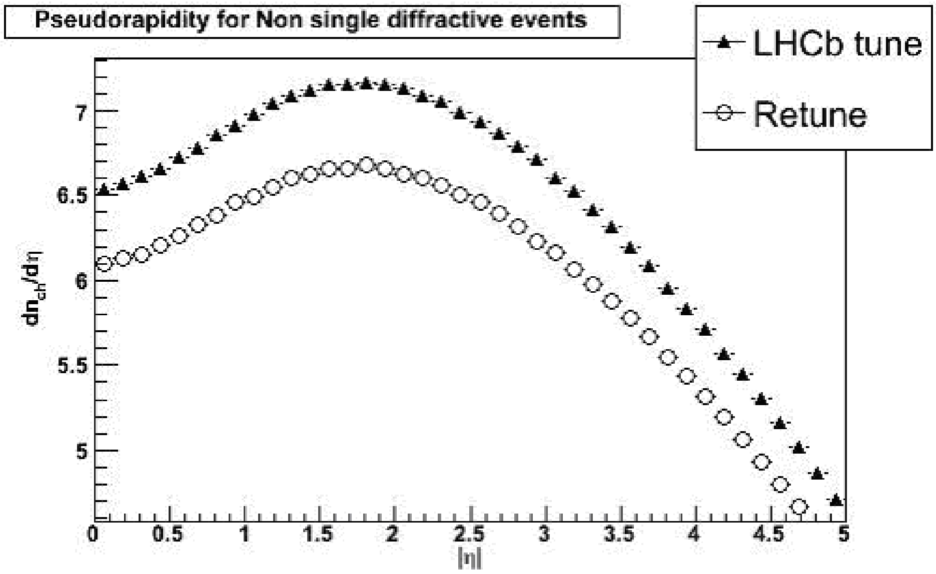

Figure 5.30: Pseudorapidity distributions for non-single diffractive events. Despite the lowering in multiplicity that results from retuning, both sets of Monte Carlo data predict a central pseudorapidity multiplicity in agreement with extrapolation from lower energy results.

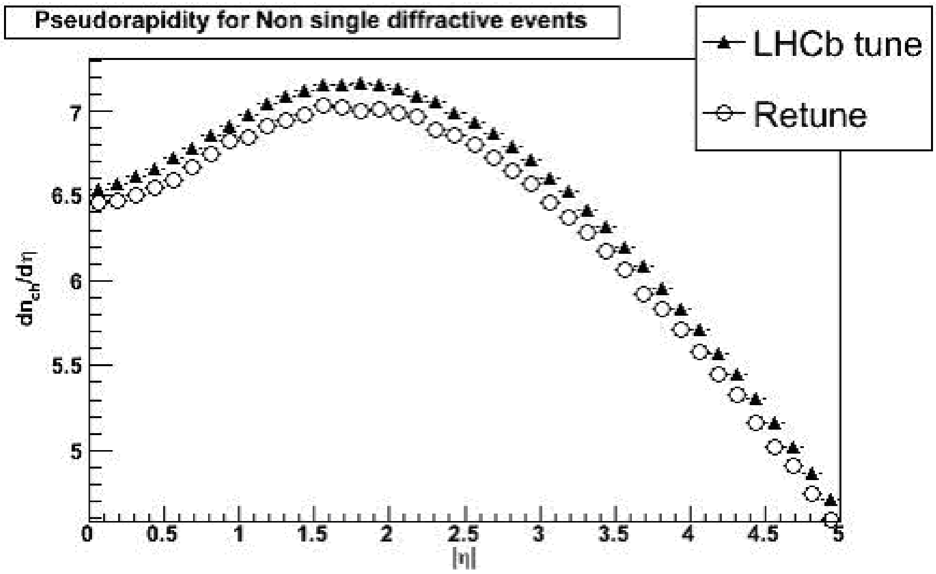

Figure 5.31: Pseudorapidity distributions for non-single diffractive events with a reduction in the $p_{\perp min}$ parameter of s sigma.

interactions; the multiplicity was also lowered by the retuning of the PARJ parameters affecting the excited meson states.

5.6 Conclusion

Gauss has been used to retune Pythia in a two stage process. The retuning of the PARJ variables, which control the probabilities of producing meson in various spin states, has lead to a substantially improved reproduction of LEP data compared to the LHCb Pythia tune currently used in Gauss. A retuning of the $p_{\perp min}$ parameter, which controls the number of parton-parton interactions in Pythia's multiple interaction model was then needed to restore the fit to CDF and UA5 data on proton anti-proton collisions. This was successfully done. The new tune and the LHCb tune differ in their predictions for the multiplicity of proton-proton events at 14 TeV, with the new tune giving a lower value. However, the multiplicity predicted by the new tune is not so low as to be worrying; it is consistent with data extrapolated from a phenomenological fit of lower energy data. There do not appear to be any other major differences between the predictions of the two tunes for LHC conditions.

The retuned values of the PARJ variables that were found in the first retuning process have now been adopted by the LHCb collaboration [61]. The retuned values of PARP(82) and PARP(90) have not been adopted because a different multiple-interactions model is now used. Tuning of this model is described in [39].

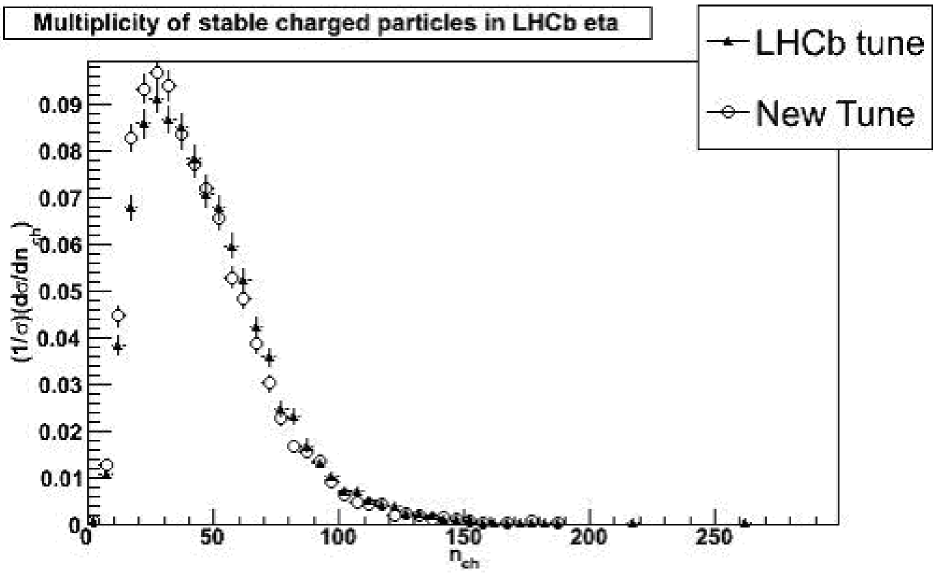

Figure 5.32: A comparison of multiplicity distributions for the LHCb tune with the new tune, for LHC conditions and generic B events.

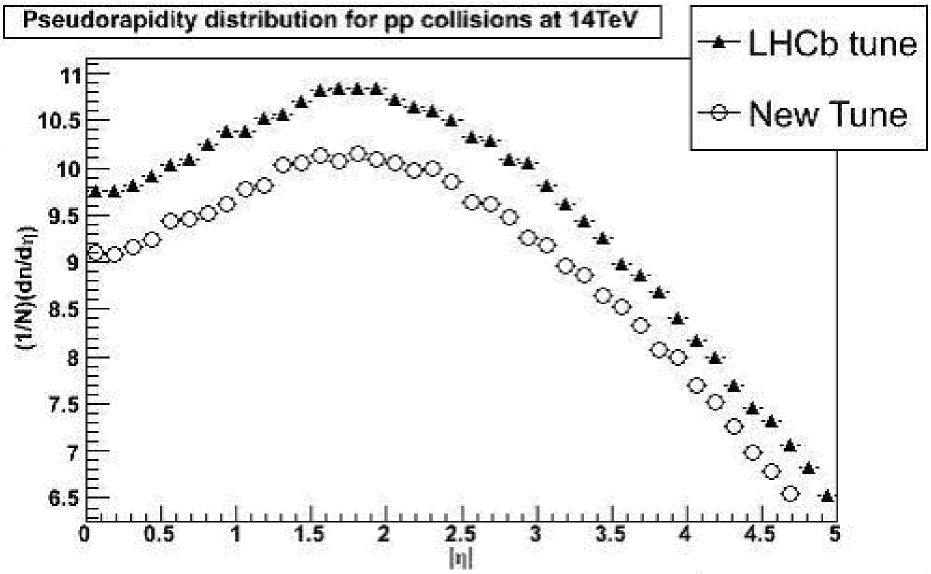

Figure 5.33: A comparison of pseudorapidity distributions for the LHCb tune with the new tune, for LHC conditions and generic B events.

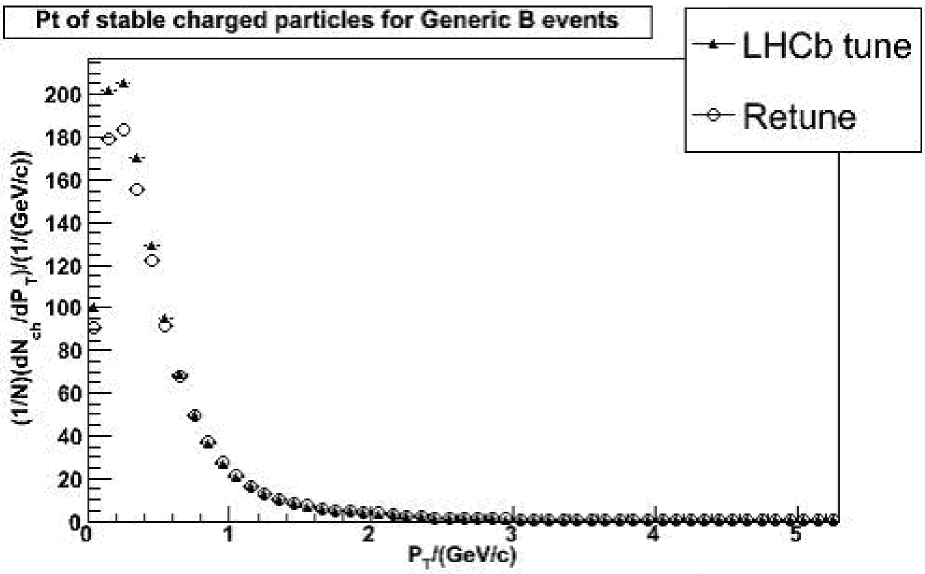

Figure 5.34: A comparison of p_T distributions for the LHCb tune with the new tune for LHC conditions for generic B events.

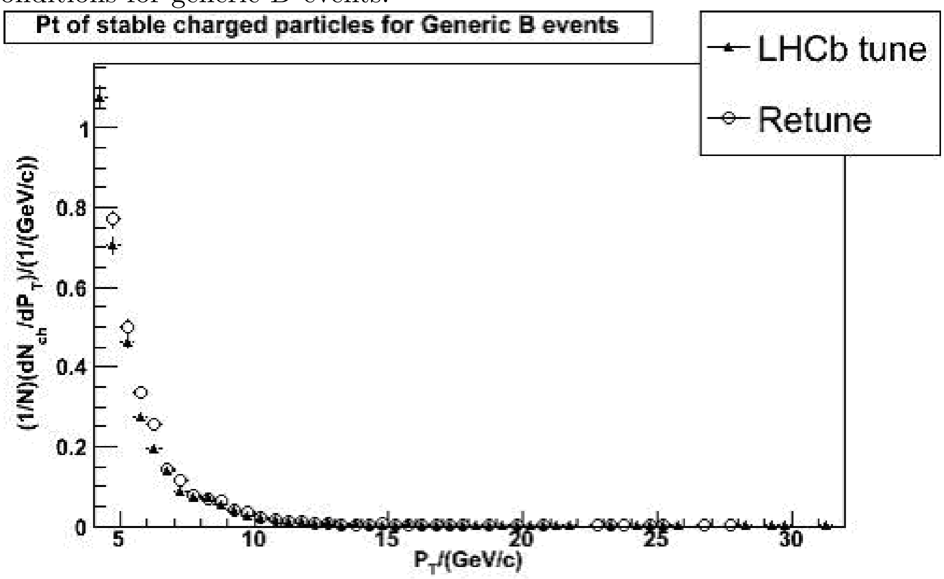

Figure 5.35: A comparison of p_T distributions for the LHCb tune with the new tune for LHC conditions for generic B events.

Chapter 6

Measurement of a_{fs} and Production Asymmetry

6.1 Introduction

The phenomenon of B-mixing means that a meson which begins in a B_s^0 state may oscillate to a $\bar{B}_s^0$ state, and vice versa. Indeed, a meson may oscillate more than once before it decays. CP violation in $B_s^0 - \bar{B}_s^0$ mixing results in a time-dependent asymmetry in final states of un-tagged flavour specific decays. This asymmetry is defined as

$$A_{fs}(t) = \frac{\Gamma(B^0 \text{ or } \bar{B}^0 \to f)(t) - \Gamma(B^0 \text{ or } \bar{B}^0 \to \bar{f})(t)}{\Gamma(B^0 \text{ or } \bar{B}^0 \to f)(t) + \Gamma(B^0 \text{ or } \bar{B}^0 \to \bar{f})(t)} \tag{6.1}$$

where the Γs are time-dependent decay rates, f is a final state in a flavour specific decay, and $\bar{f}$ is its charge conjugate. Two examples are $B_s^0 \to D_s^- \pi^+$ and $B_s^0 \to D_s^- \mu^+ \nu_\mu$, which have charge conjugates $\bar{B}_s^0 \to D_s^+ \pi^-$ and $\bar{B}_s^0 \to D_s^+ \mu^- \bar{\nu}_\mu$.

Within the Standard Model, CP violation in $B_s^0 - \bar{B}_s^0$ mixing is very small. However, it can be significantly enhanced by the presence of CP violating phases in new physics, and thus a measurement is of interest. CP violation in mixing is parameterised by the physical constant a_{fs}. The value of a_{fs} can be extracted from a measurement of $A_{fs}(t)$.

Substituting the decay rates derived in chapter 2 into equation 6.1 gives

$$A_{fs}(t) = \frac{a_{fs}(\cosh(\frac{1}{2}\Delta\Gamma t) - \cos(\Delta M t))}{2\cosh(\frac{1}{2}\Delta\Gamma t)} \tag{6.2}$$

$A_{fs}(t)$ is also affected by production asymmetry, A_p, and detection asymmetry, A_c. As will be shown in section 6.4.1.1 any two of these three may be extracted from a measurement of $A_{fs}(t)$, if the third is known from elsewhere. This chapter looks at measuring these asymmetries, in particular a_{fs} and A_p, from $B_s \to D_s\mu\nu$ decays[1]. The major advantage of the semi-leptonic decays is that many more semi-leptonic events than $B_s \to D_s\pi$ events are expected. The branching ratio for semi-leptonic decays is $(7.9 \pm 2.4) \times 10^{-3}$ [8], and the expected number of reconstructed events for 2 fb^{-1} data is 2.6×10^6 [69]. 2 fb^{-1} data corresponds to one year's data taking at full luminosity, assuming 10^7 seconds live-time per year [17]. The branching ratio for $B_s \to D_s\pi$ decays is $(3.3 \pm 0.5) \times 10^{-3}$ [8], and the expected number of reconstructed events for one year's data taking is 1.4×10^5 [70]. The major disadvantage of the semi-leptonic decays is that the neutrino cannot be detected and so the B_s cannot be fully reconstructed, making lifetime measurement difficult.

There are two ways to overcome this problem. The magnitude of the B_s momentum may be calculated if the direction of the momentum is known. In this situation the neutrino momentum may be calculated from kinematic constraints imposed by the D_s and μ momenta and the B_s mass. As will be shown in section 6.2.2 this approach leads to a two-fold ambiguity in the B_s lifetime. The work presented in this chapter uses this approach, which will henceforth be referred to as the neutrino reconstruction method. This term will be used to refer both to the method for finding the B_s momentum and to any fitting process which relies upon it.

An alternative approach is to estimate the momentum of the B_s from the momentum of the $D_s\mu$. The details of this method are given in [62], and measurements of the asymmetry parameters using this method are presented in [63] and [64]. Henceforth this

[1] Henceforth the notation is such that $B_s \to D_s\mu\nu$ implies charge-conjugation with and without oscillation. That is, $B_s \to D_s\mu\nu$ is shorthand for the combined set of $B_s^0 \to D_s^-\mu^+\nu_\mu$, $B_s^0 \to D_s^+\mu^-\bar{\nu}_\mu$, $\bar{B}_s^0 \to D_s^+\mu^-\bar{\nu}_\mu$ and $\bar{B}_s^0 \to D_s^-\mu^+\nu_\mu$.

approach will be referred to as the k-factor method. This term will be used to refer both to the method for estimating the B_s momentum and to any fitting process which relies upon it. A comparison of the neutrino reconstruction method and the k-factor method is presented in this chapter.

The studies of the neutrino reconstruction method fall into two categories: those that attempt to distinguish between the two lifetime solutions and those that use both of the solutions. The studies in the former category, presented in section 6.3, were carried out using Monte Carlo truth information produced using the LHCb simulation software. The studies in the latter category, presented in sections 6.4 to 6.5, were carried out using primarily toy Monte Carlo data. The term toy Monte Carlo is used to refer to simple Monte Carlo simulations, which generate distributions of lifetimes for the $B_s \to D_s\mu\nu$ and $B_s \to D_s\mu\nu X$ decays but which do not simulate full events or take into account the interaction of particles with the LHCb detector. The toy Monte Carlo simulations were written specifically for the studies presented in this thesis, but are based upon a modified version of the toy Monte Carlo that was written for the study presented in [63] and [64]. Details of the toy Monte Carlo are given in section 6.4.1.2. Reconstructed data were used to inform toy Monte Carlo used in section 6.5. The reconstructed data were produced using the full chain of LHCb reconstruction software, and are from the Monte Carlo data set produced in 2009 (MC09). The reconstructed data sample comprised 217354 events.

6.2 Theory

6.2.1 $B_s \to D_s\mu\nu$ Lifetime Distributions

The time-dependent decay rates for flavour specific decays were derived in chapter 2. For convenience they are restated here.

$$\Gamma_{B\to f}(t) = N_f|A_f|^2 e^{-\Gamma t}\frac{1}{2}\left[\cosh\left(\frac{1}{2}\Delta\Gamma t\right) + \cos(\Delta m t)\right] \tag{6.3}$$

$$\Gamma_{B\to\bar{f}}(t) = N_f(1-a_{fs})|\bar{A}_{\bar{f}}|^2 e^{-\Gamma t}\frac{1}{2}\left[\cosh\left(\frac{1}{2}\Delta\Gamma t\right) - \cos(\Delta m t)\right] \tag{6.4}$$

$$\Gamma_{\bar{B}\to f}(t) = N_f(1+a_{fs})|A_f|^2 e^{-\Gamma t}\frac{1}{2}\left[\cosh\left(\frac{1}{2}\Delta\Gamma t\right) - \cos(\Delta m t)\right] \tag{6.5}$$

$$\Gamma_{\bar{B}\to\bar{f}}(t) = N_f|\bar{A}_{\bar{f}}|^2 e^{-\Gamma t}\frac{1}{2}\left[\cosh\left(\frac{1}{2}\Delta\Gamma t\right) + \cos(\Delta m t)\right] \tag{6.6}$$

It will be convenient later to use four very similar expressions, F, defined by

$$F_{B\to f} = \Gamma_{B\to f}\left(\frac{1}{2}N_f|A_f|^2\right)^{-1} \tag{6.7}$$

$$F_{B\to\bar{f}} = \Gamma_{B\to\bar{f}}\left(\frac{1}{2}N_f(1-a_{fs})|\bar{A}_{\bar{f}}|^2\right)^{-1} \tag{6.8}$$

$$F_{\bar{B}\to f} = \Gamma_{\bar{B}\to f}\left(\frac{1}{2}N_f(1+a_{fs})|A_f|^2\right)^{-1} \tag{6.9}$$

$$F_{\bar{B}\to\bar{f}} = \Gamma_{\bar{B}\to\bar{f}}\left(\frac{1}{2}N_f|\bar{A}_{\bar{f}}|^2\right)^{-1} \tag{6.10}$$

These definitions are useful because they remove the dependance on a_{fs}. It is also important to note that $F_{B\to f} = F_{\bar{B}\to\bar{f}}$ and $F_{B\to\bar{f}} = F_{\bar{B}\to f}$.

6.2.2 Calculation of the B_s Lifetime

The momentum of the B_s cannot be found directly, because one cannot measure the momentum of all of its daughters. However, if the direction of the B_s is known, then one may calculate the momentum of the B_s if the momentum of the D_s and of the muon are known. The momentum of these particles can be measured with the tracking, and the direction of the B_s can be determined from vertex information provided by the VELO.

With the direction of the B_s known, the momentum of the $D_s\mu$ and the neutrino can be decomposed into components parallel and perpendicular to the direction of the B_s:

$P^{\|}_{D_s\mu}$, $P^{\perp}_{D_s\mu}$, $P^{\|}_{\nu}$ and $P^{\perp}_{\nu}$. Conservation of momentum and energy requires that

$$P^{\perp}_{D_s\mu} = -P^{\perp}_{\nu} \tag{6.11}$$

$$P_B = P^{\|}_{D_s\mu} + P^{\|}_{\nu} \tag{6.12}$$

$$E_B = E_{D_s\mu} + E_{\nu} \tag{6.13}$$

By using $E^2 = p^2 + m^2$ equation 6.13 may be rewritten in terms of equations 6.11 and 6.12. Doing so leads to a quadratic equation in $P^{\|}_{\nu}$

$$aP^{\|2}_{\nu} + bP^{\|}_{\nu} + c = 0 \tag{6.14}$$

where

$$a = 4({P^{\perp}_{D_s\mu}}^2 + m^2_{D_s\mu})$$

$$b = 4P^{\|}_{D_s}(2{P^{\perp}_{D_s\mu}}^2 - (m^2_B - m^2_{D_s\mu}))$$

$$c = 4{P^{\perp}_{D_s\mu}}^2({P^{\|}_{D_s}}^2 + m^2_B) - (m^2_B - m^2_{D_s\mu})^2$$

$P^{\|}_{\nu}$ is then given by

$$P^{\|}_{\nu} = \frac{-b \pm \sqrt{b^2 - 4ac}}{2a} \tag{6.15}$$

The B_s momentum is then given by equation 6.12.

A study was made of MC truth data from DaVinci, to determine if it was possible to distinguish the two solutions of equation 6.14. It was found that in the vast majority of 37885 Monte Carlo events studied, it is not obvious which solution is correct. Figures 6.1 shows the distributions of $P^{\|}_{\nu}$ for the correct and incorrect solutions. There are slight differences in the distributions, but the shapes are broadly similar, as is the momentum range in each case. It should be noted that there are negative solutions in both the correct and the incorrect distributions, as it is possible for the neutrino to be traveling in roughly the opposite direction to that of the B_s. A negative B_s momentum given by equation 6.12 can be ruled out as such a B_s would not be seen in the single arm of the LHCb detector. Of the 37885 events with calculable solutions, there were only

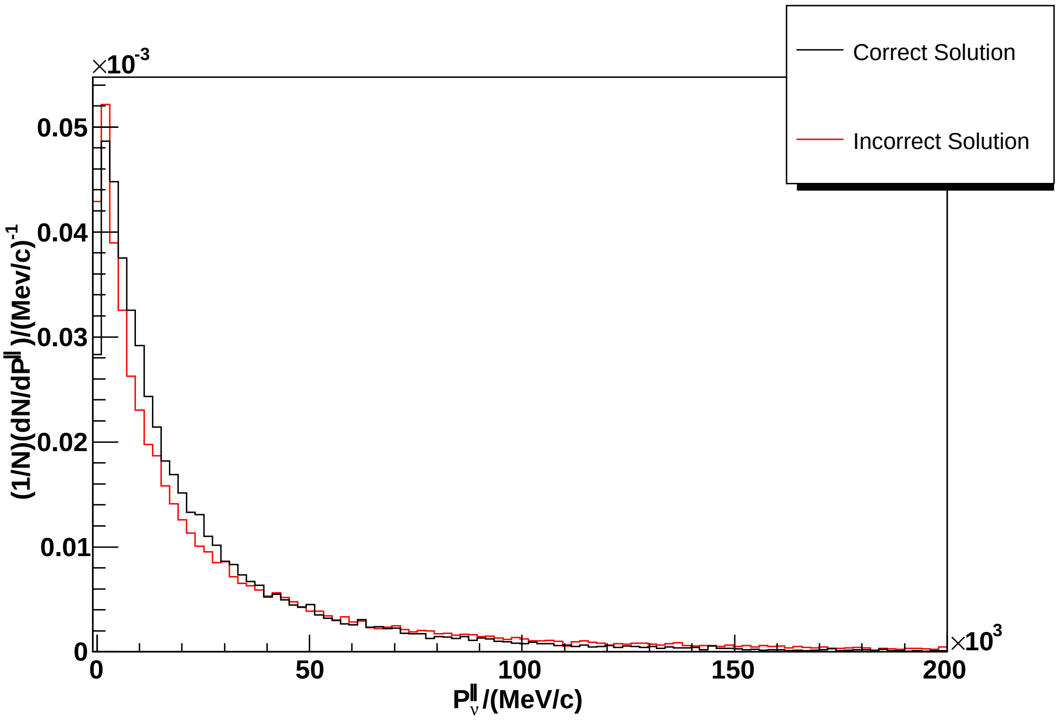

Figure 6.1: The distribution of the component of the neutrino momentum parallel to the B_s momentum, as calculated using equation 6.14. Both the correct and incorrect solutions are shown.

22 in which the B_s momentum was negative, i.e. there were only 22 in which it was immediately and obviously apparent which of the solutions to equation 6.12 was correct. In section 6.3 more sophisticated methods for finding the correct solution are examined.

It is worth noting that solving equation 6.14 can be problematic if sufficient care is not taken. DaVinci stores kinematic variables as floats, and if floats are used to calculate the solutions to equation 6.14 roughly 1 % of Monte Carlo truth $B_s \to D_s \mu \nu$ decays do not have real solutions to equation 6.14. However, this problem was overcome simply by converting the floats to doubles, after which all of the Monte Carlo truth decays studied yielded real solutions.

6.3 Selection of the Correct Lifetime

Equation 6.14 is a quadratic equation and its two solutions lead inevitably to an ambiguity in the lifetime of the B_s in any given event. Henceforth, the solution which comes from taking the negative square root will be referred to as the NSRS, and that coming from the positive solution, the PSRS. It would obviously be useful to know, on an event by event basis, whether the NSRS or the PSRS was the correct solution.

However, there are some events in which neither of the solutions to equation 6.14 are correct. There are two reasons why this can be the case[2]. First, there are events in which there is more than one primary vertex. If the primary vertex, PV, is chosen incorrectly then the direction of the B_s will be incorrectly determined, and both the solutions of equation 6.14 will be wrong. Figure 6.2 shows the distribution of PVs in Monte Carlo truth data. Second, there are events in which the B_s does not decay directly to a $D_s\mu\nu$ state. Instead, the D_s, the μ or both come from the decay of an intermediate particle. In these cases there are additional final state particles, and the conservation of momentum and energy equations 6.11, 6.12 and 6.13 used to derive equation 6.14 do not hold. Such decays are designated $B_s \to D_s\mu\nu X$ decays. $B_s \to D_s\mu\nu$ decays are considered separate from $B_s \to D_s\mu\nu X$ decays, and not a subset of them. The term semi-muonic decays is used to describe the combined set of $B_s \to D_s\mu\nu$ and $B_s \to D_s\mu\nu X$ decays. There are roughly three times as many $B_s \to D_s\mu\nu X$ decays as $B_s \to D_s\mu\nu$ decays. The precise branching ratios are given in section 6.4.2.

It will often be useful to regard an event with n PVs as n separate events, each with one PV. A numbering system is used to distinguish between different events, based on whether or not the correct PV is selected, and what the final state is. A related numbering system is used to distinguish the two momentum solutions which arise from each event type. Table 6.1 gives the details of these numbering systems.

The remainder of this section details methods for distinguishing between the different types of solution, and the different types of event. In section 6.3.1 attempts to distinguish

[2]In fact, finite detector resolution means that the solutions of equation 6.14 never match the true momentum. However, in this section, only Monte Carlo truth data is considered. Detector effects are described in section 6.5 .

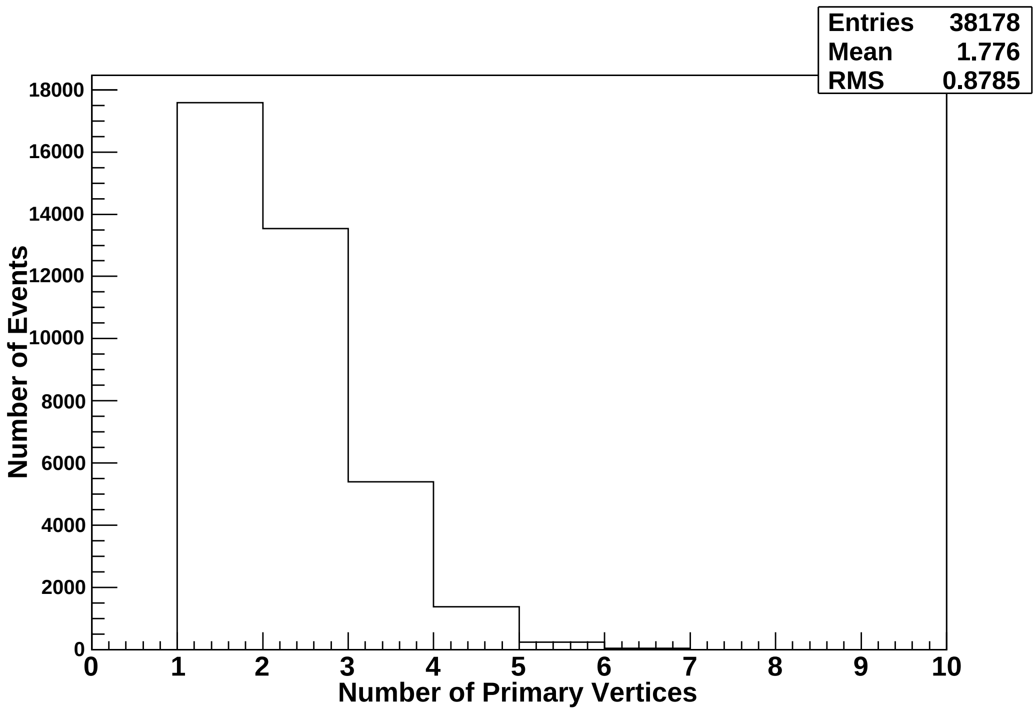

Figure 6.2: The distribution of the number of primary vertices in Monte Carlo truth events.

Decay	Primary Vertex	Event Type	Solution	Solution Type
$B_s \to D_s\mu\nu$	Correct	1	Correct	1
$B_s \to D_s\mu\nu$	Correct	1	Incorrect	2
$B_s \to D_s\mu\nu$	Incorrect	2	Better	3
$B_s \to D_s\mu\nu$	Incorrect	2	Worse	4
$B_s \to D_s\mu\nu X$	Correct	3	Better	5
$B_s \to D_s\mu\nu X$	Correct	3	Worse	6
$B_s \to D_s\mu\nu X$	Incorrect	4	Better	7
$B_s \to D_s\mu\nu X$	Incorrect	4	Worse	8

Table 6.1: The definitions of event type and solution type.

the different solutions are presented. Initially this was attempted using simple cuts based on one or two kinematic variables. Subsequently neural networks were used to achieve better results. In section 6.3.2 attempts to distinguish between the different types of event, as opposed to solutions, are presented.

6.3.1 Selection of the Correct Solution in Type-1 Events

For simplicity type-1 events, see table 6.1, are considered first in isolation. For these events one has simply to decide whether the NSRS or the PSRS is correct. The simplest way to choose between the NSRS and PSRS, is to choose always the NSRS, or always the PSRS. Examining Monte Carlo truth data from DaVinci, it was found that for 19292 events of 37863, the NSRS was the correct solution. This is $50.1 \pm 0.4\%$ of events; the method is no better than choosing at random.

The momentum of the $D_s\mu$ approximates that of the B_s. For this reason it was reasonable to think that $P_{D_s\mu}$ would be closer to the correct P_{B_s} solution than it is to the false solution. This was not a good discriminant however. The true solution was the closer to $P_{D_s\mu}$ in 19301 of 37863 events. This is $50.1 \pm 0.4\%$ of events.

The same technique was tried with $P_{D_s\mu}^{scaled}$ instead of $P_{D_s\mu}$ where

$$P_{D_s\mu}^{scaled} = P_{D_s\mu}\frac{m_{B_s}}{m_{D_s\mu}}$$

however $P_{D_s\mu}^{scaled}$ was closer to the correct solution in only 18906 of the events. This is

$50.0 \pm 0.4\%$ of events.

As these methods failed another approach was sought. Various kinematic variables were examined: the momentum of the D_s, the μ and the $D_s\mu$, broken down into components perpendicular and parallel to the B_s momentum, and transverse to the beam direction; the mass of the $D_s\mu$; the angles between the different particles; the neutrino momentum solution; the difference between the solutions. None of these was found to be a useful discriminant. In some cases the distribution of these variables looks different for events in which the PSRS is the correct solution and in events where it is the incorrect solution. In some cases there is no noticeable difference. In the cases where there is a difference, the difference is small and insufficient for effective discrimination.

In addition to using single variables as discriminants, the ratios of variables were also considered. As with single variables, these ratios were not found to be useful discriminants.

Figures 6.3 and 6.4 show two of the distributions considered. Because no useful cut was found using these variables individually, an approach to combine them using neural networks was investigated.

6.3.1.1 Neural Networks

A neural network, NN, is a network of simple processors, used for computation [66, 67]. The processors are called neurons. One important feature of NNs is that they must undergo a process of learning, or training, to achieve the desired results.

The ROOT class TMultiLayerPerceptron [68] was used to create and train a NN to separate the different solutions. The NN is of a particular class, called a multilayer perceptron, or MLP. An MLP consists of a number of input neurons, one or more hidden layer of neurons, and one or more output neuron. Figure 6.5 is a schematic of an MLP. The inputs to each neuron are summed, according to some weighting. This sum then becomes the argument for some function. In the case of the hidden layer of neurons, the function is a sigmoid[3]. In the case of the output layer the function is a linear one. The

[3] A sigmoid function is a function of the form $f(x) = \frac{1}{1+e^{-ax}}$ where a is a constant.

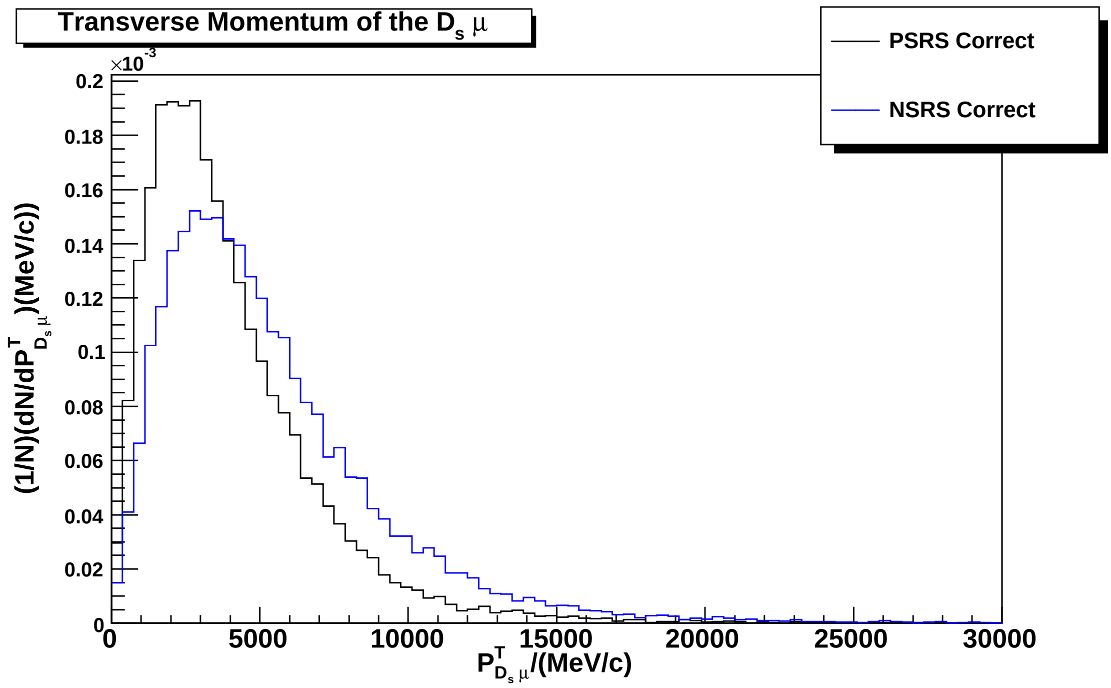

Figure 6.3: The transverse momentum of the $D_s\mu$ for events in which the PSRS is the correct solution, and events where the NSRS is the correct solution.

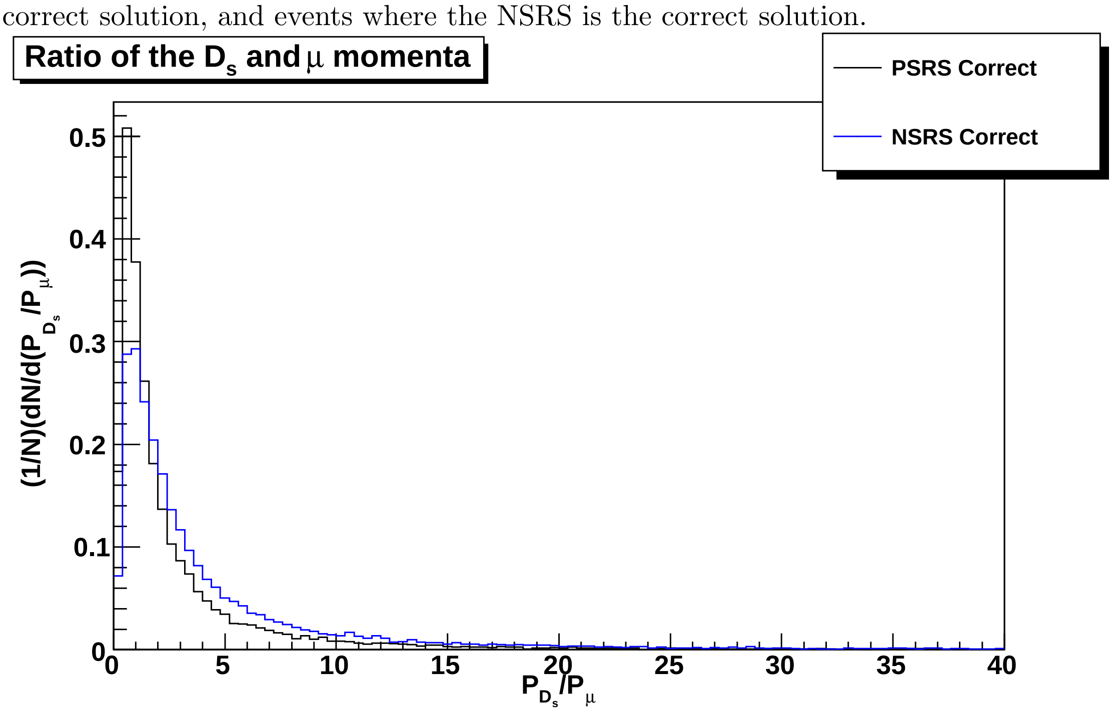

Figure 6.4: The ratio of the D_s momentum and the μ momentum for events in which the PSRS is the correct solution, and events where the NSRS is the correct solution.

values of the functions in one layer become the inputs for the neurons in the next layer. For a NN trained to distinguish between signal and background events, the ideal output is 1 for signal and 0 for background. The output which the NN gives depends on the weighting given to the inputs. To find the correct weights the NN must be trained on a data set where it is known which data are signal data and which are background data. The weights are initially chosen at random, and then adjusted based upon the NN error, which gives a comparison of the ideal output and the actual output. By adjusting the weights in this way the NN explores many different ways of using the information in the inputs. This allows correlations between the inputs, which may be useful to distinguish signal and background, to be found.

One possible problem with NN training is that the NN becomes overtrained. This means that the NN spuriously takes into consideration the noise in the data sample it was trained on. To avoid overtraining, the network performance should be checked against another data sample, for which the correct output is known.

6.3.1.2 Selection of Solutions using Neural Networks

Neural networks were used to separate the solutions in type-1 events. A number of different networks, with slightly different inputs and architectures were used. Figure 6.6 shows the output from one of these neural networks, designated NN1. Figure 6.7 shows the error from NN1 as a function of the number times it had been trained. The error is the sum over all events of (ideal output - neural network output)^2/2. The inputs for NN1 were the variables, discussed in section 6.3.1, which had allowed some discrimination between solutions. They are listed in table 6.2. NN1 had one hidden layer with 40 neurons in it.

The output from NN1 is obviously less than ideal, as both the signal and background outputs are centred at ~ 0.5 and both outputs are widely distributed. If the choice between the PSRS and NSRS is made simply by choosing the solution that produces the highest output from the NN, the correct solution is found in 23893 of 37863 events. That is, the correct solution is found in $63.1 \pm 0.5\%$ of events.

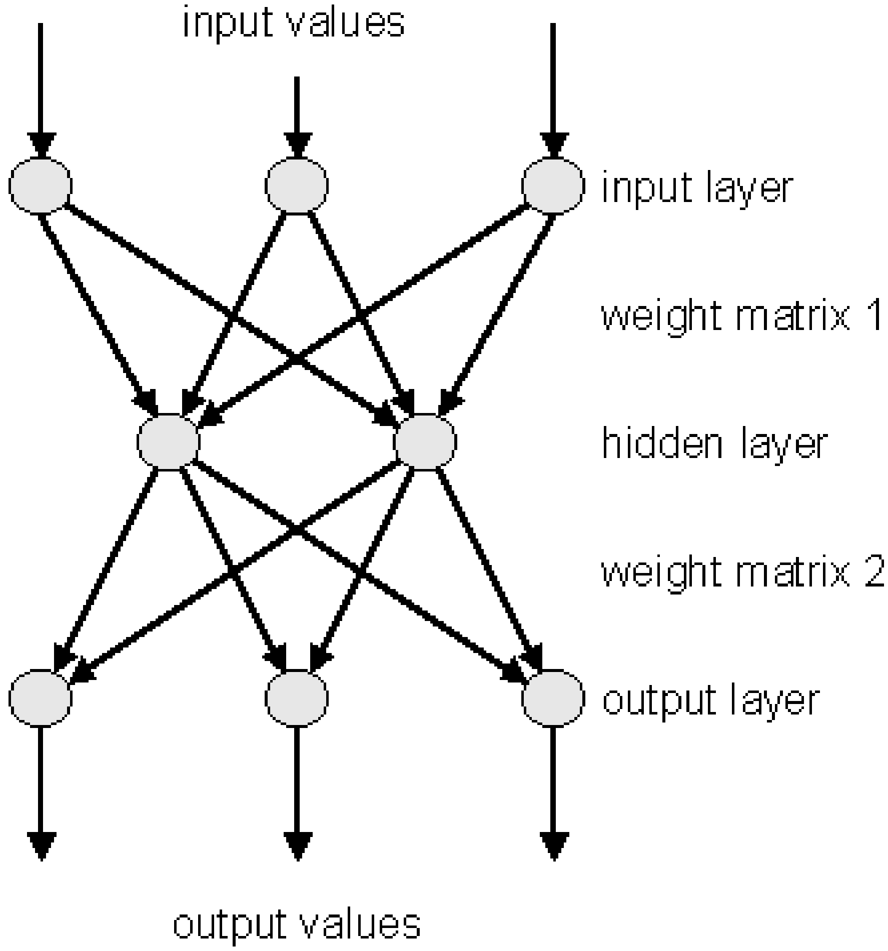

Figure 6.5: A schematic of a neural network. The inputs are given random weights and their sum forms the argument of the sigmoid functions in the hidden layers. The output of the hidden layer, randomly weighted, forms the input for the output layer. This input is the argument of a linear function. The weights are adjusted so that the outcome is as close to the desired one as possible.

Input Number	Input
1	PSRS or NSRS
2	$P_{D_s\mu}$
3	$P_{D_s\mu}^{scaled}$
4	$P_{D_s\mu}^{T}$
5	$P_{D_s\mu}^{\perp}$
6	$P_{D_s\mu}^{\parallel}$
7	$m_{D_s\mu}$
8	P_{B_s}
9	P_{D_s}
10	$P_{D_s}^{T}$
11	P_{ν}
12	$P_{\nu}^{\parallel}$
13	P_{μ}/P_{D_s}
14	$P_{\mu}/P_{D_s\mu}$
15	$-b/2a$
16	$\sqrt{b^2-4ac}/2a$

Table 6.2: The inputs for the NN1. Input number 1 tells the NN if the solution in question comes from the PSRS or the NSRS. For this a 1 or a 0 is entered. For inputs 15 and 16 a, b and c are as defined by equation 6.14

It is not easy to determine the best architecture for a NN. NNs with a greater number of neurons in the hidden layer, or with a greater number of hidden layers are more powerful than ones with fewer[4]. For this reason, a network with 100 neurons in the hidden layer and a network with two hidden layers each of 40 neurons were also trained to separate the solutions. Neither of these improved on the performance of NN1. In addition to varying the architecture of the NN, the inputs were also varied. All the inputs used were variables discussed in section 6.3.1 or ratios of them. No input or combination of inputs was found to yield better results than those presented.

The success rate for selecting the correct solution in type-1 events is unimpressive. In more realistic situations, namely where type-2, type-3 and type-4 events are also considered, the selection would be more difficult still. For this reason attempts to select solutions were abandoned. Instead, attempts to distinguish between the events were

[4]There are also disadvantages to increasing the number of layers and the number of neurons. This increases the likelihood of the NN becoming trained on noise rather than just signal, and also increases the computing time required to use the NN.

made. These are presented in section 6.3.2.

6.3.2 Selection of Type-1 Events

In section 6.3.1 it was found that the correct solution to equation 6.14 could not be found. This necessitates a fitting procedure which does not require knowledge of which solution is correct. Such a procedure is developed in section 6.4. However, there is still reason to distinguish between different types of event; only type-1 events yield correct solutions.

A data sample containing 16811 type-1 events, 13084 type-2 events, 50429 type-3 events and 38792 type-4 events. The ratio of type-1 events:type-3 events was approximately 1 : 3 and was chosen to be very close to the expected ratio; the branching ratios are given in section 6.4.2. Separation of events was done in two stages, detailed below. First, many type-2 and type-4 events were removed with simple cuts. Second, a neural network was used to separate the remaining events.

6.3.2.1 Removal of Type-2 and Type-4 Events

Three cuts were applied to remove type-2 and type-4 events.

- Require that the B_s pseudorapidity is within the LHCb acceptance. Even if the B_s was within the acceptance, an incorrect choice of PV can fake a pseudorapidity outside the acceptance.

- Require that equation 6.14 has real solutions.

- Require that both the solutions to 6.14 are positive.

$99.2 \pm 0.5\%$ of type-1 events pass these cuts, $8.0 \pm 0.2\%$ of type-2 events pass these cuts, $99.9 \pm 0.5\%$ of type-3 events pass these cuts and $9.9 \pm 0.2\%$ of type-4 events pass these cuts. It should be noted that, as Monte Carlo truth data is being used, the erroneous PVs correspond to multiple interactions. Poor reconstruction can also result in extra PVs, and different cuts may be required to remove these. Brief discussions of primary vertex resolution and of cuts to remove extra PVs are given in section 6.5.

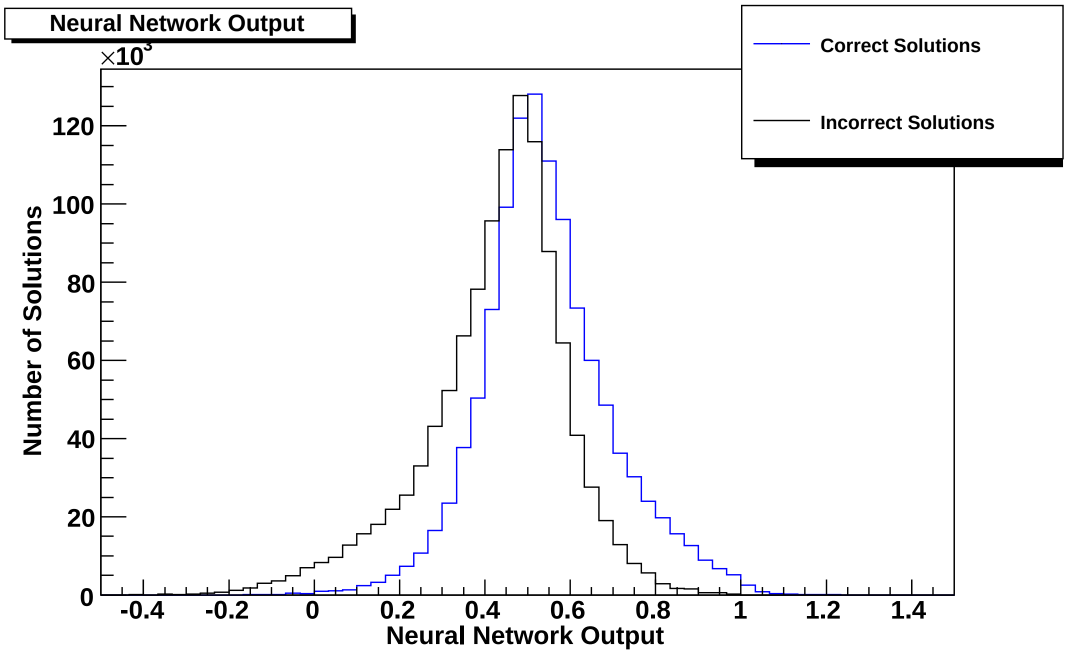

Figure 6.6: The output from NN1. The distributions of the signal and background outputs do not allow for easy discrimination.

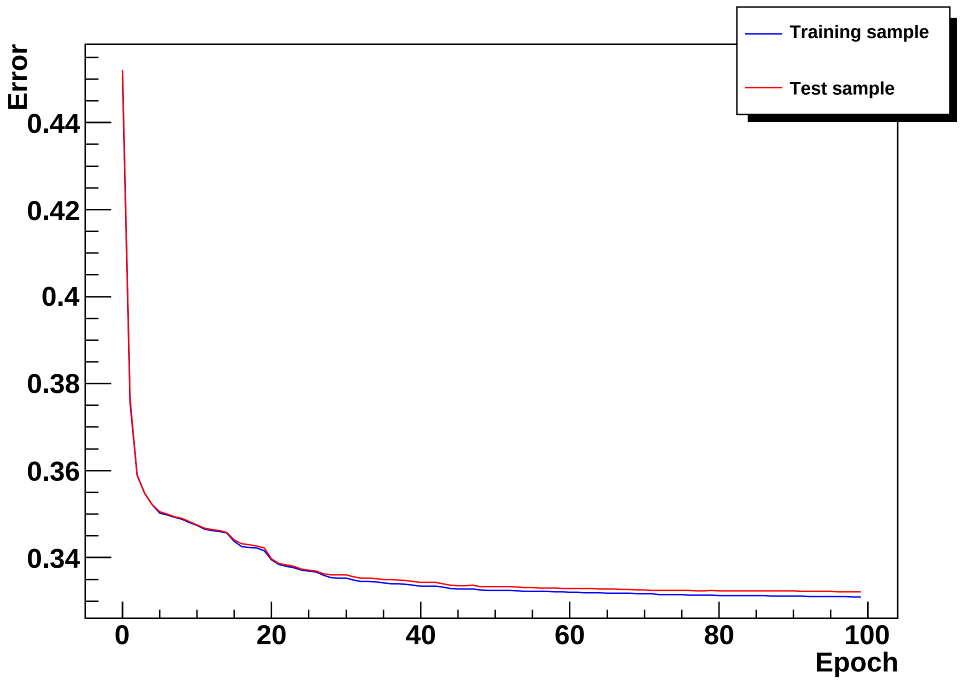

Figure 6.7: The error from NN1. The epoc is the number of iterations of the training which have been carried out.

Input Number	Input
1	$P_{B_s^{PSRS}}$
2	$P_{B_s^{NSRS}}$
3	$P_{B_s^{NSRS}}/P_{B_s^{PSRS}}$
4	$P^{\parallel}_{\nu^{NSRS}}/P^{\parallel}_{\nu^{PSRS}}$
5	$E_{\nu^{PSRS}}/E_{B_s^{PSRS}}$
6	$E_{\nu^{NSRS}}/E_{B_s^{NSRS}}$
7	$m_{D_s\mu}$
8	$P_{D_s\mu}$
9	P_{D_s}
10	$E_{D_s}/E_{\nu^{PSPS}}$
11	$E_{D_s}/E_{\nu^{NSPS}}$
12	$\theta_{B_s\nu^{PSRS}}$
13	$\theta_{B_s\nu^{NSRS}}$
14	$\theta_{\mu\nu^{PSRS}}$
15	$\theta_{\mu\nu^{NSRS}}$

Table 6.3: The inputs for NN2. For variables which depend on the solutions to equation 6.14, the superscripts NSRS and PSRS are used to distinguish the two values. $\theta_{B_s\nu}$ is the angle between the B_s and the ν, $\theta_{\mu\nu}$ is the angle between the μ and the ν.

6.3.2.2 Selection of Type-1 Events with Neural Networks

Figure 6.8 shows the output from a NN trained to distinguish type-1 events from the others. This NN will be referred to as NN2. It had one hidden layer containing 60 neurons. Table 6.3 lists the inputs used. The inputs are not the same as those for NN1 because some inputs were found to be useful for distinguishing events, but not the solutions of type-1 events. Figures 6.10 and 6.11 show distributions for one of these new inputs, the ratio of the two B_s momentum solutions. NN2 was trained on the data for the events that passed the cuts described in section 6.3.2.1.

The decision to accept or reject an event must be based on the output from NN2, specifically whether it is greater or less than some variable x. Table 6.4 shows the numbers of events passing this cut, as a function of x. A purity and efficiency are also given, where

$$\text{Purity} = \frac{\text{Number of type-1 events passing cut}}{\text{Total number of events passing cut}}$$

x	Number of Events Passing Cut	Number of Type 1 Events Passing Cut	Purity	Efficiency
$-\infty$	71965	16679	0.23	1.00
0.0	71377	16651	0.23	0.99
0.1	54906	15450	0.28	0.76
0.2	27157	11493	0.42	0.38
0.3	15224	8810	0.58	0.21
0.4	10242	7181	0.70	0.14
0.5	7888	5946	0.75	0.11
0.6	5776	4923	0.85	0.08
0.7	4362	3935	0.90	0.06
0.8	3124	2936	0.94	0.04
0.9	1951	1876	0.96	0.03
1.0	950	920	0.97	0.01
1.1	293	286	0.98	4×10^{-3}

Table 6.4: The total number of events and of type-1 events passing a cut based on the output of NN2.

and

$$\text{Efficiency} = \frac{\text{Number of events passing cut}}{\text{Total number of events in data set}}$$

Efficiency versus purity is plotted in figure 6.9.

The usefulness of this level of event separation cannot be determined without a fitting procedure to find a_{fs} and A_p. Such a procedure is discussed in sections 6.4 and 6.5. The use of event selection to improve the performance of this method is discussed again in section 6.6.2.

6.4 The Measurement of A_P and a_{fs} Without the Selection of the Correct Lifetime

Because of the difficulties in selecting the correct solution from equation 6.14 an alternative approach was adopted. It was necessary to adopt an analysis procedure that did not rely on knowing the correct lifetime. The following sections detail the methodology. Broadly, the methods may be grouped into two categories. Those which make use of both lifetime solutions per event, and those which make use of only one. The latter

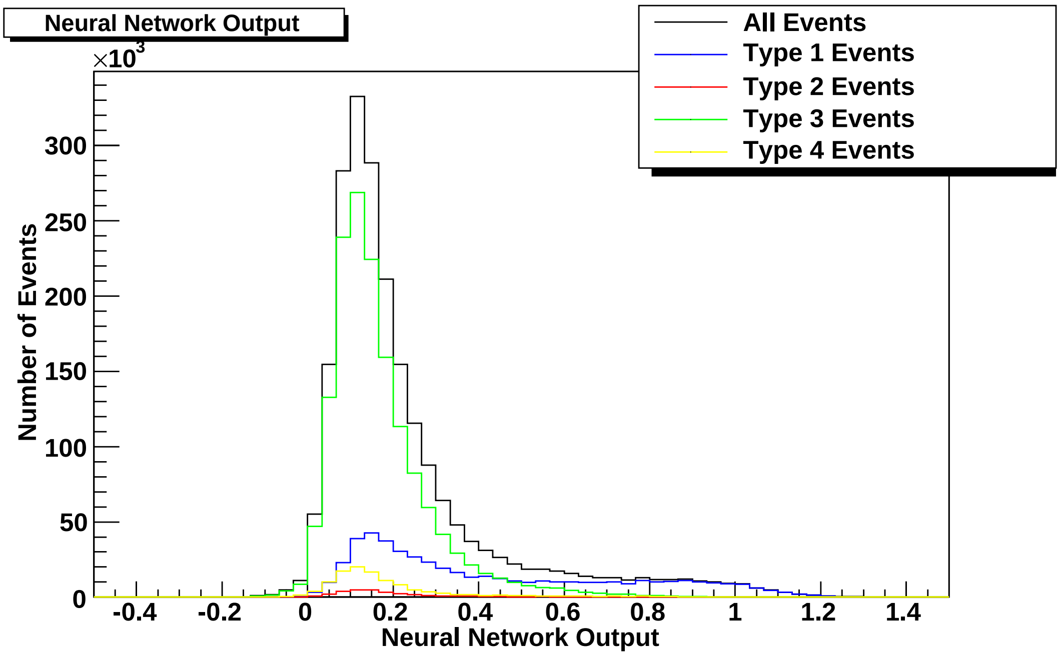

Figure 6.8: The output from NN2, trained to separate type-1 events from the other events

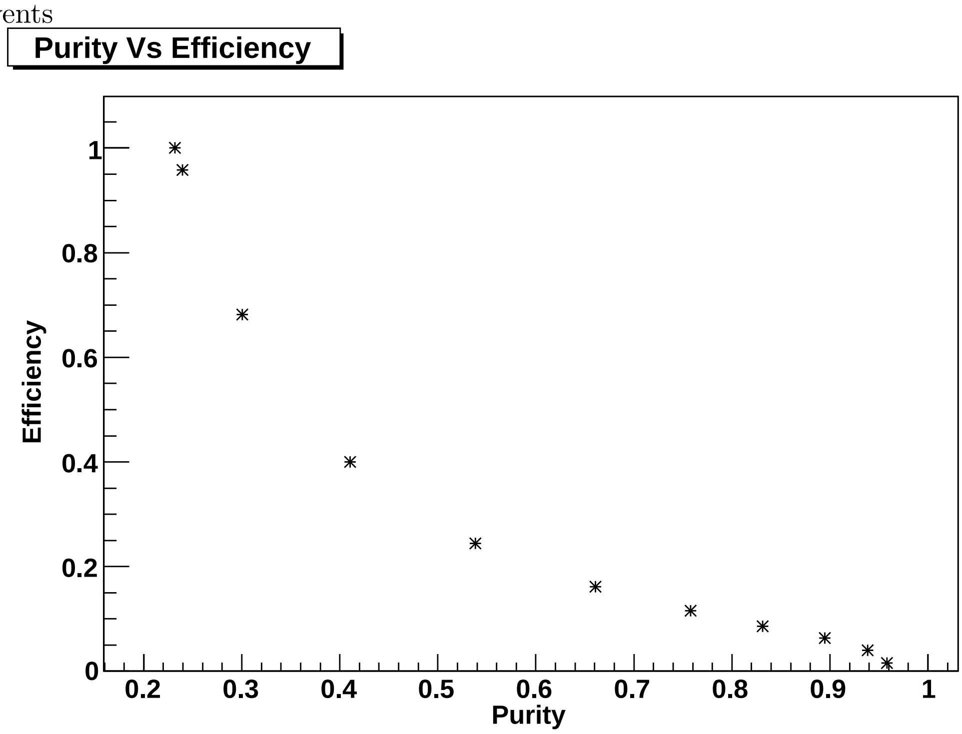

Figure 6.9: The purity vs the efficiency of type-1 event selection using the NN output as a cut.

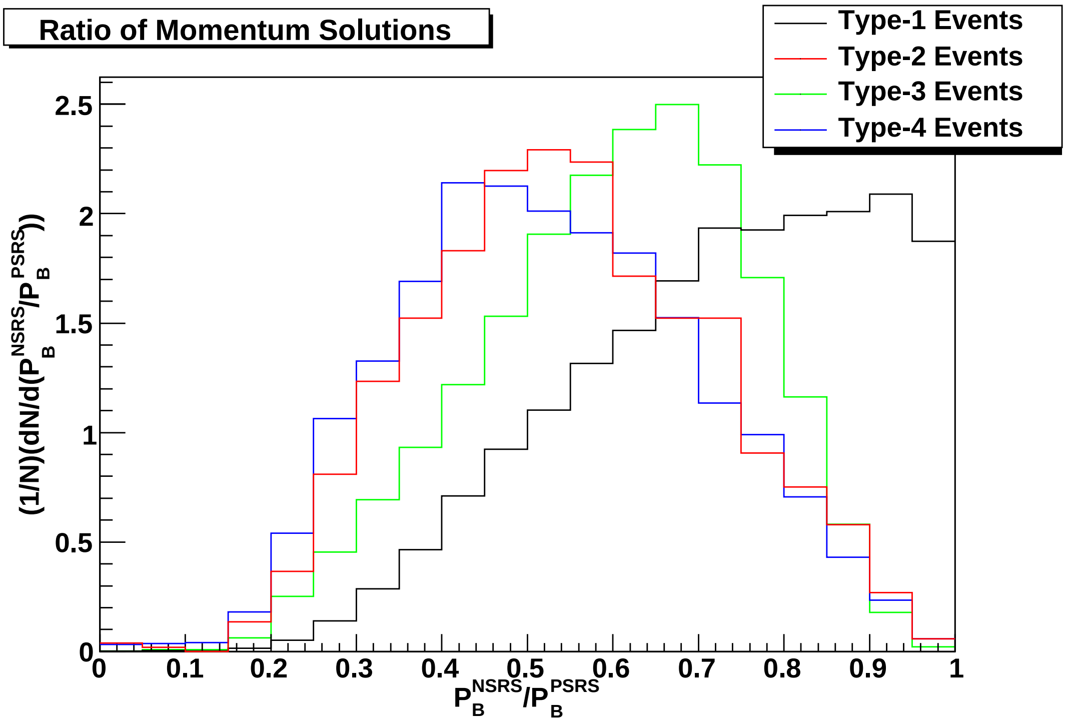

Figure 6.10: The ratio of the two B_s momentum solutions for the different types of event.

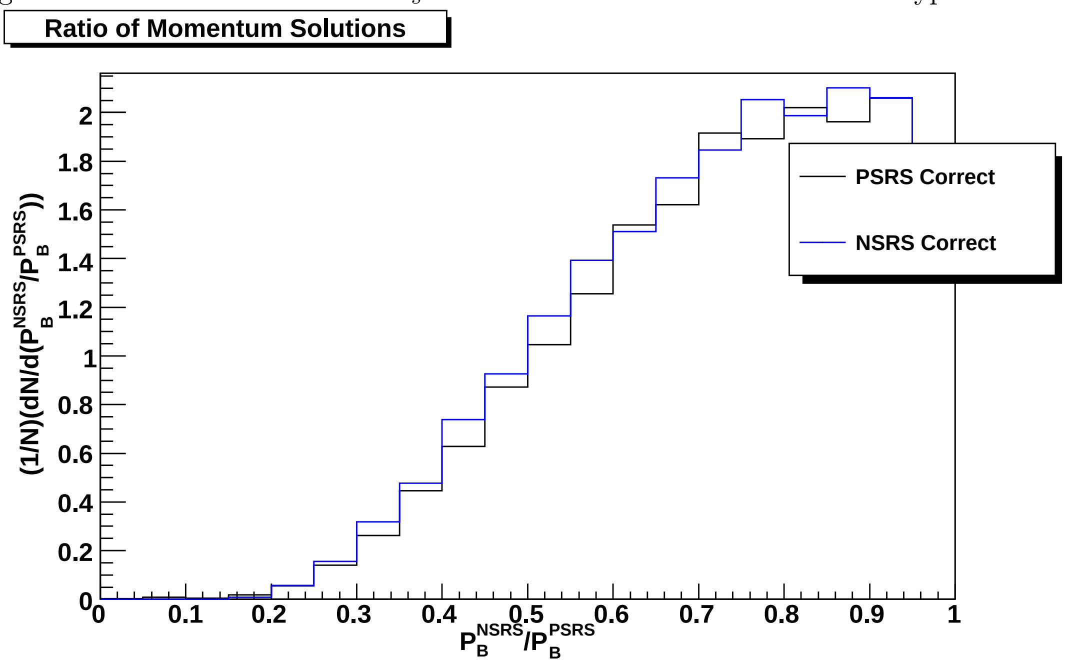

Figure 6.11: The ratio of the two B_s momentum solutions for the type-1 events, separated according to which solution is correct. The variable can be seen to offer some discriminatory power between events but not solutions.

approach has the disadvantage of losing information, but, as is shown in section 6.4.3, the former approach is made difficult by correlations between the two lifetime solutions.

In section 6.4.1 the method using one lifetime solution per event is developed for $B_s \to D_s\mu\nu$ decays. The method is extended to include $B_s \to D_s\mu\nu X$ decays in section 6.4.2. The use of two lifetime solutions per event is studied in section 6.4.3. In section 6.4.4 systematic errors are examined. Finite detector resolution is considered in section 6.5.

6.4.1 The Measurement of A_P and a_{fs} from $B_s \to D_s\mu\nu$ Decays, Using One Lifetime Per Event

6.4.1.1 Lifetime Distributions, Probability and Fitting Procedure

The time-dependent decay rate for $B \to f$ decays is related to the probability of measuring a time t, given an initial state B and a detected final state f, in the following way

$$N\epsilon_f\Gamma_{B\to f}(t) = P(t|f,B)P(f)P(B)(N+\bar{N}) \tag{6.16}$$

where $N(\bar{N})$ is the production rate of $B(\bar{B})$ mesons, ϵ_f is the detection efficiency for a final state f, $P(t|f,B)\mathrm{d}t$ is the probability of measuring a time in the interval $[t, t+\mathrm{d}t]$ given an initial state B and a measured final state f, $P(B)$ initial state is a B and $P(f)$ is the probability that a final state f is detected. Similarly

$$\bar{N}\epsilon_f\Gamma_{\bar{B}\to f}(t) = P(t|f,\bar{B})P(f)P(\bar{B})(N+\bar{N}) \tag{6.17}$$

from which it follows that

$$\frac{N\epsilon_f\Gamma_{B\to f}(t) + \bar{N}\epsilon_f\Gamma_{\bar{B}\to f}(t)}{(N+\bar{N})} = P(t|f)P(f) \tag{6.18}$$

Similarly

$$\frac{N\epsilon_{\bar{f}}\Gamma_{B\to \bar{f}}(t) + \bar{N}\epsilon_{\bar{f}}\Gamma_{\bar{B}\to \bar{f}}(t)}{(N+\bar{N})} = P(t|\bar{f})P(\bar{f}) \tag{6.19}$$

The expression for $A_{fs}(t)$ given in equation 6.1 must be modified to account for production and detection asymmetries

$$A_{fs}(t) = \frac{N\epsilon_f\Gamma_{B\to f}(t) + \bar{N}\epsilon_f\Gamma_{\bar{B}\to f}(t) - N\epsilon_{\bar{f}}\Gamma_{B\to\bar{f}}(t) - \bar{N}\epsilon_{\bar{f}}\Gamma_{\bar{B}\to\bar{f}}(t)}{N\epsilon_f\Gamma_{B\to f}(t) + \bar{N}\epsilon_f\Gamma_{\bar{B}\to f}(t) + N\epsilon_{\bar{f}}\Gamma_{B\to\bar{f}}(t) + \bar{N}\epsilon_{\bar{f}}\Gamma_{\bar{B}\to\bar{f}}(t)} \tag{6.20}$$

It follows from equations that 6.18, 6.19 and 6.20 that

$$P(f|t) = \frac{1}{2}(1 + A_{fs}(t)) \tag{6.21}$$

and

$$P(\bar{f}|t) = \frac{1}{2}(1 - A_{fs}(t)) \tag{6.22}$$

Through equations 6.21 and 6.22, $A_{fs}(t)$ is used as a the basis for a fit to extract the asymmetry parameters. The extraction of the asymmetry parameters may then be done using an unbinned log likelihood fit. The likelihood function is the product of the probabilities of observing each event in the data set:

$$L(\boldsymbol{x}) = \prod_{i=1}^{n} P(decay_i|\boldsymbol{x}) \tag{6.23}$$

where the probability, $P(decay_i|\boldsymbol{x})$, is the probability of observing the ith decay in the data set, and is given by equation 6.21 or 6.22. The vector $\boldsymbol{x}$ is the set of parameters upon which $A_{fs}(t)$ depends, their values are found by maximising $L(\boldsymbol{x})$.

The expression for $A_{fs}(t)$ defined in equation 6.20 gives a p.d.f. appropriate for a fit in which one has precisely one lifetime measurement per event. This is not the case in the present analysis, in which there are two lifetime solutions. One can create a situation in which there is only one solution per decay by simply picking one solution at random. This necessitates a slight change in $A_{fs}(t)$ but results in a fitting process essentially identical to that outlined above.

With precisely one lifetime solution per decay, $B \to f$ decays are distributed according to $\Gamma_{B\to f}$. In the present analysis there are two distributions $\Gamma^{correct}_{B\to f}$ and $\Gamma^{incorrect}_{B\to f}$, where $\Gamma^{correct}$ is the distribution of correct lifetime solutions and $\Gamma^{incorrect}$ is the distribution of incorrect lifetime solutions. Equation 6.16 is replaced with

$$N\epsilon_f\Gamma^{correct}_{B\to f}(t) = P(t_{cor} = t|f,B)P(f)P(B)(N+\bar{N}) \tag{6.24}$$

and

$$N\epsilon_f\Gamma^{incorrect}_{B\to f}(t) = P(t_{inc} = t|f,B)P(f)P(B)(N+\bar{N}) \tag{6.25}$$

where $P(t_{cor} = t|f,B)\mathrm{d}t$ is the probability that the correct lifetime solution is in the interval $[t, t+\mathrm{d}t]$, given an initial state B and a measured final state f. $P(t_{inc} = t|f,B)$ is similarly defined for the incorrect lifetime. Hence equation 6.18 is replaced with

$$\begin{aligned} P(t|f)P(f)(N+\bar{N}) &= N\epsilon_f\Gamma^{correct}_{B\to f}(t)P_{correct} + N\epsilon_f\Gamma^{incorrect}_{B\to f}(t)P_{incorrect} \\ &+ \bar{N}\epsilon_f\Gamma^{correct}_{\bar{B}\to f}(t)P_{correct} + \bar{N}\epsilon_f\Gamma^{incorrect}_{\bar{B}\to f}(t)P_{incorrect} \end{aligned} \tag{6.26}$$

where $P_{correct}$ is the probability that the correct lifetime solution is chosen. If a random selection is made, $P_{correct} = P_{incorrect} = \frac{1}{2}$. A similar equation replaces equation 6.19. If $A_{fs}(t)$ is redefined so that

$$A_{fs}(t) = \frac{\Gamma_1 + \Gamma_2 - \Gamma_3 - \Gamma_4}{\Gamma_1 + \Gamma_2 + \Gamma_3 + \Gamma_4} \tag{6.27}$$

where

$$\Gamma_1 = N\epsilon_f(\Gamma^{correct}_{B\to f} + \Gamma^{incorrect}_{B\to f})$$

$$\Gamma_2 = \bar{N}\epsilon_f(\Gamma^{correct}_{\bar{B}\to f} + \Gamma^{incorrect}_{\bar{B}\to f})$$

$$\Gamma_3 = N\bar{\epsilon_f}(\Gamma^{correct}_{B\to \bar{f}} + \Gamma^{incorrect}_{B\to \bar{f}})$$

$$\Gamma_4 = \bar{N}\bar{\epsilon_f}(\Gamma^{correct}_{\bar{B}\to \bar{f}} + \Gamma^{incorrect}_{\bar{B}\to \bar{f}})$$

it can be seen that equations 6.21 and 6.22 are still satisfied. Just as equation 6.20 provides the correct p.d.f. for fitting with precisely one lifetime per decay, so equation 6.27 provides the correct p.d.f. in situations where, for each decay, one lifetime solution is chosen at random from two.

If we use the four F functions defined in equations 6.7 to 6.10, and four more functions similarly defined for the incorrect lifetime distributions, equation 6.27 can be rewritten as

$$A_{fs}(t) = \frac{(A'_p + A'_c)(F^{correct}_{B\to f} + F^{incorrect}_{B\to f}) + (a_{fs} - \delta A)(F^{correct}_{B\to \bar{f}} + F^{incorrect}_{B\to \bar{f}})}{(2D+1)(F^{correct}_{B\to f} + F^{incorrect}_{B\to f}) + (1 - a_{fs}\delta A)(F^{correct}_{B\to \bar{f}} + F^{incorrect}_{B\to \bar{f}})} \tag{6.28}$$

where the following definitions have been used:

$$\text{Production asymmetry, } A_p = \frac{N - \bar{N}}{N + \bar{N}} \tag{6.29}$$

$$\text{Detection asymmetry, } A_c = \frac{\epsilon_f - \epsilon_{\bar{f}}}{\epsilon_f + \epsilon_{\bar{f}}} \tag{6.30}$$

$$A'_p = \frac{A_p}{1 - A_p A_c} \tag{6.31}$$

$$A'_c = \frac{A_c}{1 - A_p A_c} \tag{6.32}$$

$$D = \frac{A_p A_c}{1 - A_p A_c} \tag{6.33}$$

$$\delta A = A'_p - A'_c \tag{6.34}$$

It can be seen from equation 6.28 that any two of a_{fs}, A_p and A_c can be measured if the third is known. In the following discussions on measuring a_{fs} and A_p, it will be assumed that A_c is known. This can be justified because it can be measured independently to a very high precision [69][5].

[5] Measurement of detection asymmetry can be made by studying overconstrained, partially reconstructed channels. An example is $D^{*-} \to \bar{D}^0\pi^-$ where $\bar{D}^0 \to \pi^+\pi^-K^0_s$ and $K^0_s \to \pi^+\pi^-$. The momentum of the pions coming from the kaon can be determined even if one is not reconstructed. This allows a measurement of the reconstruction efficiency as a function of momentum.

In the work which follows, the fitting process outlined above was carried out using MINUIT [65].

6.4.1.2 Monte Carlo Data

The forms of the distributions of correct lifetime solutions are known from theory. The forms of the distributions of incorrect lifetime solutions are not known from theory, and were determined from Monte Carlo data. This was done with a toy Monte Carlo written specially for the purposes of this study. It was designed to reproduce the data produced from the LHCb generation software as closely as possible. The Monte Carlo works as follows:

- Choose a momentum. The magnitude of the B_s momentum is randomly sampled from an MC truth distribution that was produced by DaVinci. The distribution is shown in figure 6.12.

- Choose a lifetime. To choose the lifetime, the initial and final state must be chosen. The ratio of B and $\bar{B}$ initial states, and the ratio of f and $\bar{f}$ final states are governed by the production, detection and CP asymmetry. These are user-controlled parameters within the Monte Carlo. Once the initial and final states have been chosen, the lifetime may be chosen. It is randomly sampled from the theoretical distributions given by equations 6.3 to 6.6. At this stage the true decay length can be calculated. The values of $\Gamma, \Delta\Gamma$ and Δm used are the same as those in the LHCb event generation software. These are shown in table 6.5.

- Decay the B_s. The ROOT class TGenPhaseSpace [71] is used to produce the decay. It takes as its input the 4-momentum of the mother particle and the masses of the daughters. It outputs the momenta of the three daughters. As the B_s 4-momentum is needed as input for TGenPhaseSpace, a direction for the B_s must be chosen. The direction is unimportant, and may be chosen arbitrarily so long as the x, y and z components are correctly normalised [6].

[6] The direction is unimportant because no detector effects are included in the simulation. The only

Parameter	Value
Γ	$0.6852\,\mathrm{ps}^{-1}$
$\Delta\Gamma$	$0.06852\mathrm{ps}^{-1}$
Δm	$20\,\mathrm{ps}^{-1}$

Table 6.5: The values of $\Gamma, \Delta\Gamma$ and Δm which are used in Gauss, the LHCb generation software. The same settings were used in the toy Monte Carlo used for the work described in this chapter.

- Calculate the lifetimes. With the B_s direction and daughter momenta known, the two possible neutrino momenta may be calculated from equation 6.14, and hence the B_s lifetimes may be calculated. Of the two B_s lifetimes, the correct one is determined by comparison to the lifetime chosen earlier.

Figures 6.13 and 6.14 show distributions of lifetime solutions produced with this toy Monte Carlo for $B \to f$ decays, for the correct and incorrect solutions respectively. As one would expect, the distribution of incorrect lifetimes lacks most of the structure of the true lifetime distribution. There is some residual structure at low lifetimes. However, these events will be mostly be discarded by the trigger. Triggering in the toy Monte Carlo is modeled with an acceptance function, the form coming from an earlier physics study [18]

$$\eta(t) = \frac{(\beta t)^3}{1 + (\beta t)^3} \tag{6.35}$$

where t is measured in ps and $\beta = 1.29\,\mathrm{ps}^{-1}$. When the acceptance function cut is applied in the toy Monte Carlo, it is applied to the true lifetime. The incorrect lifetime passes the cut if the corresponding correct lifetime does, regardless of the value of the incorrect time. Figures 6.15 and 6.16 show the correct and incorrect lifetime distributions for $B \to f$ decays with acceptance function applied. By applying the acceptance function cut the incorrect lifetime distribution loses all structure.

In order to extract A_p and a_{fs}, it is necessary to have a function that models the distributions of incorrect lifetimes, which were produced by the toy Monte Carlo. To find the form of the function, two effects must be taken into account: the smearing of the

information needed to calculate the B_s momentum are the components of the $D_s\mu$ momentum perpendicular and parallel to the B_s momentum.

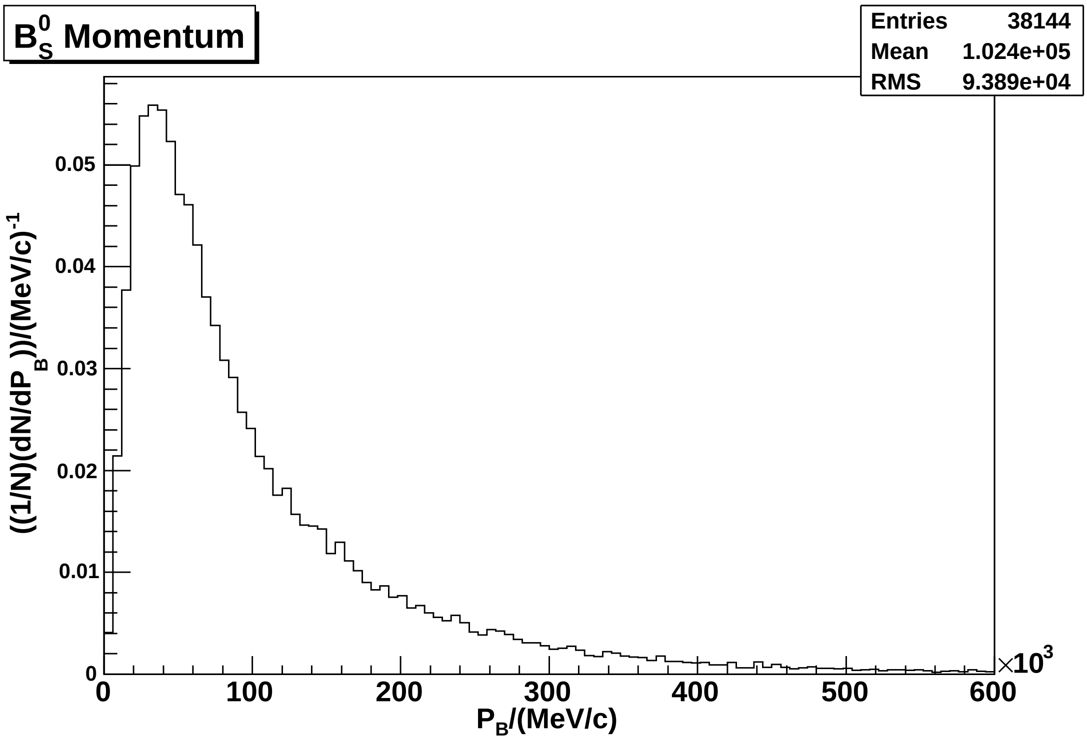

Figure 6.12: The momentum distribution for B_s^0 mesons.

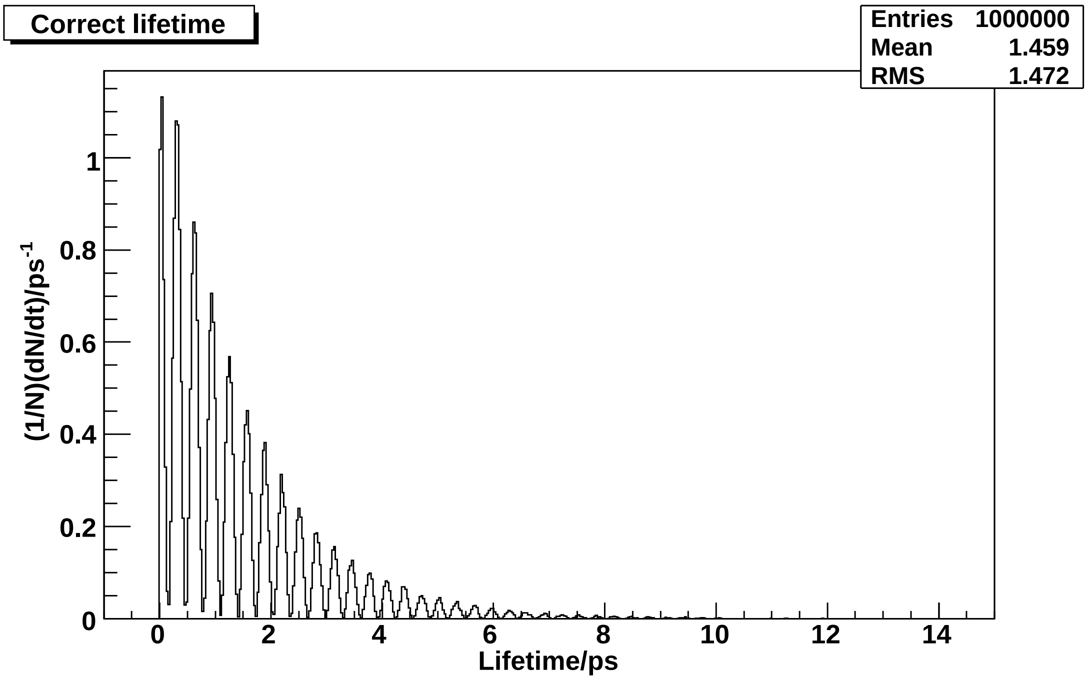

Figure 6.13: The lifetime distribution for $B \to f$ decays.

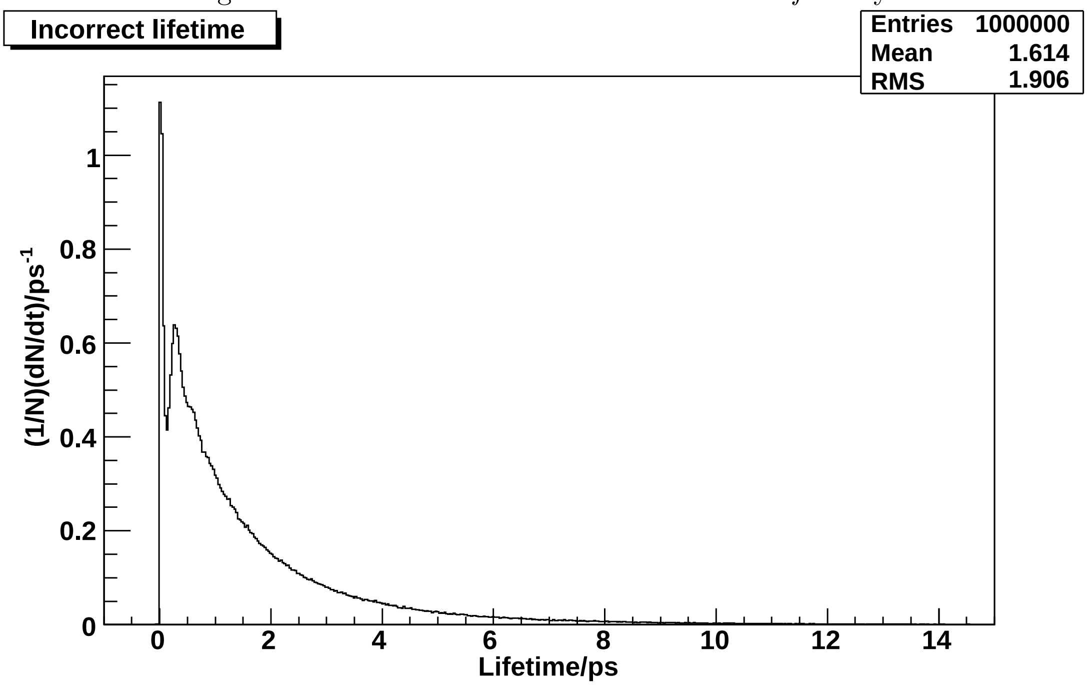

Figure 6.14: The distribution of incorrect lifetime solutions for $B \to f$ decays.

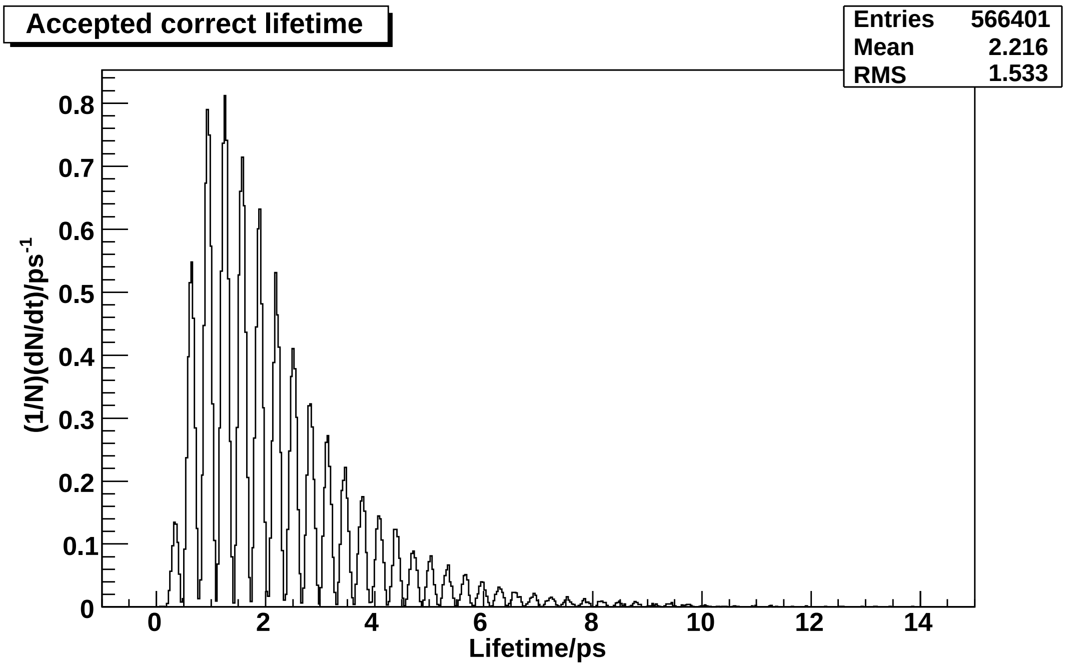

Figure 6.15: The lifetime distribution for $B \to f$ decays which pass the acceptance function cut.

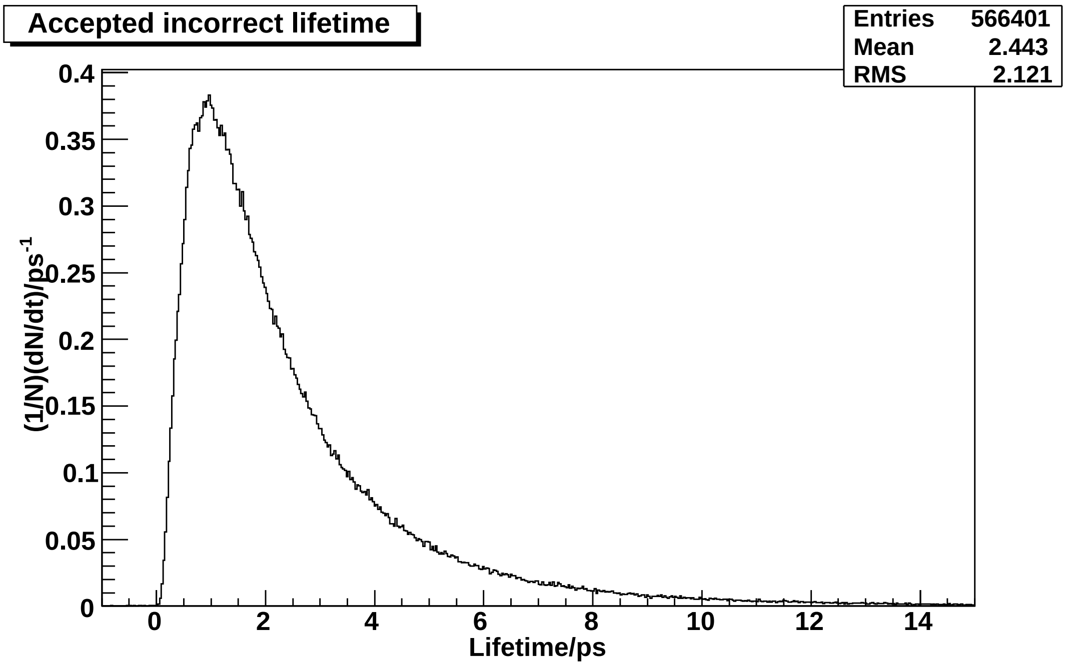

Figure 6.16: The incorrect lifetime solution distribution for $B \to f$ decays in which the correct lifetime passes the acceptance function cut.

distribution of correct lifetimes due to the incorrect the lifetime solutions being chosen, and the loss of events due to the acceptance function. Smearing can be modeled by convoluting the true lifetimes with a gaussian of width σ. The resulting form, which is derived in appendix A, is

$$F = e^{-\Gamma t} e^{\frac{1}{2}\Gamma^2\sigma^2} \left[e^{\frac{1}{8}\sigma^2\Delta\Gamma^2} \cosh\left(\frac{1}{2}\Delta\Gamma(t-\sigma^2\Gamma)\right) \pm e^{-\frac{1}{2}\Delta m^2\sigma^2} \cos\left(\Delta m(t-\sigma^2\Gamma)\right)\right] \tag{6.36}$$

It is apparent from the distribution of incorrect lifetimes, figure 6.18, that the lifetime resolution is better at low lifetimes than at high ones. To incorporate this effect, σ was given the following time dependence:

$$\sigma(t) = \begin{cases} at+b & \text{if } t < 25 \\ 25a+b & \text{it } t \geq 25 \end{cases}$$

where t is measured in picoseconds. The maximum value of $\sigma(t)$ was introduced to ensure that F is always well behaved.

To included the effect of the acceptance function cut, a function of the following form was used to model the distribution of incorrect lifetimes:

$$\begin{aligned} F^{incorrect} \quad = \quad & N\frac{(\beta t)^\alpha}{1+(\beta t)^\alpha} e^{-\Gamma t} e^{\frac{1}{2}\Gamma^2\sigma(t)^2} \left[e^{\frac{1}{8}\sigma(t)^2\Delta\Gamma^2} \cosh\left(\frac{1}{2}\Delta\Gamma(t-\sigma(t)^2\Gamma)\right)\right. \\ & \left.\pm e^{-\frac{1}{2}\Delta m^2\sigma(t)^2} \cos\left(\Delta m(t-\sigma(t)^2\Gamma)\right)\right] \end{aligned} \tag{6.37}$$

The parameters N, α, β, a and b are free parameters which were determined by a fitting the function to distributions produced by the toy Monte Carlo. The fitting process was carried out using ROOT. α, β, a and b control the shape of the distribution, whilst N is just a normalisation constant needed to ensure that

$$\int_0^\infty \eta(t) F^{correct} \mathrm{d}t = \int_0^\infty F^{incorrect} \mathrm{d}t \tag{6.38}$$

Although equation 6.38 appears imbalanced, in that the acceptance function appears in the left hand side and not the right, this is not the case. $F^{incorrect}$, as defined by equation

Parameter	Value
α	2.27
β	$1.85\,\text{ps}^{-1}$
a	0.260
b	$0.080\,\text{ps}$
N	0.752

Table 6.6: The values of α, β, a, b and N for which equation 6.37 best fits data.

6.37, is designed to model the incorrect lifetime distributions after the acceptance cut has been made, as in figure 6.16, and a factor like the acceptance function is included in equation 6.37. In the expression for $A_{fs}(t)$ defined by equation 6.27, there is no explicit mention of the acceptance function. The correct lifetime distributions must be multiplied by the acceptance function, if the incorrect lifetimes distributions are to be defined in such as way as to include the effect of the acceptance function.

The values of α, β, a, b and N found in the ROOT fit are given in table 6.6. Figures 6.17 and 6.18 show the $B \to f$ and $B \to \bar{f}$ lifetime distributions fitted with the resulting function.

Figures 6.19 and 6.20 show A_{fs}, as defined in equation 6.28 and using equation 6.37 to model the distributions of incorrect lifetimes, with zero and non-zero values of A_p. $A_{fs}(t)$ oscillates about $a_{fs}/2$ in each case, but the size of the oscillations is strongly dependent on A_p. For this reason, good lifetime resolution is more important for high precision on A_p than for high precision on a_{fs}.

The figures also show a curious feature. The size of the oscillations of $A_{fs}(t)$ decrease as $t \to 0$ but then suddenly increase at $t = 0$. This feature is most easily understood if equation 6.27 is rewritten in the form

$$A_{fs}(t) = A_{fs}^{correct}(t) f_{correct}(t) + A_{fs}^{incorrect}(t) f_{incorrect}(t) \tag{6.39}$$

where $A_{fs}^{correct}(t)$ is the expression for $A_{fs}(t)$ when only correct lifetimes are considered. It is given by equation 6.20, and shown in figure 6.21 with $a_{fs} = 0.05$, $A_p = 0.01$ and $A_c = 0$. $A_{fs}^{incorrect}(t)$ is an equivalent expression using only incorrect lifetimes,

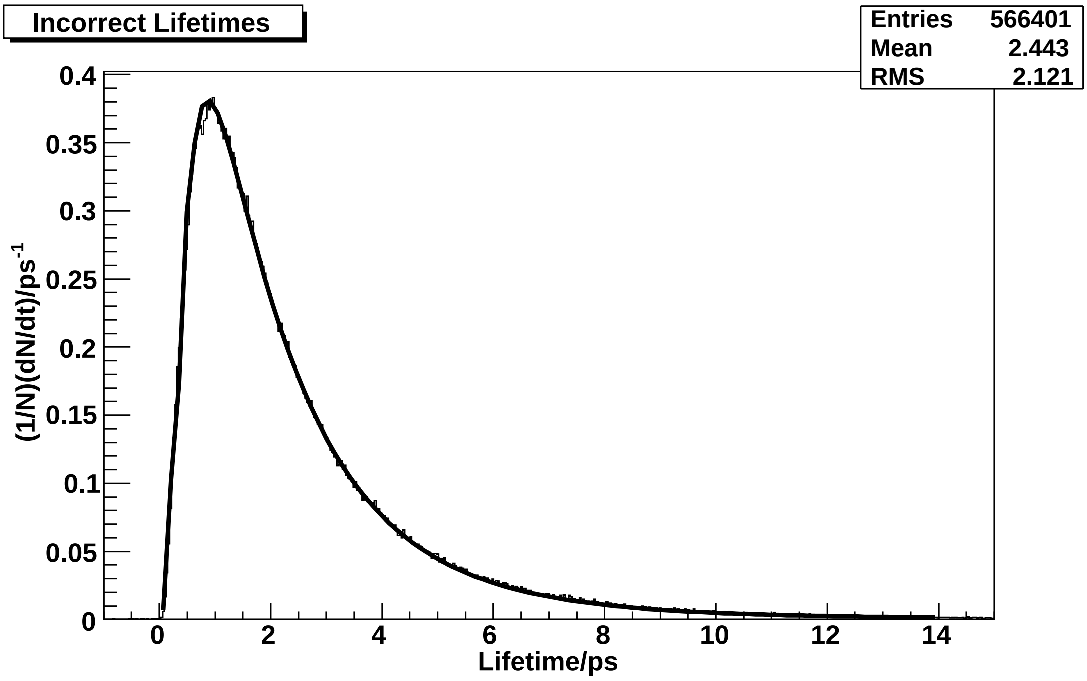

Figure 6.17: The incorrect lifetime solution distribution for $B \to f$ decays fitted with a function of the form in equation 6.37.

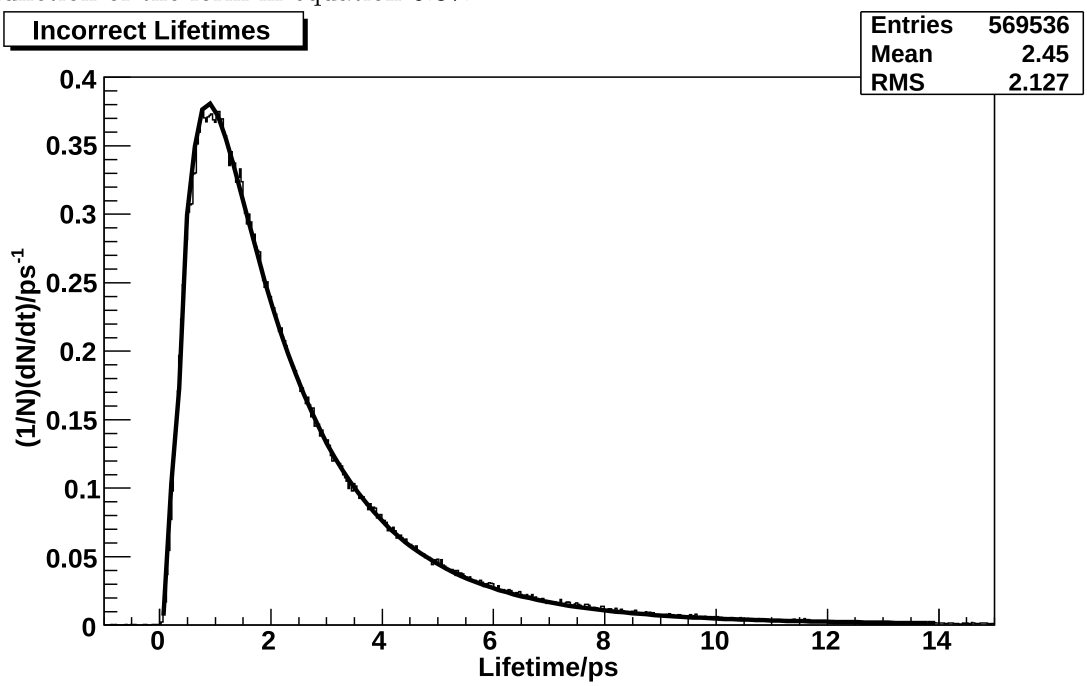

Figure 6.18: The incorrect lifetime solution distribution for $B \to \bar{f}$ decays fitted with a function of the form in equation 6.37.

it is shown in figure 6.22 with $a_{fs} = 0.05$, $A_p = 0.01$ and $A_c = 0$. $f_{correct}(t)$ and $f_{incorrect}(t)$ are simply factors needed to give the correct form for $A_{fs}(t)$. It can be seen from a comparison of equations 6.20, 6.27 and 6.39 that $f_{correct}(t) + f_{incorrect}(t) \equiv 1$. The difference between the acceptance function and the effective acceptance function for the distribution of incorrect lifetime solutions results in $f_{correct}(t = 0) = 0$ and $f_{incorrect}(t = 0) = 1$, see figure 6.23. Because the distribution of incorrect lifetime solutions do not oscillate, $A_{fs}^{incorrect}(t)$ does not oscillate, except at very low t, where small differences between the distributions are more pronounced, see figure 6.22. This is the source of the strange structure at $t = 0$ in figures 6.19 and 6.20.

6.4.1.3 Fit Results

The fitting procedure described in section 6.4.1.1 was used to extract a_{fs} and A_p from toy Monte Carlo data sets. Table 6.7 shows the parameter values which were used in generating the data. The expected number of reconstructed semi-muonic events, in a 2 fb^{-1} data set, is $(2.6 \pm 0.9) \times 10^6$ [69]. For convenience, the fitting process was tested with only 2.5×10^5 events[7]. However, the resolution of the fit parameters was found to scale with the number of events, as $1/\sqrt{N}$. 4500 toy experiments, each with 2.5×10^5 events, were performed. Figures 6.24 and 6.25 show the pull distributions for a_{fs} and A_p respectively. A pull distribution is a plot of

$$\frac{x - x_{input}}{\sigma}$$

where x is the measured value of the fit parameter and σ is the parameter error as calculated in the fitting procedure. If the fitting procedure works correctly then the distribution will be a gaussian centred on zero and with width one. Displacement from zero indicates bias in the parameter estimation and different widths indicate inaccuracy

[7] In generating the 2.5×10^5 events, certain cuts were applied. Events in which there were no real solutions to equation 6.14 were rejected. Events in which one of the two B lifetimes was negative were also rejected, because the p.d.f. used in the fit was constructed to reflect the fact the correct solution is unknown. There is no reason to completely exclude such events from the measurement of a_{fs} and A_p, but their contribution must be considered separately.

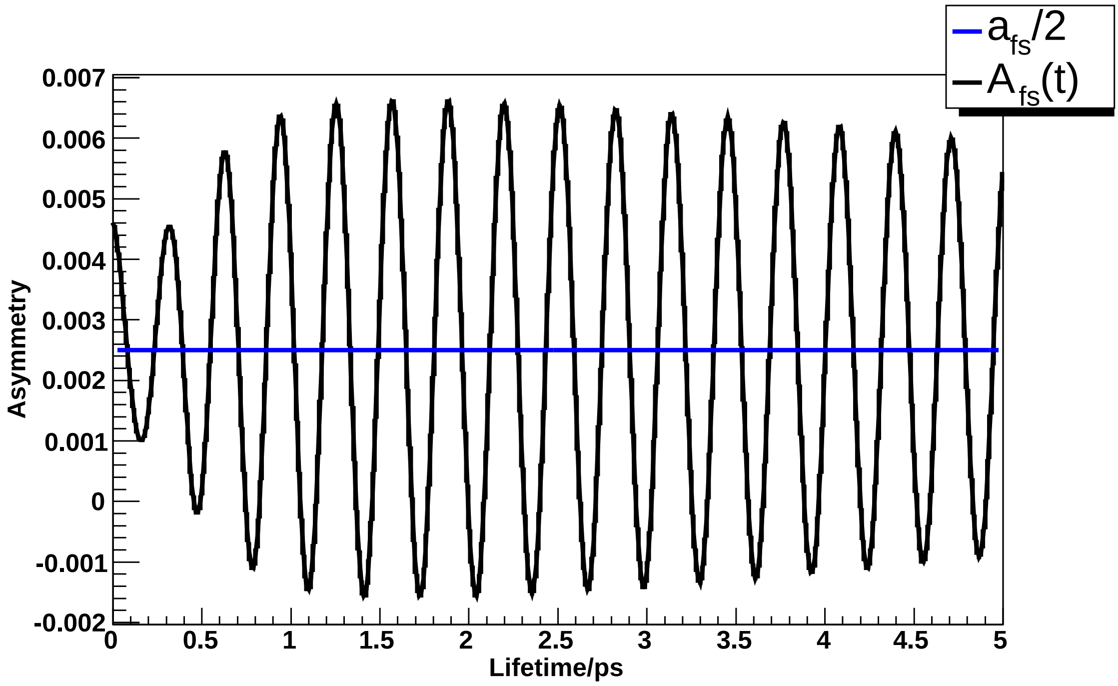

Figure 6.19: $A_{fs}(t)$ with CP asymmetry, $a_{fs} = 0.005$, and production asymmetry, $A_p = 0.01$.

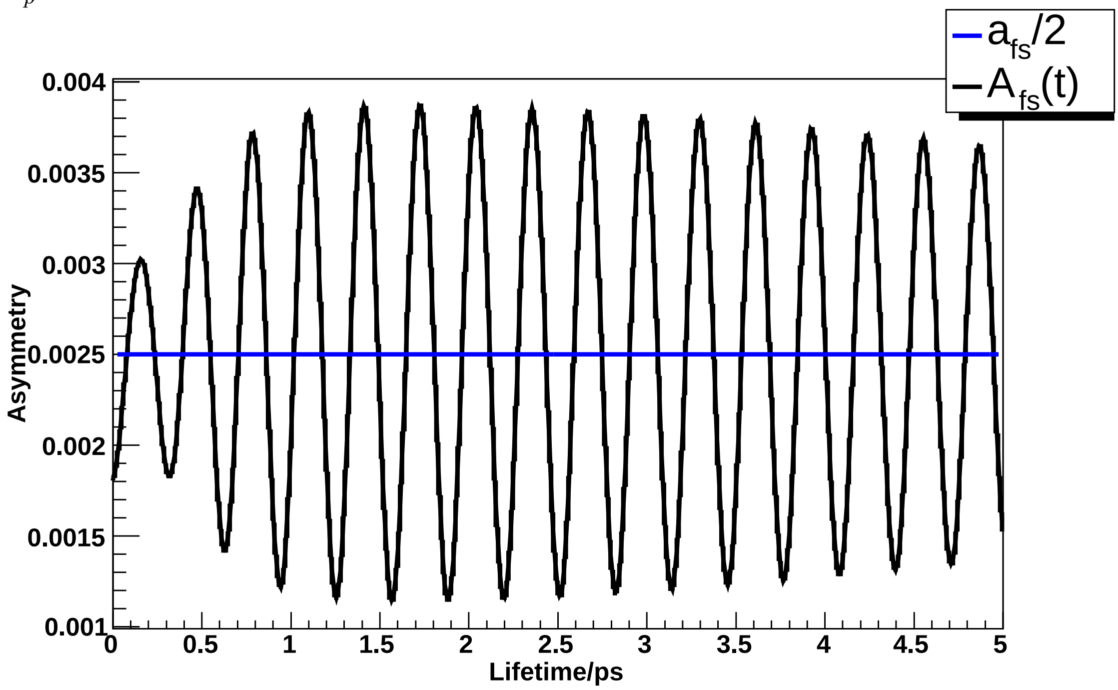

Figure 6.20: $A_{fs}(t)$ with CP asymmetry, $a_{fs} = 0.005$, and production asymmetry, $A_p = 0$.

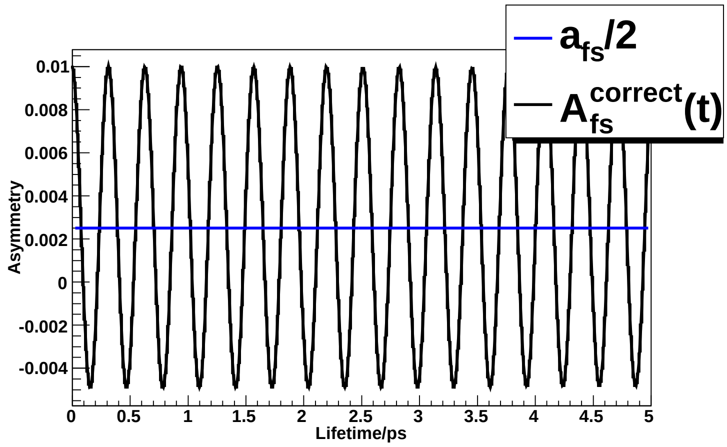

Figure 6.21: $A_{fs}^{correct}(t)$. The plot is for $a_{fs} = 0.05$, $A_p = 0.01$ and $A_c = 0$.

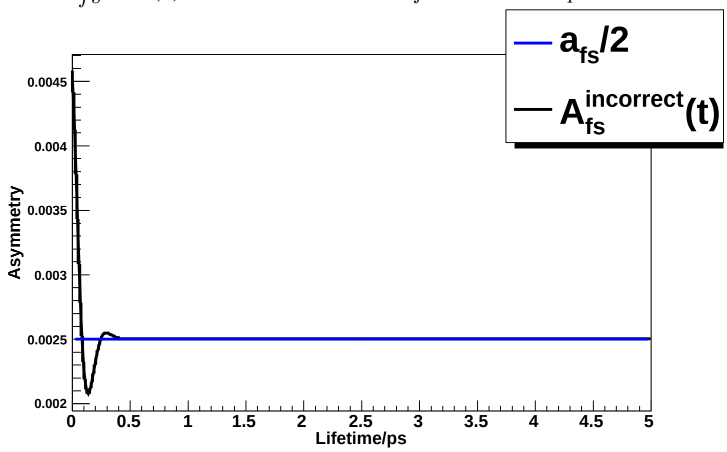

Figure 6.22: $A_{fs}^{incorrect}(t)$ which comes from replacing the distribution of correct lifetime solutions in equation 6.20 with the distribution of incorrect lifetimes. The structure at low t is the source of the peculiar oscillation size at $t = 0$ in figures 6.19 and 6.20. The plot is for $a_{fs} = 0.05$, $A_p = 0.01$ and $A_c = 0$.

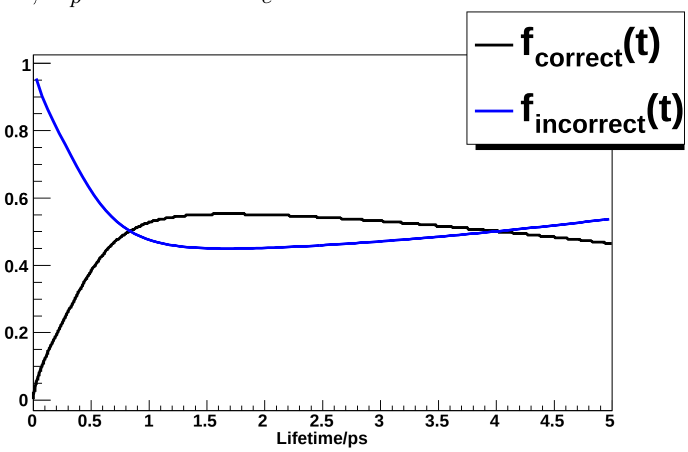

Figure 6.23: The factors multiplying $A_{fs}^{correct}(t)$ and $A_{fs}^{incorrect}(t)$ in equation 6.39.

in the error estimation. The distributions in figures 6.24 and 6.25 show no sign of bias or inaccuracy in the error estimate.

Table 6.8 lists the precision of the measurements of a_{fs} and A_p. To indicate the potential power of the neutrino reconstruction method it is compared to the k-factor method. In the latter method there is only one lifetime per decay to consider, and the expression for $A_{fs}(t)$ given in equation 6.20 is used. The precision of a_{fs} and A_p measurements were determined using a toy Monte Carlo developed for the studies presented in [63]. A lifetime resolution of 0.120 ps [62], and a data set of 2.5×10^5 events were used. It can be seen from table 6.8 that the use neutrino reconstruction method has benefits compared to the k-factor method, despite the lifetime ambiguity, when it comes to measuring A_p. There is no difference on the precision on a_{fs} between the two methods. This is consistent with the fact that good lifetime resolution is more important for a precise measurement of A_p than for a precise measurement of a_{fs}. The comparison between the two methods is, however, unfair because not all relevant decay modes are included in the toy Monte Carlo used to asses the neutrino reconstruction method. Detector effects have also been ignored, the neutrino reconstruction method therefore has perfect resolution. Further decay modes are considered in section 6.4.2 and detector resolution is considered in section 6.5. Another respect in which the comparison is not fair, is in the sizes of the event samples used. The k-factor method cannot make use of all semi-muonic events when making a measurement of A_p, because those with low $m_{D_s\mu}$ give poor lifetime resolution. The lifetime resolution of 0.120 ps is for events with $m_{D_s\mu} > 4.5\,\mathrm{GeVc}^{-2}$ [62], which corresponds to roughly 18.5 % of the total semi-muonic data set. The k-factor method can use all the semi-muonic data for a measurement of a_{fs}, because it does not require such good lifetime resolution. The comparison of the two methods in section 6.5 takes this into consideration.

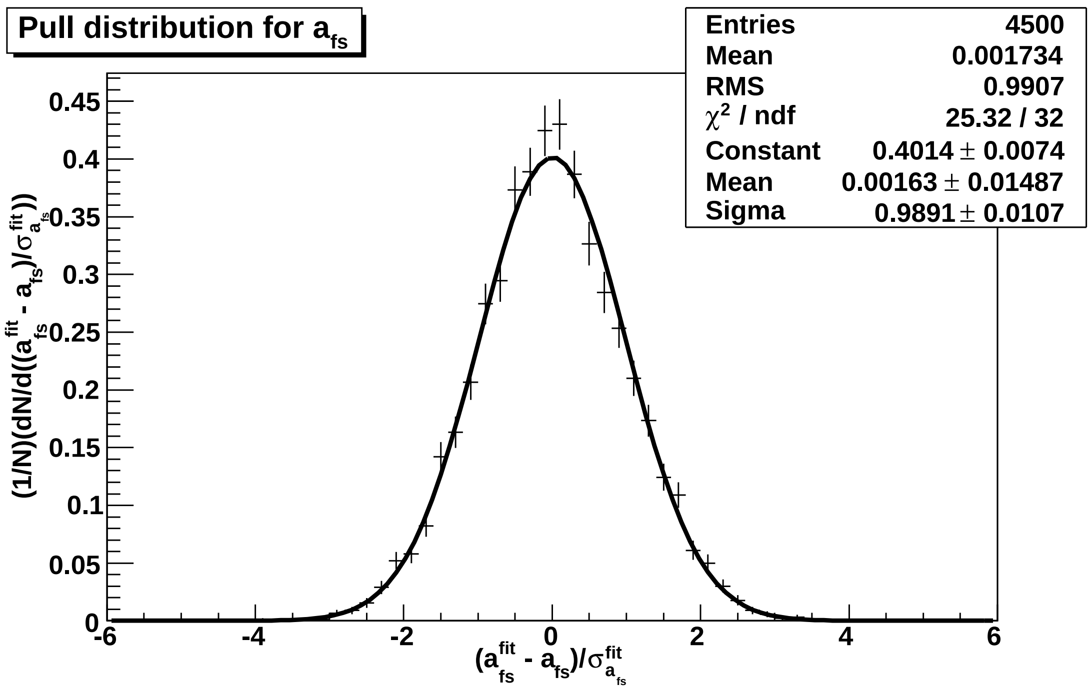

Figure 6.24: The pull distribution for a_{fs}. The fitting was done with a p.d.f. based on equation 6.28 and used only one lifetime solution per event.

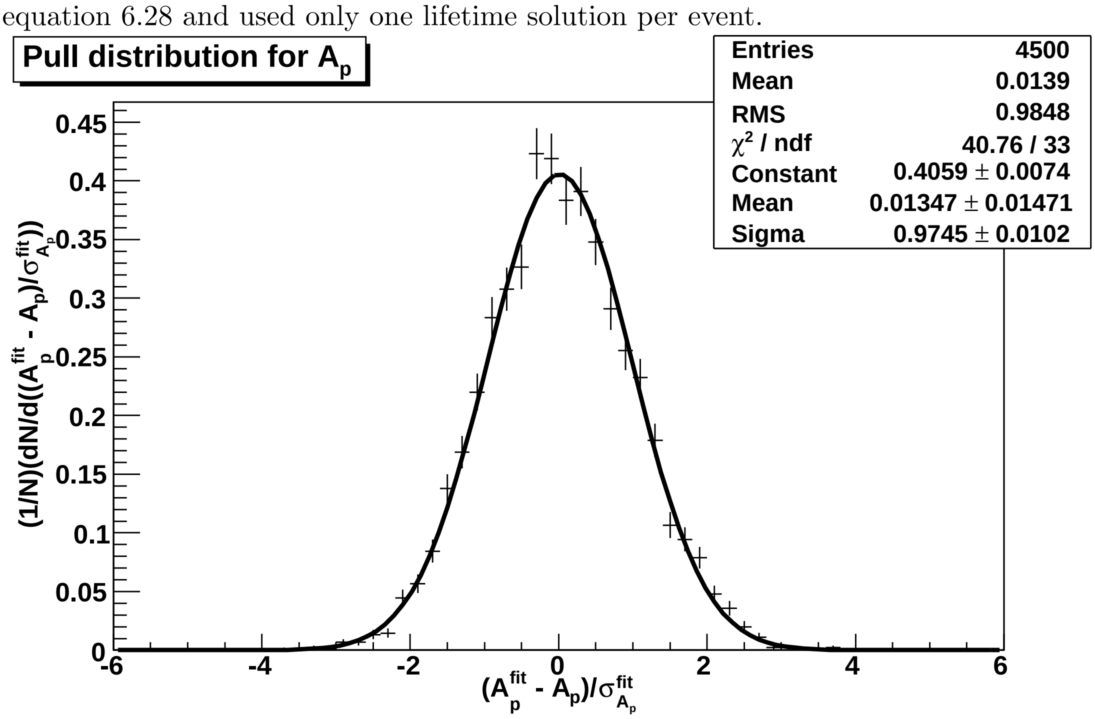

Figure 6.25: The pull distribution for A_p. The fitting was done with a p.d.f. based on equation 6.28 and used only one lifetime solution per event.

Parameter	Value
a_{fs}	5.00×10^{-3}
A_p	1.00×10^{-2}
A_c	0.00

Table 6.7: The input values for asymmetry parameters in the fitting procedure. These values were used both for the data generation and as the starting values in the fit. The value of $a_{fs} = 5.00 \times 10^{-3}$ is characteristic of the larger values of a_{fs} predicted by non Standard Model physics [10]. The production asymmetry has been estimated to be of order 1% [69], so a value of 0.01 is used. For the purposes of the present study detection asymmetry is ignored, and so set to zero, because it can be well measured in other measurements [69].

Method	N_{Events}	$a_{fs}/10^{-3}$ from fit	$A_p/10^{-2}$ from fit
ν Reconstruction	2.50×10^5	5.01 ± 4.01	1.01 ± 0.60
k-factor method	2.50×10^5	5.00 ± 4.00	1.00 ± 5.06

Table 6.8: A comparison of a_{fs} and A_p fit results for the k-factor method and the neutrino reconstruction method. The input values for the generation process are given in table 6.7. A lifetime resolution of $\sigma_t = 0.120\,\mathrm{ps}$ was used for the k-factor method fit. The fit value for the neutrino reconstruction method is the mean fit value from 4500 events. The neutrino reconstruction method gives greater precision on A_p than the k-factor method.

6.4.2 The Measurement of A_P and a_{fs} Using $B_s \to D_s\mu\nu$ and $B_s \to D_s\mu\nu X$ with one Lifetime per Event

In this section the work of section 6.4.1 is extended to include decays of the form $B_s \to D_s\mu\nu X$, where the X is any neutral particle. An example of such a decay, and the one with the highest branching fraction, is $B_s \to D_s^*\mu\nu \to D_s\mu\nu\gamma$. For $B_s \to D_s\mu\nu X$ decays both solutions to equation 6.14 are incorrect. There are 13 $B_s \to D_s\mu\nu X$ decays implemented in the LHCb software. Tables 6.9 and 6.10 list them, and their corresponding branching ratio used in Gauss.

For these decays to be incorporated into a fit, the forms of the distributions of lifetime solutions coming from the two solutions of equation 6.14 must be determined. To do this, a modified version of the toy Monte Carlo described in section 6.4.1.2 was used to simulate the more complicated decay chains involved.

Figures 6.26 to 6.29 show the distributions of lifetime solutions coming from three of the different decay modes (the others are omitted for the sake of clarity). In figures

Decay Chain	Branching ratio
$B_s \to D_s\mu\nu$	0.021
$B_s \to D_s^*\mu\nu$	0.049
$B_s \to D'_{s1}\mu\nu$	0.004
$B_s \to D_{s0}^*\mu\nu$	0.004
$B_s \to D_s\tau\nu$	0.00138
$B_s \to D_s^*\tau\nu$	0.00277
$B_s \to D'_{s1}\tau\nu$	0.00031
$B_s \to D_{s0}^*\tau\nu$	0.00031

Table 6.9: The branching ratios of various semi-leptonic B decays implemented in Gauss. Within Gauss, the τs in the decays with τs listed above are forced to decay to a μ and a neutrino. The branching ratios for the various excited D_ss are listed in table 6.10

Decay Chain	Branching ratio
$D_s^* \to D_s\gamma$	0.942
$D_s^* \to D_s\pi$	0.058
$D'_{s1} \to D_s^*\pi$	0.79
$D'_{s1} \to D_s^*\gamma$	0.21
$D_{s0}^* \to D_s^*\pi$	1

Table 6.10: The branching ratios of various excited D_ss used in Gauss.

6.26 and 6.27 the distributions have the same normalisation, so that a comparison of the structure is easier. In figures 6.28 and 6.29 the distributions are normalised according to their branching ratio. The lifetimes have been split into two groups, designated better and worse, depending on which was closer to the true lifetime. There are differences between the distributions for the different decay modes, but the distributions do have certain characteristics in common. For low t some structure remains, but this is absent for larger values of t.

The existence of these additional decay modes necessitates modifying equation 6.28. Two further lifetime distributions need to be added, to account for these decay modes. In principle a correct model for these lifetime distributions should take into account all of the decay chains, something made difficult by uncertainty in the relative branching fractions. As a simpler first step, only $B_s \to D_s\mu\nu$ and $B_s \to D_s^*\mu\nu \to D_s\mu\nu\gamma$ decays were considered. This is a good first approximation to the full situation, because $B_s \to D_s^*\mu\nu \to D_s\mu\nu\gamma$ is the dominant $B_s \to D_s\mu\nu X$ decay, and because the differences

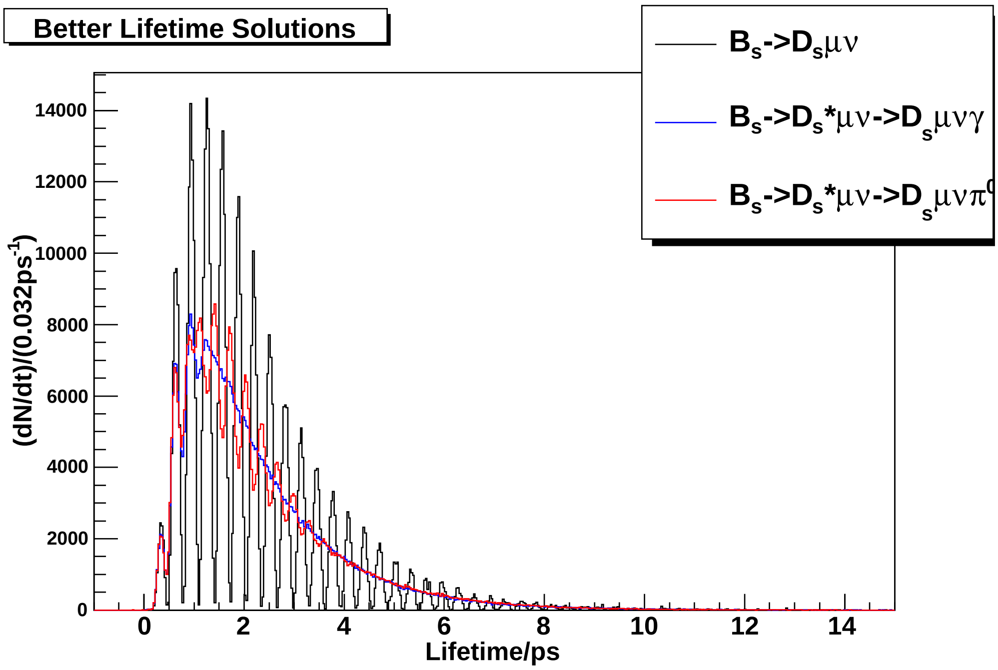

Figure 6.26: Lifetime distributions for three of the 14 semi-muonic decays implemented in Gauss. The lifetimes come from the better solutions. In the case of $B_s \to D_s \mu \nu$ these solutions have been previously called the correct, to distinguish them from the incorrect solutions. No correct solutions exist in the case of the other decay modes. There are one million events in each distribution.

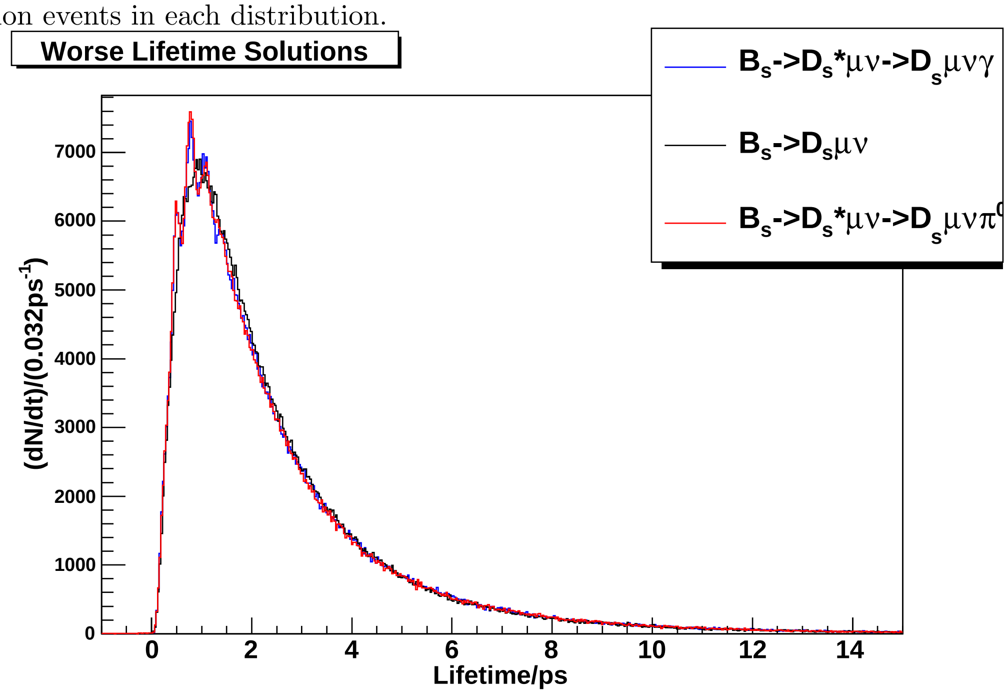

Figure 6.27: Lifetime distributions for three of the 14 semi-muonic decays implemented in Gauss. The lifetimes come from the worse solutions. There are one million events in each distribution.

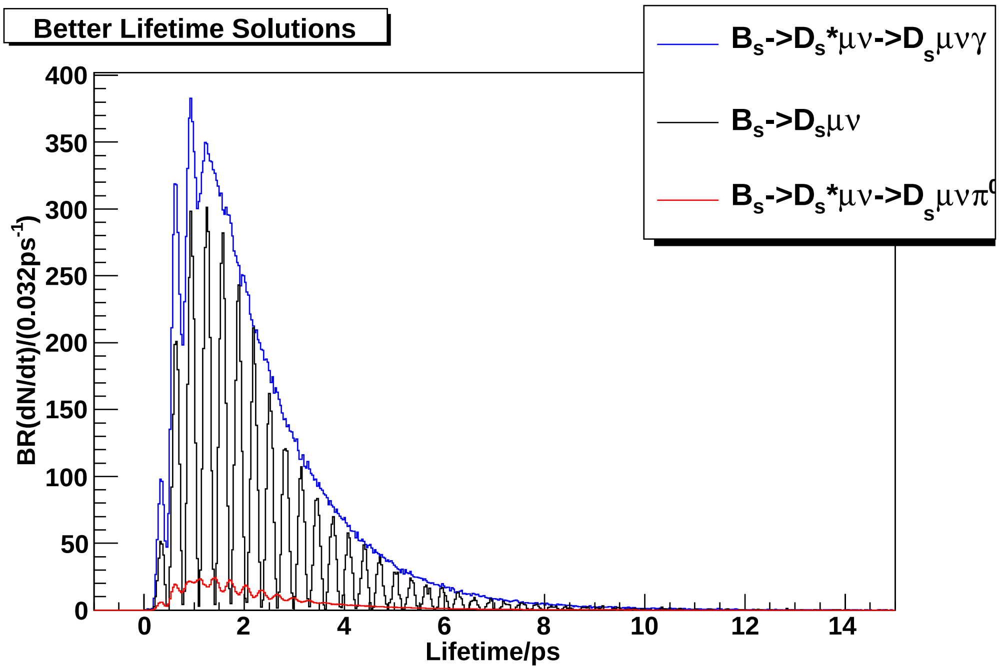

Figure 6.28: Lifetime distributions for three of the 14 semi-muonic decays implemented in Gauss, scaled by their branching ratio. The lifetimes come from the better solutions. There are one million events in each distribution.

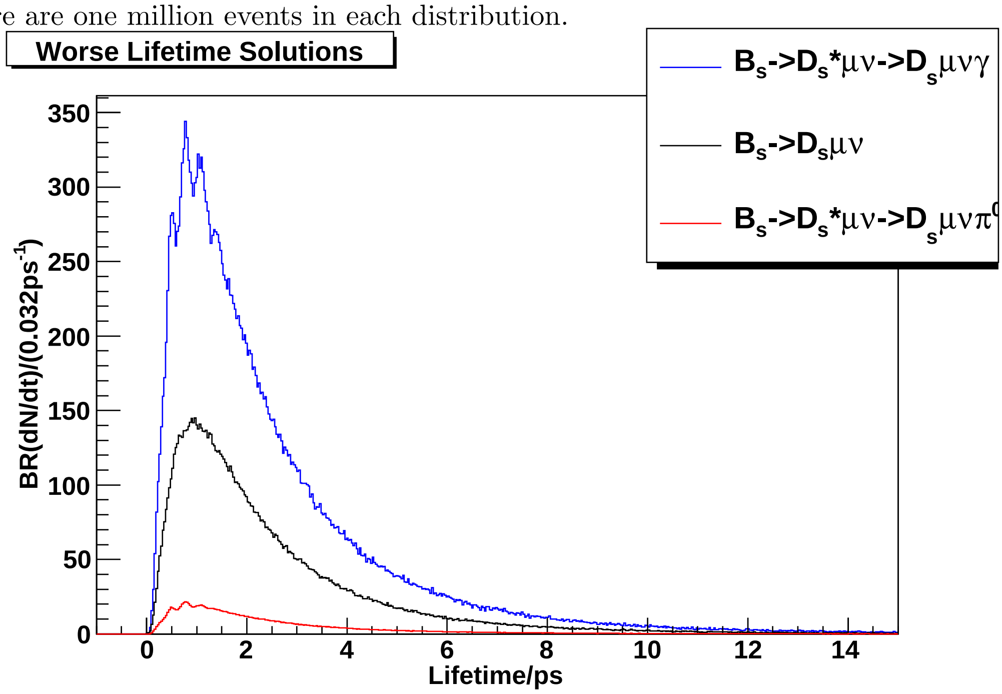

Figure 6.29: Lifetime distributions for three of the 14 semi-muonic decays implemented in Gauss, scaled by their branching ratio. The lifetimes come from the worse solutions. There are one million events in each distribution.

between the different $B_s \to D_s\mu\nu X$ lifetime distributions are small.

6.4.2.1 Probability Distribution

The expression for $A_{fs}(t)$ has to be changed to accommodate the $B_s \to D_s\mu\nu\gamma$ decays. Following an argument similar to the one set out in section 6.4.1.1, leads to equation 6.40. Equation 6.40 is comparable to equation 6.28, but instead of there being two terms for each combination of initial and final state there are four.

$$A_{fs}(t) = \frac{(A'_P + A'_c)\sum F_{B\to f} + (a_{fs} - \delta A)\sum F_{B\to\bar{f}}}{(2D+1)\sum F_{B\to f} + (1 - a_{fs}\delta A)\sum F_{B\to\bar{f}}} \tag{6.40}$$

where $\sum F_{B\to f}$ and $\sum F_{B\to\bar{f}}$ are summations of the four different lifetime distributions for $B \to f$ and $B \to \bar{f}$ decays respectively. The sum is given by

$$\sum F_{B\to f} = F^{correct}_{B\to f} + F^{incorrect}_{B\to f} + cF^{better}_{B\to f} + cF^{worse}_{B\to f}$$

The factor c is to ensure that the different decay modes contribute in the correct proportion. There are roughly three times as many $B_s \to D_s\mu\nu X$ decays as $B_s \to D_s\mu\nu$ decays, implying a value of $c \simeq 3$. Initially the value of $c = 3$ was used in the fitting and generation processes. In section 6.4.4 differing values are used in the two processes, to test systematic errors.

To extract the asymmetry parameters from data, a form is needed for the F^{better} and F^{worse} distributions. A complicated function was needed to produce a good fit to the distributions. The function used was of the form was of the form

$$
\begin{aligned}
F &= c_1 \frac{(c_2 t)^{c_3}}{c_4 + (c_2 t)^{c_3}} \exp(-c_5 t) + c_6 \exp(-0.5(\frac{t - c_7}{c_8})^2) \\
&+ c_9 \exp(-0.5(\frac{t - c_{10}}{c_{11}})^2) + c_{12} \exp(-0.5(\frac{t - c_{13}}{c_{14}})^2) \\
&+ c_{15} \exp(-0.5(\frac{t - c_{16}}{c_{17}})^2) + c_{18} \exp(-0.5(\frac{t - c_{19}}{c_{20}})^2) \\
&+ c_{21} \exp(-0.5(\frac{t - c_{22}}{c_{23}})^2) + c_{24} \exp(-0.5(\frac{t - c_{25}}{c_{26}})^2) \\
&+ c_{27} \exp(-0.5(\frac{t - c_{28}}{c_{29}})^2) + c_{30} \exp(-0.5(\frac{t - c_{31}}{c_{32}})^2) \\
&+ c_{33} \exp(-0.5(\frac{t - c_{34}}{c_{35}})^2)
\end{aligned}
\tag{6.41}
$$

The first term is intended to model the turn on and turn off of the lifetime distributions, the ten gaussian terms to model the structure. Figures 6.30 to 6.33 show the better and worse $B \to f$ and $B \to \bar{f}$ distributions fitted with such a function. The coloured curves are the individual terms in equation 6.41, the black line is sum of these terms.

6.4.2.2 Fit Results

The fitting procedure described in section 6.4.1.1 was repeated, but now only one quarter of events generated were $B_s \to D_s \mu\nu$ with the rest being $B_s \to D_s^* \mu\nu \to D_s \mu\nu\gamma$. Equation 6.40 was used as the basis for the fitting procedure. The values of the asymmetry parameters used are those in table 6.7. Pull distributions for a_{fs} and A_p are shown in figures 6.34 and 6.35. As before, each of the experiments consists of 2.5×10^5 events. The precision of the measurements of a_{fs} and of A_p are given in table 6.11. The precision of the measurement of A_p has decreased with the introduction of $B_s \to D_s^* \mu\nu \to D_s \mu\nu\gamma$ decays, whilst the precision of the measurement of a_{fs} remains the same. This is consistent with the previous findings that the precision of A_p depends much more strongly on the lifetime resolution than does the precision of a_{fs}. Despite the decrease in precision, the neutrino reconstruction method still gives a greater precision on A_p than the k-factor method does.

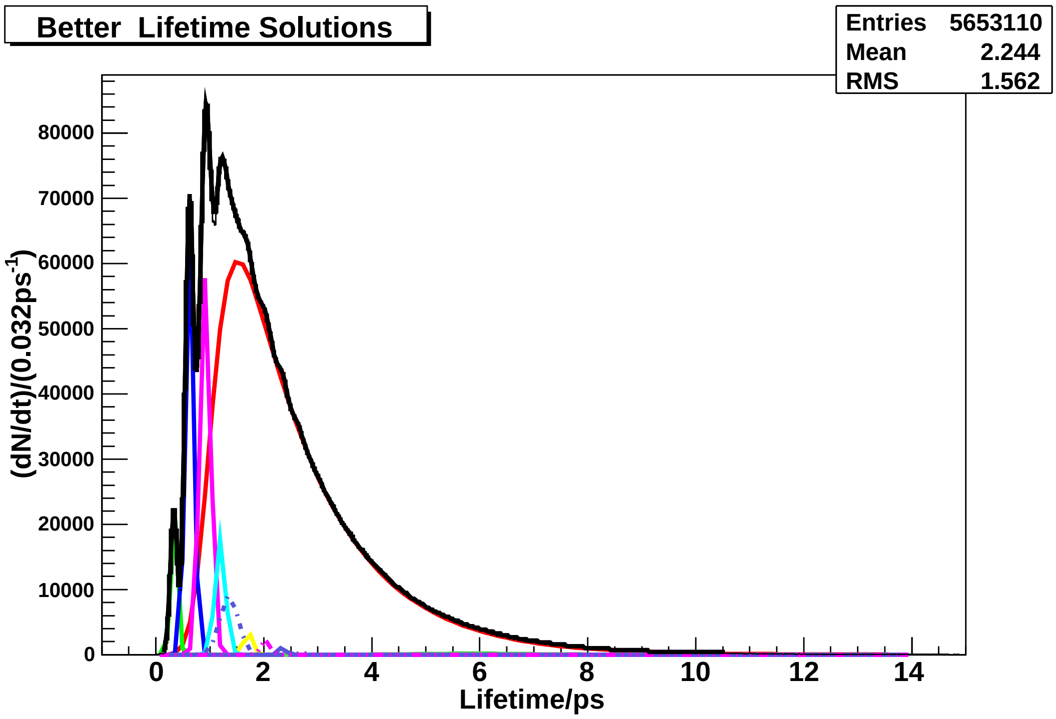

Figure 6.30: The distributions of better lifetime solutions for $B_s \to D_s^* \mu\nu \to D_s \mu\nu\gamma$ decays, with initial state B and final state f. The distribution is modeled with a function of the form 6.41.

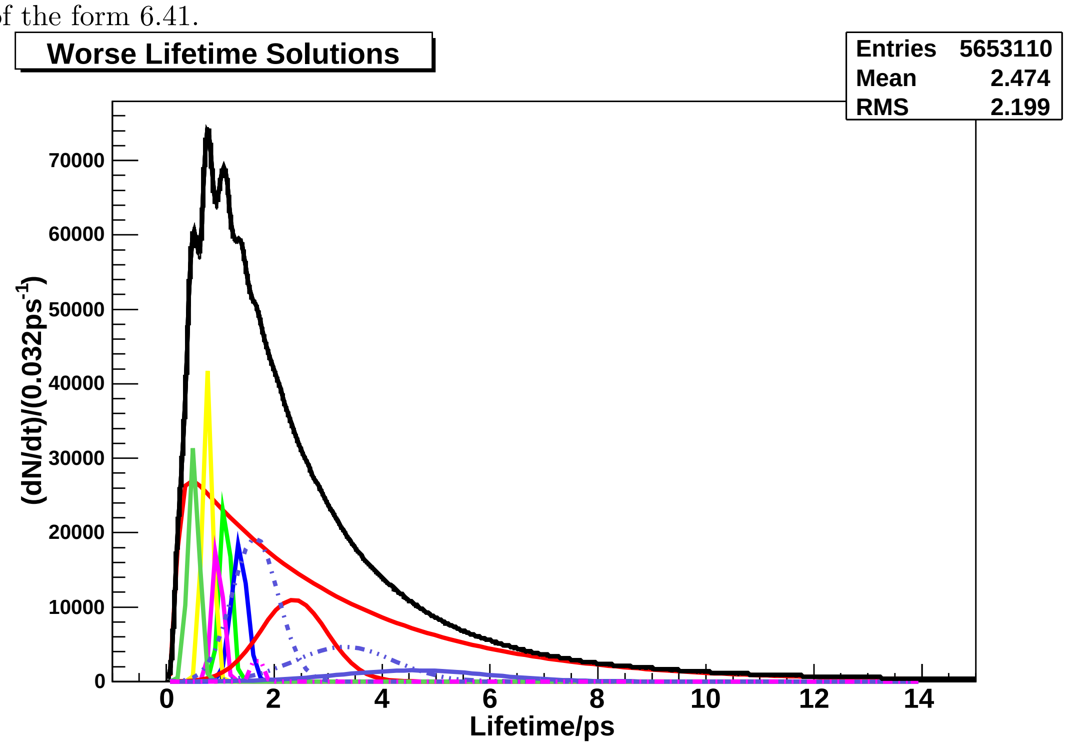

Figure 6.31: The distribution of worse lifetime solutions for $B_s \to D_s^* \mu\nu \to D_s \mu\nu\gamma$ decays, with initial state B and final state f. The distribution is modeled with a function of the form 6.41.

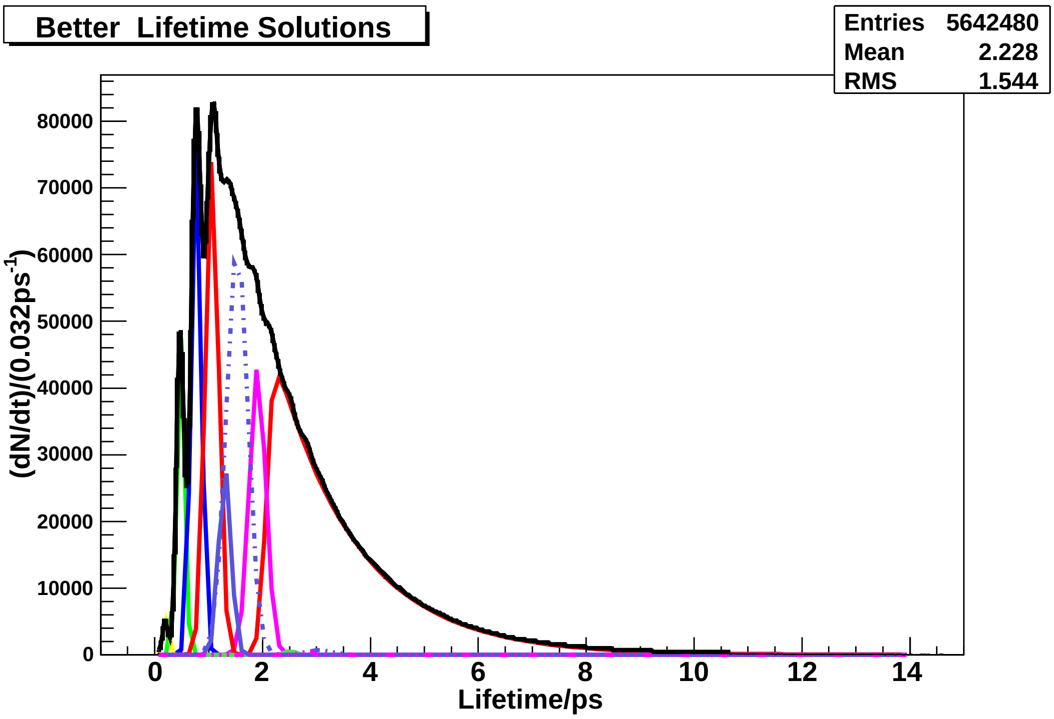

Figure 6.32: The distributions of better lifetime solutions for $B_s \to D_s^*\mu\nu \to D_s\mu\nu\gamma$ decays, with initial state B and final state $\bar{f}$. The distribution is modeled with a function of the form 6.41.

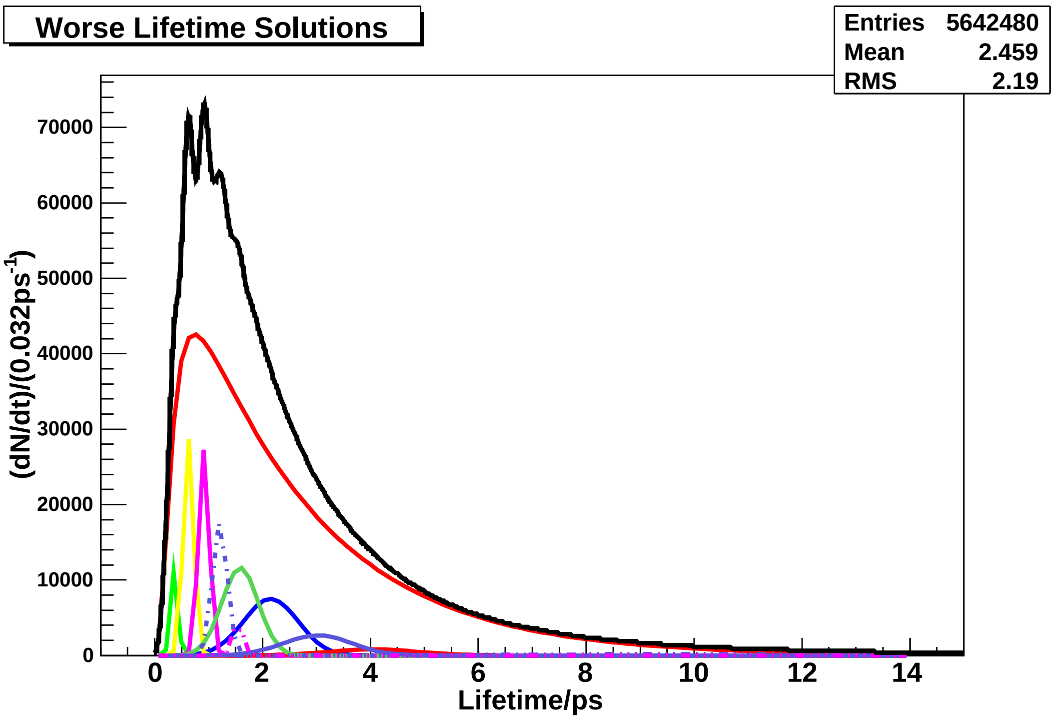

Figure 6.33: The distribution of worse lifetime solutions for $B_s \to D_s^*\mu\nu \to D_s\mu\nu\gamma$ decays, with initial state B and final state $\bar{f}$. The distribution is modeled with a function of the form 6.41.

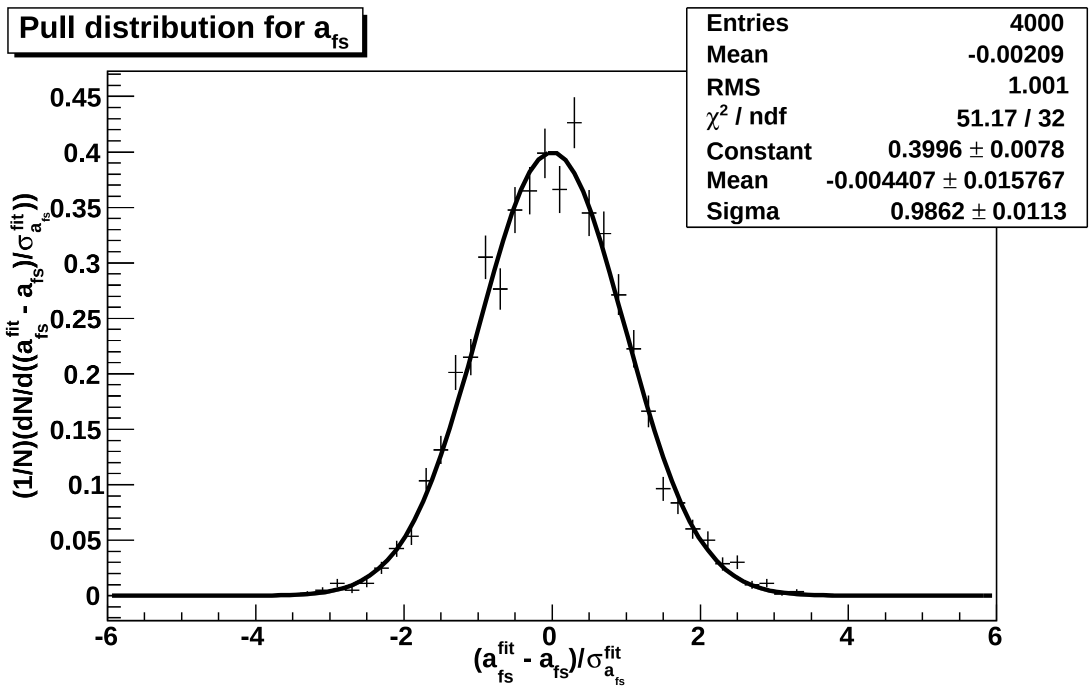

Figure 6.34: The pull distribution for a_{fs}. Equation 6.40 is used as the basis for the fitting procedure. The plot is consistent with zero bias and correctly estimated errors.

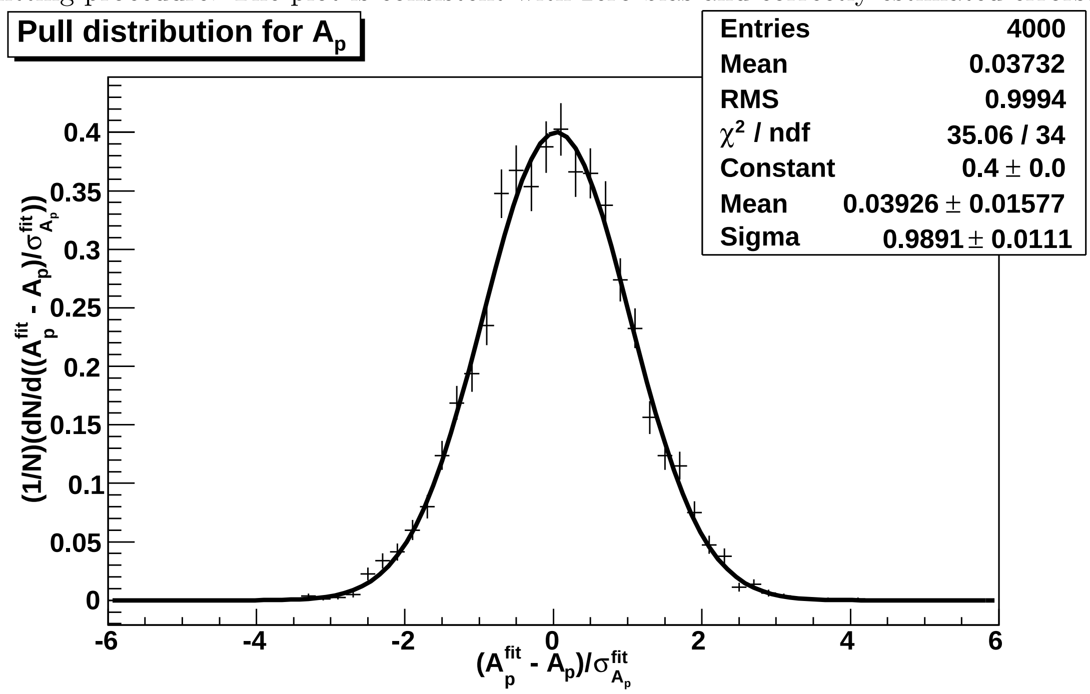

Figure 6.35: The pull distribution for A_p. Equation 6.40 is used as the basis for the fitting procedure. The plot is consistent with zero bias and correctly estimated errors.

N_{Events}	$a_{fs}/10^{-3}$ from fit	$A_p/10^{-2}$ from fit
2.50×10^5	4.99 ± 4.01	1.07 ± 1.96

Table 6.11: The fit results for the neutrino reconstruction method when $B_s \to D_s\mu\nu$ and $B_s \to D_s^*\mu\nu \to D_s\mu\nu\gamma$ decays are used. The precision of the A_p measurement using the neutrino reconstruction method has decreased with the addition of $B_s \to D_s^*\mu\nu \to D_s\mu\nu\gamma$ decay mode, *cf.* table 6.8. The neutrino reconstruction method still provides a better resolution than the k-factor method.

6.4.3 The Measurement of A_P and a_{fs} from $B_s \to D_s\mu\nu$ decays, Using two Lifetime Solutions per Decay

In section 6.4.1 the asymmetry parameters were measured using only one of the two lifetime solutions per decay. This section explores ways in which both solutions can be used. If two lifetimes are used per event, the p.d.f. used in the fitting procedure of section 6.4.1 is no longer correct. Section 6.4.3.1 details attempts to use the correct p.d.f. for using both lifetimes. This approach was found to be problematic. In section 6.4.3.2 the p.d.f. of section 6.4.1 is used as an alternative to the strictly correct p.d.f. This approach is much simpler, and still allows some benefits to come from using both solutions per decay.

6.4.3.1 The Correct p.d.f. For Fitting with Two Lifetime Solutions per Decay

When only one lifetime solution per decay was being used, the p.d.f. used in the fit described the probability of measuring a lifetime, t, given a final state f, $P(t|f)$. With two lifetime solutions per decay, one must consider either the probability of measuring times in the intervals $[t_1,\, t_1+\mathrm{d}t_1]$ and $[t_2,\, t_2+\mathrm{d}t_2]$ given a final state f, $P(t_1, t_2|f)\mathrm{d}t_1\mathrm{d}t_2$, or the probability of detecting a final state f given lifetime solutions in the ranges $[t_1,\, t_1 + \mathrm{d}t_1]$ and $[t_2,\, t_2 + \mathrm{d}t_2]$, $P(f|t_1, t_2)$. If only $B_s \to D_S\mu\nu$ decays are considered, then

$$\begin{aligned} P(t_1, t_2|f) &= P(t_{cor} = t_1|f, t_{inc} = t_2)P(t_{inc} = t_2|f) \\ &+ P(t_{cor} = t_2|f, t_{inc} = t_1)P(t_{inc} = t_1|f) \end{aligned} \tag{6.42}$$

or equivalently

$$\begin{aligned} P(t_1, t_2|f) &= P(t_{inc} = t_1|f, t_{cor} = t_2)P(t_{cor} = t_2|f) \\ &+ P(t_{inc} = t_2|f, t_{cor} = t_1)P(t_{cor} = t_1|f) \end{aligned} \tag{6.43}$$

where $P(t_{cor} = t_1|f, t_{inc} = t_2)\mathrm{d}t_1$ is the probability that the correct lifetime is in the range $[t_1,\ t_1 + \mathrm{d}t_1]$, given a measured final state f and that the incorrect lifetime solution is t_2, and $P(t_{inc} = t_2|f)\mathrm{d}t_2$ is the probability than the incorrect lifetime solution is in the range $[t_2,\ t_2 + \mathrm{d}t_2]$ given a measured final state f. There are similar expressions for a final state $\bar{f}$. $P(t_{cor} = t_1|f, t_{inc} = t_2)$ cannot be easily determined other than through study of Monte Carlo data. From equation 6.18 it is clear that

$$P(t_{cor} = t_1|f) \propto N\epsilon_f\Gamma^{correct}_{B\to f}(t_1) + \bar{N}\epsilon_f\Gamma^{correct}_{\bar{B}\to f}(t_1) \tag{6.44}$$

and

$$P(t_{inc} = t_1|f) \propto N\epsilon_f\Gamma^{incorrect}_{B\to f}(t_1) + \bar{N}\epsilon_f\Gamma^{incorrect}_{\bar{B}\to f}(t_1) \tag{6.45}$$

$P(f|t_1, t_2)$ cannot be so easily written in terms of the lifetime distributions.

$$P(f|t_1, t_2) = \frac{P(t_1, t_2|f)P(f)}{P(t_1, t_2)} \tag{6.46}$$

where $P(f)$ is the probability that a final state f is detected, and $P(t_1, t_2)$ is the probability that the two lifetimes are t_1 and t_2.

The form of $P(f|t_1, t_2)$ cannot be known unless $P(t_1, t_2|f)$ is known. For this reason, the fitting process was carried out using $P(t_1, t_2|f)$. Before any fitting was attempted using equation 6.42, a simplification was made so that the fitting process could be tested more easily. It was assumed that the two lifetime solutions were independent of one another. This allows equation 6.42 to be replaced with

$$P(t_1, t_2|f) = P(t_{cor} = t_1|f)P(t_{inc} = t_2|f) + P(t_{cor} = t_2|f)P(t_{inc} = t_1|f) \tag{6.47}$$

The relations 6.44 and 6.45 must be properly normalised:

$$P(t_{cor} = t_1|f) = \frac{N\epsilon_f \Gamma^{incorrect}_{B\to f}(t_1) + \bar{N}\epsilon_f \Gamma^{incorrect}_{\bar{B}\to f}(t_1)}{\int_0^\infty (N\epsilon_f \Gamma^{incorrect}_{B\to f}(t) + \bar{N}\epsilon_f \Gamma^{incorrect}_{\bar{B}\to f}(t))\mathrm{d}t} \tag{6.48}$$

There are similar expressions for the distribution of incorrect lifetimes, and for a final state $\bar{f}$. $\bar{N} = N_{events} - N$ was substituted into equation 6.48, where N_{events} is the number of events. N and a_{fs} were extracted from the fit. A_p can be found from N given that N_{events} is known.

There were severe problems with the fitting process. N and a_{fs} were almost 100% correlated. The errors produced by MINUIT for the two variables varied significantly from one set of data to the next, but were typically bigger than those found using only one lifetime per event. Because a factor $(1 + a_{fs})$ enters into $\Gamma^{correct}_{\bar{B}\to f}$ and $\Gamma^{incorrect}_{\bar{B}\to f}$ (see equation 6.5) there are terms in equation 6.47 with factors N, a_{fs}, N^2, a^2_{fs}, $a_{fs}N$, $a_{fs}N^2$, $a^2_{fs}N$ and $a^2_{fs}N^2$. Large correlation between the fit parameters therefore seems inevitable. Because the fitting procedure proved so difficult, despite the simplification of equation 6.47, it was abandoned and a simpler method was used.

6.4.3.2 Using the One Lifetime Solution per Decay p.d.f. with Both Lifetime Solutions

If, for each decay, one of the two lifetime solutions is discarded at random, then the correct p.d.f. for the fitting procedure comes from equation 6.28 or 6.40. Here this p.d.f. is used, but both lifetime solutions are kept. This was done first using only $B_s \to D_s\mu\nu$ events. 700 toy experiments were conducted, and a_{fs} and A_p were extracted. The data were generated in the same way, and using the same settings as in section 6.4.1.3. This procedure lead to the errors on both a_{fs} and A_p being reduced by a factor of $\sqrt{2}$ compared to those from section 6.4.1. This is unsurprising, since the using both lifetime solutions doubles the size of the data set.

Figures 6.36 and 6.37 show the pull distributions for a_{fs} and A_p produced by this fitting process. Both are centred on zero, and the distribution for A_p has a width compatible with one, but the distribution for a_{fs} has a width of $\sqrt{2}$, indicating the errors have been underestimated by a factor of $\sqrt{2}$. This suggests that the improvement in precision seen in A_p is genuine, but the improvement in the precision of a_{fs} is not.

To investigate this further the different solutions were split into different data sets. A further 100 sets of 2.5×10^5 events were generated and in each case the two lifetimes were calculated. Then the solutions were separated out into those coming from taking the positive square root in equation 6.14, and those coming from the negative square root. A fit was performed on each data set to extract a_{fs} and A_p. Then, for each of the 100 experiments, a_{fs} from one data set was plotted against a_{fs} for the other, and likewise with A_p. These plots are shown in figures 6.38 and 6.39. There is clearly no correlation between the two values of A_p, whereas there is a very strong correlation between the two values of a_{fs}. Indeed, the two different values of a_{fs} are essentially equal. This means no extra information about a_{fs} is obtained from having a second solution, whereas new information is obtained in the case of A_p. This is consistent with the earlier conclusion that the improvement in precision is valid in the case of A_p but not for a_{fs}. The two solutions provide essentially the same information about a_{fs}, because measuring it depends so weakly on the lifetime resolution. In the case of A_p the correct solution does provide information which the incorrect does not, and so doubling the number of correct solutions improves the precision of the measurement. It is thus possible to benefit from using both solutions even without the correct p.d.f. for the fit, however, one must be careful to increase the error a_{fs} that is estimated by MINUIT if one adopts this method.

The process was repeated with the inclusion of $B_s \to D_s^* \mu\nu \to D_s \mu\nu\gamma$ decays. The same result was found: a reduction by a factor of $\sqrt{2}$ in the errors on both a_{fs} and A_p, but which was only genuine in the case of A_p

6.4.4 Systematic Errors

In this section two sources of systematic error are investigated: incorrect modeling of the distributions of incorrect lifetimes and limited knowledge of the ratio of $B_s \to D_s \mu\nu$

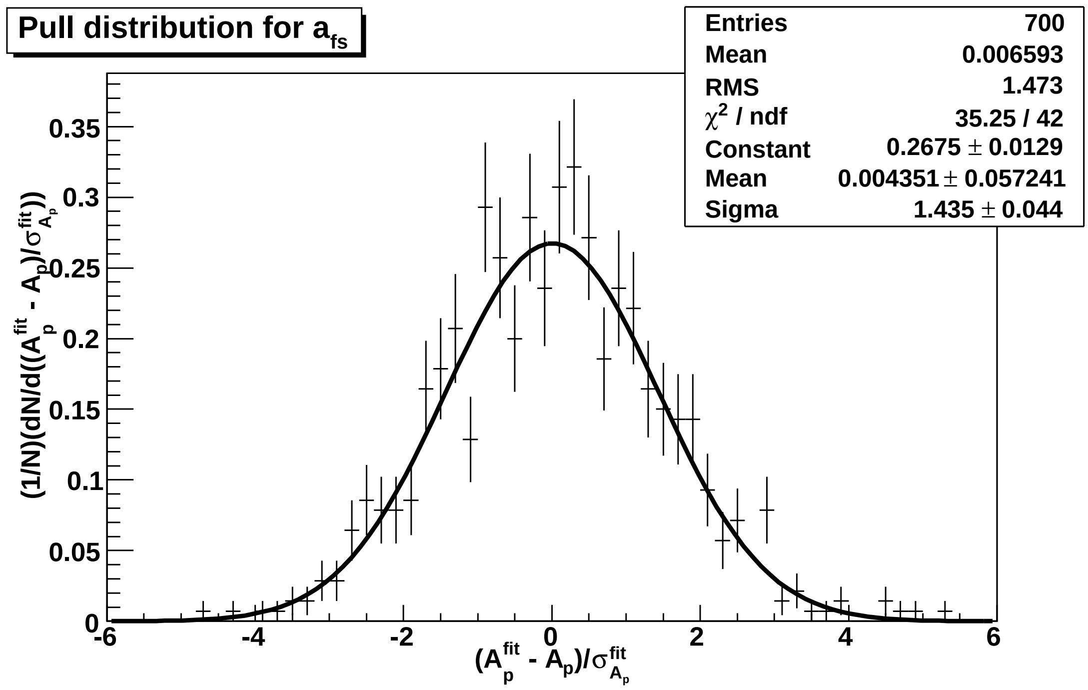

Figure 6.36: The pull distribution for a_{fs}. The fitting was done with a p.d.f. based on equation 6.28 and used both lifetime solutions per event. The width of the pull indicates the errors have been underestimated by a factor of $\sqrt{2}$

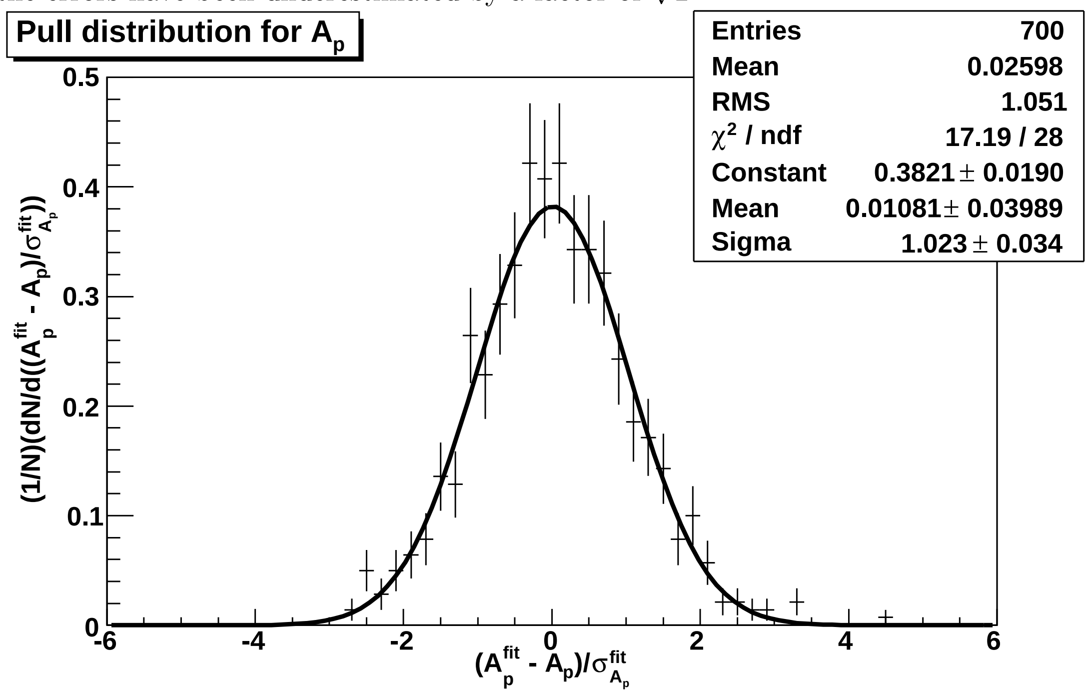

Figure 6.37: The pull distribution for A_p. The fitting was done with a p.d.f. based on equation 6.28 and used both lifetime solutions per event.

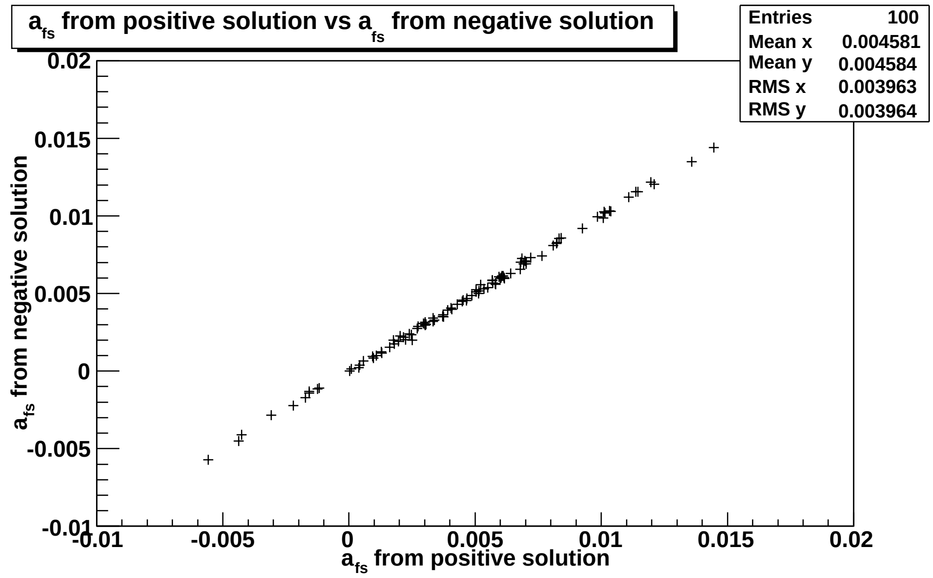

Figure 6.38: The correlation between a_{fs} measured from a data set consisting of lifetimes taken from the positive square root in equation 6.14 against a_{fs} measured using the corresponding negative square root solutions. The two values are virtually identical in each experiment.

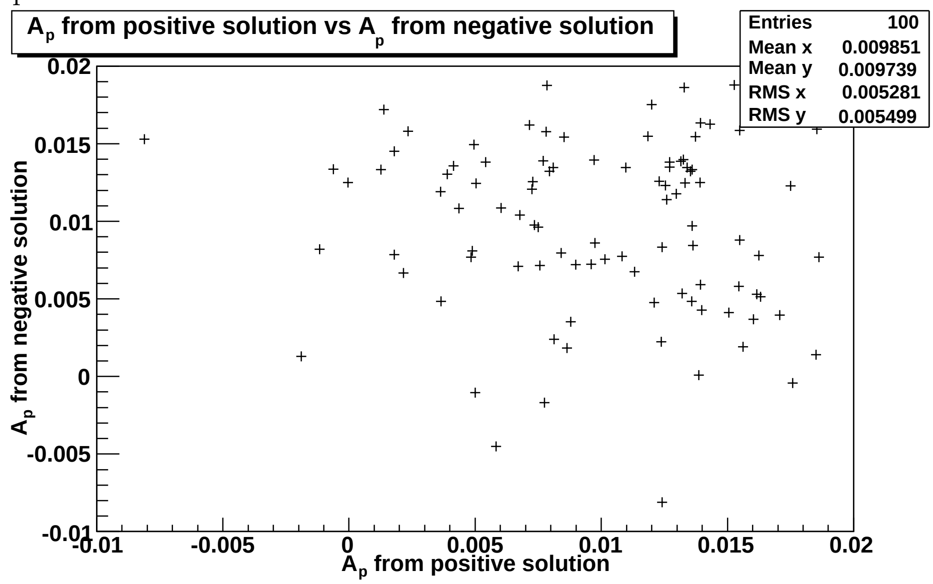

Figure 6.39: The correlation between A_p measured from a data set consisting of lifetimes taken from the positive square root in equation 6.14 against A_p measured using the corresponding negative square root solutions. There is no correlation between the two values.

to $B_s \to D_s\mu\nu X$ decays. These studies are particularly important for a comparison of the neutrino reconstruction method with the k-factor method because they do not affect the k-factor fitting procedure.

6.4.4.1 Lifetime Distributions

The shape of the incorrect lifetime distributions has been determined from Monte Carlo, and is therefore a potential source of systematic errors. To investigate this the incorrect lifetime distributions were modeled with a deliberately poor model, of the form of equation 6.49. This form was used for the incorrect solutions in $B_s \to D_s\mu\nu$ decays and all sets of lifetime distribution in $B_s \to D_s\mu\nu X$, although the values of the variables differ in the different cases. The parameter values are listed in table 6.12. Figure 6.40 shows the better lifetime solutions from $B_s \to D_s^*\mu\nu \to D_s\mu\nu\gamma$ decays, with initial state B and final state f, fitted with this function.

$$F = N\frac{(c_1 t)^{c_2}}{c_3 + (c_1 t)^{c_2}} e^{-c_4 t} \tag{6.49}$$

Figures 6.41 and 6.42 show pull distributions for a_{fs} and A_p. Table 6.13 lists the mean fit values and errors. The mean value of A_p is roughly $5\,\sigma$ away from the input value: a clear sign of a systematic error. The difference between the mean measured value of A_p and the input value is $\sigma_{A_P}^{syst} = 1.1 \times 10^{-3}$. The statistical error for 2.6×10^6 events is $\sigma_{A_p} = 5.0 \times 10^{-3}$. Modeling the incorrect lifetime distributions incorrectly leads to a small, but non-negligible, systematic error in the measurement of A_p which is roughly five times smaller than the expected precision for one year's data. Any systematic error in the measurement of a_{fs} is sufficiently small that is consistent with being zero.

6.4.4.2 Ratio of $B_s \to D_s\mu\nu$ to $B_s \to D_s\mu\nu X$ Decays

Uncertainty in the ratio of $B_s \to D_s\mu\nu$ to $B_s \to D_s\mu\nu X$ events is a source of systematic error. An estimate of this systematic error was made by generating data with a different ratio than was assumed in the fit. The ratio of $B_s \to D_s\mu\nu$ to $B_s \to D_s\mu\nu X$ used in

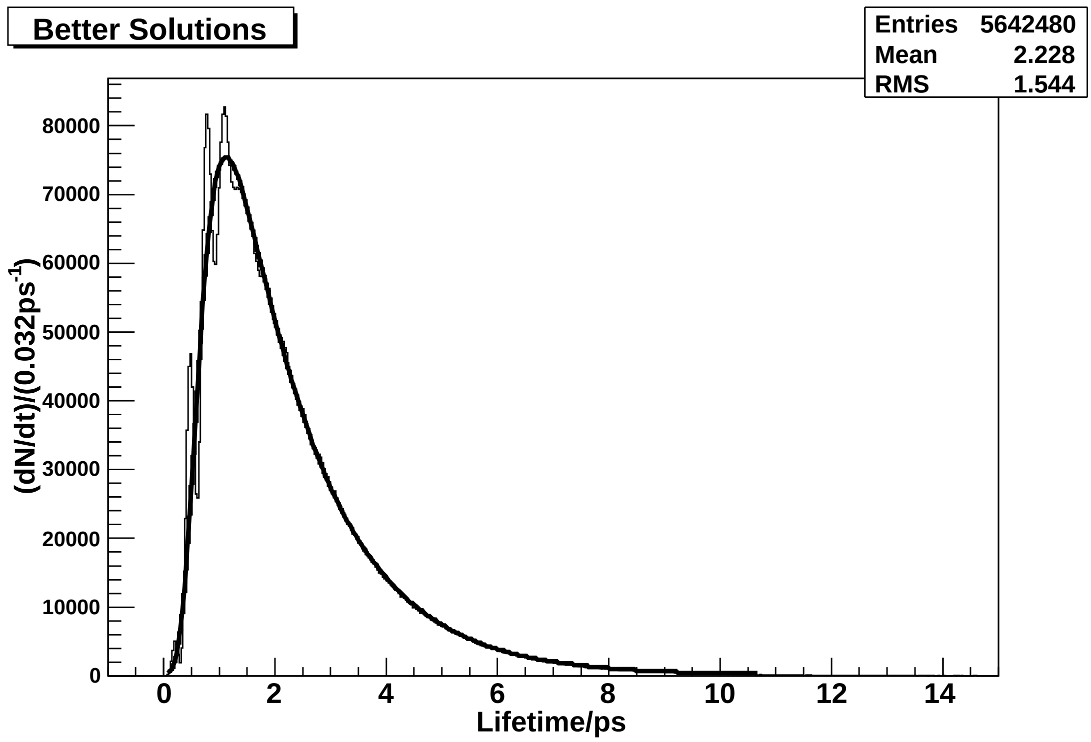

Figure 6.40: The distribution of better lifetime solutions from $B_s \to D_s^*\mu\nu \to D_s\mu\nu\gamma$ decays, with initial state B and final state f, fitted with poor model to test systematic errors.

Decay	Flavour	Solution	N	c_1/ps	c_2	c_3	c_4
$B_s \to D_s\mu\nu$	$B \to f$	Incorrect	1.04	1.275	1.79	1	0.6852
$B_s \to D_s\mu\nu$	$B \to \bar{f}$	Incorrect	1.04	1.275	1.79	1	0.6852
$B_s \to D_s\mu\nu X$	$B \to f$	Better	0.97	0.418	3.38	0.023	0.6687
$B_s \to D_s\mu\nu X$	$B \to f$	Worse	0.52	0.552	2.783	0.013	0.4983
$B_s \to D_s\mu\nu X$	$B \to \bar{f}$	Better	0.96	0.398	3.43	0.018	0.6667
$B_s \to D_s\mu\nu X$	$B \to \bar{f}$	Worse	0.52	0.5794	2.792	0.015	0.4986

Table 6.12: The parameters used when modeling the various lifetime distributions with a deliberately poor model, of the form 6.49.

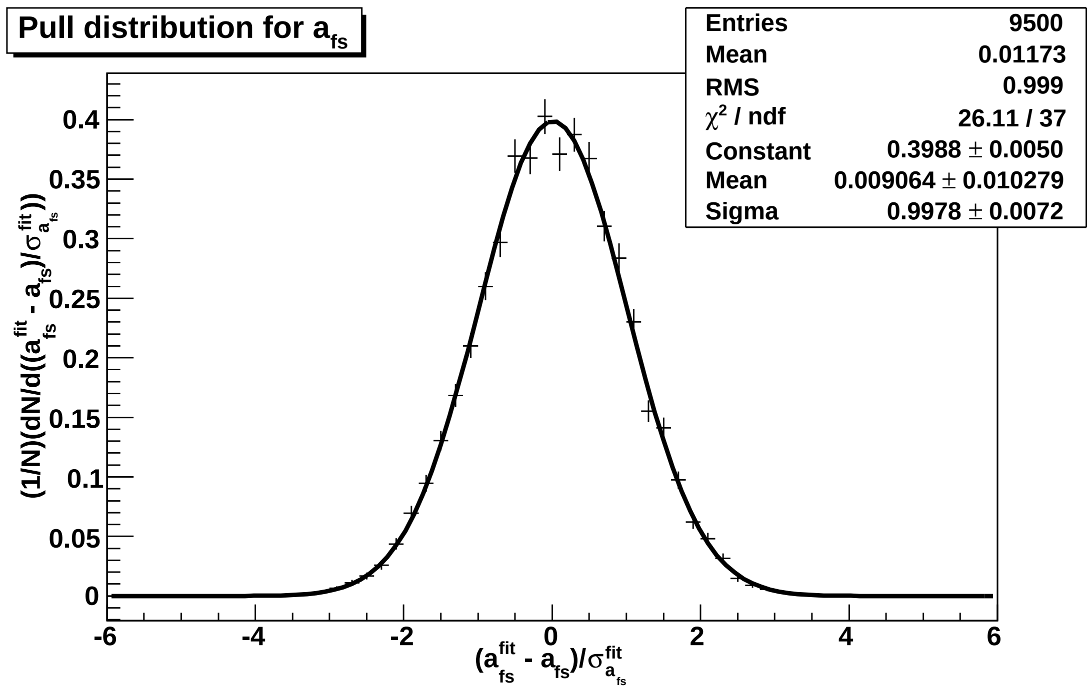

Figure 6.41: The pull distribution for a_{fs} obtained using lifetime distributions modeled with equation 6.49.

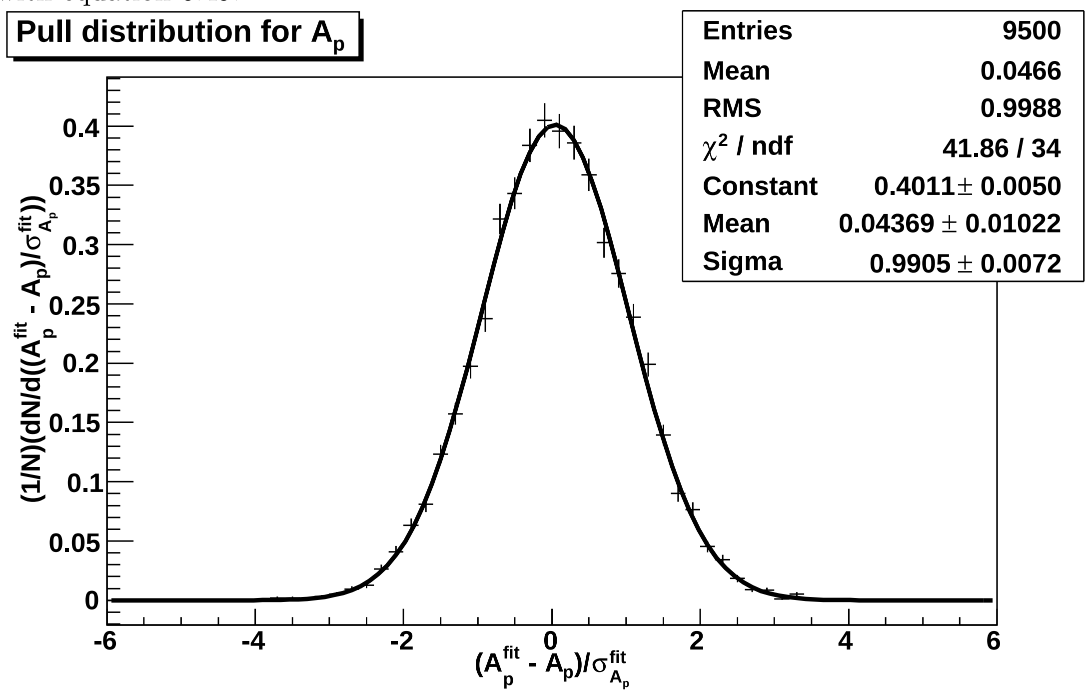

Figure 6.42: The pull distribution for A_p obtained using lifetime distributions modeled with equation 6.49.

A_p/a_{fs}	Mean $\times 10^3$	σ^{syst}_{Asym} $\times 10^3$	σ^{stat}_{Asym} $\times 10^3$	$\sigma^{stat:year}_{Asym}$ $\times 10^3$
A_p	11.1 ± 0.2	1.1 ± 0.2	22.6	4.97
a_{fs}	5.04 ± 0.04	$(4 \pm 4) \times 10^{-2}$	4.01	1.25

Table 6.13: Fit results obtained using lifetime distributions modeled with equation 6.49. σ^{stat}_{Asym} is the precision of the measurement of the parameter from 2.5×10^5 events and $\sigma^{stat:year}_{Asym}$ the precision for one year. $\sigma^{stat:year}_{Asym}$ is larger than σ^{syst}_{Asym}.

Ratio	A_p/a_{fs}	Mean $\times 10^3$	σ^{syst}_{Asym} $\times 10^3$	σ^{stat}_{Asym} $\times 10^3$	$\sigma^{stat:year}_{Asym}$ $\times 10^3$
70:30	A_p	11.59 ± 0.37	1.59 ± 0.37	22.6	4.97
70:30	a_{fs}	5.04 ± 0.06	$(4 \pm 6) \times 10^{-2}$	4.01	1.25
80:20	A_p	8.93 ± 0.37	1.07 ± 0.37	22.6	4.97
80:20	a_{fs}	5.07 ± 0.06	$(7 \pm 7) \times 10^{-2}$	4.01	1.25

Table 6.14: Fit results obtained with incorrect $B_s \to D_s\mu\nu$ to $B_s \to D_s\mu\nu X$ ratio. σ^{mean}_{Asym} is the error on the mean, σ^{syst}_{Asym} is the difference between mean fit value and input value of the asymmetry parameter, σ^{stat}_{Asym} is the precision of the measurement of the parameter from 2.5×10^5 events and $\sigma^{stat:year}_{Asym}$ the precision for one year. $\sigma^{stat:year}_{Asym}$ is larger than σ^{syst}_{Asym}.

both the fitting and generation in section 6.4.2 was 25:75. Here this ratio is kept in the fitting procedure, but ratios of 20:80 and 30:70 were used for the generation. The distributions of incorrect lifetime solutions were again modeled with a deliberately poor fit, of the form of equation 6.49. Figures 6.43 and 6.44 show the pull distributions for a_{fs} and A_p where the decays were generated in the ratio 20:80. Figures 6.45 and 6.46 show the pull distributions for a_{fs} and A_p where the decays were generated in the ratio 30:70. Table 6.14 lists fit results.

The difference between the mean measured value of A_p and the input value is $\sigma^{syst}_{A_P} \sim 1.15 \times 10^{-3}$. The expected precision from 2.6×10^6 events is $\sigma_{A_p} = 5.0 \times 10^{-3}$ The systematic error is smaller than the statistical error, although non-negligible. Any systematic error in the measurement of a_{fs} is sufficiently small that is consistent with being zero.

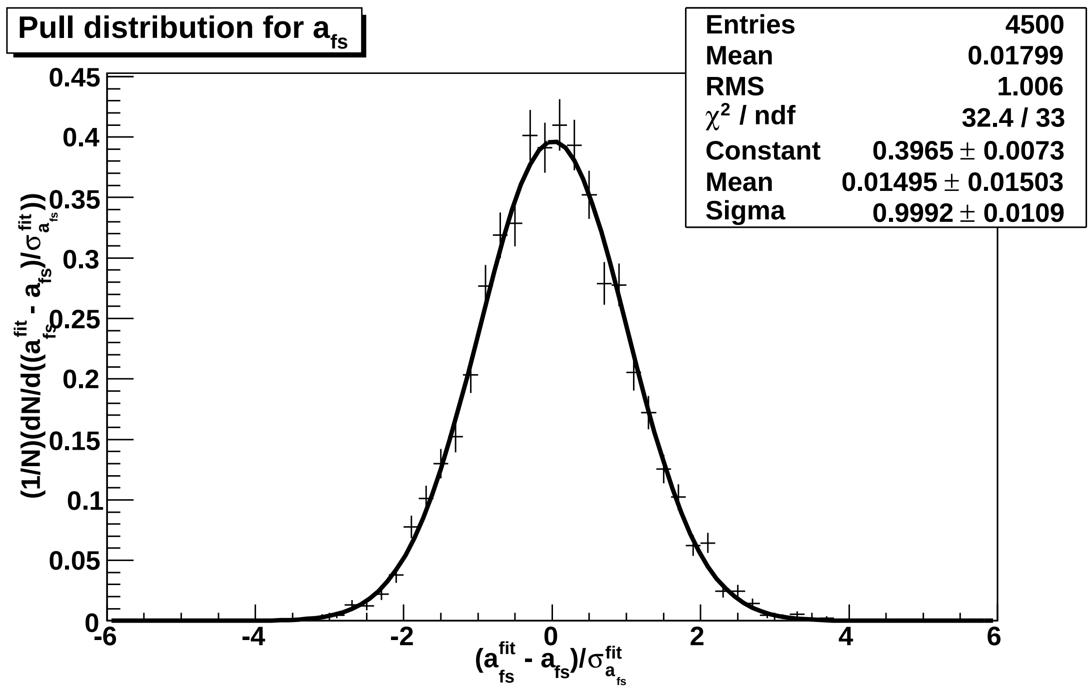

Figure 6.43: The pull distribution for a_{fs}. The generated ratio of $B_s \to D_s\mu\nu$ to $B_s \to D_s\mu\nu X$ is 20:80, but the ratio assumed in fit is 25:75. The results are consistent with zero bias.

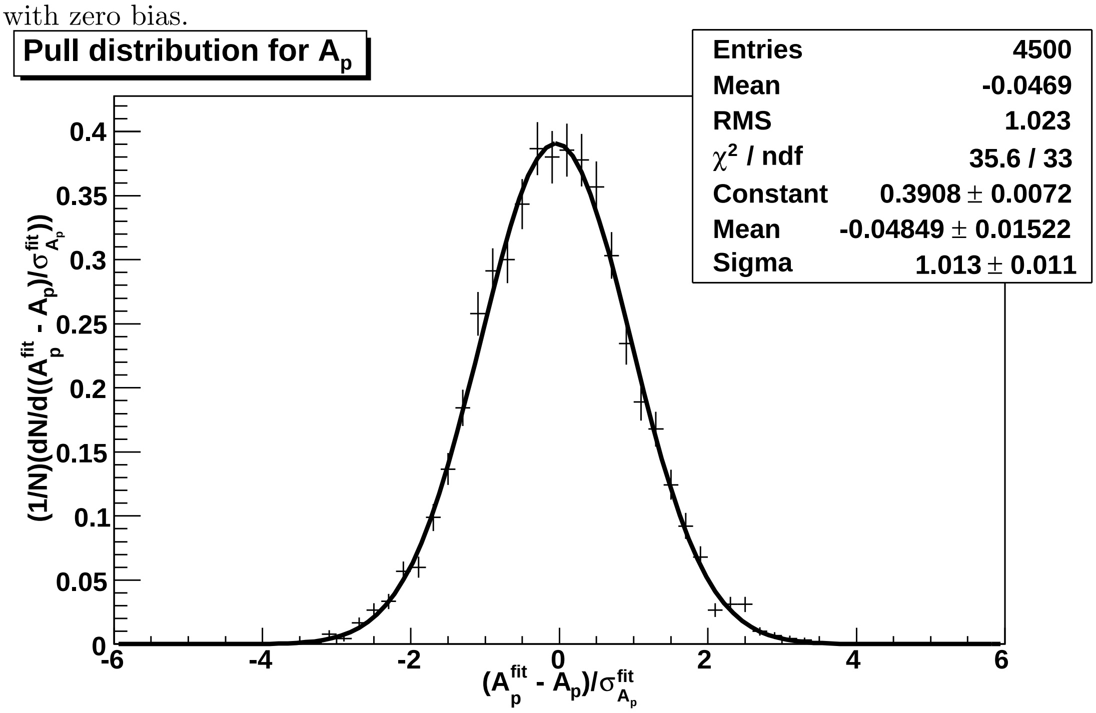

Figure 6.44: The pull distribution for A_p. The generated ratio of $B_s \to D_s\mu\nu$ to $B_s \to D_s\mu\nu X$ is 20:80, but the ratio assumed in fit is 25:75. This is evidence of a bias in the fit.

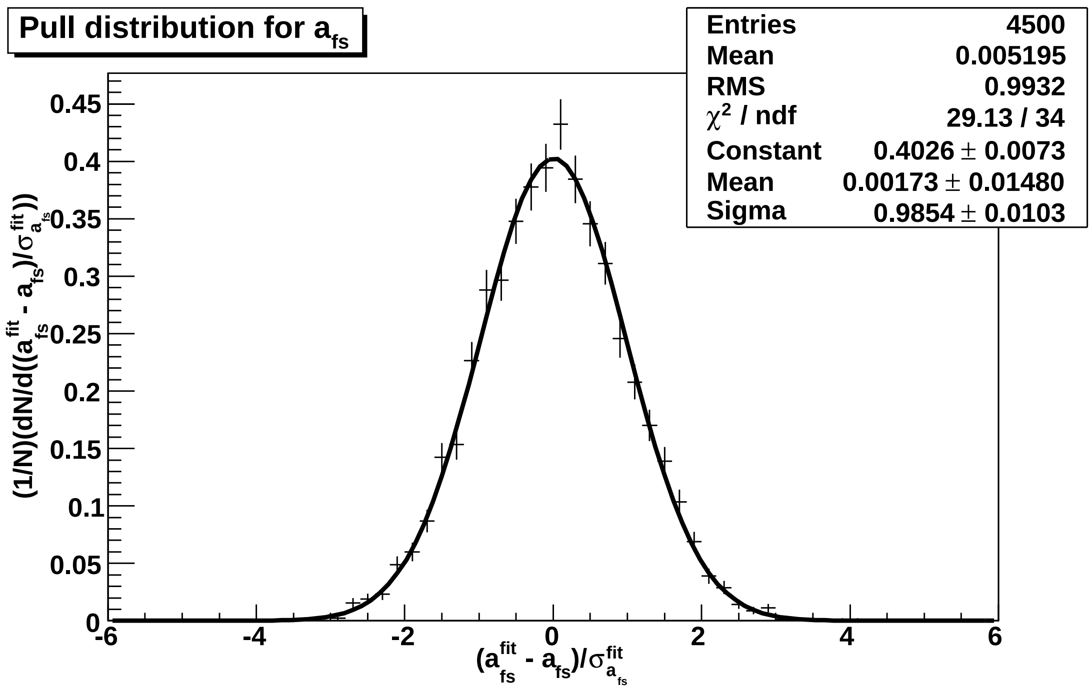

Figure 6.45: The pull distribution for a_{fs}. The generated ratio of $B_s \to D_s\mu\nu$ to $B_s \to D_s\mu\nu X$ is 30:70, but the ratio assumed in fit is 25:75.

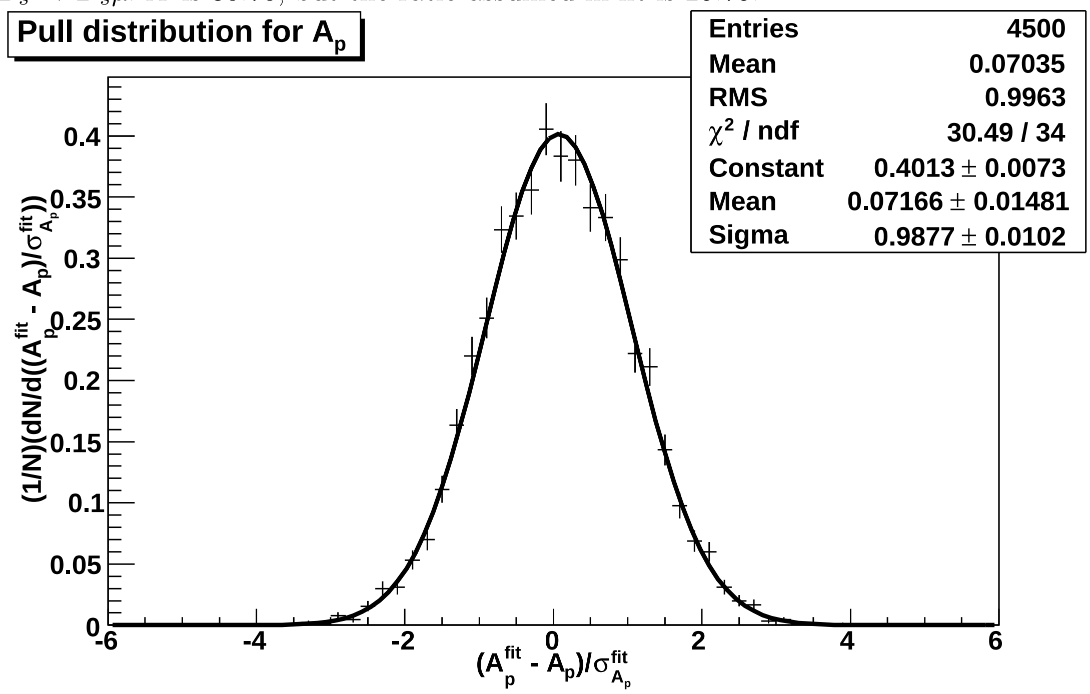

Figure 6.46: The pull distribution for A_p. The generated ratio of $B_s \to D_s\mu\nu$ to $B_s \to D_s\mu\nu X$ is 30:70, but the ratio assumed in fit is 25:75.

6.5 Detector Effects

In the previous sections it was found that the neutrino reconstruction method allowed for better precision on a measurement of A_p than the k-factor method did. However, this result was based upon a simple model in which perfect knowledge of the D_s momentum, the μ momentum, and the B_s direction was assumed, and as a result perfect lifetime resolution was achieved for $B_s \to D_s\mu\nu$ decays. In this section the effect of finite detector resolution is investigated. Finite detector resolution results in imperfect knowledge of the daughter particles' momenta, and hence finite lifetime resolution for all decays. It should be noted that the study presented in this section does not consider everything which must be considered when using real data. Instead it is intended to give a reasonable estimate of the effect of finite detector resolution, and a reasonable estimate of the precision of measurements that can be made using the neutrino reconstruction method. This was achieved by modifying the toy Monte Carlo so that it had finite lifetime resolution for $B_s \to D_s\mu\nu$ events. The resolution of these events was estimated from fully reconstructed Monte Carlo data.

In section 6.5.1, the generation of the reconstructed data is discussed. In section 6.5.2, the changes made to the toy Monte Carlo are described. The results are given in section 6.5.2.

6.5.1 Reconstructed Data

In order to make a sensible estimation of the lifetime resolution that will be achievable for $B_s \to D_s\mu\nu$ decays, reconstructed data must be used. To understand what the reconstructed data will look like, and to know how many reconstructed events can be expected, a trigger strategy and set of selection cuts are needed. At the time of writing, the most up to data study is one undertaken by Rob Lambert, presented in [69]. This study was undertaken using data from LHCb's 2006 Monte Carlo data sets (DC06 data). The study determines a set of cuts for the HLT2 trigger, and a set of offline selection cuts. It was found that 2.6×10^6 reconstructed events are expected in one year of data taking.

At the time of writing, Lambert is reoptimising the cuts using data from LHCb's 2009 data production (MC09). This work is ongoing. Some details are available to LHCb members [72]. The studies so far suggest the figure of 2.6×10^6 reconstructed events per year will increase, possibly by as much as a factor of two.

Ideally the study presented in this chapter would have used DC06 data and the trigger strategy and selection cuts presented in [69]. However, technical issues, connected with changes in DaVinci, prevented this from happening. Instead, MC09 data were used, with the cuts presented in [72]. All of the reconstructed events studied contained a single primary vertex; where there are events with multiple primary vertices, the vertex which gives the smallest impact parameter with respect to the B is chosen. Figures 6.47 to 6.49 show the primary vertex resolution. As an estimate of the number events has not yet been published for MC09 data, the figure of 2.6×10^6 will be used in this thesis.

The Monte Carlo data set contained a total of 217354 reconstructed events, of which $(27.6 \pm 0.1)\%$ are $B_s \to D_s\mu\nu$ events and the rest $B_s \to D_s\mu\nu X$. Of the 59910 $B_s \to D_s\mu\nu$ events, 15636 had no real solutions. That is, $(27.6 \pm 0.2)\,\%$ of events had no real solutions. In the case of $B_s \to D_s\mu\nu X$ events, 20535 out of 157444 events had no solutions. That is $(13.0 \pm 0.0)\,\%$ of events had no real solution. There is statistically significant difference between the fraction of $B_s \to D_s\mu\nu$ events and the fraction of $B_s \to D_s\mu\nu X$ events that are lost as a result of there being no real solutions to equation 6.14. However, this difference is unlikely to greatly affect the precision achievable using the neutrino reconstruction method, because it does not significantly greatly alter the ratio of $B_s \to D_s\mu\nu$:$B_s \to D_s\mu\nu X$ events available to analyse. $(24.4 \pm 0.1)\,\%$ of events with real solutions to equation 6.14 are $B_s \to D_s\mu\nu$ events, compared to $(27.6 \pm 0.1)\,\%$ for the whole data set. The reasons for the difference between $B_s \to D_s\mu\nu$ events and $B_s \to D_s\mu\nu X$ events is not clear. However, because of the small effect of this difference on the ratio of event types, the reasons for the differences are not examined here.

Figure 6.50 shows a plot of $t_{reco} - t_{truth}$ for $B_s \to D_s\mu\nu$ decays, where t_{reco} is the reconstructed lifetime, using the better of the two solutions and t_{truth} is true lifetime. Figure 6.51 shows the same data, fitted with a double gaussian function.

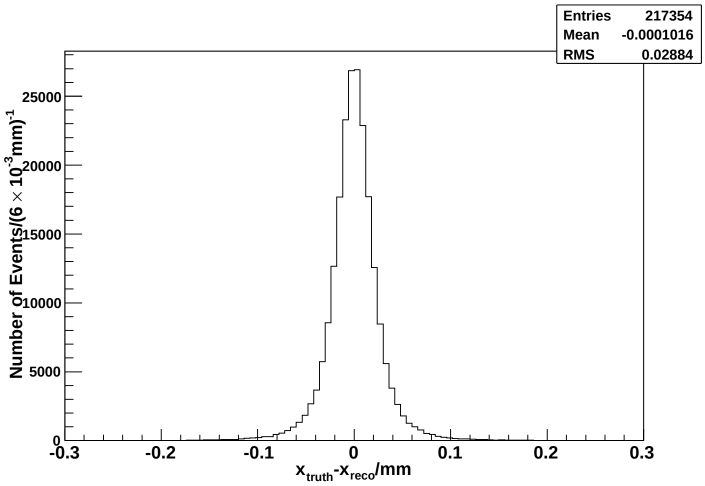

Figure 6.47: The resolution of a measurement of the x component of the PV position.

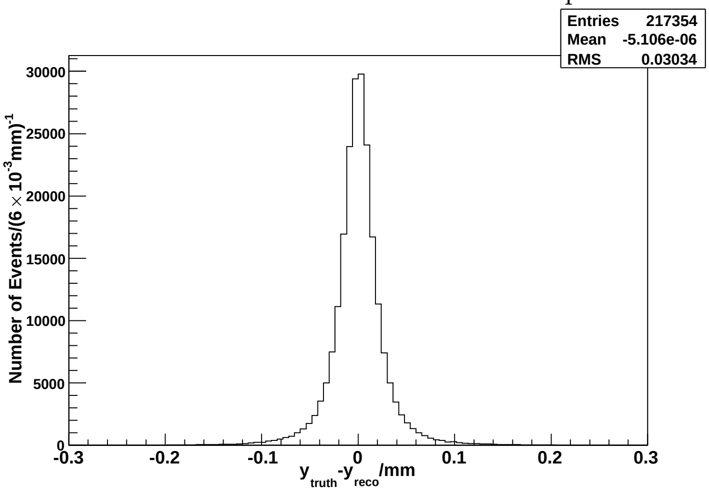

Figure 6.48: The resolution of a measurement the y component of the PV position.

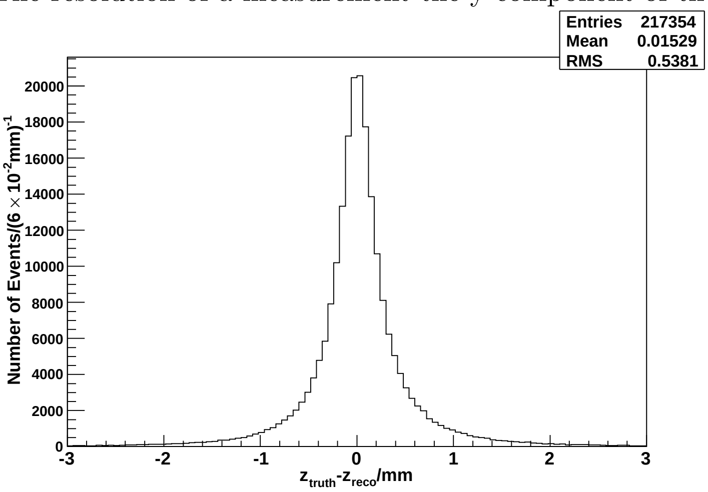

Figure 6.49: The resolution of a measurement the z component of the PV position.

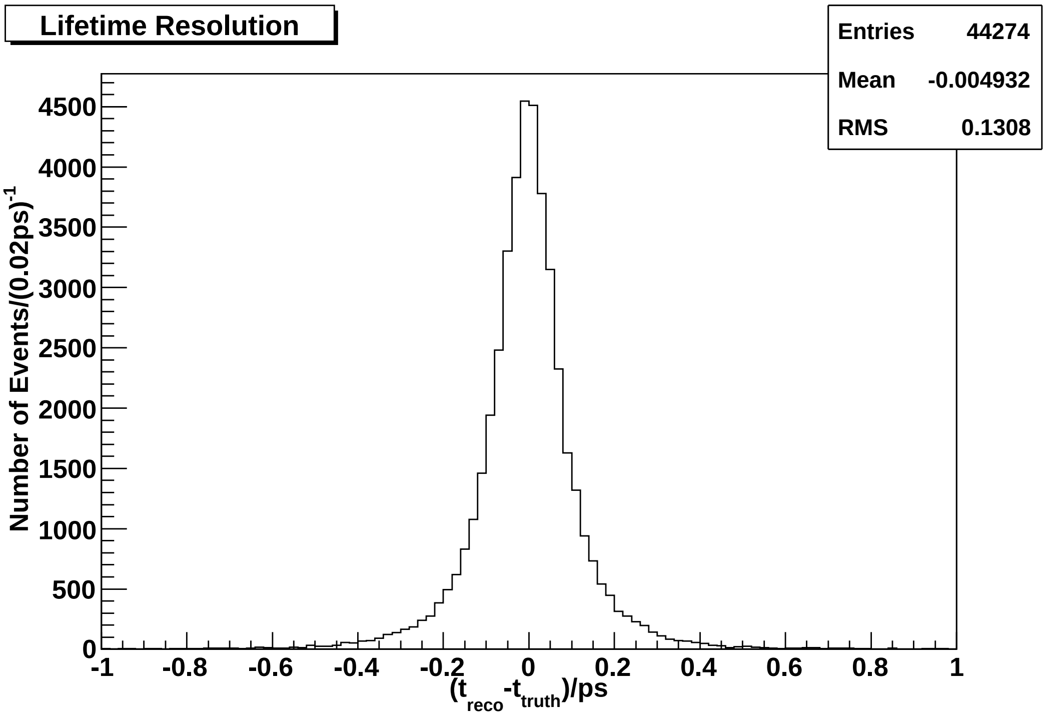

Figure 6.50: The lifetime resolution of reconstructed $B_s \to D_s\mu\nu$ events. The reconstructed lifetime comes from using the better of the two lifetime solutions.

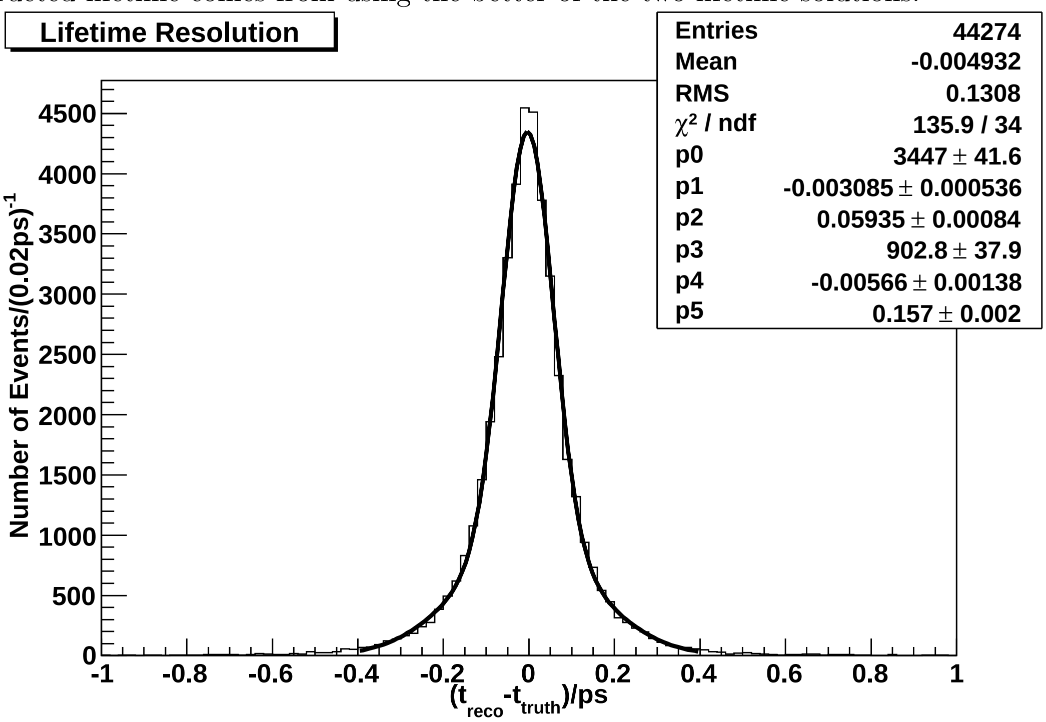

Figure 6.51: The lifetime resolution modeled with a double gaussian function. The parameters p_1 and p_4 are the means of the two guassians, p_2 and p_5 are the widths, and p_0 and p_3 are normalisation factors. Roughly 59 % of events are contained within the narrow gaussian.

6.5.2 The Modified Toy Monte Carlo Simulation

In this section, a toy Monte Carlo designed to model the effects of finite detector resolution is discussed. Even when perfect knowledge of the particle's momentum was allowed, the incorrect $B_s \to D_s\mu\nu$ lifetime solutions did not contribute to the measurement of A_p. The distributions of lifetime solutions coming from the $B_s \to D_s\mu\nu X$ decays had very little structure, and it is reasonable to believe it would be entirely lost due to detector effects. It is therefore reasonable to believe that only the better[8] lifetime solution from $B_s \to D_s\mu\nu$ decays will contribute to a measurement of A_p.

A toy Monte Carlo was used to model the effects of finite lifetime resolution. It was simpler than the one used in section 6.4.1.2. The eight different distributions of lifetime solutions in equation 6.40 were generated from distributions using an acceptance reject method, and not using the method described in 6.2.2[9]. Crucially, the distributions of correct lifetime solutions were replaced with ones which included smearing of the lifetime.

The smearing was modeled by convoluting the distributions, given by equations 6.3 and 6.5, with a gaussian. For a gaussian of width σ_t this gives:

$$\begin{aligned} F &= e^{\Gamma t} e^{\frac{1}{2}\Gamma^2\sigma_t^2} \left[e^{\frac{1}{8}\sigma_t^2\Delta\Gamma^2} \left\{ \frac{1}{2} e^{\frac{1}{2}\Delta\Gamma(t-\sigma^2\Gamma)} \mathrm{Freq}\left(\frac{1}{2} - \sigma_t\left(\Gamma - \frac{1}{2}\Delta\Gamma\right)\right) \right.\right. \\ &\quad + \frac{1}{2} e^{-\frac{1}{2}\Delta\Gamma(t-\sigma_t^2\Gamma)} \mathrm{Freq}\left(\frac{1}{2} - \sigma_t\left(\Gamma + \frac{1}{2}\Delta\Gamma\right)\right) \\ &\quad \left.\left. \pm e^{-\frac{1}{2}\Delta m^2\sigma_t^2} \mathrm{Re}\left\{ e^{i\Delta m(t-\Gamma\sigma-t^2)} \times \left(\frac{1}{2} + i\frac{1}{2}\mathrm{erfi}\left(\frac{\Delta m\sigma_t + i(\frac{t}{\sigma} - \sigma_t\Gamma)}{\sqrt{2}}\right)\right)\right\}\right\}\right] \end{aligned} \tag{6.50}$$

[8]With finite detector resolution equation 6.14 no longer gives an exactly correct momentum for $B_s \to D_s\mu\nu$ decays.

[9]The Monte Carlo used here is designed to give an estimate of the precision attainable with the neutrino reconstruction method. This was because most of the distributions, once smeared due to finite detector resolution, will be featureless. It it therefore not necessary to model them exactly to obtain the precision of a measurement of a_{fs} and A_p, and so a simple Monte Carlo is used. However, the better the distributions obtained from experimental data are known, the smaller systematic errors will be. A more detailed study of detector effects should be undertaken in future studies.

where the frequency function, Freq(y), is defined by

$$\mathrm{Freq}(y) = \frac{1}{\sqrt{2\pi}} \int_{-\infty}^{y} e^{-\frac{1}{2}x^2} \mathrm{d}x \qquad (6.51)$$

the imaginary error function, erfi(z) is related to the real error function is related to the real error function, erf(z) by

$$\mathrm{erfi}(z) = -i\mathrm{erf}(iz) \qquad (6.52)$$

The derivation of equation 6.50 is given in appendix A. Figure 6.51 suggests a double gaussian provides a better description of the lifetime resolution that a single gaussian. A double gaussian can be modeled simply by summing functions of the form 6.50. The parameters shown in figure 6.51 were used in the modified toy Monte Carlo.

The distribution of worse lifetime solutions from the $B_s \to D_s\mu\nu$ decays was generated using the function 6.37. For the $B_s \to D_s\mu\nu X$ decays, the simple, featureless functions of the form 6.49 were used. The same parameters that used in the examination of systematic errors were used here. These distributions are not intended to be accurate models experimental data. However, they can be expected to given a reasonable estimate of the precision which will be achievable in measurements of a_{fs} and A_p.

One further change in relation to the previous toy Monte Carlo was the value of Δm. The previous toy had used $\Delta m = 20\,\mathrm{ps}$ on the grounds that this is the value used in Gauss. For the purposes of this study, the more realistic value of $\Delta m = 17.77\,\mathrm{ps}$ is used [11]. The model used to extract a_{fs} and A_p used the same functions to model the distributions of lifetimes as the Monte Carlo used to generate the data.

For one year's data taking, the expected number of events that can be analysed by the neutrino reconstruction method is 2.6×10^6. Of these, 2.2×10^6 events have solutions to equation 6.14. Analysing 2.2×10^6 events gives the following resolutions: $\sigma_{A_p} = 16.5 \times 10^{-3}$ and $\sigma_{a_{fs}} = 1.34 \times 10^{-3}$.

The k-factor method can use the full 2.5×10^6 events to measure a_{fs}. This gives a precision of 1.25×10^{-3}. A smaller number of events is used to obtain the precision on A_p for the k-factor method. This is because measurement of A_p with the k-factor method relies upon dividing the set of events into two subsets, based on $D_s\mu$ mass cut. The two subsets have $3\,\mathrm{GeV}c^{-2} < m_{D_s\mu} < 4.5\,\mathrm{GeV}c^{-2}$ and $m_{D_s\mu} > 4.5\,\mathrm{GeV}c^{-2}$. In [62], the lifetime resolution of both sets is modeled by a single Gaussian function. The higher mass sample contains 18.5 % of the events, and has a lifetime resolution of $\sigma_t = 0.12\,\mathrm{ps}$ [62, 63]. The lower mass sample has a lifetime resolution of $\sigma_t = 0.27\,\mathrm{ps}$, which is too large to be useful for an A_p measurement. This gives a resolution[10] of $\sigma_{A_p} = 20 \times 10^{-3}$.

It is also worth comparing the neutrino reconstruction method with the $B_s \to D_s\pi$ channel. Only 1.4×10^5 event are expected per year, but the expected lifetime resolution is $\sigma_t = 0.036\,\mathrm{ps}$. This leads to a precision on A_p of $\sigma_{A_p} = 5.3 \times 10^{-3}$, and on a_{fs} of $\sigma_{a_{fs}} = 5.35 \times 10^{-3}$. This is a better precision than the neutrino reconstruction method, despite the smaller number of events. There may be ways to improve the precision achieved with the neutrino reconstruction method, these are discussed in section 6.6.2. $B_s \to D_s\mu\nu$ is a better channel than $B_s \to D_s\pi$ for measuring a_{fs}, because lifetime resolution is less important and so the precision depends mainly on the number of events used.

6.6 Future Studies

The analysis presented is incomplete in the sense that it does not provide a method which could be applied to experimental data. Before LHC data could be analysed a full study of event selection would be needed, as would a better understanding of backgrounds. This is discussed in section 6.6.1.

In section 6.6.2 a few other studies which it may be useful to study in the future are presented. These differ from the studies discussed in section 6.6.1 in that they are not essential for a workable analysis, but may be beneficial. As these have not been studied in detail they are necessarily speculative, however some justification is given in each case for why they may be useful.

[10] This value does not come directly from [63], because the results in [63] assume a different number of events per year, based on older selection cuts [62]. The figure of $\sigma_{A_p} = 20 \times 10^{-3}$ comes from scaling the precision given in [63].

6.6.1 Necessary Studies

Future studies should switch from toy Monte Carlo data to fully reconstructed data. For this to happen, the selection of $B_s \to D_s\mu\nu$ events must be reoptimised with the most up to date Monte Carlo data. Backgrounds other than $B_s \to D_s\mu\nu X$ must be considered. Background studies also need to be included in the k-factor studies.

The double gaussian function used to model the lifetime resolution, does not give a perfect description of the Monte Carlo data. A more sophisticated modeling of this data should be undertaken. Again, this applies to the studies of the k-factor method, as well as the neutrino reconstruction method.

A investigation of why a smaller percentage of $B_s \to D_s\mu\nu$ events have solutions to equation 6.14, than $B_s \to D_s\mu\nu X$ events should be made.

6.6.2 Potentially Useful Studies

6.6.2.1 Complementary Use of the k-Factor Method and Neutrino Reconstruction Method.

Throughout this thesis, the neutrino reconstruction method has been presented as a competitor to the k-factor method. However, this need not be the case. The k-factor method could be used to analyse data where $m_{D_s\mu} > 4.5\,\mathrm{GeVc}^{-2}$, with the neutrino reconstruction method being used to analyse data with $m_{D_s\mu} < 4.5\,\mathrm{GeVc}^{-2}$. Figure 6.52 shows the lifetime resolution that the neutrino reconstruction method achieves for low mass data set. It is very similar to the lifetime resolution achieved for the whole data set. The neutrino reconstruction method is therefore able to analyse data the K-factor method cannot. $4.5\,\mathrm{GeVc}^{-2}$ may not be the best value of the mass cut if this approach is adopted, and so an optimisation of this cut should be undertaken.

6.6.2.2 The Angle Between the B_s and $D_s\mu$ Momenta

Improving the lifetime resolution would improve the resolution on A_p. Similarly, being able to divide the data into sets with higher and lower lifetime resolution can also improve

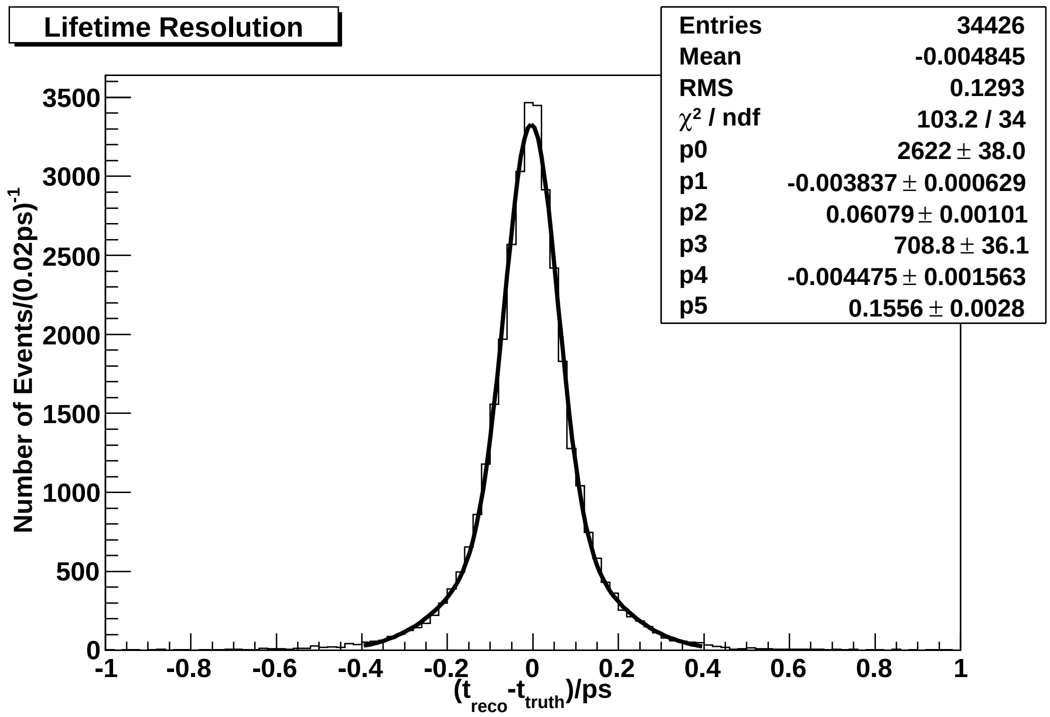

Figure 6.52: The lifetime resolution of reconstructed $B_s \to D_s\mu\nu$ events where $m_{D_s\mu} < 4.5\,\mathrm{GeVc^{-2}}$. The lifetime resolution for this subset of the data is very similar to the resolution for the whole data set.

Event	Solution	θ_{true}	θ_{reco}	$\frac{dP_{B_s}}{d\theta}_{true}$	$\frac{dP_{B_s}}{d\theta}_{reco}$	$P_{B_s}^{true}$	$P_{B_s}^{reco}$
445	PSRS	0.0270	0.0233	-47592	-11700	193	-
445	NSRS	0.0270	0.0233	39502	2980	97	123
10446	PSRS	0.00326	0.00228	5337	3780	397	-
10446	NSRS	0.00326	0.00228	-402	-277	109	108

Table 6.15: Reconstructed and truth information for two events. The worse momentum resolution in event 445 is due to worse angular resolution and a steep dependance of the momentum solutions on the angle.

the resolution of A_p. The B_s momentum solutions depend only on $m_{D_s\mu}$, the modulus of $P_{D_s\mu}$ and the angle between the B_s momentum and $D_s\mu$ momentum, θ. Of these, θ typically has the lowest resolution. The calculated momentum can also depend quite strongly on θ, this is shown for two events, designated event 446 and 10445, shown in figures 6.53 to 6.56. Cutting on $\mathrm{d}P_{B_s}/\mathrm{d}\theta$ and/or error on the measurement of θ may be a useful way of distinguishing events with good resolution from ones with poor resolution.

The momentum resolution of event 10446 is better than that of event 445, see table 6.15. The difference between the reconstructed and true values of θ is also smaller for event 445, as is $\mathrm{d}P_{B_s}/\mathrm{d}\theta$. These variables have potential as cuts, but it still must be determined how well the reconstructed value of $\mathrm{d}P_{B_s}/\mathrm{d}\theta$ reflects the truth value, and how well the error on θ reflects the difference between the truth and reconstructed values. A further difficulty with using $\mathrm{d}P_{B_s}/\mathrm{d}\theta$ is that its value differs for the two lifetime solutions.

6.6.2.3 Event Separation

The ratio of $B_s \to D_s\mu\nu$ and $B_s \to D_s\mu\nu X$ events affects the precision of the measurement of A_p. Figure 6.57 shows how the precision varies with the purity of $B_s \to D_s\mu\nu$ sample. The change in precision with the number of events in the sample is also shown. The level of event separation achieved with NNs in section 6.3.2 would be beneficial. However, whether the separation would be as successful with reconstructed data needs to be determined. It is worth noting that information from the calorimeters about photons or pions from excited D_s mesons might be useful for event separation. This was not used in section 6.3.2.

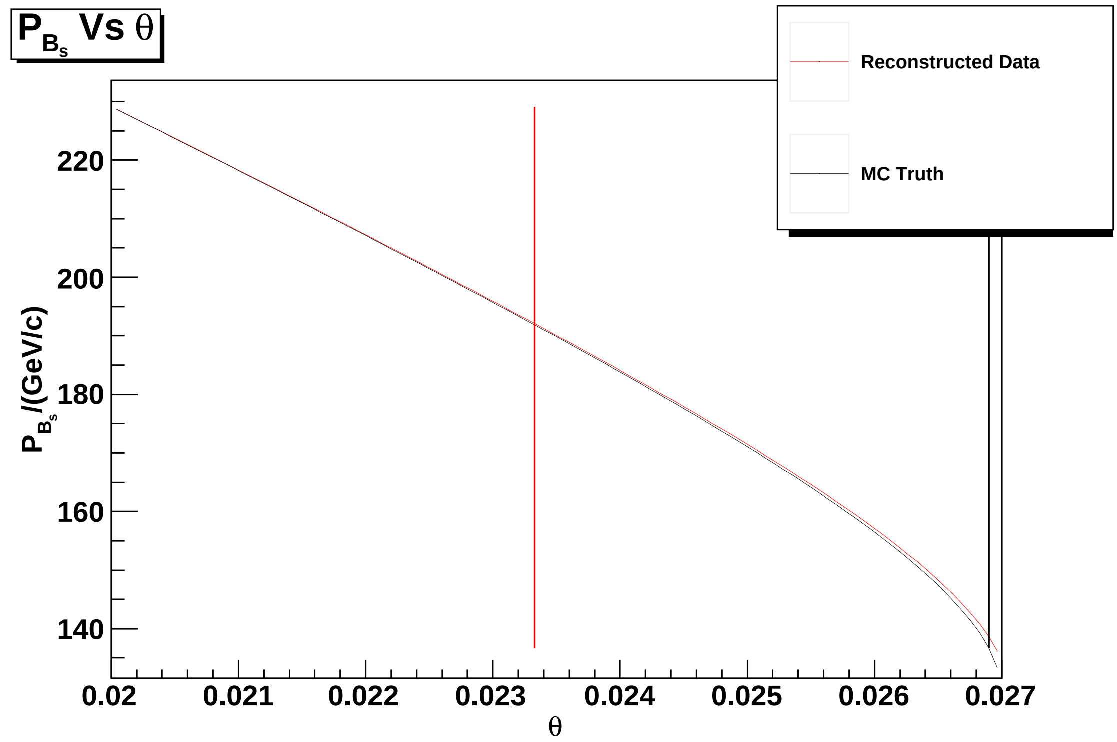

Figure 6.53: The dependance of P_{B_s} on θ for event 445, where the PSRS to equation 6.14 is taken. The vertical lines indicate the reconstructed and truth values of θ.

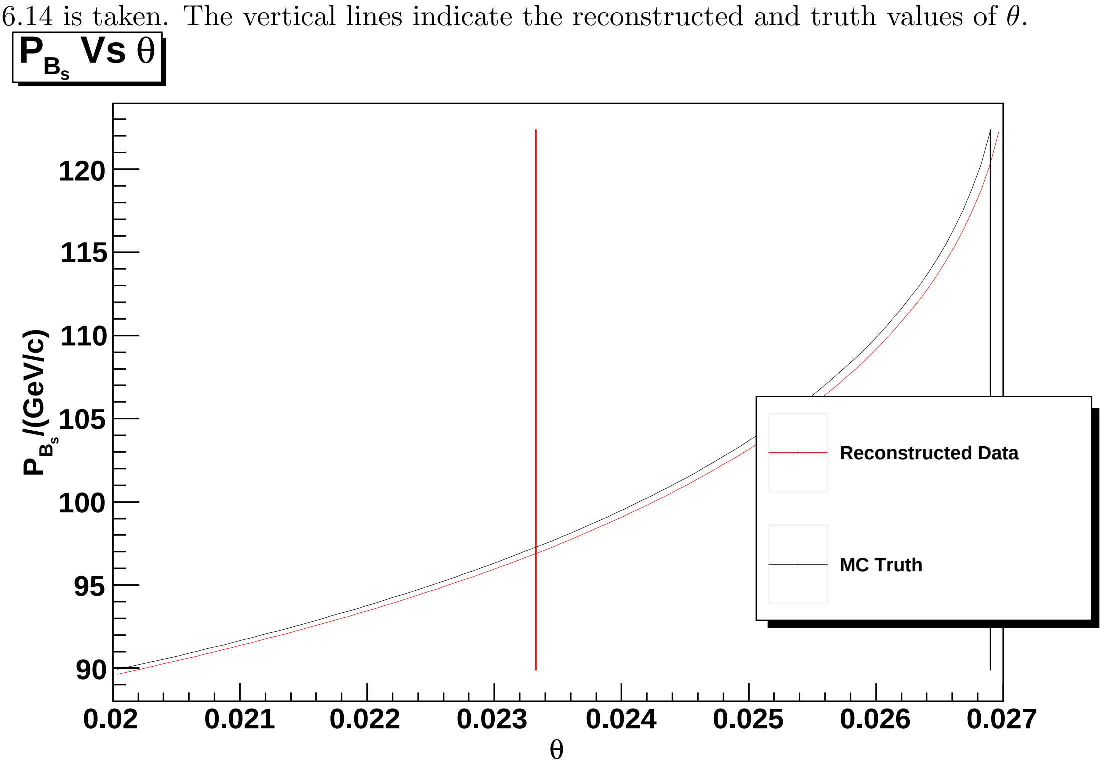

Figure 6.54: The dependance of P_{B_s} on θ for event 445, where the NSRS to equation 6.14 is taken. The vertical lines indicate the reconstructed and truth values of θ.

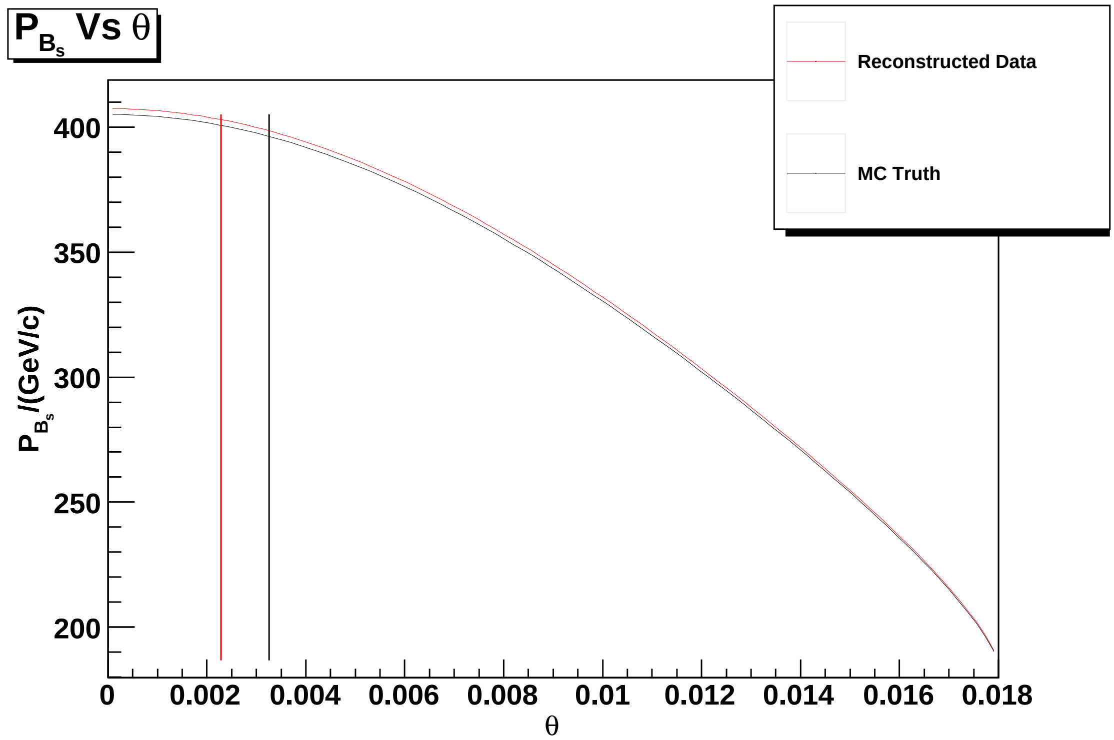

Figure 6.55: The dependance of P_{B_s} on θ for event 10446, where the PSRS to equation 6.14 is taken. The vertical lines indicate the reconstructed and truth values of θ.

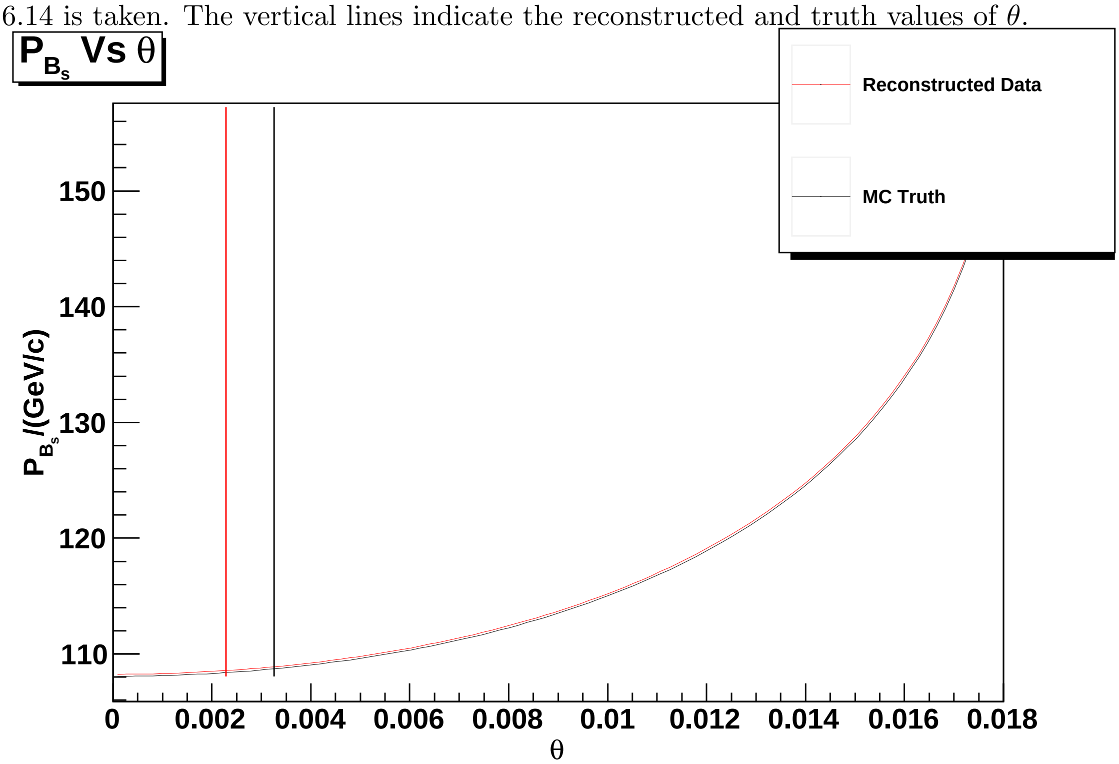

Figure 6.56: The dependance of P_{B_s} on θ for event 10446, where the NSRS to equation 6.14 is taken. The vertical lines indicate the reconstructed and truth values of θ.

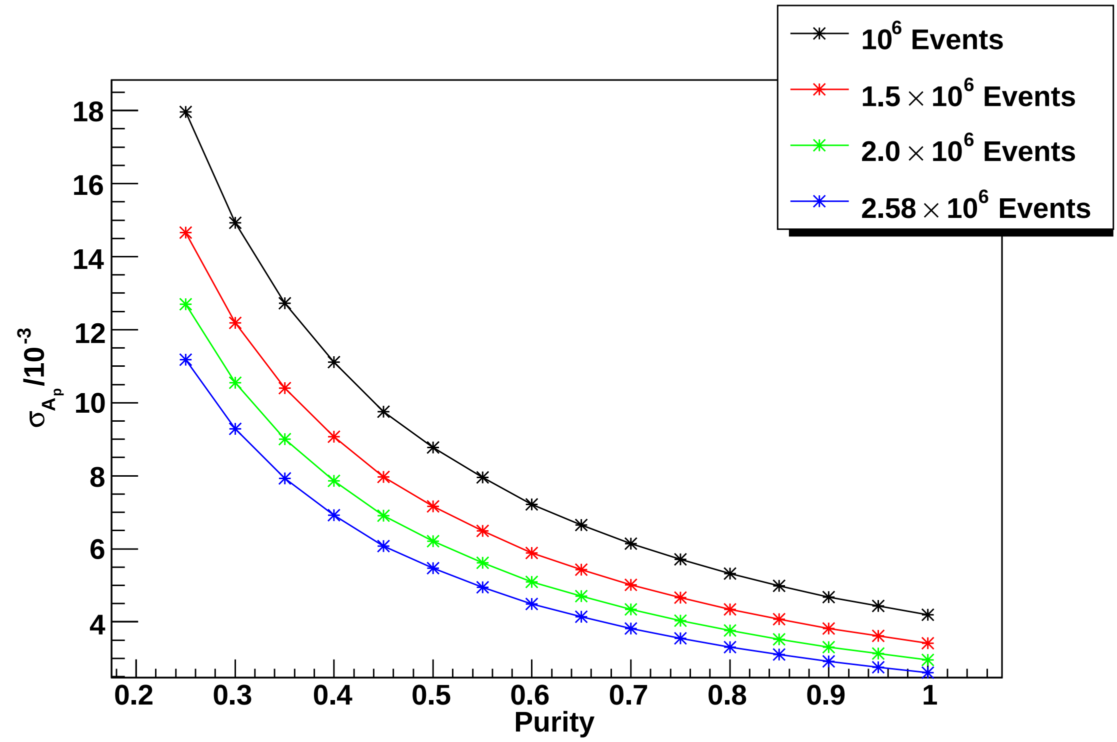

Figure 6.57: The precision of a measurement of A_p as a function of the fraction of $B_S \to D_s\mu\nu$ events in the event sample.

6.6.2.4 Event Recovery

Some events are lost because there is no real solution to equation 6.14. This is because position of the vertices, and the D_s and muon momentum are not perfectly measured. It may be possible to vary the values of these measurement, for events with no solutions, and thus produce a solution.

6.7 Conclusions

The measurement of CP violation in mixing and production asymmetry for B_s mesons was made for the LHCb. The study looked at time-dependent, un-tagged charge asymmetry in the semi-muonic decays $B_s \to D_s\mu\nu$ and $B_s \to D_s\mu X$. In particular the method of determining the B_s momentum from kinematic constraints was investigated.

The method relies upon a knowledge of the direction of the B_s momentum, gained from vertexing information, and combines it with measurements of the D_s and μ momenta. This method is referred to as the neutrino reconstruction method. This leads in to a two-fold ambiguity in the B_s lifetime.

It was found that distinguishing the two lifetimes is highly problematic, and an approach that does not rely on this information is necessary. This method was compared to an alternative approach, the k-factor method, in which the B_s momentum is estimated from the $D_s\mu$ momentum. The neutrino reconstruction method obtains precisions of $\sigma_{A_p} = 16.5 \times 10^{-3}$ and $\sigma_{afs} = 1.34 \times 10^{-3}$. The k-factor method obtains precisions of $\sigma_{A_p} = 20.0 \times 10^{-3}$ and $\sigma_{afs} = 1.25 \times 10^{-3}$. A greater precision for A_p can be achieved with the $B_s \rightarrow D_s\pi$ channel, however there may be ways of improving the $B_s \rightarrow D_s\mu\nu$ analysis further. These have been discussed briefly, but require further study before their usefulness can be understood.

Chapter 7

Conclusions

Various mirrors required for the RICH 1 detector have been characterised. The four spherical mirrors all had the required optical properties: $D_0 < 2.5\,\mathrm{mm}$ and radius of curvature $= 2700 \pm 27\mathrm{mm}$. The reflectivities of a series of sample mirrors, with different reflective coatings, were measured to ensure that a satisfactory reflectivity could be achieved. Ultimately, the design specification for reflectivity were met: $R > 70\,\%$ for wavelengths in the range $200\,\mathrm{nm} < \lambda < 250\,\mathrm{nm}$ and $R > 85\,\%$ in the wavelength range $250\,\mathrm{nm} < \lambda < 600\,\mathrm{nm}$. Three carbon fibre mirrors were tested to determine if the performance of the spherical mirrors would degrade due to irradiation or exposure to C_4F_{10}. No degradation of the reflectivity, D_0 or radius of curvature was observed after an 11 month exposure to C_4F_{10} and a 10 kGy radiation dose. It was found that the RICH 1 flat mirrors were manufactured to within the design specifications.

The main Monte Carlo generator used by LHCb is Pythia. This has been retuned so that the modeling of LEP data is more accurate; the previous tuning over produced various types of meson and gave too great a charged multiplicity in e^+e^- collisions. Specifically, the retuning processed focused on the variables PARJ(11),. . . ,PARJ(17) which control the probability that mesons are produced in various spin states. The retuning significantly improved the reproduction of LEP data. Retuning the PARJ variables resulted in a need to retune the parameters controlling multiple interaction in hadronic collisions, to ensure that the multiplicity in hadronic events was correctly simulated. The

$p_{\perp min}$ parameter was retuned. This parameter imposes a momentum cut-off in multiple interactions, and so limits the number of interactions that can take place. The $p_{\perp min}$ parameter is energy dependant, for the 14 TeV the retuned value is $p_{\perp min} = 3.45\pm$ GeV. The retuned settings predict a central multiplicity, $\langle dN_{ch}/d\eta\rangle_{|\eta|<0.25} = 6.03 \pm 0.02$ for LHC events. This is consistent with the phenomenologically extrapolated value of $\langle dN_{ch}/d\eta\rangle_{|\eta|<0.25} = 6.27 \pm 0.5$. The retuned values of the PARJ variables have been adopted by the LHCb collaboration. The retuned value of $p_{\perp min}$ has not been adopted, because LHCb now uses a later version of Pythia, which contains a new multiple interactions model. This new model has been tuned elsewhere [39].

An investigation into the LHCb's potential to measure CP violation in mixing and production asymmetry in B_s mesons, using semi-leptonic decays, was carried out. Reconstruction of the B_s momentum is not possible because the neutrino cannot be detected. This problem was overcome by using kinematic constraints and vertexing information to calculate the neutrino momentum. This method is called the neutrino reconstruction method. The neutrino momentum is given by the solution of a quadratic equation, meaning that for each decay two neutrino momenta are calculated. At least one of these is incorrect; in events where the primary vertex is incorrectly identified or the decay mode is $B_s \to D_s\mu\nu X$ rather than $B_s \to D_s\mu\nu$, both solutions are incorrect. It was found that distinguishing between the correct and incorrect solutions cannot be reliably done.

However, the asymmetries can be measured without any discrimination made between either solutions. This method was compared to an alternative method, the k-factor method, in which the B_s momentum is estimated rather than calculated. The neutrino reconstruction method achieved a resolution on a measurement of a_{fs}, which characterises CP violation, of $\sigma_{a_{fs}} = 16.5 \times 10^{-3}$ for 2.2×10^6 events. This corresponds to one year's data at full luminosity. The resolution for the production asymmetry is $\sigma_{A_p} = 1.34 \times 10^{-3}$. Further studies, involving a more detailed analysis of reconstructed data, are needed. However, the current investigation suggests that the neutrino reconstruction method provides a better resolution than the k-factor method. The k-factor method achieves a resolution of $\sigma_{A_p} = 20 \times 10^{-3}$. CP violation in mixing and production asymmetry can also be measured with the $B_s \rightarrow D_s\pi$ channel. This achieves precisions of $\sigma_{a_{fs}} = 5.35 \times 10^{-3}$ and $\sigma_{A_p} = 5.3 \times 10^{-3}$ with one year's data.

Appendix A

Modeling the Effect of Finite Lifetime Resolution

The decay rates derived in chapter 2 are of the form

$$\Gamma = f(a_{fs})e^{-\Gamma t}\left(\cosh\left(\frac{\Delta\Gamma t}{2}\right) \pm \cos(\Delta m t)\right) \tag{A.1}$$

where the $f(a_{fs})$ depend on the initial and final states of the decay. To model finite lifetime resolution these expressions are convoluted with a gaussian of width σ[1].

This gives

$$\Gamma = f(a_{fs})\int_0^\infty e^{-\Gamma t'}\left(\cosh\left(\frac{\Delta\Gamma t'}{2}\right) \pm \cos(\Delta m t')\right)\frac{1}{\sqrt{2\pi}\sigma}e^{\frac{(t-t')^2}{2\sigma^2}}\,\mathrm{d}t \tag{A.2}$$

It is useful to rewrite this as

$$\begin{aligned}
\Gamma &= f(a_{fs})\mathrm{Re}\left\{\int_0^\infty e^{-\Gamma t'}\left(\frac{1}{2}e^{\frac{\Delta\Gamma t'}{2}} + \frac{1}{2}e^{-\frac{\Delta\Gamma t'}{2}} \pm e^{i\Delta m t'}\right)\frac{1}{\sqrt{2\pi}\sigma}e^{\frac{(t-t')^2}{2\sigma^2}}\,\mathrm{d}t'\right\} &\text{(A.3)}\\
&= f(a_{fs})\mathrm{Re}\left\{\int_0^\infty \left(\frac{1}{2}e^{(-(\Gamma-\frac{1}{2}\Delta\Gamma)t'} + \frac{1}{2}e^{-(\Gamma+\frac{1}{2}\Delta\Gamma)t'} \pm e^{-(\Gamma-i\Delta m)t'}\right)\frac{1}{\sqrt{2\pi}\sigma}e^{\frac{(t-t')^2}{2\sigma^2}}\,\mathrm{d}t'\right\} &\text{(A.4)}
\end{aligned}$$

[1]More complicated models can be obtained easily from this by adding up Gaussians of different width.

Modeling finite resolution therefore reduces to the problem of calculating

$$\frac{1}{\sqrt{2\pi}\sigma}\int_0^\infty e^{-At'}e^{\frac{(t-t')^2}{2\sigma^2}}\mathrm{d}t' \tag{A.5}$$

for different values of A. Equation A.5 can be simplified if it is rewritten as

$$\frac{1}{\sqrt{2\pi}\sigma}e^{-At+\frac{1}{2}A^2\sigma^2}\int_0^\infty e^{-\frac{1}{2\sigma^2}(t'-(t-\sigma^2 A))^2}\mathrm{d}t' \tag{A.6}$$

Making the change of variables, $x = t'/\sigma$, gives

$$\begin{aligned}\frac{1}{\sqrt{2\pi}\sigma}\int_0^\infty e^{-\frac{1}{2\sigma^2}(t'-(t-\sigma^2 A))^2}\mathrm{d}t' &= \frac{1}{\sqrt{2\pi}}\int_0^\infty e^{-\frac{1}{2}(x-(\frac{t}{\sigma}-\sigma A))^2}\mathrm{d}x \\ &= \frac{1}{\sqrt{2\pi}}\int_{-\infty+(\frac{t}{\sigma}-\sigma A)}^{(\frac{t}{\sigma}-\sigma A)} e^{-\frac{1}{2}x^2}\mathrm{d}x\end{aligned} \tag{A.7}$$

For real A,

$$\frac{1}{\sqrt{2\pi}}\int_{-\infty+(\frac{t}{\sigma}-\sigma A)}^{(\frac{t}{\sigma}-\sigma A)} e^{-\frac{1}{2}x^2}\mathrm{d}x = \frac{1}{\sqrt{2\pi}}\int_{-\infty}^{(\frac{t}{\sigma}-\sigma A)} e^{-\frac{1}{2}x^2}\mathrm{d}x = \mathrm{Freq}\left(\frac{t}{\sigma}-\sigma A\right) \tag{A.8}$$

where the frequency function, Freq, is defined by

$$\mathrm{Freq}(y) = \frac{1}{\sqrt{2\pi}}\int_{-\infty}^{y} e^{-\frac{1}{2}x^2}\mathrm{d}x \tag{A.9}$$

and is related to the error function by

$$\mathrm{Freq}(y) = \frac{1}{2}+\frac{1}{2}\mathrm{erf}\left(\frac{y}{\sqrt{2}}\right) \tag{A.10}$$

In ROOT the Freq function is implemented with TMath::Freq.

For the complex $A = \Gamma - i\Delta m$, equation A.7 becomes

$$\frac{1}{\sqrt{2\pi}}\int_{-\infty+(\frac{t}{\sigma}-\sigma A)}^{(\frac{t}{\sigma}-\sigma A)} e^{-\frac{1}{2}x^2}\mathrm{d}x = \frac{1}{2}+i\frac{1}{2}\mathrm{erfi}\left(\frac{-\Delta m\sigma + i\left(i\frac{t}{\sigma}-\sigma\Gamma\right)}{\sqrt{2}}\right) \tag{A.11}$$

where erfi is the imaginary error function, related to the real error function by

$$\text{erfi}(z) = -i\text{erf}(iz) \tag{A.12}$$

The imaginary error function is not implement directly in ROOT. However, it is related to the complex error function, w, which is implemented, by

$$w(z) = e^{-z^2}(1 - i\text{erfi}(-z)) \tag{A.13}$$

The real and imaginary parts of $w(z)$ are calculated in ROOT by RooMath::FastComplexErrFuncRe and RooMath::FastComplexErrFuncIm respectively. Using equations A.8 and A.11, equation A.2 becomes

$$\begin{aligned}
\Gamma/f(a_{fs}) = \int_0^\infty e^{-\Gamma t'} \left(\cosh\left(\frac{\Delta\Gamma t'}{2}\right) \pm \cos(\Delta m t')\right) \frac{1}{\sqrt{2\pi}\sigma} e^{\frac{(t-t')^2}{2\sigma^2}} \mathrm{d}t \\
= \frac{1}{2}\exp\left(-\left(\Gamma - \frac{1}{2}\Delta\Gamma\right)t + \frac{1}{2}\sigma^2\left(\Gamma - \frac{1}{2}\Delta\Gamma\right)^2\right) \text{Freq}\left(\frac{t}{\sigma} - \sigma\left(\Gamma - \frac{1}{2}\Delta\Gamma\right)\right) \\
+\frac{1}{2}\exp\left(-\left(\Gamma + \frac{1}{2}\Delta\Gamma\right)t + \frac{1}{2}\sigma^2\left(\Gamma + \frac{1}{2}\Delta\Gamma\right)^2\right) \text{Freq}\left(\frac{t}{\sigma} - \sigma\left(\Gamma + \frac{1}{2}\Delta\Gamma\right)\right) \\
\pm\text{Re}\left\{\exp\left(-\Gamma t + \frac{1}{2}\sigma^2\Gamma 2 - \frac{1}{2}\Delta m^2\sigma 2\right)\exp(i\Delta m(t - \Gamma\sigma^2))\right. \\
\left.\times\left(\frac{1}{2} + i\frac{1}{2}\text{erfi}\left(\frac{-\Delta m\sigma + i\left(\frac{t}{\sigma} - \sigma\Gamma\right)}{\sqrt{2}}\right)\right)\right\}
\end{aligned} \tag{A.14}$$

taking out common factors

$$\begin{aligned}\int_0^{\infty} e^{-\Gamma t'} \left(\cosh\left(\frac{\Delta\Gamma t'}{2}\right) \pm \cos(\Delta m t')\right) \frac{1}{\sqrt{2\pi}\sigma} e^{\frac{(t-t')^2}{2\sigma^2}} \mathrm{d}t \\ = e^{\Gamma t} e^{\frac{1}{2}\Gamma^2 \sigma 2} \Big[e^{\frac{1}{8}\sigma^2\Delta\Gamma^2} \{ \\ \frac{1}{2} e^{\frac{1}{2}\Delta\Gamma(t-\sigma^2\Gamma)} \mathrm{Freq}\left(\frac{1}{2} - \sigma\left(\Gamma - \frac{1}{2}\Delta\Gamma\right)\right) \\ + \frac{1}{2} e^{-\frac{1}{2}\Delta\Gamma(t-\sigma^2\Gamma)} \mathrm{Freq}\left(\frac{1}{2} - \sigma\left(\Gamma + \frac{1}{2}\Delta\Gamma\right)\right) \\ \pm e^{-\frac{1}{2}\Delta m^2\sigma^2} \mathrm{Re}\Big\{ e^{i\Delta m(t-\Gamma\sigma^2)} \\ \times \left(\frac{1}{2} + i\frac{1}{2}\mathrm{erfi}\left(\frac{\Delta m\sigma + i(\frac{t}{\sigma} - \sigma\Gamma)}{\sqrt{2}}\right)\right)\Big\}\Big]\end{aligned} \tag{A.15}$$

In the limit of $t \gg \sigma$ the Freq term tends towards unity and the erfi term towards i. Equation A.15 then simplifies greatly

$$\begin{aligned}\int_0^{\infty} e^{-\Gamma t'} \left(\cosh\left(\frac{\Delta\Gamma t'}{2}\right) \pm \cos(\Delta m t')\right) \frac{1}{\sqrt{2\pi}\sigma} e^{\frac{(t-t')^2}{2\sigma^2}} \mathrm{d}t \\ = e^{-\Gamma t} e^{\frac{1}{2}\Gamma^2\sigma^2} \left[e^{\frac{1}{8}\Delta\Gamma^2} \cosh\left(\frac{1}{2}(t - \sigma^2\Gamma)\right) \pm e^{-\frac{1}{2}\Delta m^2\sigma^2} \cos(\Delta m(t - \Gamma\sigma^2)\right]\end{aligned} \tag{A.16}$$

Bibliography

[1] S. Weinberg, A Model of Leptons, Phys. Rev. Lett. 19 (1967) 1264-1266.

[2] A. Salam and J. C. Ward, Gauge theory of elementary interactions, Phys.Rev. 136 (1964) B763-B768

[3] J. Cronin et al., Evidence for the 2π Decay of the K_2^0 Meson, Phys Rev Lett 13 (138), 1964

[4] A. D. Sakharov, Violation of CP Invariance, c Asymmetry, and Baryon Asymmetry of the Universe, Pisma Zh. Eksp. Teor. Fiz. 5 (1967) 32-35

[5] The Babar Physics Book, P.F. Harrison and H.R. Quinn, SLAC-R-504, October 1998

[6] CP Violation, I.I. Bigi and A.I Sanda, Cambridge University Press, 2000

[7] L. Wolfenstein, Parameterization of the Kobayashi-Maskawa Matrix, Phys. Rev. Lett. 51 (1983) 1945.

[8] Review of Particle Physics, C. Amsler et al., Physics Letters B667, 1 (2008)

[9] I. Dunietz et al, In Pursuit of New Physics with B_s Decays, CERN-TH/2000-333, 2000

[10] Z. Ligeti et al., Implications of the CP asymmetry in semileptonic B decay, arXiv:hep-ph/0604112 (2006).

[11] The Heavy Flavour Averagin Group: http://www.slac.stanford.edu/xorg/hfag/

[12] T. Aaltonen et al., the CDF Collaboration, Measurement of CP asymmetry in semileptonic B decays, CDF-note 9015, 070816 (2007), available through http://www-cdf.fnal.gov/physics/new/bottom/070816.blessed-acpbsemil/public-acp-bsemil.ps

[13] V. M. Abazov et al., the D0 Collabotation,Combined D0 Measurements Constraining the CP-violating Phase and Width Difference in the B_s^0 System, http://arxiv.org/abs/hep-ex/0702030

[14] R. Lambert and F. Muheim, Generator Study of the Production Asymmetry in LHCb, LHCb note 2007-124, October 2007

[15] E. Norrbin and T. Sjöstrand, Production and Hadronization of Heavy Quarks, Eur. Phys. J. C. 17 (2000) pp. 137-161.

[16] E. Norrbin and R. Vogt, Section 5 in Chapter Bottom production, in The Proceedings of the 2000 Workshop on Standard Model Physics (and more) at the LHC, CERN, Geneva 25th May 1999. G. Altareli and M. L. Mangano eds. CERN- 2000-004 (2000).

[17] The LHCb Collaboration, The LHCb Detector at the LHC, JINST 3 (2008) S08005

[18] The LHCb Collaboration, LHCb Reoptimized Detector and Performance, CERN/LHCC 2003-030, September 2003.

[19] The LHCb Collaboration, LHCb TDR 3: RICH TDR, CERN/LHCC 2000-037, September 2000.

[20] The LHCb Collaboration, LHCb TDR 5: VELO TDR, CERN/LHCC 2001-0011, May 2001.

[21] The LHCb Collaboration, LHCb TDR 1: LHCb Magnet TDR, CERN/LHCC 2000-007, January 2000.

[22] The LHCb Collaboration, LHCb TDR8: LHCb Inner Tracker, CERN/LHCC 2002-029, November 2002

[23] The LHCb Collaboration, LHCb TDR 6: LHCb Outer Tracker, CERN/LHCC 2001/024, September 2001.

[24] The LHCb Collaboration, LHCb TDR2: LHCb Calorimeters TDR¡ CERN/LHCC 2000-036, September 2000.

[25] The LHCb Collaboration, LHCb TDR 4: Muon System TDR, CERN/LHCC 2001-010, May 2001.

[26] The LHCb Collaboration, LHCB TDR 10: Trigger System TDR, CERN LHCC 2003-031, LHCb TDR 10, September 2003

[27] The LHCb Collaboration, LHCb TDR 11: LHCB Computing, CERN/LHCC 2005-019, June 2005.

[28] The Pythia website: http://home.thep.lu.se/ torbjorn/Pythia.html

[29] The Herwig website: http://hepwww.rl.ac.uk/theory/seymour/herwig/

[30] The EvtGen website: http://www.slac.stanford.edu/ lange/EvtGen/

[31] The Geant4 website: http://geant4.web.cern.ch/geant4/

[32] The Ganga website: http://ganga.web.cern.ch/ganga/

[33] COMPAS, Research and Development Consortium, Turnov, Czech Republic. Manufactourers of the RICH 1 flat mirrors.

[34] Composite Mirror Applications Inc., the manufactourers of the RICH 1 spherical mirrors: http://www.compositemirrors.com/index.htm

[35] SESO, the company which coated the RICH 1 spherical mirrors: http://www.seso.com/index.htm

[36] Perkin Elmer, manufactourers of the spectrophotometer used to measure the reflectivity of various mirror samples: http://www.perkinelmer.com

[37] The LabView website: http://www.ni.com/labview/

[38] M. Laub, Development of opto-mechanical tools and procedures for the new generation of RICH-detectors at CERN, Ph.D. Thesis, LHCb 2001-130; Geneva, CERN.

[39] A. Muir, Pythia Minimum Bias Studies and the RICH 1 Spherical Mirror for the LHCb Experiment, University of Bristol PhD Thesis, 2006.

[40] Study of radiation in the LHCb cavern: http://lhcb-background.web.cern.ch/lhcb-background/Radiation/RadLevels.htm

[41] http://ftgsoftware.com/

[42] M. Taborelli, EDMS document 3-TS-MME-SC-AES-2006-08-01, https://edms.cern.ch/document/775574/1

[43] M. Taborelli, EDMS document 8-TS-MME-SC-AES-2006-18-06, https://edms.cern.ch/document/809926/1

[44] G.J Barber et al., Development of lightweight carbon-fiber mirrors for the RICH 1 detector of LHCb, Nuclear Instruments and Methods in Physics Research A 593 (2008) 624-637

[45] R. Barate et al, Resonant structure and flavour tagging in the $B\pi^{\pm}$ system using fully reconstructed B decays, Physics Letters B 425 (1998) 215-226

[46] R. Akers et al, Observations of $\pi - B$ charge-flavour correlations and resonant $B\pi$ and BK production, Z. Phys. C 66,19-29 (1995)

[47] P. Abreu et al, Observation of orbitally excited B mesons, Physics Letters B 345 (1995) 598-608

[48] T Affolder et al, Observation of orbitally excited B mesons in $p\bar{p}$ collisions at $\sqrt{s} = 1.8\,\mathrm{TeV}$, Physical Review D, Volume 64, 072002, 2001

[49] N. Brook et al, A Study on the tuning of minimum bias events at LHCb, LHCb 2005-023.

[50] G D Lafferty et al, 1995, J.Phys.G.Nucl.Part.Phys: 21 A1-A151

[51] Torbjörn Sjörstand et al, Pythia 6.3 Physics and Manual, hep-ph/0308153 LU TP 03-38, August 2003

[52] Minuit homepage: http://seal.web.cern.ch/seal/workpackages/mathlibs/minuit/index.html

[53] ROOT homepage: http://root.cern.ch/

[54] DELPHI Collaboration, Tuning and test of fragmentation models based on identified and precision event shape data, Z. Phys C 73, 11-59, 1996.

[55] Alpgard et al, Comparison of p anti-p and pp interactions at =53 GeV, Phys. Lett. B, 122b, 183, 1982.

[56] Alner et al, Scaling of pseudorapidity distributions at C.M. energies up to 0.9 TeV, Z. Phys., C33, 1, 1986.

[57] Alner et al, A general study of proton-antiproton physics at =546 GeV, Phys. Resp., 154, 247-383, 1987.

[58] Abe et al., Pseudorapidity distributions of charged particles produced in anti-p p interactions at =630 GeV and = 1800 GeV, Phys. Rev. D, 41, 2230, 1990.

[59] Vladimir Uvarov, Inclusive Particle Production at LEP, http://delphiwww.cern.ch/pubxx/conferences/moriond00

[60] P. Abreu et al, Tuning and test of fragmentation models based on identified particles and precision event shape data, Z. Phys. C73, 11-59, 1996

[61] A talk given by Patrick Robbe concerning LHCb Monte Carlo data, which notes the inclusion of the retune Pythia settings: http://indico.cern.ch/getFile.py/access?contribId=8resId=1materialId=slidesconfId=36700

[62] Olivier Leroy et al, Selection of $B_s^0 \to D_s^- \mu^+ \nu_\mu$ events in LHCb, LHCb-note 2007-029, April 2007

[63] Paul Szczypka, Study of the Sensitivity to Flavour-Specific Asymmetries with the LHCb Detector, CERN-THESIS-2008-045, 2008.

[64] Nick Brook et al, LHCb's Potential to Measure Flavour-Specific CP-Asymmetry in Semileptonic and Hadronic B_s^0 Decays, LHCb-note 2007-054, January 2008

[65] Minuit homepage:
http://seal.web.cern.ch/seal/workpackages/mathlibs/minuit/index.html

[66] Neural Networks by J.G. Taylor, published by Alfred Waller Ltd, 1995.

[67] Neural Network Desaign by Hagan, Demuth and Beale, published by PWS Publishing Complany, 1996.

[68] TMultiLayerPerceptron documentation:
http://root.cern.ch/root/html310/TMultiLayerPerceptron.html

[69] Rob Lambert, LHCb Hybrid Photon Detectors and Sensitivity to Flavour Specifc Asymmetry in Neutral B-Meson Mixing, CERN-THESIS-2009-001, 2009

[70] J. Borel et al, The $B_s \to D_s^- \pi^+$ and $B_s \to D_s^\mp K^\pm$ selections, LHCb Note 2007-017, 13 April 2007

[71] The TGenPhaseSpace website: http://root.cern.ch/root/html/TGenPhaseSpace.html

[72] A talk given by Rob Lambert, on his DC09 work:
http://indico.cern.ch/conferenceDisplay.py?confId=77071